

Tailored Nanophononic Wavefields  
Probed by Nano-focused Electron Pulses  
in Ultrafast Transmission Electron Microscopy

angenommene

DISSERTATION

zur Erlangung des mathematisch-naturwissenschaftlichen Doktorgrades

„Doctor rerum naturalium“

der Carl-von-Ossietzky Universität Oldenburg

von

Nora Bach

aus Celle

Oldenburg, 2022

Mitglieder der Prüfungskommission

Gutachter: Prof. Dr. Sascha Schäfer, Institut für Physik

Zweitgutachter: Prof. Dr. Christoph Lienau, Institut für Physik

Weiteres Mitglied der Prüfungskommission

Prof. Dr. Christian Schneider, Institut für Physik

Tag der mündlichen Prüfung: 19. Dezember 2022

**Abstract**

Nanomaterials and -technologies such as nano-electromechanical systems (NEMS) play an increasingly important role in everyday life. In spatially inhomogeneous systems like nanostructured semiconductor membranes, excitation mechanisms and relaxation processes are often governed by pronounced interfacial couplings and local excitations. Whereas a broad range of experimental techniques has been developed to characterize ultrafast dynamics, local probing methods capable of resolving spatiotemporal processes in the femtosecond-nanometer range still pose experimental challenges. Ultrafast transmission electron microscopy (UTEM) requires high-brightness femtosecond electron sources and a detailed understanding of Coulomb interactions in nanoscale electron pulses for further method improvement.

Addressing this prerequisite for future schemes of laser-driven electron sources, the first part of this thesis reports on the experimental and theoretical investigations of electron pulses with high charge-densities emitted from a laser-driven Schottky field emitter. The impact of stochastic and mean-field Coulomb effects on transverse and longitudinal pulse properties is experimentally characterized, while numerical simulations provide microscopic insights into the relevant parameters that determine the pulse quality. The systematically evaluated pulse properties allow for identifying optimized electron-source parameters for ultrafast electron experiments and form the basis for the development of advanced photoemitters.

As a prototypical nanostructure for optically inducing nanoscale acoustic waveforms, a metal/semiconductor heterostructure is introduced which consists of a Si membrane patterned with a Pt stripe. Analytical modelling within the framework of continuum elasticity theory yields important insights into the impact of layer interfaces on acoustic resonance frequencies and the spatial localization of phonon eigenmodes in the bilayer region. The propagating distortion wave launched at the Si/Pt interface is locally monitored with high spatiotemporal resolution by ultrafast convergent beam electron diffraction. Numerical simulations reveal the dominant contributions to the time-dependent deformation gradient tensor. The overall microscopic origin of the observed membrane bending and high-frequency oscillations is found to be consistent with a superposition of Lamb waves frequency-matched to local strain resonances. The provided versatile platform for the generation of confined nanophononic fields combined with technical UTEM improvements will further contribute to a better understanding of phonon couplings in nanoscale systems and enable progress in developing novel semiconductor-heterostructure-based NEMS.



---

# Contents

---

<b>List of Figures</b>	<b>ix</b>
<b>List of Tables</b>	<b>xi</b>
<b>List of Movies</b>	<b>xiii</b>
<b>List of Abbreviations and Symbols</b>	<b>xv</b>
<b>1 Introduction</b>	<b>1</b>
<b>2 Fundamentals of ultrafast transmission electron microscopy and ultrashort electron pulses</b>	<b>7</b>
2.1 Conventional TEM instrumentation . . . . .	10
2.2 Image contrast . . . . .	13
2.3 Tip-shaped electron sources . . . . .	15
2.3.1 ZrO/W Schottky field emitter . . . . .	17
2.3.2 Cold field emitter . . . . .	19
2.4 Phase-space description of electron beams . . . . .	20
2.5 Energy spread and dispersive broadening of electron pulses . . . . .	23
2.5.1 Intrinsic energy spread . . . . .	24
2.5.2 Stochastic Coulomb interactions and mean-field effects . . . . .	24
2.5.3 Spatial pulse broadening . . . . .	25
2.5.4 Spectral pulse broadening . . . . .	27
2.5.5 Temporal pulse broadening and chirp . . . . .	28
2.5.6 Longitudinal Boersch effect and stochastic virtual source size growth	31
<b>3 Coulomb interactions in high-coherence femtosecond electron pulses from tip emitters</b>	<b>35</b>

3.1	Introduction . . . . .	38
3.2	Setup . . . . .	39
3.3	Coulomb interactions close to the emitter tip . . . . .	40
3.4	Transverse beam properties and spectral width of electron pulses . . . . .	42
3.5	Temporal structure of high-charge electron pulses . . . . .	44
3.6	Simulation . . . . .	45
3.7	Discussion . . . . .	47
3.8	Conclusion . . . . .	49
3.9	Supplementary Material . . . . .	49
<b>4</b>	<b>Nanophononic waveguides</b>	<b>51</b>
4.1	Basic principles of elasticity theory . . . . .	52
4.1.1	Tensor representation of structural deformations . . . . .	52
4.1.2	Symmetry simplifications . . . . .	55
4.1.3	Compact symbolic tensor notation . . . . .	57
4.1.4	Elastodynamic wave equation . . . . .	58
4.1.5	Bulk phonon dispersions . . . . .	59
4.1.6	Velocity surfaces . . . . .	61
4.2	Guided acoustic waves in confined nanostructures . . . . .	63
4.2.1	Lamb waves in isotropic media . . . . .	64
4.2.2	Anisotropic Lamb wave description . . . . .	66
4.2.3	Transverse magnetic modes in a planar dielectric waveguide . . . . .	71
<b>5</b>	<b>Diffraction theory and diffractive probing of ultrafast structural dynamics</b>	<b>77</b>
5.1	Diffraction modes in TEM . . . . .	78
5.2	Kinematical scattering theory . . . . .	81
5.2.1	First Born approximation for weak interaction potentials . . . . .	82
5.2.2	Diffraction of a perfect crystal . . . . .	84
5.2.3	Excitation error and shape function . . . . .	86
5.3	Dynamical scattering theory . . . . .	89
5.3.1	Bloch wave method . . . . .	90
5.3.2	Two-beam approximation . . . . .	92
5.3.3	Analogy with Rabi-oscillations in two-level systems . . . . .	95
5.3.4	Determination of sample thickness . . . . .	95
5.3.5	Howie-Whelan equations . . . . .	96

5.4	Thermal effects on scattering intensities . . . . .	98
5.4.1	Debye-Waller factor in the Debye model . . . . .	99
5.4.2	Thermal diffuse scattering . . . . .	100
5.5	Structural dynamics studied by UTEM . . . . .	101
<b>6</b>	<b>Ultrafast strain propagation and acoustic resonances in nanoscale bilayer systems</b>	<b>105</b>
6.1	Main text . . . . .	108
6.2	Supplementary material . . . . .	118
6.2.1	Atomic displacement dynamics in a linear chain model . . . . .	118
6.2.2	Analytical model for the description of resonant strain modes . . . . .	119
6.2.3	Acoustic Impedances and Sound Velocities for common materials . . . . .	123
6.2.4	Optical bilayer Fabry-Pérot interferometer . . . . .	124
<b>7</b>	<b>Tailored nanophononic wavefield in a patterned bilayer system probed by ultrafast convergent beam electron diffraction</b>	<b>127</b>
7.1	Introduction . . . . .	132
7.2	Ultrafast convergent beam electron diffraction . . . . .	133
7.3	Numerical simulation of nanophononic distortion field . . . . .	135
7.4	Lamb wave decomposition . . . . .	139
7.5	Conclusion . . . . .	142
7.6	Supplementary material . . . . .	145
7.6.1	Sample system . . . . .	145
7.6.2	Ultrafast transmission electron microscope in CBED mode . . . . .	145
7.6.3	Extraction of Bragg-scattered line profiles . . . . .	146
7.6.4	Convergent beam electron diffraction pattern . . . . .	147
7.6.5	Line sensitivity to specific tensor components and reciprocal lattice vector components . . . . .	148
7.6.6	Theoretical description of Bragg line profiles . . . . .	150
7.6.7	Numerical simulation of structural dynamics in Pt-stripe/Si-membrane heterostructure . . . . .	150
7.6.8	Acoustic Lamb wave description for anisotropic silicon . . . . .	152
7.6.9	Debye Waller analysis . . . . .	155
<b>8</b>	<b>Summary and perspectives</b>	<b>157</b>
8.1	Future developments of laser-driven electron sources . . . . .	160

8.1.1	Perspectives for laser-driven ZrO/W emitters . . . . .	160
8.1.2	Novel pulsed electron sources based on tungsten tips . . . . .	161
8.1.3	Pulse compression schemes . . . . .	162
8.2	Ultrafast nanodiffraction in UTEM . . . . .	163
8.2.1	Advanced local probing with probe aberration correctors . . . . .	163
8.2.2	Inelastic scattering effects and energy filtering . . . . .	166
8.2.3	Lamb wave interactions and phonon confinement . . . . .	167
8.2.4	Nonlinear phononics . . . . .	169
<b>A</b>	<b>Short introduction into Rabi-oscillations</b>	<b>171</b>
	<b>Bibliography</b>	<b>173</b>
	<b>Publications, conferences and awards</b>	<b>227</b>
	<b>Danksagung</b>	<b>231</b>

---

## List of Figures

---

2.1	Schematic illustration of the stroboscopic optical-pump/electron-probe scheme in a UTEM . . . . .	8
2.2	Schematic of a TEM and its basic operation modes . . . . .	11
2.3	High-resolution TEM imaging . . . . .	14
2.4	Potential landscape and geometry of a tip-shaped electron emitter. . . . .	17
2.5	Electron pulse properties of the Göttingen UTEM instrument. . . . .	18
2.6	Gaussian-beam propagation . . . . .	23
2.7	Dispersive and charge-induced electron pulse broadening . . . . .	25
2.8	Spatiotemporal evolution of the electron density emitted from a flat photocathode . . . . .	27
2.9	Dispersion-induced shear and chirp of electron pulses . . . . .	30
2.10	Spatial coherence of electron pulses influenced by stochastic Coulomb interactions . . . . .	33
3.1	Experimental and simulation geometry and phase space representations . .	41
3.2	Experimental beam properties of photoelectron pulses . . . . .	43
3.3	Longitudinal electron pulse characterization . . . . .	45
3.4	Simulated electron pulse properties . . . . .	46
4.1	Compression, pure shear, and rotational distortions in crystal lattices . . .	53
4.2	Components of the stress tensor . . . . .	54
4.3	Elastic stiffness constants for different crystal structures . . . . .	57
4.4	Relationships between stress, strain, and displacement . . . . .	59
4.5	Phonon dispersion curves of bulk silicon . . . . .	61
4.6	Sound velocities in bulk and confined media . . . . .	63
4.7	Lamb waves in acoustic waveguides . . . . .	67
5.1	Diffraction of a Pt/Si heterostructure . . . . .	79
5.2	Basic principle of CBED . . . . .	80

5.3	Diffraction and momentum transfer at a crystal lattice . . . . .	83
5.4	Schematic representation of the excitation error in a CBED pattern . . . . .	87
5.5	Two-beam approximation in scattering theory and Rabi-oscillations . . . . .	94
5.6	Thickness measurement of crystalline samples . . . . .	96
5.7	Bright-field imaging of strain waves in UTEM . . . . .	102
5.8	Ultrafast dark-field domain imaging of charge-density wave dynamics . . . . .	103
6.1	Strain dynamics in a nanoscale Pt/Si-bilayer film numerically simulated by a discrete one-dimensional linear chain model . . . . .	111
6.2	Acoustic resonance frequencies in a metal/silicon bilayer . . . . .	113
6.3	Acoustic mode profile and wave localization . . . . .	114
6.4	Schematic drawing of bilayer system . . . . .	119
6.5	Resonance frequencies for the metal/semiconductor bilayer system with corresponding maximum displacement for selected frequency branches . . . . .	122
6.6	Resonance frequencies for the metal/semiconductor bilayer and common values for acoustic impedances and sound velocities . . . . .	123
6.7	Optical resonance spectrum of a bilayer Fabry-Perot interferometer . . . . .	125
7.1	Strain dynamics in a silicon membrane patterned with tungsten bars and void-arrays . . . . .	129
7.2	Ultrafast convergent beam electron diffraction on a Pt/Si heterostructure . . . . .	134
7.3	Transient Bragg line profiles . . . . .	136
7.4	Simulated acoustic wave dynamics close to the Pt-stripe/Si-membrane het- erostructure . . . . .	137
7.5	Temporal evolution of Bragg line profile . . . . .	140
7.6	Mode decomposition of the acoustic wave field . . . . .	142
7.7	Spatiotemporal dynamics of the acoustic wave field . . . . .	143
7.8	Delay-dependent angular shifts of exemplary Bragg lines . . . . .	146
7.9	Determining scaling factor of the numerical results . . . . .	152
7.10	Comparison of the numerically obtained displacement field . . . . .	155
7.11	Debye Waller analysis for the Pt/Si bilayer region . . . . .	156
8.1	CBED patterns of a silicon membrane pre and after energy-filtering . . . . .	166
8.2	Nonlinear dynamical phenomena in 2D material resonators . . . . .	170

---

## List of Tables

---

4.1	Overview of tensors needed to describe structural deformations . . . . .	55
6.1	Material properties of the Pt/Si-bilayer . . . . .	110



---

## List of Movies

---

Movie 3.1 Diverging electron pulse . . . . .	49
--	----



---

## List of Abbreviations and Symbols

---

### Abbreviations

Abbreviation	Description
BFP	Back-focal plane
CBED	Convergent beam electron diffraction
CCD	Charge-coupled device
CDW	Charge-density wave
CFEG	Cold-field emission gun
CL, CLA	Condenser lens, condenser-lens aperture
CMOS	Complementary metal-oxide semiconductor
DQE	Detective quantum efficiency
DTEM	Dynamical transmission electron microscopy
DWF	Debye-Waller factor
EELS	Electron energy loss spectroscopy
FWHM	Full width at half maximum
MFP	Mean free path
NBD	Nano-beam diffraction
ROI	Region of interest
SAED	Selected area electron diffraction
SNR	Signal-to-noise ratio
STEM	Scanning transmission electron microscopy
TEM	Transmission electron microscopy (or microscope)
TMDC	Transition metal dichalcogenide
TDS	Thermal diffuse scattering
UED	Ultrafast electron diffraction
UEM	Ultrafast electron microscopy

Abbreviation	Description
ULEED	Ultrafast low-energy electron diffraction
UTEM	Ultrafast transmission electron microscopy (or microscope)
U-CBED	Ultrafast convergent beam electron diffraction

## Latin symbols

Symbol	Description
$A_n$	Antisymmetric Lamb mode with mode index $n \in \mathbb{N}_0$
$a_{\text{Si, Pt}}$	Crystal lattice constant of silicon or platinum
$a_i$	Crystal lattice vectors ( $i \in [1, 2, 3]$ )
$B$	Brightness
$B_{\text{u}}^{\text{sample}}, B_{\text{u}}^{\text{lab}}$	Real-space basis of a unit cell in the sample-fixed or lab-fixed coordinate system
$B_{\text{F}}^{\text{lab}}$	Real-space basis of a deformed unit cell in the lab-fixed coordinate system
$C$	Elastic stiffness
$C_c, C_s$	chromatic, spherical aberration coefficient
$C_h$	Fourier coefficient of crystal potential
$c$	Light velocity
$E$	Young's modulus <i>or</i> Electron kinetic energy
$\Delta E$	Energy spread
$E_0$	Initial kinetic energy
$E_{\text{F}}$	Fermi energy
$F$	Structure factor
$f$	Frequency <i>or</i> Atomic scattering factor
$F, F^{\text{sample}}$	Displacement gradient tensor (in the sample-fixed coordinate system)
$G, g, G_{hkl}$	(Norm of) reciprocal lattice vector (of a Bragg reflection (hkl))
$G_{\text{u}}^{\text{sample}}, G_{\text{u}}^{\text{lab}}$	Reciprocal-space basis of a unit cell in the sample-fixed or lab-fixed coordinate system

Symbol	Description
$G_{\text{F}}^{\text{lab}}$	Reciprocal-space basis of a deformed unit cell in the lab-fixed coordinate system
$H, h$	Thickness of thin film
$I$	Electron beam current
$I_{hkl}$	Intensity of a Bragg reflection (hkl)
$K$	Spring constant
$k$	Scattering wave vector of (crystallographic definition $ k  = 1/\lambda$ ) or Wavenumber in dispersion relations (condensed matter notation $ k  = 2\pi/\lambda$ )
$k_0$	Wavenumber, wave vector of incident electron beam
$k_{\nu}^{\text{L}}, k_{\nu}^{\text{T}}$	Out-of-plane wavevector components
$l$	Layer thickness
$M$	Beam quality factor
$m_{\text{e}}$	Electron mass
$N_{\text{e}}$	Number of electrons
$n$	Acoustic mode index or Refractive index
$p_{x,y,z}$	Canonical momenta
$p_s$	Sheared electron distribution
$q$	Wavenumber, spatial frequency
$R$	Rotation matrix or Radius
$r$	Radial position or Radius of curvature
$r_{\text{G}}$	Position of Bragg scattered excess line
rms	Root-mean-square
$r_v, r_Z$	Velocity/ impedance ratio
$S_n$	Symmetric Lamb mode with mode index $n \in \mathbb{N}_0$
$s$	momentum change
$s_E$	Shear constant
$s_g$	Excitation error
$S_n$	Symmetric Lamb mode with mode index $n \in \mathbb{N}_0$
$T$	Temperature

Symbol	Description
	<i>or</i> Propagation time
	<i>or</i> Round-trip time
$T_{m,n,o}$	Translational vector
$t$	Time
	<i>or</i> Traction
	<i>or</i> Sample thickness
$\Delta t$	Temporal delay
$U$	Crystal potential
$U_a$	Acceleration voltage
$U_{\text{extm sup, tip}}$	Electrostatic potentials at the suppressor/extractor/tip in the electrode assembly
$u$	Displacement
$v$	Velocity (Electron velocity or acoustic sound velocity)
$v_{L, T}$	Longitudinal, transverse sound velocity
$X, Y, Z$	Directions in the lab-fixed coordinate system
$x, y, z$	Spatial coordinates
	<i>or</i> Directions in the sample-fixed coordinate system
$Z$	Acoustic impedance
$\Delta z$	Defocus

### Greek symbols

Symbol	Description
$\alpha$	Rotation angle
	<i>or</i> Divergence/ convergence angle
	<i>or</i> Lamb wave parameter
$\beta$	Rotation angle
	<i>or</i> ratio of (electron) velocity to light velocity
$\Gamma$	Eccentricity
	<i>or</i> Christoffel tensor
$\gamma$	Rotation angle
	<i>or</i> Lorentz factor
$\delta$	Kronecker delta

<b>Symbol</b>	<b>Description</b>
$\epsilon$	Elastic strain
$\epsilon_{n, \text{rms}, r, q}$	Emittance (normalized, root-mean-squared, radial, quantum)
$\epsilon_0$	Permittivity of free space
$\Theta_D$	Debye temperature
$\theta, \theta_B$	Scattering angle, Bragg angle
$\Delta\theta$	angular shift of Bragg scattered lines
$\kappa$	Optical wavevector component <i>or</i> Wave vector inside a crystal
$\lambda$	Electron or photon wavelength <i>or</i> Lamé constant
$\mu$	Lamé constant
$\nu$	Poisson's ratio
$\xi$	Optical wavevector component <i>or</i> Extinction distance
$\rho$	Material or charge density
$\sigma$	Elastic stress
$\sigma_{\alpha, E, p, r, t}$	standard deviation of angle, energy, momentum, position, pulse duration
$\tau$	Pulse duration <i>or</i> Temporal delay time
$\Phi$	Electrostatic potential
$\Phi_W, \Phi_W^{\text{eff}}$	(effective) work function
$\chi$	Spectral chirp
$\psi$	Electron wave function
$\omega$	Beam waist <i>or</i> Angular frequency <i>or</i> Elastic rotation



## Introduction

---

Phenomena associated with vibrations and waves are among the most beautiful things we can explore in physics. Many natural and technical processes in our environment behave periodically by repeating themselves constantly in time and space, like a pendulum, light, and sound. Unlike waves propagating through bulk media, spatially confined systems exhibit vibrations at quantized resonance frequencies depending on the exact geometry, material properties, and imposed boundary conditions. In this context, nanomechanical resonators such as ultra-thin films [1–4], doubly clamped beams or strings [5–8], or singly clamped nanopillars [9–11] are of great importance in modern technology as ubiquitous building blocks for micro- and nano-electromechanical systems [12–15]. Flexural motions (typically in the several megahertz to few gigahertz range) are excited by resonant actuation [16], parametric pumping [17], or even by thermal noise [18]. An enormous challenge is to reach the quantum mechanical ground state of a nanomechanical oscillator [19, 20]. In contrast to macroscopic systems, nanomechanical structures host a range of intriguing attributes like remarkably high quality factors and ultra-low effective masses [21] for high-performance mass- [22–24] and force-sensing [25, 26].

In addition to drum-like oscillations of thin membranes which are strongly dependent on the lateral membrane size and the tension applied by the rigid frame [17], confined systems also exhibit localized thickness oscillations. Similar to optical modes in a Fabry-Pérot interferometer [27], acoustic phonon modes in homogeneous thin-films can form standing waves at resonance frequencies of several hundreds of gigahertz corresponding to few tens of nanometer wavelengths [28–31]. In monolayer materials, the mode frequencies of longitudinal strain waves are simply governed by the sound velocity and the thickness of the resonator [32]. Control over the excited mode orders and amplitudes can be achieved through tailoring the spatiotemporal stress distribution induced by ultrashort

laser pulses [32]. Systems consisting of multiple elastically mismatched layers, however, exhibit more complex strain dynamics since boundary conditions at the interfaces have a strong impact on the coupling of individual phononic modes. The modelling of multilayers or nanostructured films has so far often been based on numerical approaches including one-dimensional linear chain [33–36] and two-dimensional finite-element simulations [37, 38]. Although experimentally observed ultrafast structural dynamics are accurately reproduced, more general insights into local excitations in confined geometries are not provided in such models. Intuitive analytical models based on continuum elasticity theory have already been established in the late 19th/early 20th century to describe propagating surface waves [39], Rayleigh-Lamb waves [40], and interlayer Stonely waves [41] in acoustic waveguides, but remain to be systematically employed for analyzing the ultrafast strain dynamics in nanoscale heterostructures. As one central part this thesis, we apply an analytical acoustic-mode description in a prototypical semiconductor/metal bilayer system optically excited by femtosecond laser pulses, derive explicit expressions for allowed acoustic mode frequencies, and demonstrate the emergence of localized modes within individual layers (see Chapter 6).

Valuable experimental insights into layer-specific structural deformations are offered by ultrafast electron (see e.g. [42–49]) and x-ray diffraction techniques (see e.g. [50–53]) with high spatial resolution in reciprocal space. In real space, micrometer-sized areas are typically illuminated, so that mostly homogeneous material systems have been investigated in the past [54–58]. However, ultrafast phenomena such as the coherent electron transfer in organic solar cells [59], super-diffusive spin transport in spintronic multilayer systems [60] or even quasi-ballistic thermal transport across interfaces [61] demonstrate the importance of studying heterostructures for future nanotechnological applications. The relevant processes on the nanometer scale have been difficult to access until the development of ultrafast transmission electron microscopy (UTEM). Pioneering work in Berlin in the 1980s [62] and substantial progress in the group of A. H. Zewail at Caltech [63, 64] and at the Lawrence Livermore National Laboratory [65] demonstrated the feasibility of pump-probe studies in electron microscopy. Today, UTEM is an established and versatile method that can image ultrafast structural dynamics at laboratory-scale with high spatial resolution and 100-femtosecond to picosecond temporal resolution [66–71]. Enabled by different electron microscopic contrast mechanisms, this method allows to quantitatively investigate dynamics in a variety of degrees of freedom (lattice, electrons, spin). Moreover, electron pulses can be localized in sub-nanometer sized foci [71], which now opens up the

possibility to study ultrafast dynamics locally even in highly inhomogeneous structures, for example near interfaces or at nanostructures.

In a previous work at the University of Göttingen, ultrafast convergent beam electron diffraction (U-CBED) has been applied for the quantitative mapping of light-driven acoustic phonon modes in a mesoscopically symmetry-broken graphite thin-film with 28-nm spatial and 700-fs temporal resolution [72]. Highly valuable insights are gained into high-amplitude coherent expansion, as well as into shear acoustic waves that generate a complex spatio-temporal distortion pattern. However, detailed control of the spatiotemporal evolution of nanophononic wavefields remains challenging. An exemplary approach to spatially tailor sample excitations lies in multi-component heterostructures that provide strong and controllable excitation gradients. As a central part of this thesis (see Chapter 7), we establish such a model system by patterning a semiconductor membrane with a platinum stripe and employ U-CBED to study local structural dynamics in a particular distance close to the bilayer region which acts as a tailored wave source.

For the electron pulse generation in UTEM, common implementations employ flat photocathodes illuminated by ultrashort laser pulses [73]. The spatial coherence of the photoemitted electrons is, however, limited by the size of the illuminated area on the photocathode, which means that the high resolution capabilities of a conventional electron microscope cannot be fully exploited. Facing the challenges in obtaining high-quality electron pulses to resolve structural dynamics with above-nanometer-scale coherence lengths [74–76], different approaches have recently been pursued to increase the brightness as a central figure-of-merit. These include the implementation of optimized photocathode materials to reduce the photoemission excess energy [77–79] and the use of tip-shaped photocathodes to confine photoelectron emission to nanometer sized areas [71, 73, 80–84]. Whereas these two minimization schemes provide clear design criteria for advanced photoelectron sources in the single-electron-per-pulse limit, operating the electron sources in the regime of high electron densities remains challenging due to Coulomb interactions that significantly constrain the beam quality. Over the past decade, charge interactions for electron pulses emitted from flat photocathodes have been extensively studied [85–94], but their effect in electron pulses emitted from small emission areas under strong excitation fields and large divergence angles has much less been understood. In the first main part of this thesis, we quantitatively characterize the influence of Coulomb effects on the transverse and longitudinal pulse properties in such a photocathode geometry of a transmission electron microscope and reveal space-charge behaviors distinctively different from flat photocathode emission (see Chapter 3).

## Outline

This cumulative thesis is composed of three original publications in Chapters 3, 6 and 7, each giving a short introduction into the topic, illustrating the experimental and theoretical work, and discussing the respective results. Chapters 2, 4 and 5 are structured in such a way that they embed the three publications in a broader scientific context.

Chapter 2 gives a brief introduction into the UTEM method and electron pulses. This includes a technical description of conventional TEM instrumentation as a basis for experimental work presented in Chapter 7 and an overview of typical electron sources used in TEM. In order to access the capabilities of electron sources, important parameters in phase space are detailed before a particular emphasis is placed on the impact of Coulomb interactions on spatial, temporal, and spectral properties of electron pulses.

Chapter 3 presents the experimental and theoretical investigation of the electron pulse properties emitted from a laser-driven Schottky field emitter operated in the high-bunch-charge regime. The article “Coulomb interactions in high-coherence femtosecond electron pulses from tip emitters” covers the quantitative characterization of transverse and longitudinal pulse properties governed by stochastic and mean-field Coulomb interactions. Moreover, numerical simulations offer additional insights into experimental parameters dominating the electron pulse broadening.

Chapter 4 illustrates the importance of obtaining a deep understanding in phonon dynamics in nanophononic waveguides and gives an overview of the fundamental relations between displacements, strain and stress within the framework of continuum elasticity theory. By focusing on guided Rayleigh-Lamb waves in thin plates, the foundation is laid for the analytical model of strain dynamics in bilayer heterostructures presented in Chapter 6.

Chapter 5 gives an introduction into elastic scattering theory. Starting from typical diffraction modes in TEM, we proceed with the fundamentals of kinematic and dynamic scattering theory relevant for the analysis and interpretation of experimental data in Chapter 7. The chapter is closed by a short overview of pioneering UTEM works addressing the investigation of structural dynamics using different contrast mechanisms.

In Chapter 6, key dependencies of the optically excited acoustic phonon frequency spectrum in an elastically mismatched metal/semiconductor bilayer system are explored. The article “Ultrafast strain propagation and acoustic resonances in nanoscale bilayer systems” gives an analytical description of the acoustic response and yields intriguing

insights in the importance of interlayer strain coupling on the localization of phonon modes.

Chapter 7 reports on the local probing of structural dynamics in a metal/semiconductor heterostructure that exhibits a strong and controlled excitation gradient. In the article “Tailored nanophononic wavefield in a patterned bilayer system probed by ultrafast convergent beam electron diffraction”, we demonstrate that U-CBED is an ideal tool to quantitatively access nanophononic strain fields and disentangle complex strain dynamics. Our experimental work is complemented by numerical simulations offering insights into the dominating components of the time-dependent deformation gradient tensor.

Finally, the main results of the three publications are summarized in Chapter 8, and ideas on further research on laser-driven electron sources, as well as prospective studies in the field of nanophononics are presented.



# Fundamentals of ultrafast transmission electron microscopy and ultrashort electron pulses

---

Ultrafast transmission electron microscopy (UTEM) is an emerging, powerful technique for investigating the temporal evolution of dynamical processes in matter triggered by a short-pulsed excitation of structural, electronic, and spin degrees of freedom. The method is inspired by all optical pump-probe techniques in the fields of condensed matter physics [95, 96] and femtochemistry [97–99]. First, an initial laser pulse (pump) is used to trigger dynamics in the specimen. After well-defined delay times  $\Delta t$ , the out-of-equilibrium state is accessed by means of ultrashort electron pulses (probe). The relative timing between the electron probe and laser pump pulse is controlled by an optical delay stage (Fig. 2.1). TEM images, diffraction patterns, or electron spectra of the transient state of the sample are recorded directly by a camera or an electron energy spectrometer at the end of the TEM column.

This approach of pump-probe studies in electron microscopy was initially pursued in pioneering work by the group of O. Bostanjoglo in the 1980s [62], but earned particular attention in the 2000s through experiments at Lawrence Livermore National Lab and in the group of A. H. Zewail at the California Institute of Technology. Two complementary approaches were followed in these groups: On the one hand, Bostanjoglo and collaborators focused on a redesign of the standard electron source and operation procedure, today termed dynamic transmission electron microscopy (DTEM) [100, 101]. This technique enables the investigation of non-reversible transient processes initiated by a single excitation (*single-shot*) and probed with high-charge electron bunches (containing up to  $10^9$  electrons per nanosecond pulse). The imaging of reversible dynamics in a *stroboscopic* pump-probe scheme in UTEM on the other hand is based on electron pulses which

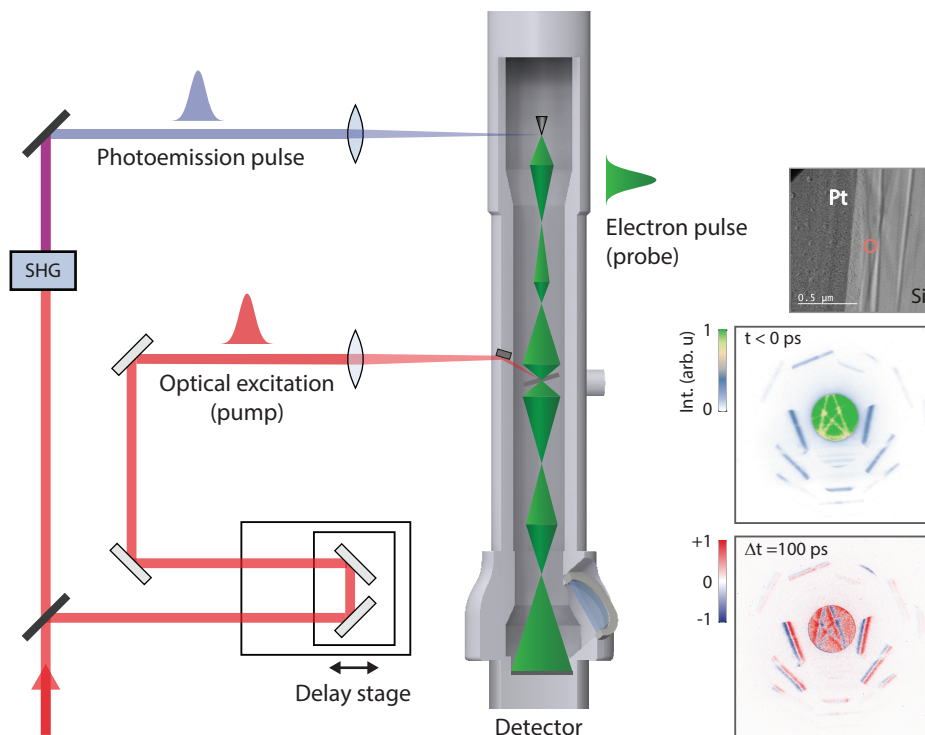


**Figure 2.1:** Schematic illustration of the stroboscopic optical-pump/electron-probe scheme in a UTEM. The instrument is based on a commercial TEM which is modified to allow for both optical sample excitation and side-illumination of a tip-shaped electron source (SHG: second-harmonic generation). The generated high-coherence photoelectron pulses are, for example, suitable to probe structural dynamics in nanostructured systems with high spatial resolution. Right side, top: nanoscale heterostructure consisting of a polycrystalline platinum stripe patterned on a single-crystalline silicon membrane. Middle, bottom: CBED patterns recorded in an approximate distance of 200 nm from the platinum stripe on the membrane (position marked with red circle in real-space image) before optical excitation and relative changes for a pump-probe temporal delay of 100 ps.

contain on average a single or a few electrons per pulse. The experimental development of both pathways and their further implementations in laboratories worldwide have allowed studies, in which a wide repertoire of available contrast methods has been extended by simultaneous temporal resolution on the femtosecond scale. These methods include time-resolved bright-field and dark-field microscopy [102, 103], Lorentz microscopy [104], convergent beam electron diffraction (CBED) [105, 106] and scanning TEM (STEM) measurements [107].

An essential challenge of this methodology is the generation of ultrashort electron pulses with a high spatial beam quality, which is decisively influenced by the specific design of the electron source. A common implementation employs planar photocathodes illuminated with short laser pulses. For this type of emitter, the spatial coherence of the

---

photoemitted electrons is limited by the size of the illuminated area on the photocathode, which restricts the high spatial resolving power of a conventional electron microscope. In the past decade, novel approaches to generate coherent ultrashort electron pulses using localized photoemission from nanoscale tips have therefore been developed. Several nonlinear photoemission regimes such as multiphoton photoemission and strong-field photoemission from nanostructures have been intensively investigated [82–84, 108, 109].

The Göttingen UTEM was the first to use electron pulse generation from a tip-shaped photocathode [71]. In particular, coherent electron pulses are obtained using linear photoemission from a (100)-oriented single-crystalline tungsten tip covered with zirconium oxide. In this way, UTEM allows for unique access to ultrafast dynamics on the nanometer scale. The potential of strongly focused electron beams has already been demonstrated in experiments on the quantum coherent manipulation of free electrons with light [110–115] and on local structural dynamics [72]. Recent advances towards the investigation of the spatio-temporal structure of phonon modes emitted from a heterostructure with a strong excitation gradient are reported in Ref. [116] and presented as part of this cumulative thesis in Chapter 7. Versatile other applications of the Göttingen UTEM include the imaging of current-driven magnetization dynamics [117, 118], the ultrafast nanoimaging of the order parameter in a structural phase transition [119], and the observation of a photoinduced transition between two incommensurate charge-density wave (CDW) superstructure in a TaS<sub>2</sub> thin film [120]. By employing laser-driven cold field emitters as another promising tip-shaped photoelectron source, applications that require enhanced coherence properties, such as electron holography, become accessible [80, 121].

For the optical sample excitation (pump), different illumination configurations have been employed for the Göttingen JEOL 2100F microscope, such as a laser-beam path allowing for an illumination either at 55° (*side-illumination*) [71] or at 6° (*top-illumination*) [119, 122] with respect to the electron beam. Tunable excitation methods become accessible by new developments of amplified laser systems that use optical parametric amplifiers generating a broad frequency range from the low-ultraviolet to the mid-infrared.

The purpose of this chapter is to give an introduction into the fundamentals of conventional TEM and revisit the generation principles and properties of ultrashort pulses of tip-shaped electron emitters. As a basis for detailed investigations of high photocurrent densities (Chapter 3), the emphasis is on the impact of Coulomb interactions on spatial, temporal, and spectral properties of electron pulses.

## 2.1 Conventional TEM instrumentation

Due to the wave character of electrons and light, a TEM shares a lot of its functionality with a classical light microscope. Typical acceleration voltages between 80 keV and 300 keV, however, are related to electron wavelengths from 4.18 pm to 1.97 pm, respectively, shifting the theoretical Abbe diffraction limited spatial resolution far below the shortest wavelength in the visible range. Furthermore, versatile imaging modes at magnification stages covering several orders of magnitude allow for a large number of different types of experiments to be carried out in a TEM.

As shown in the simplified schematic of a TEM in Fig. 2.2a, the first stage of a conventional TEM, the *gun* of the instrument, houses the electron source that has a strong impact on the beam properties, and a series of electrostatic lenses forming the electron beam. Subsequently, the electrons can be accelerated to relativistic velocities. Coupled into the *column* behind the exit aperture of the accelerator, the electron beam is formed by condenser lenses (CL) to illuminate a specimen. By varying the excitation strength of the second magnetic lens (CL3) in the condenser system,<sup>1</sup> the electron focus is placed at different positions relative to the sample plane [71, 124–126]. Precise tuning of beam diameter, convergence angle, and current is achieved by employing different relative lens excitations in combination with a specifically selected condenser-lens aperture (CLA) size. Exemplary beam envelopes as a function of the CL3 excitation strength reveal few-nm focal spot sizes at different convergence semi-angles measured in diffraction mode (see Fig. 2.5b). The form of the caustics follow a Gaussian behavior (solid curves in Fig. 2.5b). Small condenser lens aperture sizes select near-axis electron beams and simultaneously reduce the electron current, which results in low beam emittances. For properly chosen settings, even sub-nm focus conditions are achievable (see Fig. 2.5c).

In the paraxial ray description, the focal length of an electromagnetic lens, controlled by the excitation strength, scales with the inverse square of the corresponding magnetic field component along the optical axis. The strongest lens, i.e. the lens with the shortest focal length (typically a few millimeters), is the objective lens that is placed around the specimen plane. Among the limits of all lenses, the ones of the objective lens, which are characterized by coefficients  $C_s$  and  $C_c$  for spherical and chromatic aberrations, respectively, have a major influence on the resolution limit in TEM, so that it is no

---

<sup>1</sup>The second condenser lens of a JEOL JEM-2100F microscope is called CL3. It is equivalent to the second condenser lens C2 described in literature [123].

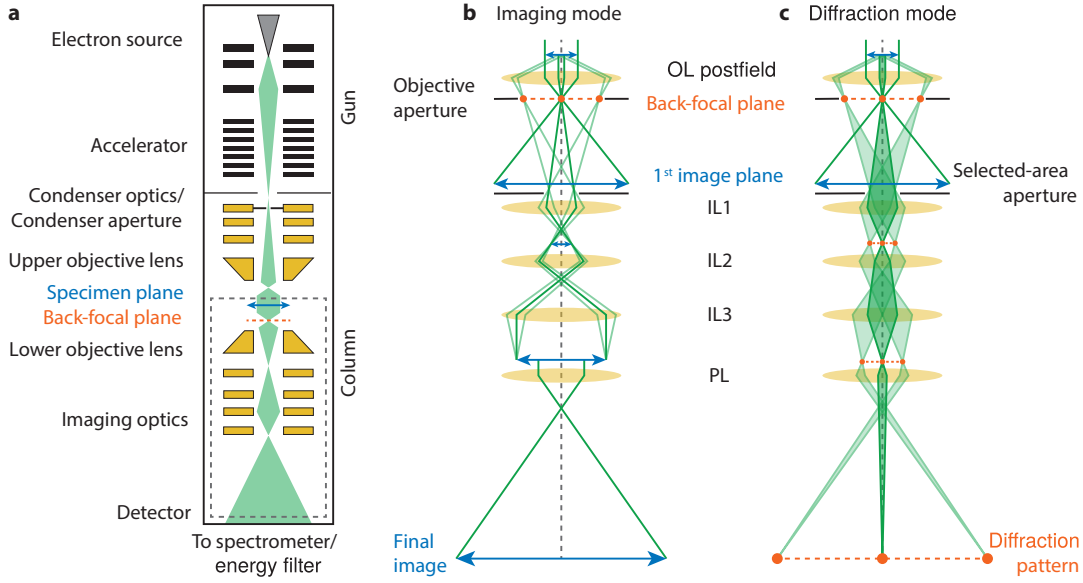


**Figure 2.2:** Schematic of a TEM and its basic operation modes. **(a)** Schematic setup with main components of a conventional TEM. The dashed gray box indicates the field of view of b and c. **(b)** Ray diagram of the imaging system set to imaging mode. Note that, although shown below the objective lens (OL) postfield, in reality, the back-focal plane is located within the objective pole piece (see a). **(c)** Ray diagram of the imaging system set to diffraction mode. Illuminating a single-crystalline sample by a collimated electron beam yield confined Bragg peaks in the focal plane of the objective lens. Other diffraction modes are explained in Ch. 5.1. Figure reprinted and caption adapted from Ref. [129] with permission from the author.

longer given by the Abbe criterium. Through state-of-the-art aberration corrections, however, the sub-angstrom range is accessible in high-resolution electron microscopy, and radiation-sensitive samples can be investigated at sub-100 keV acceleration voltages [127, 128].

After the specimen, the imaging system, that consists of intermediate and projector lenses, transfers the electron exit wave onto an electron-sensitive detector. Depending on the excitation strengths of the intermediate lenses either a magnified real-space image (Fig. 2.2b) or a diffraction pattern (Fig. 2.2c, formed in the back-focal plane (BFP) of the objective lens) is projected on the detector. Furthermore, a selection of spatial frequencies and circular specimen regions of interest is possible by inserting the objective lens aperture or the selected-area aperture in the BFP or the first image plane, respectively. As an alternative to a selected-area aperture, a biprism can be inserted in the first image plane, allowing for the characterization of the transverse beam coherence (see hologram in Fig. 2.5d) and for a simultaneous recording of phase and amplitude of the exit wave.

In order to fulfill different experimental requirements, a wide range of electron-sensitive detectors is available. Traditionally, electron microscopes are equipped with a fluorescent phosphor screen to observe the image by eye [130, Ch. 4.7]. Pixelated image data is nowadays acquired with digital detectors usually attached to the bottom of the microscope column. Among those, indirect cameras for electron detection convert high-energy incident electrons to photons which, through a fiber optic plate or lens, are coupled to a camera. They are based on a charge-coupled device (CCD) or a complementary metal-oxide semiconductor (CMOS) chip [130]. Read-out electronics of these sensors either shift pixel rows (CCD) through the detector, or actively address individual pixels (CMOS) for faster frame rates [131].

However, not only do the primary electrons show shot noise, but noise is also accumulated in the different conversion steps of the detector system [130, Ch. 4.7.4]. The loss of signal-to-noise ratio (SNR) is described by the detective quantum efficiency (DQE) as a function of spatial frequency [132]. Technologically, a high DQE is achieved with back-thinned, radiation-hard CMOS chips for direct electron detection [133]. They are particularly suitable for low-dose applications in biological cryogenic and low-dose ultrafast experiments. Other direct electron detectors are hybrid pixel detectors, that consist of a sensor layer bonded to a separate chip with CMOS read-out electronics. These detectors aim towards sub-ns temporal resolution. Impinging electrons generate a continuous data stream of electron events, for which position, time-of-arrival, and time-over-threshold are saved. At the expense of spatial resolution, event-based imaging is a promising technique for the analysis of electron-photon correlations [134], for continuous illumination picosecond imaging [135], and dose-optimized high-speed STEM [136, 137].

The final electron energy distribution can be characterized by electron energy spectra recorded with a spectrometer that specially separates electrons according to their velocity when they enter a magnetic prism [138, Ch. 2.2]. The most recent advances in this TEM technology are energy-filter devices [138, Ch. 2.6], that can be operated in two different modes: electron energy spectroscopy with improved resolution and energy-filtered imaging or diffraction, for which electrons in a defined energy range can be selected by a slit whereas other electrons, e.g. inelastically scattered electrons, are blocked [139, 140].

TEM specimens are typically thin films with a thickness between few atomic layers and around 200 nm, usually prepared in a multi-step fabrication procedure [141, Ch. 10]. The model system for the investigation of ultrafast structural dynamics used in this thesis consists of a commercially available single-crystalline silicon membrane patterned

with a platinum stripe. Preparation processes for this heterostructure involve electron beam lithography [117], which has proven particularly useful in micro- and semiconductor technology for the production and structuring of thin films, and thermal evaporation for the deposition of platinum. Process parameters have been optimized to pattern two-dimensional structures with high edge sharpness of about 10 nm. Concerning versatile requirements of an experiment, TEM specimen holders of different functionality (e.g. double-tilt, in-plane rotation, heating/cooling) can be used [141, Ch. 8].

## 2.2 Image contrast

During interaction processes with the sample, the incident electron wave is spatially modified in amplitude and phase, giving rise to two different contrast channels in TEM. Within the Abbe wave-optical theory, the underlying two steps of image formation include the collection of the electron exit wave  $\Psi_e(\mathbf{r}) = a(\mathbf{r}) \exp(i\varphi(\mathbf{r}))$  in the back focal plane (BFP) of the objective lens and a wave transfer into real space [142]. In the BFP, the electron wave is described by a Fourier transform  $\mathcal{F}(\Psi_e)$ , which yields the spectrum of the exit wave with two-dimensional spatial frequency  $\mathbf{q} = (q_x, q_y)$ . During the propagation and interference of all plane waves spread from Fourier points  $q$  towards the detector, amplitude  $a$  and phase  $\varphi$  of the exit wave are altered by apertures, coherent aberrations, and damping envelope functions. All of these specimen-independent effects modulating the spatial frequencies of the Fourier spectrum in the imaging process are collected in the wave transfer function  $T(\mathbf{q}) = B(\mathbf{q}) \exp(-i\chi(\mathbf{q}))$ , where  $B(\mathbf{q})$  is the aperture function and  $\chi$  represents a phase shift approximately independent of position  $\mathbf{r}$  in real space. Back-transformation of the modulated exit wave yields the image wave  $\Psi_{\text{im}} = \mathcal{F}^{-1}[T\mathcal{F}(\Psi_e)] = A(\mathbf{r}) \exp(i\Phi(\mathbf{r}))$ . However, since only amplitudes squared can be recorded, essential information about the phases is lost. An important contribution to determine the illuminated object uniquely was made by Zernike who showed that phase contrast could be obtained by inserting a ' $\lambda/4$ '-plate into a part of the Fourier plane [143, 144]. As a result of the introduced phase shift  $\chi(q) = \pm\pi/2$  between the scattering beam ( $q = 0$ ) and the diffracted beam ( $q \neq 0$ ), real-valued amplitude and imaginary phase are exchanged with respect to the electron exit wave yielding perfect phase contrast and a lost amplitude information. In a more general model, amplitude and phase information are mixed. If the TEM specimen acts as a weak object imprinting only very small amplitude and phase modulations on the incident electron wave, the complex relationship between

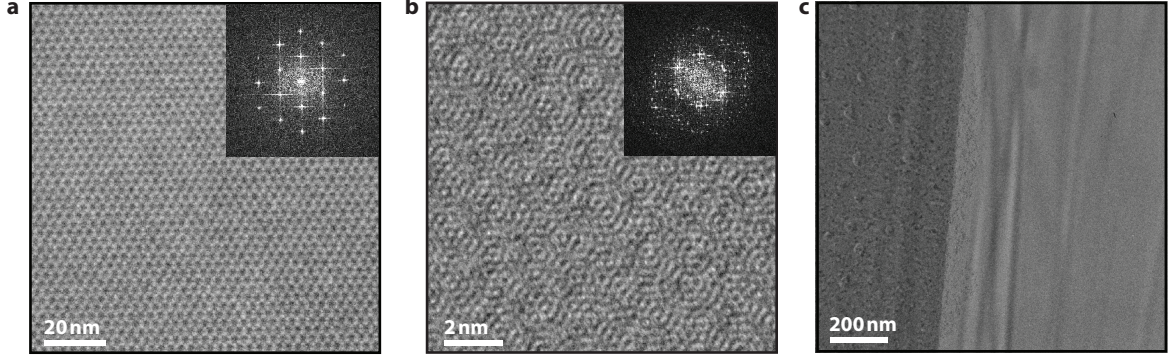


**Figure 2.3:** High-resolution TEM imaging. (a) Real-space image of a MoSe<sub>2</sub> thin film showing a Moiré pattern with hexagonal symmetry. (b) Real-space image of a Moiré pattern in twisted MoSe<sub>2</sub> with hexagonal symmetry. Insets show Fourier transformations. (c) Intensity variations and bending contours in a silicon membrane patterned with a platinum stripe.

both contributions to image contrast becomes obvious. Weak phase and amplitude objects introduce a phase shift  $\varphi_q < 1$ , and the local amplitude is assumed to differ from one by  $t_q(\mathbf{r})$  with  $t_q \ll 1$  [142]. Expansion of the electron exit wave results in the intensity

$$\begin{aligned} |\Psi_{\text{im}}|^2 &= A^2 = 1 - 2\text{Re}[t_q - i\varphi_q] \exp(i\chi) \cos(2\pi\mathbf{q}\mathbf{r}) \\ &= 1 - 2[t_q \cos(\chi) + \varphi_q \sin(\chi)] \cos(2\pi\mathbf{q}\mathbf{r}) \end{aligned} \quad (2.1)$$

of the image wave. Considering again the phase shift of the Zernike phase plate, the equation reduces to  $|\Psi_{\text{im}}|^2 = 1 - 2\varphi_q \sin(\chi(\mathbf{q})) \cos(2\pi\mathbf{q}\mathbf{r})$  revealing the mentioned contributions from the object phase to the recorded wave amplitude squared only.

Balancing spherical aberrations  $C_s$  of the objective lens against a particular defocus  $\Delta z$ , the lowest-order coherent wave aberration function  $\chi(\mathbf{q}) = \frac{2\pi}{\lambda} \left( \frac{C_s}{4} (\lambda q)^4 + \frac{1}{2} \Delta z (\lambda q)^2 \right)$  can be optimized with respect to the width of the low-frequency passband [130, 142]. Two-dimensional Fourier transforms of images acquired in the Scherzer defocus contain a wide range of frequencies, which forms the basis of high-resolution images of amorphous samples or superstructures (see Moiré pattern of MoSe<sub>2</sub> and corresponding Fourier transform in Figure 2.3a,b) with optimum phase contrast [123]. For thicker samples, intensity variations arise from additional contrast features such as spatially varying thickness or specimen composition, and bending contours (Fig. 2.3c).

Owing to the partial temporal and spatial coherence, the contrast-transfer function is damped at high spatial frequencies by temporal and spatial coherence envelopes [130, 141, 142]

$$E^{\text{tc}}(\mathbf{q}) = \exp \left[ -\frac{\pi^2}{2} \frac{\sigma_E^2}{(eU_a^*)^2} C_c^2 \lambda^2 q^4 \right] \quad (2.2)$$

and

$$E^{\text{sc}}(\mathbf{q}) = \exp \left[ -\pi^2 \frac{\sigma_\theta^2}{\ln(2)} \left( C_s \lambda^2 q^3 + \Delta z q \right)^2 \right], \quad (2.3)$$

respectively. Clearly, the partial coherence manifests itself in a finite source size for which  $\sigma_\theta$  is the spread of a rotationally symmetric Gaussian distribution of small incidence angles, and in a finite wavelength or energy spread  $\sigma_E^2$ . At high relativistic acceleration voltages  $U_a^* = U_a \left( 1 + \frac{eU_a}{2m_0c^2} \right)$ , incoherent contributions to the final image corresponding to a range of energies in the incident beam are less pronounced.

### 2.3 Tip-shaped electron sources

At present, the combination of versatile nanoscale imaging (direct space), diffraction (reciprocal space), and spectral (energy space) analysis techniques of conventional transmission electron microscopy with the temporal resolution achieved by the advent of fs-laser systems plays a key role in the investigation of ultrafast nanoscale dynamics. Typically, high-frequency fields, such as externally applied electric potentials, light or magnetic fields, initiate dynamical processes on multiple length- and time-scales. At interfaces and in structured materials, a multitude of non-local relaxation processes occurs, such as ballistic and diffusive charge carrier and phonon transport, both within the individual phases and across their interfaces. For the spatiotemporal imaging and the separation of the individual contributions,  $\mu\text{m}$ - to  $\text{nm}$ -scale resolution is desirable. In the temporal domain, following the evolution of quasi-particle excitations, coupling mechanisms, and subsequent transport in real time demands high temporal resolution over a broad range of  $\mu\text{s}$  to fs time scales.

The main challenge is therefore to prepare high-coherent electron pulses, which has recently motivated different electron source implementation schemes [73, 145] based on ultrafast photoemission from planar [46, 63, 146–151] or tip-shaped photocathodes [71, 80, 82, 152–154]. By focusing ultrashort laser pulses onto the photocathode, electrons are emitted by means of the (nonlinear) photoelectric effect in combination with additional manipulation schemes enabling electrons to overcome the crystal potential barrier. Common photocathode materials are metals such as gold, silver and tungsten, or refractory ceramics like  $\text{LaB}_6$ . In case of planar photocathodes used in time-resolved diffraction

techniques, such as tr-RHEED [54, 155–157], ultrafast electron crystallography [158] or MeV diffraction [56, 159], front and back illumination of metal films on optically transparent substrates is possible.

As will be shown below, the quality of photoemitted electrons is strongly influenced by the size of the illuminated area. The high spatial resolution of state-of-the-art electron microscopes can therefore only be partially exploited with flat photocathodes. In contrast, strongly accelerated electron pulses emitted from tip emitters occupy a significantly reduced area of transverse phase space such that sharply focused and well-collimated electron beams with a high degree of coherence become accessible. Concerning intensively investigated non-linear *multiphoton photoemission* and *strong-field photoemission* from nanostructures [82–84, 108, 109, 154, 160], localization of the emittance area far below the laser focus size is achieved. However, such approaches lead to energy-broadened electron pulses that limit temporal coherence and are disadvantageous in applications like spectroscopy. Today, *single-photon photoemission* processes allowing for a simple tunability of the photoemission current and electron pulse length via the laser fluence and laser pulse duration have become beneficial for the investigation of ultrafast dynamics employing electrons as probes.

By using a conventional ZrO/W *Schottky emitter* tip illuminated with work-function-matched photoemission wavelengths [71], strongly localized single-photon photoemission is achieved from the geometrically-tuned front facet [161]. High electric field strengths applied to a *cold field emitter* such as a W(310) nanotip lead to a large portion of electron tunneling through the potential barrier and offer flexibility in the employed optical wavelength.

The following sections introduce the reader to the fundamental operation principles of typical tip-shaped electron sources operated in conventional TEM and as laser-driven photoemission sources. The quality of an electron beam for imaging, local probing or diffraction is described by the evolving probability distribution in electron phase space spanned by spatial and momentum coordinates. Associated beam properties comparable to beam properties in light optics are characterized by the beam *emittance*, beam *brightness*, and *coherence*.

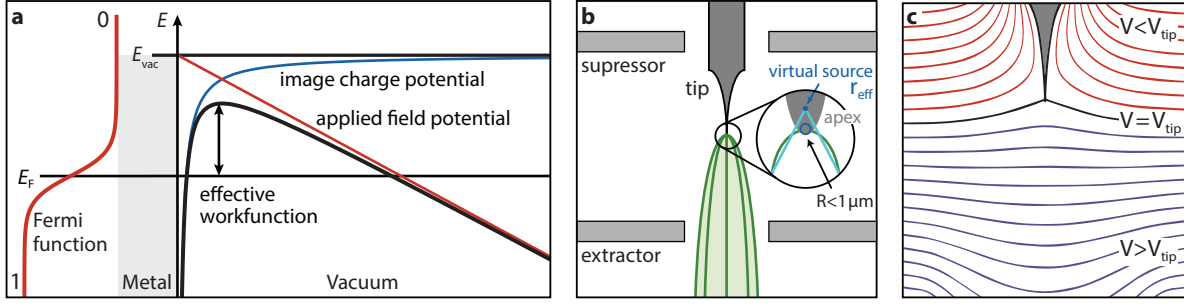


**Figure 2.4:** Potential landscape and geometry of a tip-shaped electron emitter. (a) The total potential (black) includes contributions from the high electric field (red) and the image charge potential (blue). The material specific workfunction is decreased to an effective workfunction determined by the Schottky effect. (b) Emitter geometry with nanoscale electron source. Inset: Typical Schottky field emitter tips have a physical curvature radius  $R$  of a few 100 nm. Backprojection of electron trajectories yields the much smaller virtual source size with radius  $r_{\text{eff}}$ . (c) Calculated equipotential lines in the vicinity of the tip visualize that electrons emitted above the field-reversal point (black line) are suppressed. Figure panel c is adapted from Ref. [126].

### 2.3.1 ZrO/W Schottky field emitter

The Schottky ZrO/W field emitter (Fig. 2.5 a) consists of a (100)-oriented single crystalline tungsten tip with a radius of curvature of  $r < 1 \mu\text{m}$  [162]. When the emitter tip is heated by a current through a polycrystalline hairpin tungsten filament, ZrO diffuses from a droplet-shaped reservoir at the shank of the tip [163, 164]. In continuous operation mode, temperatures of  $T \approx 1800 \text{ K}$  thermally excite electrons, which results in a broadened Fermi-Dirac distribution (left side of Fig. 2.4 a) allowing electrons in the tail of the distribution to overcome the work function  $\Phi_{\text{W}}$ . Extraction fields on the order of  $0.5 \text{ V/nm}$  additionally reduce the potential barrier which is known as the Schottky effect (see Fig. 2.4 a). The fraction of the hot electron distribution that overcomes the potential barrier and is emitted into vacuum, is further increased by a zirconium oxide overlayer at the tip apex formed during heating. It reduces the tungsten work function below  $4.6 \text{ eV}$  [165]. This effect is especially pronounced for the nanoscale W(100) front facet (see inset of Fig. 2.5 a for corresponding schematic), for which values of about  $2.7 \text{ eV}$  are reported [166–169]. The correlation between adatoms on the surface and the changed work function is controversially discussed within a phenomenological theory based on surface electric dipoles [166, 170]. Operating field strength and temperature are known to strongly affect the emitter geometry which is generally not in mechanical equilibrium. Electron emission from the Schottky field emitter is consequently expected to exhibit shorttime fluctuations and longtime performance changes [126, 161].

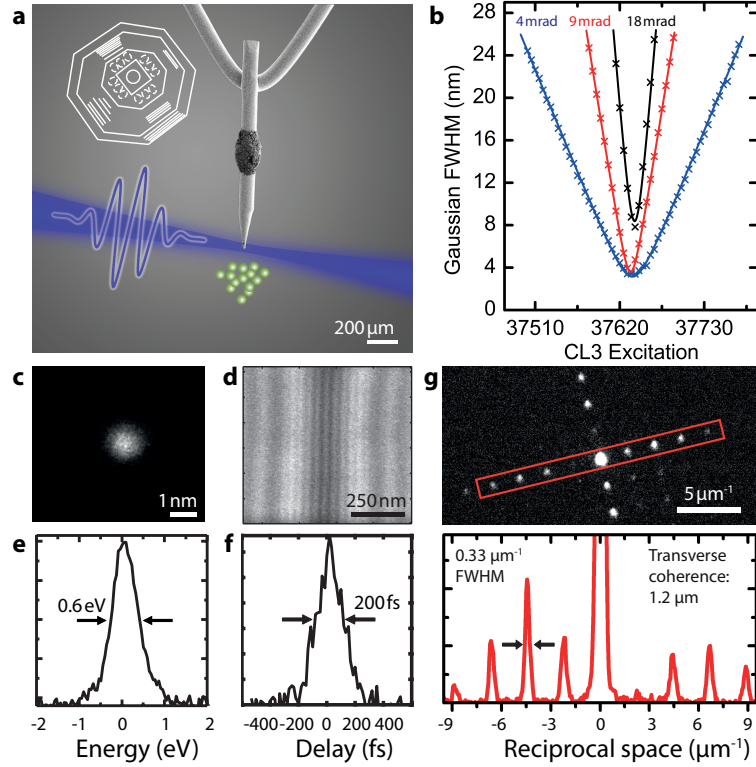


**Figure 2.5:** Electron pulse properties of the Göttingen UTEM instrument. (a) Optical side illumination of a single-crystalline, (100)-oriented, faceted tungsten tip emitter attached to a heating filament with a  $\text{ZrO}_2$  reservoir deposited on the emitter shank. Inset: Schematic facet structure of the emitter apex. (b) Beam caustics for a range of convergence semi-angles. (c, e, f) Due to the currently achievable electron focus size, spectral, and temporal width in the Göttingen UTEM instrument, nanoscale probing of ultrafast dynamics is achievable with high temporal and spectral resolution. (d) Exemplary photoelectron hologram generated with a Möllenstedt biprism emphasizing the photoelectron coherence properties achievable in the UTEM. (g) High dispersion diffraction pattern from a 463 nm replica grating recorded with a collimated photoelectron beam. Extracted coherence length: 1.2  $\mu\text{m}$ . Figure adapted from Ref. [171]. Copyright 2017 IEEE.

In order to control the emission site, the emitter of a standard Schottky emitter assembly unit ( $U_{\text{sup}} < U_{\text{tip}} < U_{\text{ext}}$ , Fig. 2.4b) is negatively biased and placed between a suppressor electrode ( $U_{\text{sup}}$ ) and an extractor anode ( $U_{\text{ext}}$ ). Relative potentials govern the extraction field enhanced at the emitter apex and the divergence of the emitted electron beam. The electron beam behaves as if it emanates from a virtual source with radius  $r_{\text{eff}}$  (see inset in Fig. 2.4b). The precise tuning of the electric field distribution in the vicinity of the apex (Fig. 2.4c) allows for different operation modes [172] optimized for increased charge densities or high-coherence electron beams as described through numerical models and experimental studies [71, 172, 173]. Shaft and tip electrons emitted from beyond the field-reversal point (black line in Fig. 2.4c) are forced back to the tip surface and are thus

suppressed [172]. The current density of the *field-assisted thermal emission* is given by the Schottky equation [174]

$$j_S(F, T) \propto (k_B T)^2 \exp\left(-\frac{\Phi_W - \sqrt{\frac{e^3 F}{4\pi\epsilon_0}}}{k_B T}\right). \quad (2.4)$$

Here,  $\Phi_W$  is the material- and facet-specific work function,  $k_B$  is the Boltzmann constant, and  $\epsilon_0$  is the vacuum permittivity. The field-dependent effective reduction of the work function  $\Phi_W^{\text{eff}} = \Phi_W - \sqrt{e^3 F / 4\pi\epsilon_0}$  is governed by the electric field  $F = \frac{U_{\text{ext-tip}}}{k_{\text{geo}} r}$  at the nanotip (see Fig. 2.4a), where  $k_{\text{geo}}$  is a geometric field enhancement factor dependent on the tip and electrode geometry [175]. By decreasing the temperature below 1400 K, continuous electron emission is suppressed. However, the lowered potential barrier obtained in continuous operation can also be harnessed in photoemission mode using optical wavelengths adapted to the decreased work function. In particular, localized single-photon photoemission from the front facet is reached focusing a photoemission laser beam at around 400-nm wavelength onto the tip apex, yielding transverse and longitudinal beam properties comparable to continuous Schottky field emitters [71].

### 2.3.2 Cold field emitter

A typical cold field emitter consists of a sharp single-crystalline tungsten needle with a (310)-crystal front facet for which a work function of 4.35 eV is reported [176]. Electron emission from the electrically-biased, non-heated nanotip is a purely field-assisted process. For external electric fields on the order of a few V/nm, the potential barrier becomes thin enough to allow quantum-mechanical tunneling of electrons into vacuum. The tunneling current density, related to the local field strength  $F = \frac{U_{\text{ext}}}{k_{\text{geo}} r}$ , is given by the Fowler-Nordheim equation [177]

$$j_{\text{FN}}(F) \propto F^2 \exp\left(-\frac{4\sqrt{2m} \Phi_W^{3/2}}{3e\hbar F}\right). \quad (2.5)$$

Since the emission area is—in contrast to the Schottky field emitter—already confined by the small radius of curvature, no additional bias voltage needs to be applied [141]. Despite ultra-high vacuum conditions, the cold field emitter surface suffers from gas adsorption and ion sputtering, leading to a decrease and instabilities of the emission current. Regular cleaning and re-flattening of the surface is achieved by short heating cycles.

When the cold field emitter is illuminated with laser pulses, two contributions to the photoemitted current can be separated [80]. In a first process, the so-called *field-assisted photoemission*, electrons absorb enough energy to populate energy levels above the potential barrier and are directly emitted into vacuum. The second mechanism, called *photoassisted field emission*, describes the emission of electrons by tunneling through the potential barrier after transient photoexcitation to higher energy levels. Depending on the employed optical wavelength  $\lambda$ , this process can be characterized by an effective work function  $\Phi_\lambda$ , highlighting the tunability of the photoemission process: Short optical wavelengths yield lower effective work functions enabling larger photoemission currents for a given extractor voltage [178].

## 2.4 Phase-space description of electron beams

Since electron sources naturally deviate from an ideal, point-like, monochromatic emission site, photoelectrons are generated at different positions on the surface of the source with a statistical distribution of emission directions, velocities, and kinetic energies. The particle density distribution within an electron beam is in general described by the evolution of a six-dimensional phase space spanned by space and momentum coordinates [179]. Recalling Liouville's theorem [180], the initially populated volume element in phase space remains constant as long as the beam is modulated neither by apertures, nor by non-conservative fields. In order to derive invariant properties of the electron beam with respect to modulations by electromagnetic lenses, we assume a close-to paraxial propagation of charged particles along the optical axis  $z$ . Following this approximation, electron trajectories can be analyzed in a four-dimensional sub-space defined by transverse positions  $x$ ,  $y$  and canonical momenta  $p_x$ ,  $p_y \ll p_z$ . The enclosed domain in the corresponding trace space, the hyperemittance, is invariant with respect to  $z$ . For  $(x, x')$ - and  $(y, y')$ -planes intersecting each other orthogonally along the  $z$ -axis, trajectory slopes  $x'$  and  $y'$ , approximately corresponding to angles  $\alpha$  of the trajectories to the optical axis, are expressed by

$$x' := \frac{dx}{dz} = \frac{p_x}{p_z} \approx \alpha_x \quad \text{and} \quad y' := \frac{dy}{dz} = \frac{p_y}{p_z} \approx \alpha_y. \quad (2.6)$$

Decoupling of particle motions  $x(z)$  and  $y(z)$  leads to the two-dimensional emittances

$$\epsilon_x = \frac{1}{\pi} \iint_{\Omega_x} dx dx' \quad \text{and} \quad \epsilon_y = \frac{1}{\pi} \iint_{\Omega_y} dy dy' \quad (2.7)$$

defined over sub-spaces  $\Omega_{x,y}$  of the four-dimensional trace space  $\Omega = (x, y; x', y')$ .

So far, no restrictions have been made on the exact trace space area  $\Omega$ . A quantitative formulation of the experimentally accessible emittance is based on standard deviations of the spatial and angular coordinates, as well as covariance terms accounting for linear phase-space distortions [181]:

$$\epsilon_{\text{rms},x}(z) = \beta\gamma\sqrt{\langle x^2 \rangle \langle \alpha_x^2 \rangle - \langle x\alpha_x \rangle^2} \quad \text{and} \quad \epsilon_{\text{rms},y}(z) = \beta\gamma\sqrt{\langle y^2 \rangle \langle \alpha_y^2 \rangle - \langle y\alpha_y \rangle^2}. \quad (2.8)$$

Relativistic factors  $\beta = v_{x,y}/c$  and  $\gamma = (1 - \beta^2)^{-\frac{1}{2}}$  are introduced to compare the quality of electron beams at different kinetic energies and longitudinal momenta  $p_z \approx p_0 = \beta\gamma m_e c$ . At an electron focus position, the transverse root-mean-square (rms)-emittances simplify to  $\epsilon_{\text{rms},x} = \beta\gamma \cdot \sigma_x \sigma_{\alpha_x}$  and  $\epsilon_{\text{rms},y} = \beta\gamma \cdot \sigma_y \sigma_{\alpha_y}$ , with the standard deviation of the beam diameter  $\sigma_{x,y}$  and the angular spread  $\sigma_{\alpha_{x,y}}$ .

The minimum radial emittance (axial symmetry assumed) for a fully coherent beam is obtained from the Heisenberg uncertainty principle emerging as the product  $\sigma_r \sigma_\alpha \geq \frac{\hbar}{2}$ . Using  $\sigma_\alpha = \frac{\sigma_{p_\perp}}{p_z}$ , the relation

$$\frac{p_z}{\beta\gamma} \epsilon_{\text{rms},r} = \sigma_r \sigma_{p_\perp} \quad (2.9)$$

yields

$$\epsilon_{\text{qm}} = \frac{\beta\gamma}{p_z} \cdot \frac{\hbar}{2} = \frac{\hbar}{2m_e c}. \quad (2.10)$$

The longitudinal momentum  $p_z$  is calculated from the acceleration voltage:

$p_z = \frac{1}{c} \sqrt{(eU_a)^2 + 2U_a e m_e c^2}$ . For acceleration voltages  $U_a = 120$  kV and  $U_a = 200$  kV, the quantum emittances are  $\epsilon_{\text{qm}} = 0.26$  nm·mrad and  $\epsilon_{\text{qm}} = 0.19$  nm·mrad, respectively.

While apertures cut out divergent electron beam trajectories and thereby reduce the virtual source size and beam emittance, the time-averaged brightness  $B$  is invariant against such beam-modifying elements assuming aberration-free optics [179]. At the center of a Gaussian-shaped beam, the beam brightness is given by the ratio of the electron beam current  $I$  and the rms-emittances

$$B = \frac{I}{4\pi^2 \epsilon_{\text{rms},x} \epsilon_{\text{rms},y}}. \quad (2.11)$$

Alternatively, the reduced beam brightness  $B_r = B/U_a$  and the normalized brightness  $B_n = \frac{B}{(\beta\gamma)^2}$  are defined. In order to compare chopped continuous sources and pulsed electron sources with each other, it is useful to introduce a peak brightness which takes into

account the repetition rate  $f_{\text{rep}}$  of the pulsed laser and the pulse duration  $\tau$  of the electron pulses:  $B_p = \frac{B_n}{f_{\text{rep}}\tau}$ . Optimal for most time-resolved experiments are electron bunches with a small emittance and high brightness. In conventional TEM, routinely used Schottky field emitters and cold field emitters are well-characterized and known as high-brightness electron sources. Harnessing the localization of single-photon photoemission from these emitters, the beam (peak) brightness can be easily tailored to match the experimental requirements. Maximum brightness values are on the same order of magnitude as results reached in continuous mode electron microscopy [126, 145].

A prerequisite for high-quality phase-contrast images that reveal, e. g., high-resolution details in an electron micrograph, refers to the coherence of illumination considered in both the transverse and the longitudinal direction [182]. Originally developed in the field of optics for visible light but also valid in electron optics [183], the fundamental idea of coherence is intuitively grasped in interference experiments. As already mentioned in section 2.2, a limited degree of electron beam coherence damps information transfer. The (partially) coherent superposition of incident and scattered waves is characterized by the degree of coherence, limited to the range between 0 (fully incoherent) and 1 (fully coherent). In transverse direction, the degree of coherence is defined by

$$K = \frac{\epsilon_{\text{qm}}}{\epsilon_{\text{rms}}}, \quad (2.12)$$

which is inversely proportional to the beam quality factor  $M^2 \geq 1$  of an optical Gaussian-beam profile with diffraction-limited beam waist  $w_0$  (Fig. 2.6) [184]:

$$w(z) = w_0 \sqrt{1 + \left( \frac{z\lambda M^2}{\pi w_0^2} \right)^2} \quad \text{with} \quad z_{\text{R}} = \frac{1}{M^2} \frac{\pi w_0^2}{\lambda}. \quad (2.13)$$

Here,  $w$  is the beam waist of the  $1/e^2$  irradiance contour, and  $z_{\text{R}}$  is the Rayleigh distance, at which  $w_{z_{\text{R}}} = \sqrt{2}w_0$ . The square of the beam quality factor is defined as

$$M^2 = \frac{w_0\alpha_0}{w_{0,\text{d}}\alpha_{0,\text{d}}} = \frac{\pi}{\lambda} w_0\alpha_0, \quad (2.14)$$

with diffraction limited beam waist  $w_{0,\text{d}}$  and divergence angle  $\alpha_{0,\text{d}}$ .

In the minimum beam waist, the angular spread is inversely proportional to the

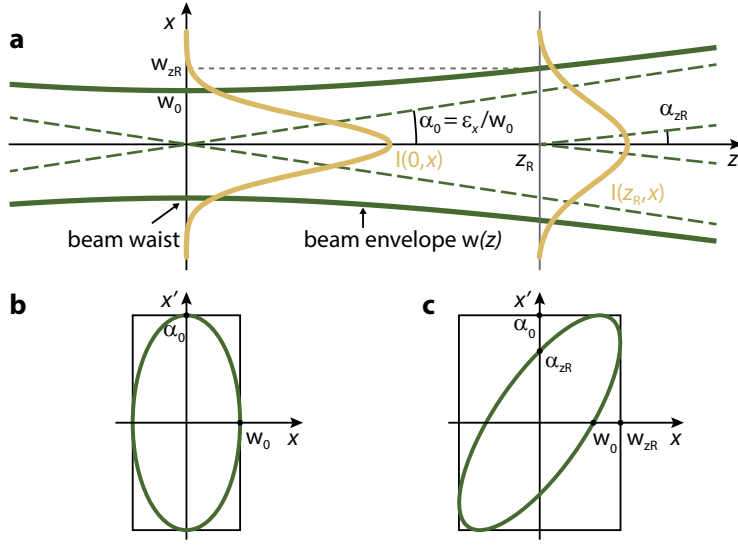


**Figure 2.6:** Gaussian-beam propagation. (a) Representation of an electron beam with a Gaussian beam shape, for which  $w(z)$  is the  $1/e^2$ -irradiance as a function of propagation distance  $z$ . Two intensity profiles are shown at the focus and at the Rayleigh distance  $z_R$ . (b,c) When the beam gradually changes from a convergent to a divergent beam in drift space, the transverse ellipse shears.

transverse (t) coherence length [185]

$$l_{\text{coh},t} = \frac{\hbar}{m_e c \beta \gamma \sigma_\alpha} = \frac{\hbar}{m_e c} \frac{\sigma_x}{\epsilon_x}, \quad (2.15)$$

which sets an upper limit for the size of the observable spatial period in the sample. This characteristic length can be determined from high-dispersive diffraction patterns or from interference fringes [see Ref. [71] and details in Figs. 2.5d and 2.5g for  $\mu\text{m}$ -scale transverse coherence lengths achieved for the Schottky field emitter].

In the longitudinal dimension (l), the energy spread  $\sigma_E$  with contributions from the emission process and mean-field space charge effects determine the temporal coherence length and time,

$$l_{\text{coh},l} = \frac{\hbar v_e}{\sigma_E} \quad \text{and} \quad \tau_{\text{coh}} \geq \frac{\hbar}{\sigma_E}, \quad (2.16)$$

respectively [186].

## 2.5 Energy spread and dispersive broadening of electron pulses

The initial shape and the charge-induced transformation of the electron distribution in real space and in phase space strongly vary for different cathode geometries and charge density regimes. The main challenge to find optimized emission parameters for high-quality beams has therefore been subject to many experimental [88, 90, 173, 185, 187] and theoretical studies [85, 90–94, 173, 188–191]. Due to the nature of the emission processes introduced

above, electron pulses already start propagating with a finite energy width that results in a shear of the longitudinal phase-space density and is associated with a temporal pulse broadening (Fig. 2.7a). In addition to this impact on the temporal resolution in ultrafast experiments, the quality of electron pulses is limited by Coulomb interactions (Fig. 2.7b,c): As will be explained below, space-charge-induced broadening and stochastic interactions affect the kinetic energy distribution of the electrons, the real-space charge distribution, and the transverse coherence properties of electron pulses.

### 2.5.1 Intrinsic energy spread

In a single-photon photoemission process, the laser pulse duration and the photon energy  $\hbar\omega$  are directly translated into the initial electron pulse duration  $\sigma_{t,0}$  and kinetic energy spread  $\Delta E$ , respectively. At a temperature of  $T = 0$  K, the major contribution to the energy broadening  $\Delta E_{\text{eff}} = \hbar\omega - \Phi_{\text{W}}^{\text{eff}}$  is intrinsically linked to the energy difference between electrons emitted from the Fermi level  $E_{\text{F}}$  and lower-state electrons passing the potential barrier by absorption of the full photon energy. Significantly reduced kinetic energy broadening is consequently achieved by photon energies just above the effective work function. Yet, due to the temperature-dependent Fermi-Dirac distribution [192, 193], the field-assisted photoemission operation temperature  $T = 1400$  K results in a kinetic energy broadening of  $\Delta E_{\text{th}} \approx 240$  meV even for excitation wavelengths just above the workfunction [113]. In pulsed photoemission mode, it is useful to operate the electron source with transform-limited laser pulses that have the lowest possible optical bandwidth [194]. For example, an energy width  $\Delta E_{\text{ph}} \gtrsim 36$  meV is obtained for a transform-limited 50-fs pulse.

### 2.5.2 Stochastic Coulomb interactions and mean-field effects

The quality of electron beams and multi-electron pulses that contain  $\langle N_e \rangle$  electrons on average is also influenced after the emission process, in particular by Coulomb interactions. An anomalous broadening of the energy distribution and of the spatial foci already arises from stochastic Coulomb interactions between neighboring electrons in the regime of low numbers of electrons per pulse and for  $\langle N_e \rangle < 1$  (Fig. 2.7a). In the longitudinal direction, the resulting irreversible energy broadening is called *Boersch effect* [195]. As a consequence of the induced change in axial velocity, uncorrectible chromatic aberrations are acquired [188, 190]. The stochastic lateral shift in electron positions and the velocity

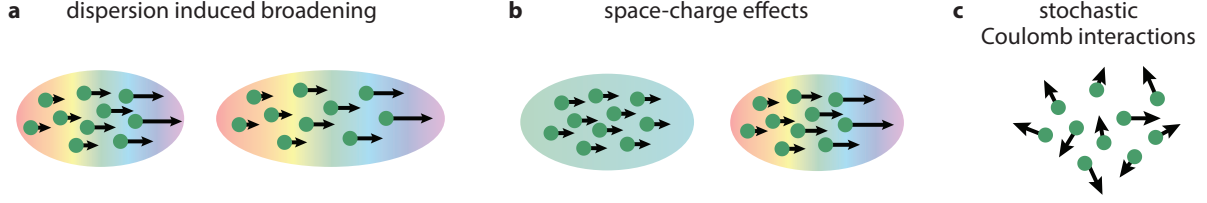


**Figure 2.7:** Dispersive and charge-induced electron pulse broadening. (a) For a given energy spread, electrons travel at different velocities which leads to a temporal pulse broadening. (b) Due to the space-charge effect in the high-charge regime, leading electrons are accelerated and trailing electrons are decelerated. (c) Stochastic Coulomb interactions are nearest-neighbor interactions arising from particle fluctuations in the charge density.

component perpendicular to the optical axis is known as *trajectory-displacement effect*, which was first investigated by Loeffler [196] and limits the achievable beam brightness [197]. In the regime of high charge densities that contain a large number of electrons ( $\langle N_e \rangle \gg 1$ ), the linear *space-charge effect* becomes more predominant—a phenomenon that is described by a mean Coulomb field. In this approximation, the ensemble averaged Coulomb interaction is considered. Leading electrons are accelerated and trailing electrons are decelerated (Fig. 2.7b), which thereby induces a reversible deformation of the phase-space distribution.

### 2.5.3 Spatial pulse broadening

The generation of short pulses in the few-fs regime requires active phase-space manipulation schemes for recompression. For the deceleration and acceleration of electrons in radio-frequency cavities [86, 185, 198, 199] or in terahertz fields [200], the charge distribution needs to exhibit space-charge forces that scale linearly as a function of position. The only distributions fulfilling this restriction are uniformly filled three-dimensional ellipsoidal charge distributions that have linear self-fields in all three dimensions [89, 201, 202]: Inside a cylindrically symmetric ellipsoid (a spheroid) with maximum radius  $R$  and half-length  $L$  (see Fig. 2.8a for schematic drawing and coordinate system), the electrostatic potential  $\Phi_{\text{acc}}(r, z)$  as a function of the radial coordinate  $r = \sqrt{x^2 + y^2}$  and the longitudinal propagation direction  $z$  reads

$$\Phi_{\text{acc}}(r, z) = \frac{\rho_0}{2\epsilon_0} (MR^2 - M_r r^2 - M_z z^2). \quad (2.17)$$

The charge density is given by  $\rho_0 = 3N_{\text{extee}}/4\pi R^2 L$ . The form factors  $M_r$  and  $M_z$  satisfy the equation  $2M_r + M_z = 1$  and depend only on the length ratios of the spheroidal primary

axes. The parameter  $M$  is defined via the geometrical eccentricity  $\Gamma = \sqrt{R^2/L^2 - 1}$  of the spheroid.<sup>2</sup> Three characteristic shapes can be distinguished in terms of the form factors:  $M_r = M_z = 1/3$  represents a sphere-like charge distribution,  $M_r = 0$ ,  $M_z = 1$  ( $L \ll R$ ) gives a disk-like charge distribution (*pancake*-limit in the nomenclature of Ref. [89]), and  $M_r = 1/2$ ,  $M_z = 0$  ( $L/R \rightarrow \infty$ ) a thin cylinder-like charge distributions (*cigar*-limit). Using  $\mathbf{E} = -\nabla\Phi_{\text{acc}}$ , the linear electric field components originating from the space-charge potential are given by

$$E_r(r) = \frac{\rho_0}{\epsilon_0} M_r r \quad \text{and} \quad E_z(z) = \frac{\rho_0}{\epsilon_0} M_z z. \quad (2.18)$$

Although Coulomb interactions still change the size and shape of the charge distribution, it remains an ellipsoid for linear internal fields (see Fig. 2.8a).

In the case of flat photocathode geometries often used in ultrafast diffraction experiments, an ideal 3D uniform ellipsoidal charge distribution is achieved by employing ultrashort laser pulses with a specifically shaped transverse profile and pulse duration  $\sigma_{\tau,0}$ . On the cathode surface, a surface charge density  $\sigma_{c,0}$  is excited to create a cylindrical disk of charges close to the emitter surface (see Fig. 2.8a). If (i) the maximum velocity acquired by the electrons during the photoemission process is much smaller than the ratio of the surface charge field and the acceleration field, and (ii) this ratio is much smaller than unity, the disk-like charge distribution eventually changes its shape to a 3D ellipsoid (*waterbag* bunch) [89, 203]. In order to characterize the uniformity of the charge distribution within the ellipsoid, it is beneficial to investigate the six-dimensional phase-space distribution obtained from numerical simulations [89]. Indeed, a linear behavior of the ellipsoidal bunch (red dots in Fig. 2.8b) is found in the decoupled 2D phase space  $(x, p_x)$  as predicted for the *pancake*-regime (black line in Fig. 2.8b). In contrast, Gaussian (blue dots) and flattop (green dots) radial profiles exhibit a strongly non-linear behavior.

In UTEM employing nanoscale tip emitters, different geometrical eccentricities are expected due to the confined emission site and the electron pulse acceleration in a high extraction field [173]. As obtain from numerical simulations (see Movie 3.1), the high initial electron density quickly evolves from a conical into a disk-like shape.

---

<sup>2</sup>Note that the eccentricity defined by this formula is real for an oblate spheroid and purely imaginary for a prolate spheroid.

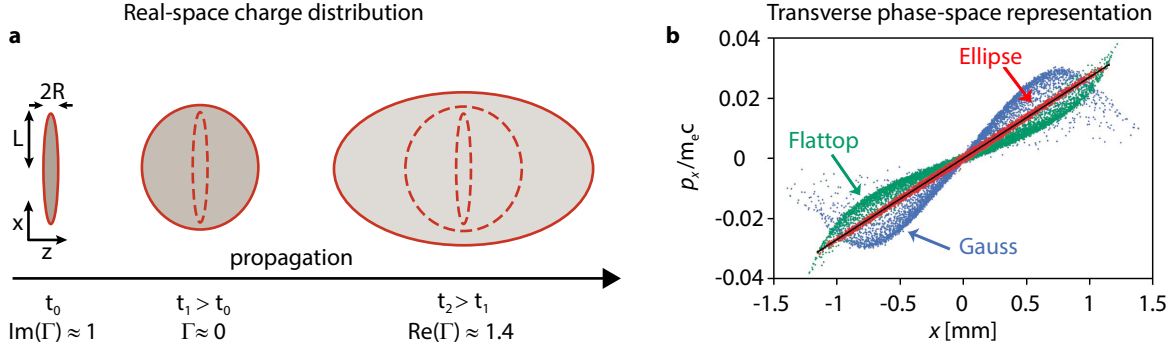


**Figure 2.8:** Spatiotemporal evolution of the electron density emitted from a flat photocathode. (a) Cross sections of a homogeneously charged ellipsoid at three time steps during propagation in a constant and uniform acceleration field. Linear space-charge forces give rise to particle velocities, which are also linear functions of position (indicated by arrows). As a result, the initial charge density distribution expands and changes its form characterized by the eccentricity  $\Gamma$  while remaining homogeneous. (b) Particle simulations of the electron density distribution in the transverse  $x - p_x$  phase space 50 ps after initiation of an ellipsoidal (red dots), a flattop (green dots), and a Gaussian (blue dots) radial profile. The linear behavior predicted for the ideal pancake-regime is represented by the black line. Reprinted with permission from Ref. [89]. Copyright 2004 by the American Physical Society.

#### 2.5.4 Spectral pulse broadening

For nonrelativistic electron pulses described by the model of initially oblate spheroids, the initial potential energy contained in the tight packing of electric charges is assumed to be completely converted into kinetic energy as the pulse disperses [85, 204]. If the initial charge distribution is uniform, the space-charge induced kinetic energy width for the final charge distribution with equal longitudinal and transverse velocities can therefore be approximately expressed as  $\Delta E = mv_0 \Delta v$ . Here,  $v_0$  is the center of mass velocity of the emitted electron pulse. The rate  $\Delta v$  of lateral broadening of the electron bunch in the direction of pulse propagation scales with the square root of the average electron number  $\langle N_e \rangle$  in the pulse [85, 187, 204].

Due to a small emission area at the tip apex, a large beam divergence angle, and strong extraction fields, space-charge behaviors are expected that drastically differ from flat photocathodes [173, 205]. Specifically, it is found that space-charge effects predominantly occur quasi-instantaneously within a distance of a few micrometers from a laser-driven Schottky emitter [173].  $N$ -body simulations and experiments reveal a linear scaling of the energy broadening with the average number of electrons per pulse (instead of the  $\sqrt{\langle N_e \rangle}$ -scaling found for flat photocathodes). Further tunability of the energy broadening is achieved at the expense of longer initial electron pulse durations: For lower temporal

electron densities, the energetic broadening can be reduced. For a more detailed analysis, the reader is referred to Ref. [173], also reprinted in the next chapter.

### 2.5.5 Temporal pulse broadening and chirp

Detailed insights into structural dynamics demand diffraction patterns recorded with high temporal resolution. The theoretical lower bound of the electron pulse duration is determined by the optical pulse duration that is nowadays much shorter than structural dynamics on the ps-timescale. Space-charge effects during the pulse propagation from the source to the sample, however, distort the spectral distribution of the electrons and result in a considerable broadening in time [85, 187]. In the first stage of the propagation, the electron pulse duration increases quadratically with the propagation time according to a numerical modelling of electrons that are photoemitted from a flat photocathode and accelerated in a homogenous electric field [85]. For example, after 40 cm propagation, electron pulses ( $E = 30$  keV,  $N_e = 10^4$ – $10^5$ ) of 90 fs initial duration are already broader than 1 ps. In order to minimize the space-charged induced broadening, it is therefore important to reduce the overall length of UED devices.

Another efficient way that facilitates diffractive imaging with high-temporal resolution is based on a different emitter geometry, i.e. nanoscale tip-emitters, that allows for large acceleration fields. The combination of both approaches has recently been implemented in compact ultrafast point-projection microscopy [154, 206, 207] to study charge dynamics [154] and in ULEED setups [206] that allow for surface sensitive measurements to access a broad range of ultrafast phenomena [49, 74, 208, 209] with a temporal resolution of 1 ps.

For tip-shaped photocathodes in strong extraction fields as in UTEM, Coulomb effects observed in the sample plane are largely accumulated within the first few micrometers after photoemission [173]. As a result of the dispersive propagation through the Schottky field emitter assembly unit, this quasi-instantaneously broadened energy distribution can be linked to the pulse duration and chirp at the sample plane. The time that electrons of initial energy  $E_0$  take to propagate along an on-axis potential  $\Phi(z)$  can be derived from the velocity expression

$$v(t) = \frac{dz}{dt} = \sqrt{\frac{2}{m_e} (E_0 + e\Phi(z))}. \quad (2.19)$$

A separation of variables results in the integral solution for the time-of-flight

$$T_{\text{flight}} = \int_0^{d_{\text{tot}}} \frac{dz}{\sqrt{2(E_0 + e\Phi(z))/m_e}} \quad (2.20)$$

over a propagation distance  $d_{\text{tot}}$ . Depending on the exact tip and electrode geometry, different field models in individual acceleration stages are considered. Between the tip apex of radius  $R$  and the extractor electrode in a distance  $d_{\text{tip} \rightarrow \text{ext}}$  (Figs. 2.9a, 3.1b), we employ a parabolic potential [175]

$$\Phi(z) = U_{\text{ext}} \left( 1 - \frac{\ln(d_{\text{tip} \rightarrow \text{ext}}/z)}{\ln(2d_{\text{tip} \rightarrow \text{ext}}/R)} \right). \quad (2.21)$$

The time-of-flight difference  $\Delta T_{\text{tip} \rightarrow \text{ext}}$  (FWHM) for electrons with different initial kinetic energies is then obtained from

$$\Delta T_{\text{tip} \rightarrow \text{ext}} = \frac{R\sqrt{m_e} \ln(d')}{\sqrt{2e}U_{\text{ext}}} \sqrt{\Delta E_0} + \frac{d_{\text{tip} \rightarrow \text{ext}}\sqrt{m_e} (\ln(d') - 1)}{\sqrt{2e^3}U_{\text{tip} \rightarrow \text{ext}}^3} \Delta E_0 + \mathcal{O}(E_0^{3/2}). \quad (2.22)$$

Here,  $d' = 2d_{\text{tip} \rightarrow \text{ext}}R^{-1}$  is introduced as a relative distance for simplification reasons. For the chosen parameters, the two terms in Eq. 2.22 differ by two orders of magnitude. The first term can be neglected and we identify the prefactor of the  $\Delta E_0$ -term as a linear spectral shear. Over a distance of 520  $\mu\text{m}$ , the time-of flight difference accumulated for  $\Delta E_0 = 0.6 \text{ eV}$  electron pulses is  $\Delta T_{\text{tip} \rightarrow \text{ext}} = 133 \text{ fs}$ . The subsequent acceleration stage between the extractor electrode and the focus anode (distance  $d_{\text{ext} \rightarrow \text{foc}}$ , Fig. 2.9a) is described by a homogeneous plate-capacitor-like potential [93]

$$\Delta T_{\text{ext} \rightarrow \text{foc}} = \sqrt{\frac{m_e}{2eU_{\text{ext}}}} \cdot \left| -\frac{d_{\text{ext} \rightarrow \text{foc}}}{e(U_{\text{foc}} - U_{\text{ext}})} \left( 1 - \frac{v_i}{v_f} \right) \right| \Delta E \quad (2.23)$$

with the electron momentum distribution  $\Delta p = \sqrt{\frac{m_e}{2E}} \Delta E$ , initial velocity  $v_i$  and final velocity  $v_f$ . This leads to  $\Delta T_{\text{ext} \rightarrow \text{foc}} = 138 \text{ fs}$  over a distance of 27.5 mm. In a similar approach, the additional pulse duration that is acquired between the focus anode and the final acceleration unit of the electron gun, is calculated, yielding  $\Delta T_{\text{ext} \rightarrow \text{foc}} = 15 \text{ fs}$  for 120-keV pulses.

The evolving shear in longitudinal phase space as a function of propagation distance (Fig. 2.9b) is summarized by a shear constant with contributions  $s_{E,i} = \partial T_i / \partial E$ . The

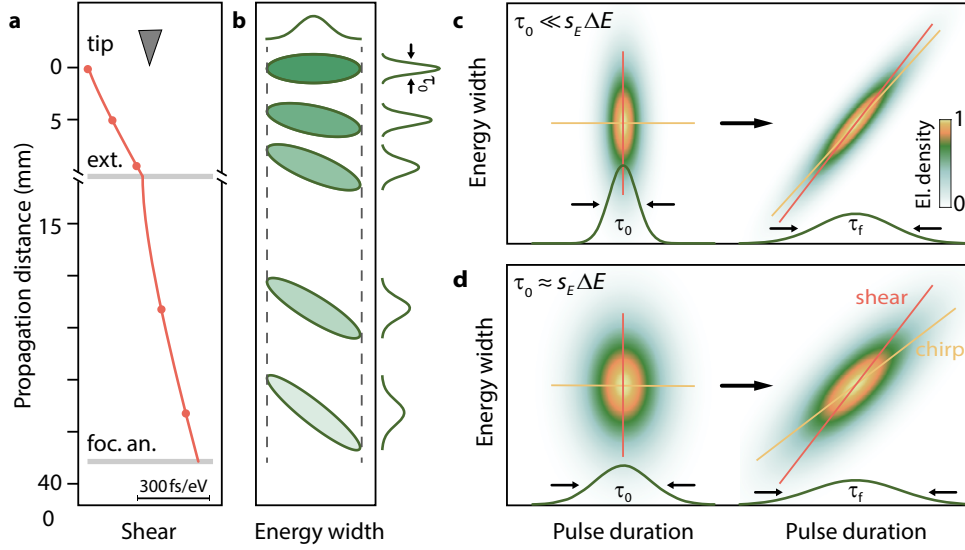


**Figure 2.9:** Dispersion induced shear and chirp of electron pulses. (a) A propagation along the optical axis of the emitter assembly unit corresponds to a shearing  $s_E$  (fs/eV) of the phase-space density. At two different acceleration stages, i.e. a parabolic- and a plate capacitor-like on-axis potential between the tip (0 keV) and the extractor (1 keV) or the extractor and focus anode (4.3 keV), respectively, similar contributions to the final shear are accumulated over largely different distances. The distance between tip and extractor is scaled by a factor of 2500. (b) Evolution of the longitudinal phase space distribution. For a given energy distribution, the increase of the shear is directly translated into the temporal domain. (c) Model of the sheared phase-space density as a Gaussian distribution. In the limit of initially short electron pulses, the electron pulse chirp is given by the inverse shear, and the electron pulse duration is directly linked to the spectral width. (d) For initial electron pulse durations similar to the duration calculated for a chosen energy spread and final shear, chirp and shear differ from each other due to the importance of the initial pulse duration.

shear is governed by the electrostatic potentials in the emitter gun (Fig. 2.9a), while propagation behind the focus anode only yields a small contribution [173]. The sheared electron distribution  $p_s(t, E)$  can be modeled by the Gaussian distribution

$$p_s(t, E) = \frac{1}{2\pi\sigma_{t,0}\sigma_E} \exp\left(-\frac{(t - s_E E)^2}{2\sigma_{t,0}^2}\right) \exp\left(-\frac{E^2}{2\sigma_E^2}\right) \quad (2.24)$$

with the energy width  $\sigma_E$  and initial pulse duration  $\sigma_{t,0}$ . For electron pulses experiencing correlated space-charge broadening effects, this model provides a valid approximation only if uncorrelated distributions in energy and time are assumed. Within this model, the final electron pulse duration  $\tau_f$  (FWHM) in the sample plane is obtained as

$$\tau_f = \sqrt{\tau_0^2 + s_E^2 \Delta E^2}, \quad (2.25)$$

in which  $\tau_0$  is the initial pulse duration (FWHM). The time derivative of the mean energy finally yields the spectral chirp  $\chi$  of the electron ensemble in energy and time space:

$$\chi = \frac{\partial \langle E \rangle}{\partial t} = \frac{\Delta E^2 s_E}{\Delta E^2 s_E^2 + \tau_0^2}. \quad (2.26)$$

To identify the dominating contribution to the final pulse duration (Eq. 2.25), we consider two different cases characterized by a parameter  $\rho^2 = 1 - \left(\frac{\sigma_{t,0}}{\tau_i}\right)^2$  (see also Ref. [210]): For initially short electron pulses ( $\sigma_{t,0} \ll s_E \sigma_E$ ,  $\rho^2 = 1$ ), the pulse duration depends linearly on the energy width,  $\tau_f = s_E \Delta E$ , and the chirp is given by the inverse shear  $\chi = 1/s_E$  as seen from Fig. 2.9c. In the other case ( $\sigma_{t,0} \approx s_E \sigma_E$ ,  $\rho^2 = 0$ ), shear and chirp strongly deviate from each other (Fig. 2.9d) and the final pulse duration is determined by  $\sigma_{t,0}$ .

### 2.5.6 Longitudinal Boersch effect and stochastic virtual source size growth

While so far reversible space-charge and dispersive effects have been discussed, we now focus on stochastic charge fluctuations that lead to an irreversible degradation of the beam quality. In particular, Coulomb interactions close to the emitting surface, where electrons accumulate in a weak potential field, or in the vicinity of crossovers contribute to the energetic Boersch effect. Extensive studies in this topic have been done by Jansen [188] who developed analytical models that predict the Boersch contribution to energy spectra of continuous electron beams from tip-shaped emitters. Major influences are attributed to the specific particle density, as well as to the spatial extension of the beam.

The analytical model assumes initially uncorrelated particles and expressed the full  $N$ -particle problem as a sum of two-particle effects. Results are therefore expected to be valid also for electron pulses. Further approximations consider two different types of electron collisions, namely complete and weak collisions, characterized by different strengths of trajectory disturbances [211, Ch. 7.3.3]. Depending on the charge regime, the collision types can be associated with different thermodynamic mechanisms that explain the maximum energy spread possible [211, Ch. 7.5]. The application of the model for a ZrO/W Schottky emitter reveals that charge distributions are characterized by a narrow core and long tails [190, 212]. The corresponding *Lorentzian*- and *Holtmarkian*-regimes reflect the generally asymmetric intrinsic energy distribution of Schottky field emitters [212]. The dominant mechanism leading to a stochastic increase in energy spread in Lorentzian- and Holtmarkian-regimes is the conversion of the potential energy into kinetic energy. For large particle densities, *Gaussian* distributions are found for which the

thermodynamic limit is best described by the transformation of an anisotropic distribution of internal kinetic energy into an isotropic distribution by reduction of the axial velocity during acceleration.

Besides the impact of the initial particle density on the energy spread, also the extraction field is an important control parameter. For the same number of electrons emitted from sources of different sizes, the Boersch effect becomes more pronounced for large tip radii and low extraction fields [190], which results from long dwell times close to the emitter tip in this case.

In addition to the stochastic broadening of the energy spread with increasing charge densities, two more effects can be observed: First, the cloud of negative charges close to the emitter surfaces reduces the electric potential which partly repels the emitted electrons. As a result, energy spectra are linearly shifted to higher energies in the original energy scale for an increasing average number of electrons per pulse [179, Ch. 49]. The second effect is related to the shape of the measured energy spectra that evolve a (asymmetric) double-peak structure for higher charge densities, reported for both, flat photocathodes [88] and tip-shaped emitters [173]. An analysis of the longitudinal phase-space distribution could reveal more details on the origin of this effect.

Similar to the stochastic Boersch effect in the longitudinal direction, analytical approximations by Jansen [214] estimate contributions to the virtual source radius from different particle density regimes. An interpolation of the different regimes [211] reveals a non-linear increase of electron spot sizes with the continuous beam current, which is also simulated for electron bunches from a laser-driven tungsten tip [213]. As expected from the dependence of the degree of spatial coherence on the virtual source size  $\mu \propto \exp[-(\pi r_{\text{eff}})^2]$ , the interference visibility decays nearly exponentially with increasing charge density in both experimental data and simulations [213] for ultrashort electron pulses (see Fig. 2.10). The strong spatiotemporal confinement of electrons close to the emitter tip leads to a coherence drop by 35 % for 1.4 electrons/pulse (doubling the effective source size) compared to the low-charge regime of approximately 0.03 electrons/pulse [213]. In the following chapter, we present experimental results on the stochastic emittance growth directly obtained through electron beam caustics recorded in a UTEM instrument.

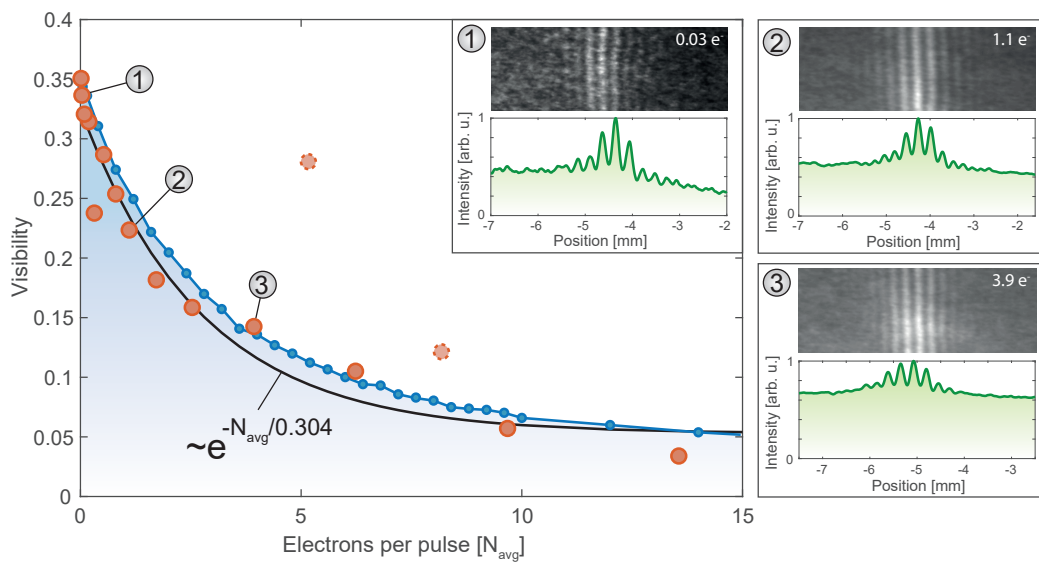


**Figure 2.10:** Spatial coherence of electron pulses influenced by stochastic Coulomb interactions. As a measure of the degree of spatial coherence, the visibility is evaluated from interference experiments using an electrostatic bisprism. With increasing number of electrons per pulse (orange experimental data points), the visibility decays exponentially (indicated by black line representing an exponential fit) due to Coulomb interactions close to the electron source. The experimental results are well-reproduced by the visibility calculated from the increase of the effective source size (blue curve). Insets 1 to 3 show example electron detector images of the measurement (top) and vertically integrated line profiles (green). Reprinted with permission from Ref. [213]. Copyright 2022 American Chemical Society.



### **Coulomb interactions in high-coherence femtosecond electron pulses from tip emitters**

---

In the quickly evolving field of ultrafast electron microscopy, the implementation of stroboscopic laser-pump/electron-probe schemes has dramatically expanded the capabilities of standard TEM. As advanced UTEM instruments rely on high-coherence ultrashort electron probe pulses, photoemission from different types of photocathodes with pulsed and continuous laser light has extensively been studied (see e.g. Refs. [71, 73, 82, 83, 108, 215, 216]). In Göttingen [71, 110] and more recently in Beijing [81] and Oldenburg, a laser-driven Schottky field emitter has been integrated into a conventional TEM. By adjusting the photon energy to the work function of the tungsten front facet, which is covered with zirconium oxide [166, 167], localized single-photon photoemission is achieved [71]. In the space-charge-free regime, i.e. for a single or a few electrons per pulse, unprecedented electron pulse properties have been achieved. At the Göttingen UTEM, for example, electron pulses durations down to 200 fs, narrow energy width of 0.6 eV and sub-nm electron focal spot diameters have been demonstrated [71].

As will be reported in this chapter, extending the investigations for few electrons per pulse in a TEM to the regime of increased bunch charges, new insights into Coulomb interactions that constrain the electron pulse properties in both the longitudinal and transverse directions are obtained. In particular, mean-field and stochastic effects cause reversible and irreversible pulse deformations. The quantitative characterization reveals a dependence of the spatial, spectral and temporal pulse properties on the bunch charge that strongly differs from the behavior known for flat photocathodes. As identified by a simplified model of the dense electron pulses propagating in a high and strongly divergent extraction field, Coulomb interactions predominantly occur within a distance of a few

micrometers from the emitter. The following article is thus an important contribution to the generation and control of tailored electron pulses, elucidating further operation modes of ultrafast electron microscopy. In particular, for experiments requiring only picosecond temporal resolution, the use of temporally broad laser pulses can enable imaging, diffraction and spectroscopy with large electron currents while maintaining nanoscale resolution.

The experimental work described in the first publication was directed by S. Schäfer. N. Bach and T. Domröse conducted the experiment. Th. Rittmann wrote the source code for the analysis of the shear and chirp with contributions from N. Bach. The chosen model of the electrostatic potential in the electron gun is based on numerical simulations done by S. Strauch as part of her master's thesis. T. Domröse performed the numerical simulations of the transverse and longitudinal beam properties in discussion with N. Bach and S. Schäfer. N. Bach, T. Domröse and S. Schäfer wrote the manuscript with contribution from A. Feist and C. Ropers.

---

Nora Bach, Till Domröse, Armin Feist, Thomas Rittmann, Stefanie Strauch,  
Claus Ropers, and Sascha Schäfer  
*Structural Dynamics* **6**, 04301 (2019)  
doi: 10.1063/1.5066093

Tip-based photoemission electron sources offer unique properties for ultrafast imaging, diffraction and spectroscopy experiments with highly coherent few-electron pulses. Extending this approach to increased bunch-charges requires a comprehensive experimental study on Coulomb interactions in nanoscale electron pulses and their impact on beam quality. For a laser-driven Schottky field emitter, we assess the transverse and longitudinal electron pulse properties in an ultrafast transmission electron microscope at a high photoemission current density. A quantitative characterization of electron beam emittance, pulse duration, spectral bandwidth, and chirp is performed. Due to the cathode geometry, Coulomb interactions in the pulse predominantly occur in the direct vicinity to the tip apex, resulting in a well-defined pulse chirp and limited emittance growth. Strategies for optimizing electron source parameters are identified, enabling advanced ultrafast transmission electron microscopy approaches, such as phase-resolved imaging and holography.

### 3.1 Introduction

The observation of ultrafast nanoscale dynamics promises a profound understanding of the spatio-temporal dynamics of elementary excitations in solids and thus new avenues for tailoring and controlling the flow of energy, charges, and spins in nanostructured materials. Experimental methods to access processes on femtosecond time and nanometer length scales are highly desired. Substantial progress has recently been achieved employing ultrafast optical near-field techniques [217–220], terahertz scanning tunneling microscopy [221, 222], and pump-probe approaches with x-ray [51, 223, 224] or electron pulses [63, 225]. Due to their large scattering cross-section and their intrinsically short wavelength, electrons are a natural choice for ultrafast nanoscale imaging. In particular, ultrafast electron microscopy (UEM) [64, 66, 69, 71, 102] and diffraction (UED) [87, 225–227] have provided a rich picture of femtosecond and picosecond processes such as optically triggered phase transitions in correlated materials [44, 74, 157, 228] and phonon dissipation [45, 47, 48, 72, 151, 227, 229] in nanostructures. The spatio-temporal resolution in these approaches crucially depends on the transverse and longitudinal electron pulse characteristics, including pulse duration, spatial coherence, and bunch charge. In UED-type experiments, few nm-scale transverse coherence lengths are often sufficient to resolve the temporal dynamics in diffraction patterns of materials with a small unit cell [227]. A higher degree of spatial coherence becomes important for resolving the dynamics related to larger unit cells, detailed spot profile analyses, and phase ordering phenomena [74–76]. For ultrafast electron imaging at nanometer length scales, a central figure-of-merit is the beam brightness, which is directly proportional to the electron current per occupied phase space area [181]. The beam brightness can be enhanced by reducing the photoemission excess energy, achievable by optimized photocathode materials [77, 79, 88]. In addition, minimizing the source size has a significant impact on the brightness and, in the past, was indispensable for the development of state-of-the-art continuous high-brightness electron sources, such as Schottky [152, 230] and cold field emitters [231], as well as single- and few-atom sources [232, 233]. The concept of tip-shaped electron sources has therefore been adopted for pulsed photoemitters with nm-sized emission areas [71, 82, 83, 108, 121, 153, 154, 172, 206]. The increased coherence properties of such tip-emitted electron pulses and their application for locally probing ultrafast phenomena were recently demonstrated for the quantum coherent optical control of free-electron states [112] and the nanoscale mapping of ultrafast structural [72] and magnetic dynamics [234].

For dense electron beams and multi-electron pulses, Coulomb interactions constrain the

beam quality in both the longitudinal and transverse directions. Specifically, the mean Coulomb field induces a reversible deformation of the phase space distribution, whereas stochastic (pulse-to-pulse) local charge fluctuations irreversibly spread the ensemble-averaged phase space distribution. This phenomenon is described as stochastic trajectory displacements [196] for the transverse direction, and termed the Boersch effect [195] for the energy broadening corresponding to the longitudinal direction.

During the last few decades, brightness limitations caused by Coulomb interactions have been the subject of many experimental [87, 88, 185, 235] and theoretical studies [85, 90–94, 188, 190, 197, 205] considering continuous electron sources as well as pulsed photoemitters.

Reversing the mean-field induced linear chirp of electron pulses is an important topic in ultrafast electron imaging, diffraction, and spectroscopy. Coherent phase space manipulation via deceleration and acceleration of electrons in oscillating radio-frequency cavities [185, 199] or by using terahertz fields [200, 236] has resulted in temporal pulse durations down to a few femtoseconds.

Despite the large body of work on Coulomb interactions in ultrashort electron pulses, little is known on their impact on pulses derived from nanoscale emitters [205, 237]. In particular, the small emission area, the large beam divergence angle, and strong extraction fields at nanotips suggest space-charge behaviors distinctively different from flat photocathode emission. A further brightness improvement of laser-driven tip emitters calls for a systematic study.

In this work, we demonstrate the application of tip-shaped photocathodes in a regime for which high photocurrent densities are formed in the vicinity of the emitter. Quantitative characterization of the longitudinal and transverse electron beam properties allows for identifying different operation modes of the photoemitter, optimized for high temporal or high spatial resolution. A simplified numerical model is presented to describe the experimental dependence of the transverse beam coherence, spectral bandwidth, and temporal chirp on the bunch charge.

## 3.2 Setup

The Göttingen ultrafast transmission electron microscope (UTEM) is based on a Schottky field-emission JEOL JEM-2100F TEM instrument, which we modified to allow for a laser-triggered photoelectron mode and for optical sample excitation [71]. Femtosecond

electron pulses are generated by employing localized single-photon photoemission from the apex of a Schottky-type ZrO/W field emission tip which is placed into an electrostatic electrode assembly (Fig. 3.1 a). The photoemitter is side-illuminated with 400-nm laser pulses focused to a spot diameter of about 20  $\mu\text{m}$  (full-width-at-half-maximum, FWHM) at a 250-kHz repetition rate. The electron bunch charge and pulse duration are varied by the laser intensity and pulse duration. The acceleration field at the tip apex is governed by the applied electrostatic potentials at the extractor ( $U_{\text{ext}}$ ) and suppressor ( $U_{\text{sup}}$ ) electrodes. At the focus electrode, the central section of the electron beam is filtered by an aperture with an effective size depending on the electrode potentials. For example, a transmission ratio through the focus electrode in the range of 0.1-1 % is expected for potentials of  $U_{\text{ext}} = 1 \text{ kV}$  and  $U_{\text{sup}} = -300 \text{ V}$  (relative to the emitter).

Behind the focus anode, the electron pulses are accelerated to an electron energy of up to 200 keV (here operated at 120 keV), coupled into the electron optics of a TEM column (condenser aperture: 100  $\mu\text{m}$ , transmission ratio about 25 %). Electron beam caustics are recorded by through-focus series around the sample plane. The minimum electron spot diameter and angular spread in the sample plane yield the transverse pulse properties [71].

For the temporal characterization of ultrashort electron pulses, we perform electron-light cross-correlation measurements utilizing the inelastic scattering of free electrons at momentum-broadened femtosecond light fields [110, 210, 238]. From the dependence of the electron energy spectra on the electron-light delay, we extract the electron pulse duration and chirp.

### 3.3 Coulomb interactions close to the emitter tip

During illumination with the 400-nm laser pulse, photoelectrons are generated at the tip apex with a distribution of kinetic energies, emission directions, and sites. The beam structure and its propagation can be described by an evolving probability distribution in phase space spanned by the spatial and momentum electron coordinates. For close-to paraxial beam propagation, the phase space can be separated into transverse (Fig. 3.1 d) and longitudinal sub-spaces (Fig. 3.1 c), spanned by corresponding spatial coordinates as well as angular and energy coordinates [181].

The initially populated region in phase space is defined by the spread in photoemission momenta and positions. In the space-charge-free regime, the occupied phase-space volume stays constant during free-space propagation or under pulse manipulation by conservative

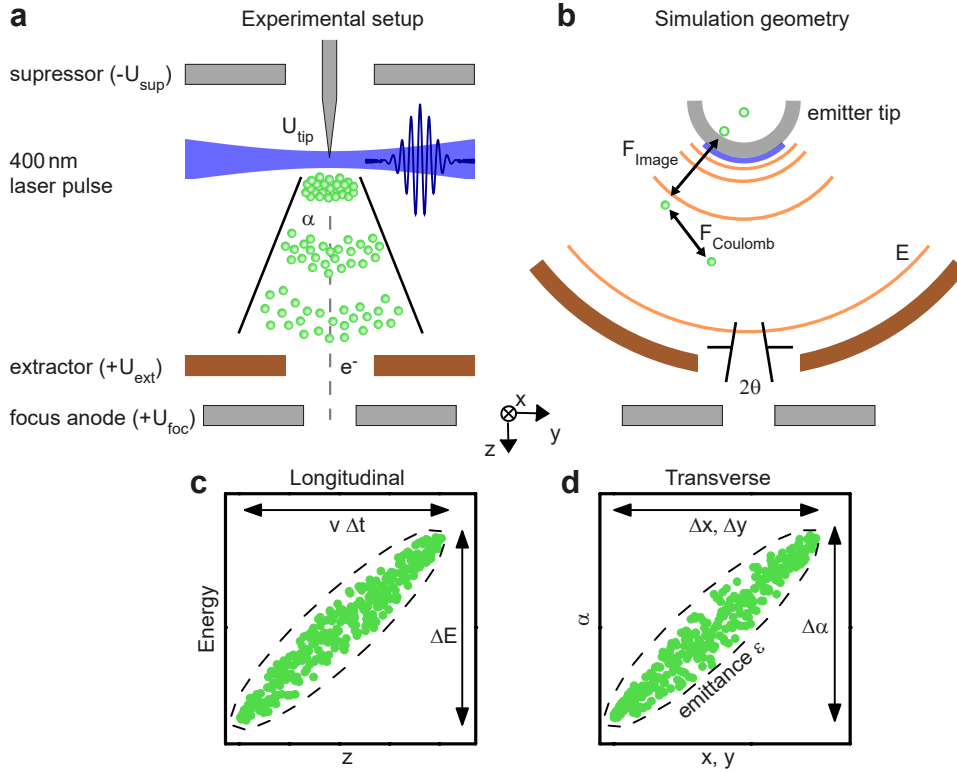


**Figure 3.1:** Experimental and simulation geometry and phase space representations. (a) Experimental electrode assembly with the Schottky-type ZrO/W field emission tip. Electrostatic potentials are given relative to the potential of the emitter. (b) Simulation geometry based on a spherical capacitor model. Propagation of the electron pulse considers the acceleration in the external electrostatic field; Coulomb interaction of the electrons within the pulse and with image charges at the emitter. (c) and (d) Sketched electron distribution (green dots) in the phase spaces corresponding to the longitudinal (c) and transverse directions (d). Longitudinal and transverse pulse properties are characterized by the energy spread and pulse duration and angular and spatial width, respectively. The transverse beam quality is given by the beam emittance, which is related to the occupied phase-space area.

fields [239] and thus, determines the minimal focus size of the pulsed electron beam and its minimum temporal width. For higher bunch charges, space-charge effects within the electron pulse result in linear and non-linear distortions of the phase space density and additional irreversible blurring due to stochastic Coulomb interactions [85, 89, 181, 240]. For quantifying the occupied phase-space area, the root-mean-square (rms) emittance [181] was introduced a quantity closely related to the beam-quality parameter in optics [184] and to the relative spatial and temporal coherence lengths [71].

### 3.4 Transverse beam properties and spectral width of electron pulses

In characterizing the transverse electron beam properties, beam caustics are measured for different numbers of electrons per pulse and laser pulse durations. In Fig. 3.2a, the rms electron spot radii,  $\sigma_r$ , are plotted as a function of defocus. We note that for the chosen gun settings, 0.15 electrons at the sample position correspond to about 10–100 photoemitted electrons at the tip. Larger beam currents (at reduced coherence) can be obtained for different gun settings optimized for an enhanced transmission ratio [71]. The observed minimum beam sizes are significantly affected by Coulomb interactions, increasing from about 3 nm in the low-current/long-pulse regime (open yellow circles) to above 9 nm for larger bunch charges and short initial pulse durations (blue solid circles). The effect of space-charge induced broadening on the electron focal spot profiles is directly visible in the spot cross-sections (Fig. 3.2d).

For quantitatively assessing the beam properties, we extract the beam emittances, given by  $\epsilon_{n,\text{rms},r} = \beta\gamma\sigma_r\sigma_\alpha$  with the relativistic Lorentz factor  $\gamma$  and  $\beta = v_e/c$  (with  $v_e$  and  $c$  being the electron and light velocities in vacuum, respectively). The corresponding angular spread of the beam,  $\sigma_\alpha = 4.4$  mrad, is determined in the far-field, and stays constant for the range of pulse parameters studied here.

The resulting emittance values are plotted in Fig. 3.2b, exhibiting an approximately linear growth with increasing electron pulse charge. Larger initial pulse durations result in less increase in the emittance, signifying weaker Coulomb interactions. As a reference, we also determined the beam emittance generated by a continuous-wave photoemission laser (405-nm wavelength, average optical power varied between 0.2 mW and 3.5 mW). The mean emittance value (orange line) coincides with the value for pulsed electron beams in the low-charge limit. For comparison with transverse beam properties in light optics, we also show the extracted beam quality factor  $M^2 = \epsilon/\epsilon_q$  (Fig. 3.2b, right axis) [71]. The quantity  $\epsilon_q = \hbar/(2m_e c)$  is the minimum emittance for a fully coherent beam, as obtained from the Heisenberg uncertainty principle for the product  $\sigma_r\sigma_\alpha$ . Furthermore, utilizing the corresponding  $M^2$  values and considering Gaussian-shaped beams, the caustic behavior of the electron pulses is well reproduced over the whole defocus range (solid curves in Fig. 3.2a).

Heating the tip to induce conventional Schottky emission, the caustic of the continuous electron beam was characterized. We obtain an emittance of 6.8 nm·mrad (gray line), comparable to the results for low-current photoelectron pulses.

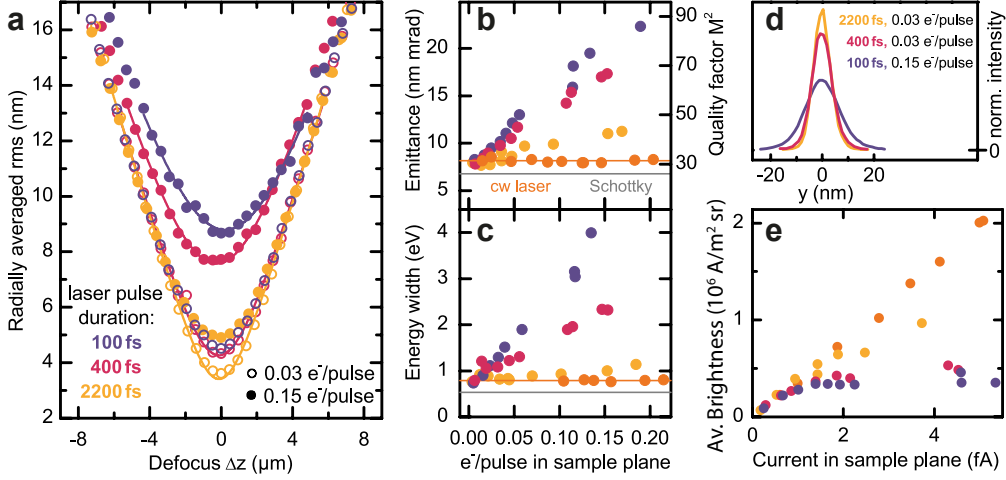


**Figure 3.2:** Experimental beam properties of photoelectron pulses. (a) Exemplary beam caustics are plotted for three different 400 nm laser pulse durations and two different electron bunch charges, characterized by the number of electrons counted in the sample plane. Laser pulse duration is varied by dispersive broadening in a 10-cm BK7 or SF6 glass bar. The solid curves are adapted to the experimental data, considering the caustic behavior of an electron beam with a beam quality factor  $M^2$  (cf. figure (b)). (b) and (c) Transverse electron beam emittance and energy width depending on the electron pulse charge in the sample plane (estimated bunch charge at the emitter: up to 200 electrons per pulse). As reference for a space-charge-free beam, the emittance and energy width of a continuous photoelectron beam and for continuous thermal electron emission are given (orange symbols and gray line, respectively). (d) Focal spot profiles of the electron pulses for selected initial pulse durations and bunch charges exhibiting a close-to Gaussian shape. (e) Electron beam brightness depending on beam current shows a linear scaling in the low-charge regime and saturation at higher bunch charges. The saturation level depends on the initial pulse duration. An equal color coding for the initial pulse durations is used in all panels.

At the focal plane ( $\Delta z = 0$ ), the electron beam profiles remain Gaussian in shape, indicating that spherical aberrations of the objective lens (spherical aberration constant  $C_s = 1.4 \text{ mm}$ ) are negligible, and no significant nonlinear beam distortions are introduced by space-charge interactions within the pulse. Notably, within the experimental resolution, no shift in the longitudinal position of the focal plane is observed for higher pulse charges, i.e., the minimum spot diameter occurs at  $\Delta z = 0$ . This observation indicates the absence of considerable space-charge induced linear distortions in the transverse phase space.

The averaged beam brightness, as shown in Fig. 3.2e, saturates at larger bunch charges due to Coulomb-induced emittance growth. Larger average brightness values are achievable for temporally stretched photoemission pulses (yellow dots), allowing for a tailoring of the photoemission parameters to the required beam brightness in ultrafast electron imaging experiments. As a limiting case, the continuous photoelectron beam exhibits no emittance growth in the utilized current range, resulting in a linear scaling of the beam brightness

with the beam current.

Space-charge effects on the pulses' longitudinal phase-space structure are characterized by considering the width of the electron energy distribution. Similar to the emittance dependencies, we observe a linear increase in the spectral width with bunch charge and weaker space-charge effects for longer initial pulse durations (Fig. 3.2c). For continuous laser illumination, the spectral bandwidth is set by the initial energy width after photoemission and the instrumental energy resolution.

### 3.5 Temporal structure of high-charge electron pulses

Space-charge broadening in the longitudinal direction results in an increase in the electron pulse duration. For quantitative characterization of the temporal electron pulse structure, we spatio-temporally overlap the electron pulses with an optical field driven by ultrashort laser pulses (800-nm central wavelength, 50-fs pulse duration, 10-mJ/cm<sup>2</sup> fluence), reflected off a single-crystalline silicon membrane (35-nm thickness). For electrons arriving at the membrane while the transient optical field is present, inelastic electron-light scattering yields photon sidebands (spaced by the incident photon energy) in the electron energy spectra, as shown in Figs. 3.3a and 3.3b. Due to the short pulse duration of the optical field, the temporal delay range  $\tau$  over which higher-order sidebands are observed corresponds to the electron pulse duration.

Exemplarily, two spectro-temporal maps are chosen to demonstrate the influence of the number of electrons per pulse (Figs. 3.3a and 3.3b). The corresponding electron energy spectra are shown in Fig. 3.3c. In the few-electron regime (Fig. 3.3a), photon sidebands are only visible in an interval of a few hundred femtoseconds. For higher bunch charges, besides the spectral broadening discussed above, photon sidebands appear over a 2-ps delay range, signifying considerable temporal pulse broadening. Integration of the gain-scattered electrons over the delay time  $\tau$  yields a quantitative measurement of the temporal profile of the electron pulses (Fig. 3.3d). The extracted pulse durations (FWHM) are plotted in Fig. 3.3e as a function of the space-charge-induced spectral broadening. Between the shortest value of 350 fs for an energy width of 0.9 eV and the longest of 1700 fs for 5.3 eV, the pulse duration depends slightly sub-linearly on the imprinted energy width.

Furthermore, a pronounced chirp of the pulses is observed, as seen in Figs. 3.3a and 3.3b. In particular, space-charge effects lead to an acceleration/deceleration of the electrons

at the leading/trailing edge. Thereby, the electron's energy and its longitudinal position within the bunch are strongly correlated, providing for a direct mapping between the spectral and temporal profiles (Figs. 3.3c and 3.3d). The chirp, plotted in Fig. 3.3f, is quantitatively extracted by performing a Fourier analysis of the spectral sidebands (on the gain side) and analyzing the phase of frequency components corresponding to the sideband periodicity.

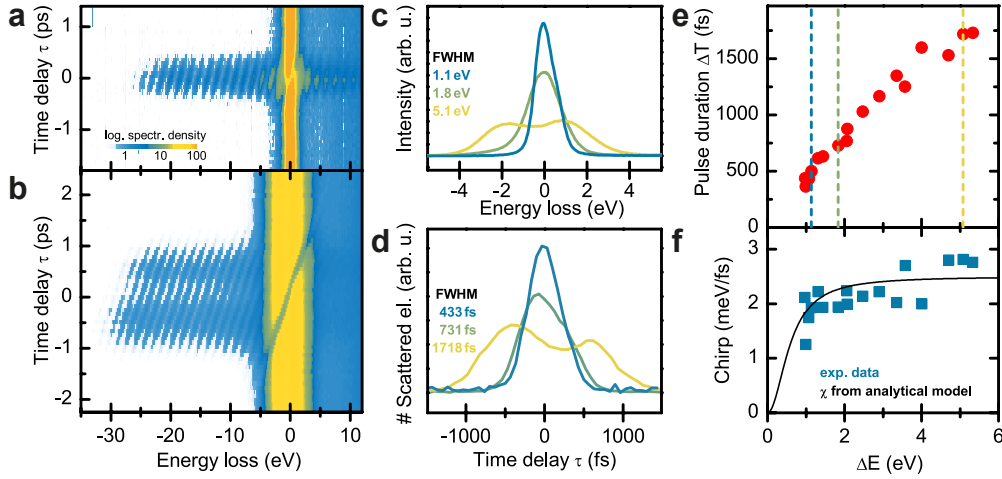


**Figure 3.3:** Longitudinal electron pulse characterization. (a,b) Energy spectra depending on the time delay between the excitation of an optical field (50-fs optical pulse duration, electron-light interaction facilitated by reflection off a thin silicon membrane) and the arrival time of the electron pulses (photoemission laser pulse duration: 100 fs). Photon sidebands on the energy-gain and -loss side are formed during temporal overlap, yielding an electron-light cross correlation. For low-charge electron pulses (a), short cross-correlation times are observed, substantially broadening for higher bunch charges (b). Color scale is chosen to highlight the temporal width of photon-sideband intensity on the gain-side of the spectra. (c,d) Space-charge induced spectral and temporal broadening is observed in the electron energy spectra (c) and temporal electron pulse profiles (d, extracted from the delay-dependent intensity of higher order photon sidebands). (e) Electron pulse duration (FWHM) scales linearly with its energy width. Dotted lines: position of spectral and temporal profiles shown in c and d, respectively. (f) Electron pulse chirp (blue symbols) is derived from the inclination of the photon sidebands. The experimental data is well described by an analytical model (black line) considering an energy-independent shear amplitude due to pulse propagation and a space-charge-induced spectral broadening close to the emitter tip.

### 3.6 Simulation

For the numerical simulation of the transverse and longitudinal electron beam properties in the space-charge regime, we consider a simplified electron-optical geometry consisting of a spherical photocathode and an extractor electrode (Fig. 3.1b). In the simulation,

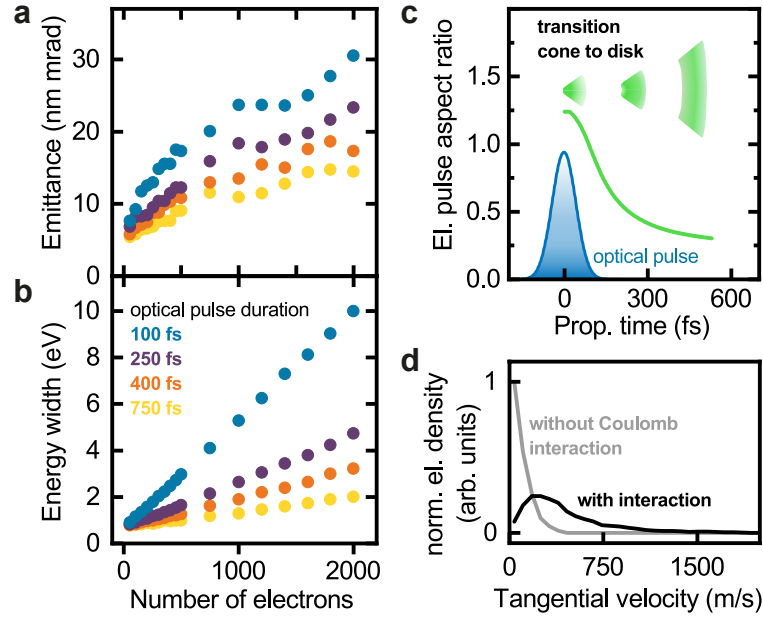


**Figure 3.4:** Simulated electron pulse properties. (a,b) Transverse electron beam emittance and energy width depending on the number of emitted electrons and the initial pulse durations. A linear scaling with the charge density is found. (c) Aspect ratio (longitudinal relative to transverse pulse width) of electron pulse depending on the delay after arrival of the photoemission laser pulse at the tip apex. After photoemission, the pulse evolves from a conical to a disk-like shape. Blue curve: intensity profile of the photoemission laser. (d) Distribution of tangential electron velocities (i.e., velocity components perpendicular to the radius vector from the center of the spherical emitter apex) at a radial distance of  $315\ \mu\text{m}$  from the emitter for the space-charge-free regime (gray curve) and with Coulomb interactions (black curve, considering 2000 electrons/pulse and an initial pulse duration of 100 fs).

photoelectrons are randomly generated according to a homogeneous probability density at the surface of a spherical tip apex (240 nm tip radius,  $\pi/2$  opening angle of emission surface, isotropic photoemission direction). Geometric dimensions of the model are chosen such that the emitting area and the distance between the tip and the extractor ( $d_{\text{tip-ext}} = 350\ \mu\text{m}$ ) resemble the experimental conditions. The electron pulse is propagated from the emitter to the extractor employing a Verlet algorithm [241], considering the interaction with the external electrostatic field, intrapulse Coulomb forces, and contributions from image charges at the emitter.

The influence of Coulomb interactions on the transverse and longitudinal properties of the electron pulses is investigated by varying the number of electrons per pulse for a set of initial pulse durations. To properly account for the beam apertures in the experiment, we select the central section of the simulated electron bunch for the beam analysis. The acceptance angle  $2\theta$  of the effective aperture (172 mrad) and the initial energy distribution after photoemission (0.9 eV) were adapted to the experimental emittance and the spectral

width in the space-charge-free regime. The aperture size provides for a transmission ratio comparable to the beam limiting aperture (opening angle 200 mrad) in trajectory simulations within the non-spherical field-distribution of the suppressor-extractor geometry. We note that for our experimental conditions, the transmission ratio does not depend on the initial electron bunch charge and duration, so that a linear scaling between the photoemitted electron current and the current in the sample plane can be applied.

The beam emittances and energy widths of the electron pulses are shown in Figs. 3.4a and 3.4b, respectively. In close correspondence to the experimental results, a linear scaling of both properties with the bunch charge is found. In addition, longer initial pulse durations (i.e., for stretched laser pulses) largely reduce space-charge effects at a given bunch charge. The overall magnitude of Coulomb-induced emittance-growth for a given spectral broadening reproduces the experimental findings. Fully quantitative agreement would require detailed knowledge on the in-operando emitter tip shape and the local photoemission probability on its surface.

### 3.7 Discussion

At tip-shaped photocathodes, electrons are accelerated by large electrostatic extraction fields on the order of  $10^8$ – $10^9$  V/m and form a strongly diverging beam, with the beam eccentricity [89] changing from a conical to a disk-like shape (Fig. 3.4c and Movie in the supplementary material). Therefore, the initially high charge density (around  $50e^-/(\mu\text{m})^3$ ) around the emitter apex quickly disperses, and the emitted electrons experience considerable Coulomb forces for a short time only. The Coulomb effects observed in the sample plane are largely accumulated within the first few micrometers after photoemission. For example, about 80% of the final spectral width is gained within the first  $4\mu\text{m}$  of the propagation distance, for an electron bunch charge of 150 electrons and 100 fs initial pulse duration. After the beam-defining aperture in the focus electrode, the pulse contains less than one electron on average, so that intra-pulse Coulomb interactions, e.g., at cross-overs, are negligible. We note that such a combination of high-charge density at the tip and subsequent space-charge-free propagation drastically differs from the regimes studied for many-electron femtosecond pulses generated from flat photocathodes, often utilized in ultrafast electron diffraction studies [86] or in dynamic TEM with nanosecond temporal resolution [242].

Using the quasi-instantaneous space-charge-induced electron broadening at the tip, we arrive at an analytical model which links the energy width to the pulse duration and chirp at the sample position. In particular, we consider the propagation time  $T = \int dz [2/m_e(E_0 + e\Phi(z))]^{-1/2}$  of electrons with an initial energy  $E_0$  along the optical axis, where  $m_e$  and  $e$  are the electron mass and its charge and  $\Phi(z)$  is the on-axis potential. To properly include the static field enhancement at the tip, we choose a parabolic electrostatic potential [175] between the tip and the extractor, and plate-capacitor-like geometries for the subsequent acceleration stages. From the slope of  $T(E)$ , we evaluate the shearing angle of the longitudinal phase space distribution due to propagation from the source to the sample, yielding a shear of  $\frac{\partial T}{\partial E} = s_E = 480 \text{ fs/eV}$ .

Whereas the space-charge induced energy broadening occurs within  $4 \mu\text{m}$  after photoemission (within approximately 200 fs after photoemission), the translation of this broadened energy distribution into a temporal width is mainly accumulated during the first two acceleration stages, i.e., in-between the photocathode, extractor, and focus anodes (shear contributions of 46 % and 48 %, respectively). Only a minor shear results from the further propagation behind the focus anode.

In the inelastic electron-light scattering experiments (Fig. 3.3), the spectral chirp of the electron pulses is evident from the change of the mean electron energy with time. In general, the relationship between the shear in longitudinal phase space and the observed spectral chirp depends on the shape of the electron distribution function [210]. Considering a sheared Gaussian distribution  $f_s(t, E) = N e^{-\frac{(t-s_E E)^2}{2\sigma_t^2}} e^{-\frac{E^2}{2\sigma_E^2}}$ , in which  $\sigma_E$  is the electron energy width,  $\sigma_t$  the initial pulse duration, and  $N$  the normalization constant, we obtain the chirp  $\chi = \frac{\partial \langle E \rangle}{\partial t} = \frac{\sigma_E^2 s_E}{\sigma_E^2 s_E^2 + \sigma_t^2}$ . For  $\sigma_t = 100 \text{ fs}$  and  $s_E = 400 \text{ fs/eV}$ , the experimental data are well reproduced (Fig. 3.3f, black curve). We note that for distributions with  $\sigma_E s_E > \sigma_t$ , i.e., in the limit of large shear or spectral width, the electron pulse chirp is given by the inverse shear,  $\chi = \frac{1}{s_E}$ . In this limit, the electron pulse duration at the sample  $\Delta T = s_E \Delta E$  is directly linked to the spectral width. The shear constant  $s_E$  is governed by the chosen electrostatic potentials in the emitter gun, providing an approach to monitor pulse durations and to minimize the temporal spread for a given space-charge-induced spectral broadening.

Different from the reversible distortion of the electron distribution in the longitudinal direction, transverse electron pulse properties are affected by an emittance growth. In order to gain a microscopic picture of the underlying processes from the simulation results, we consider the electron velocities at a radial distance of  $315 \mu\text{m}$  from the emitter. In a

spherical coordinate system with its origin at the center of the emitter half sphere, the tangential velocity component, i.e., perpendicular to the radial vector, is a measure of the deviation from a fully coherent beam. The velocity distribution in the space-charge-free case (Fig. 3.4d, gray curve), is related to the initial photoemission velocity. Space-charge interactions result in a pronounced broadening of the distribution of tangential velocities (Fig. 3.4d, black curve), signifying an increase in the back-projected electron source size and thus an increased beam emittance.

### 3.8 Conclusion

In conclusion, we systematically evaluated the properties of a laser-driven Schottky field emitter for ultrafast transmission electron microscopy, operated in a regime of a high-density of photoemitted electron bunches. The observed pulse properties are well described by a simplified model of dense electron pulses propagating in a high and strongly divergent extraction field. Electron pulse properties in the longitudinal and transverse directions are governed by reversible space-charge induced spectral broadening with subsequent pulse shearing, and stochastic emittance growth, respectively, predominantly occurring within a distance of a few micrometers from the emitter. Large extraction fields at the emitter apex allow for dense nanoscale pulses with only moderate Coulomb-induced beam deterioration. The presented theoretical framework and demonstrated control of electron pulse properties generally apply for nanoscale photocathodes in similar gun geometries, and enable the generation of tailored electron pulses adapted to the specific requirements of ultrafast electron imaging, diffraction, and spectroscopy experiments.

### 3.9 Supplementary Material

See supplementary material for details on the space-charge free electron pulse propagation as obtained from numerical simulations (video).

**Movie 3.1: Diverging electron pulse.**

The electron pulse strongly diverges due to the high extraction field and changes its geometrical eccentricity from a conical to a disk-like shape.

---

The movie is available as Supplementary Material on the *Structural Dynamics* website at the following link: [aca.scitation.org/doi/suppl/10.1063/1.5066093](http://aca.scitation.org/doi/suppl/10.1063/1.5066093).

### **Acknowledgements**

This work was funded by the Deutsche Forschungsgemeinschaft (DFG) as part of the Collaborative Research Center Atomic Scale Control of Energy Conversion (DFG-SFB 1073, project A05) and in the Priority Program Quantum Dynamics in Tailored Intense Fields (DFG-SPP 1840). We gratefully acknowledge support from the Lower Saxony Ministry of Science and Culture and funding of the instrumentation by the DFG and Volkswagen Foundation. S.S. acknowledges support by the Volkswagen Foundation through a Lichtenberg professorship.

---

### Nanophononic waveguides

---

Focusing on fast processes occurring on small length scales, nanophononics is emerging as a growing research field addressing fundamental questions on how acoustic vibrations can be manipulated and controlled to pave the way towards novel technological applications [243]. High-frequency acoustic phonons in the gigahertz–terahertz (GHz–THz) range strongly impact thermal [61, 244–246] and electronic [247, 248] transport mechanisms, and exhibit optomechanical couplings with tailored light fields on the nanoscale [249–251]. The significance of acoustic phonons is met by recent interdisciplinary advances in the engineering of efficient thermoelectric [252], noise-controlled electromechanical [13], and high-quality optomechanical [253–255] devices. Discrete vibrational motions in nanoscale waveguides are also receiving increasing attention as versatile, ultrasensitive detectors [22, 24, 25, 256–259] with breakthroughs in the quantum mechanical regime [19].

Acoustic phonon engineering that aims for dispersion relations different from bulk systems is based on phonon confinement achieved in nanoscale systems of reduced dimensionality like thin membranes [260–262] and nanowires [263]. Inspired by previous concepts applied in photonics and electronics, another sophisticated approach to control acoustic phonon propagation and the density of states includes periodic structures such as phonon mirrors, filters, and resonant cavities within phononic crystals [264]. Modulating elastic properties, phononic waveguides have recently been demonstrated to allow for complete energy band gaps [265–268] preventing phonon propagation at certain frequency ranges and to overcome significant loss problems arising from scattering at defects and imperfections [269, 270]. In analogy to the quantum Hall effect [271], active topological protection is achieved by breaking the time-reversal symmetry.

Therefore, the investigation of all these confined and architected nanostructures has already been a promising scientific pursuit, motivated by both an exploration of funda-

mental wave phenomena in elastic media and directed towards applied sciences. Especially Lamb waves in nanostructured plates provide a way to realize complex phononic wave fields. However, profound understanding of phonon lifetimes [28, 272], the impact of predeformation [273, 274], and interfacial effects [275] in polycrystalline and heterogeneous acoustic waveguides remains crucial for the design and device engineering, and depends upon the study of prototypical model systems, such as (nano-patterned) semiconductor thin films [31, 260, 276, 277] and two-dimensional membranes [54, 72, 278]. Also, the controlled generation and probing of localized phononic wave fields in well-defined nanoscale structures with high temporal resolution is still challenging. Employing ultrafast convergent beam electron diffraction to a platinum/silicon heterostructure [116], we combine both, an ideal system for tailored nanophononic wavefields and a technique applicable for the quantitative retrieval of time-dependent local deformations. In general, the problem of acoustic wave propagation is based on elasticity theory, which is introduced in the following and subsequently applied to a fundamental description of Lamb waves in isotropic and anisotropic media.

## 4.1 Basic principles of elasticity theory

For a quantitative discussion of propagating acoustic waves and localized oscillations in linearly elastic solids, basic elasticity equations are briefly reviewed in the following. The medium of interest is regarded in the continuum-mechanical approach which means that all physical and material specific properties are considered as continuous functions representing averages of microscopic quantities [279]. Here, all equations are given in Cartesian coordinates and the reader is referred to comprehensive books [279–285] for an equivalent notation in spherical and cylindrical coordinates.

### 4.1.1 Tensor representation of structural deformations

An intuitive measure for structural deformations is the spatial variation of a displacement vector field  $\mathbf{u}$ . To incorporate the directional specificity in anisotropic media, we describe the lattice distortions by tensor algebra, as commonly applied in various fields in physics. The individual displacement derivatives  $\frac{\partial u_i}{\partial x_j}$  define the local displacement gradient tensor  $\mathbf{F}$ ,

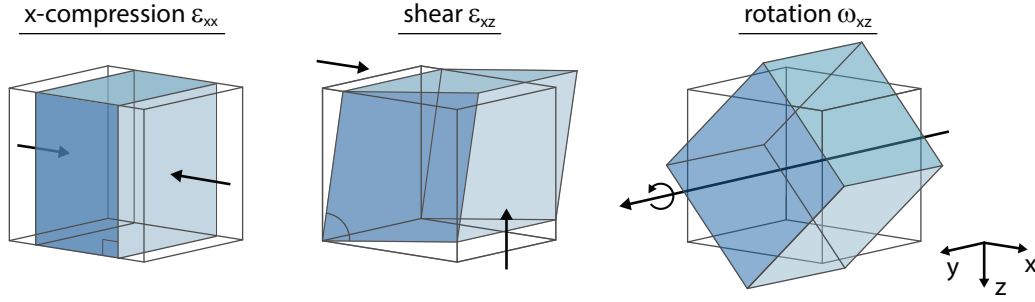


**Figure 4.1:** Compression, pure shear, and rotational distortions in crystal lattices. For selected deformation gradient tensor components, schematic representations of associated lattice distortions are shown.

which in linear elasticity theory reads:

$$F_{ij} - \delta_{ij} = \underbrace{\frac{1}{2} \left( \frac{\partial u_i}{\partial x_j} + \frac{\partial u_j}{\partial x_i} \right)}_{\text{symmetric, } \epsilon_{ij}} + \underbrace{\frac{1}{2} \left( \frac{\partial u_i}{\partial x_j} - \frac{\partial u_j}{\partial x_i} \right)}_{\text{antisymmetric, } \omega_{ij}} \quad (i, j = 1, 2, 3). \quad (4.1)$$

Here,  $\delta_{ij}$  is the Kronecker delta. In a simple physical interpretation, the application of  $F_{ij} - \delta_{ij}$  to an undistorted real-space basis leads to a deformed unit cell basis that describes a locally strained and/or rotated lattice, depending on the contributions of the symmetric strain and antisymmetric rotation tensors  $\epsilon$  and  $\omega$ , respectively. A schematic illustration of the distortions associated with the individual deformation gradient tensor components is found in Fig. 4.1. Throughout this thesis, bold face letters are used for tensors, matrices, and vector fields. As the number  $n$  of independent indices (here 2) defines the tensor rank, the stress and strain, as well as their sum, are second-order rank tensors with in general  $3^n$  (here 9) elements.

A quantity characterizing associated forces, that return the solid to its equilibrium state, are tractions  $t_i$ . Considering a small rectangular parallelepiped ( $dx dy dz$ ) within the elastic medium, these restoring forces act on each surface with the subscript  $i$  denoting to surface normals  $\hat{e}_i$ . As seen from Fig. 4.2a,  $t_i$  is in general not parallel to  $\hat{e}_i$ . Each traction may be written in terms of its Cartesian components in the form [284, Ch. 3.1.1]

$$t_i(\hat{\mathbf{e}}) = \sigma_{ik} \hat{e}_k \quad (i, k = 1, 2, 3). \quad (4.2)$$

Unless otherwise noted, we use the Einstein summation convention [286], in which a repeated index denotes summation over the range of the index. The coefficients  $\sigma_{ik}$  are the components of the second-rank stress tensor  $\boldsymbol{\sigma}$ , also known as a generalized

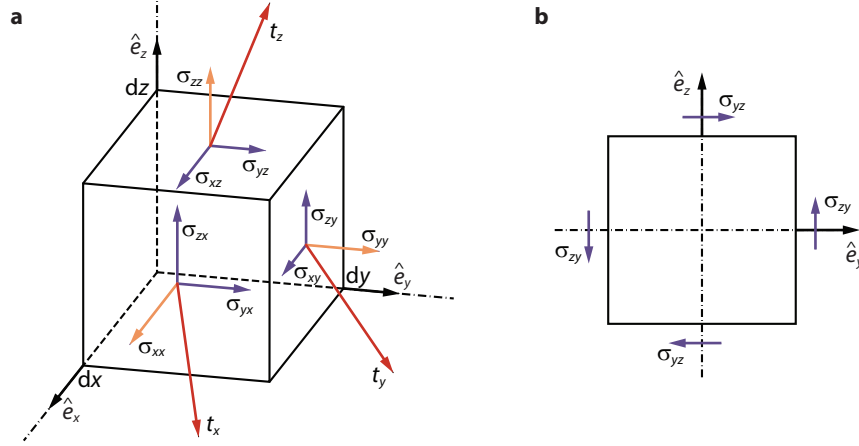


**Figure 4.2:** Components of the stress tensor. (a) Definition of the stress tensor components. Each surface of the cubic volume element experiences one normal ( $\sigma_{ii}$ ) and two in-plane shear components ( $\sigma_{ij}$ ,  $i \neq j$ ) of stress. Normal stresses cause length changes of a differential element, shear stresses cause angular changes of the element. Traction  $t_i$  acting on the surfaces of the cube are defined by Eq. 4.2. (b) 2D visualization of the symmetry relation  $\sigma_{ij} = \sigma_{ji}$  in the case of vanishing angular momentum.

‘pressure’ that is defined as a force per unit area. Whereas thermodynamic pressure is a unidirectional quantity, an arbitrary stress can be decomposed into nine components. Each component is specified by a magnitude and two basis vectors. The first index  $i$  of the stress component  $\sigma_{ik}$  denotes the *direction*  $\hat{e}_i$  in which the stress acts. The second index  $k$  corresponds to the *normal* vector  $\hat{e}_k$  of the plane area *on* which the stress acts. Even though  $\sigma_{xx}$  and  $\sigma_{xy}$  act in the same  $x$ -direction, the nature of the stress components is different. Equal indices describe a tension or compression depending on the sign of  $\sigma_{ii}$ ; stress tensor components with mixed indices describe shear deformations. For small deformations, the elastic stress is related to the strain field (Cauchy’s method) by the first-order term of the Taylor expansion [284, Ch. 3.2; 279, App. A5]

$$\sigma_{ij}(\epsilon_{kl}) = \sigma_{ij}(0) + \left( \frac{\partial \sigma_{ij}}{\partial \epsilon_{kl}} \right)_{\epsilon_{kl}=0} \epsilon_{kl} + \frac{1}{2} \left( \frac{\partial^2 \sigma_{ij}}{\partial \epsilon_{kl} \partial \epsilon_{mn}} \right)_{\substack{\epsilon_{kl}=0 \\ \epsilon_{mn}=0}} \epsilon_{kl} \epsilon_{mn} + \dots \quad (4.3)$$

With  $\sigma_{ij}(0) = 0$ , we obtain the *constitutive equation*

$$\sigma_{ij} = C_{ijkl} \epsilon_{kl} \quad (i, j, k, l = 1, 2, 3) \quad (4.4)$$

for (an)isotropic elastic materials. In analogy to Hooke’s law describing the elongation of a spring by action of a force, the generalization of this law expressed by Eq. 4.4

states that the strain of an elastic material is proportional to the stress it encounters. The coefficients  $C_{ijkl} = \left(\frac{\partial \sigma_{ij}}{\partial \epsilon_{kl}}\right)$  are components of the fourth-rank stiffness tensor [284, Ch. 3.2.1]. While  $\epsilon$  and  $\sigma$  represent physical quantities,  $\mathbf{C}$  is a characteristic of the elastic material similar to the spring constant as a measure for the spring's stiffness. For crystal structures, stiffness constants are on the order of  $10^{11}$  N/m<sup>2</sup> (100 GPa), which is five orders of magnitude larger than for soft biological tissues. Since this elastic property may vary for different crystalline directions, it is necessary to specify the chosen coordinate system. A summary of the presented tensors and constitutive relations that describe linear elastic deformations of solids is given in Tab. 4.1.

**Table 4.1:** Overview of tensors needed to describe structural deformations.

tensor	rank	measured quantity	units	subscript notation	compact notation
$\epsilon$	2	strain	-		
$\omega$	2	rotation	-	$F_{ij} = \epsilon_{ij} + \omega_{ij} + \delta_{ij}$	$\mathbf{F} = \epsilon + \omega + \mathbf{1}$
$\mathbf{F}$	2	displacement gradient	-		
$\mathbf{t}(\hat{e})$	1	traction	GPa	$t_i = \sigma_{ik} \hat{e}_k$	$\mathbf{t} = \boldsymbol{\sigma} \cdot \hat{e}$
$\boldsymbol{\sigma}$	2	stress	GPa	$\sigma_{ij} = C_{ijkl} \epsilon_{kl}$	$\boldsymbol{\sigma} = \mathbf{C} : \epsilon$
$\mathbf{C}$	4	stiffness	GPa		

### 4.1.2 Symmetry simplifications

Although the stiffness tensor has generally  $3^4 = 81$  components, symmetry relations considerably reduce the number of independent elements needed for the full quantification. Two types of symmetry observations can be distinguished, addressing the stress and strain tensors on the one hand, and the crystal symmetry of the material itself on the other hand.

From the conservation of angular momentum valid for centro-symmetric crystals, it follows that  $\sigma_{ij} = \sigma_{ji}$  (Fig. 4.2b). Together with the symmetric strain tensor  $\epsilon_{ij} = \epsilon_{ji}$ , the resulting two so-called minor symmetries for the stiffness tensor  $\mathbf{C}$  reduce the number of independent elastic constants from 81 to 36 [284, Ch. 3.2; 287, Ch. 4; 283, Ch. 2.1]:

$$C_{ijkl} = C_{jikl} \quad \text{and} \quad C_{ijkl} = C_{jilk}. \quad (4.5)$$

The number of tensor components for the general anisotropic case can be further reduced to 21 due to energy conservation: By recalling the constitutive equation (Eq. 4.4) and

assuming the existence of a strain-energy function  $U = \frac{1}{2} C_{ijkl} \epsilon_{ij} \epsilon_{kl}$  [279, App. A5; 283, Ch. 2.9; 280, Ch. 3] such that  $\sigma_{ij} = \partial U / \partial \epsilon_{ij}$ , we find the major symmetry

$$C_{ijkl} = C_{klij} \quad (4.6)$$

for any non-zero real symmetric strain tensor  $\boldsymbol{\epsilon}$ .<sup>3</sup>

With these symmetry considerations in mind, the generalized Hooke's law in terms of displacements becomes

$$\sigma_{ij} = C_{ijkl} \frac{\partial u_l}{\partial x_k}. \quad (4.7)$$

Another consequence of the observed symmetry relations is that a pair of unordered indices  $(i, j)$  can give only six independent values, yielding the contracted Voigt notation [288]:

$$\begin{aligned} (11) &\leftrightarrow 1 & (22) &\leftrightarrow 2 & (33) &\leftrightarrow 3 \\ (23) = (32) &\leftrightarrow 4 & (31) = (13) &\leftrightarrow 5 & (12) = (21) &\leftrightarrow 6. \end{aligned} \quad (4.8)$$

Hence, we can rewrite  $(C_{ijkl})_{i,j,k,l=1,2,3}$  in the form of a  $6 \times 6$  matrix

$$\begin{pmatrix} C_{11} & C_{12} & C_{13} & C_{14} & C_{15} & C_{16} \\ & C_{22} & C_{23} & C_{24} & C_{25} & C_{26} \\ & & C_{33} & C_{34} & C_{35} & C_{36} \\ & & & C_{44} & C_{45} & C_{46} \\ & & & & C_{55} & C_{56} \\ \text{Sym.} & & & & & C_{66} \end{pmatrix}. \quad (4.9)$$

Here, the definition  $C_{\alpha\beta} = C_{ijkl}$  is introduced, in which  $\alpha$  is related to  $(ij)$  and  $\beta$  is related to  $(kl)$ .

As first stated by Pierre Curie in 1894 [289], the coefficient tensor  $\mathbf{C}$  also has to be in accordance with the symmetry of the physical system. The maximum number of 21 independent elastic constants applies to triclinic lattices. Less independent entries are sufficient for crystals with higher symmetries: For example, the stiffness tensor of a hexagonally symmetric material (e.g.  $2H$ -polytype transition metal dichalcogenides [290]) is invariant for all rotations around the 6-fold principle axis and is composed of five independent components (Fig. 4.3, left panel), of which two yield the  $C_{66}$ -component. For

---

<sup>3</sup>The same result is obtained by Green's method deriving the stress-strain relation from the energy function  $U$  [279, App. A5].

cubic crystals (including the diamond lattice of Si), three mutually orthogonal planes of mirror symmetry and the four-fold rotational symmetry yield three stiffness-components (Fig. 4.3, middle panel). The elastic properties of an isotropic solid are invariant for any change of axes and are specified by two independent constants (Fig. 4.3, right panel). These are the material-dependent Lamé constants  $\lambda = C_{12}$  and  $\mu = C_{44} = (C_{11} - C_{12})/2$ , sometimes referred to as the dynamic viscosity (in fluid dynamics) and shear modulus, respectively [279, Ch. 5.1.1, 284, Ch. 3.2.3].

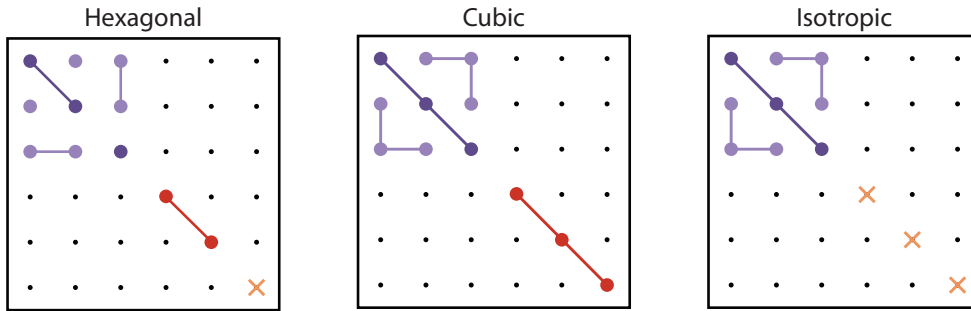


**Figure 4.3:** Elastic stiffness constants for different crystal structures. Non-zero components of the stiffness tensor in Voigt notation (see Eq. 4.9) are indicated by filled circles, equal components by connected circles, and components marked with a cross can be calculated from  $(C_{11} - C_{12})/2$ . Due to specific crystal symmetries, the number of independent stiffness components is significantly reduced to 5 (hexagonal), 3 (cubic) and 2 (isotropic). In standard notation, we typically find  $C_{11} \approx C_{33} > C_{12} \approx C_{13}$  as visualized by different color gradients, and  $C_{11} > C_{44}$ .

### 4.1.3 Compact symbolic tensor notation

While the subscript notation used so far is useful for direct numerical implementations, the more compact symbolic tensor notation (see also last column of Tab. 4.1) allows for a more insightful algebraic formulation and discussion of guided acoustic waves in anisotropic media (see section 4.2.2). In this approach introduced by Auld [281, Ch. 1F], the  $3 \times 3$  matrix representation of the strain tensor

$$\boldsymbol{\epsilon} = \frac{1}{2} \begin{pmatrix} \frac{\partial u_1}{\partial x_1} & \frac{\partial u_1}{\partial x_2} & \frac{\partial u_1}{\partial x_3} \\ \frac{\partial u_2}{\partial x_1} & \frac{\partial u_2}{\partial x_2} & \frac{\partial u_2}{\partial x_3} \\ \frac{\partial u_3}{\partial x_1} & \frac{\partial u_3}{\partial x_2} & \frac{\partial u_3}{\partial x_3} \end{pmatrix} + \frac{1}{2} \begin{pmatrix} \frac{\partial u_1}{\partial x_1} & \frac{\partial u_2}{\partial x_1} & \frac{\partial u_3}{\partial x_1} \\ \frac{\partial u_1}{\partial x_2} & \frac{\partial u_2}{\partial x_2} & \frac{\partial u_3}{\partial x_2} \\ \frac{\partial u_1}{\partial x_3} & \frac{\partial u_2}{\partial x_3} & \frac{\partial u_3}{\partial x_3} \end{pmatrix}, \quad (4.10)$$

becomes

$$\boldsymbol{\epsilon} = \frac{1}{2} \left( \nabla_{\mathbf{x}} \mathbf{u} + (\nabla_{\mathbf{x}} \mathbf{u})^T \right), \quad (4.11)$$

where  $\nabla_{\mathbf{x}}\mathbf{u}$  is the gradient of the displacement vector field  $\mathbf{u}$ . The symbolic notation of Eq. 4.2 is  $\mathbf{t} = \boldsymbol{\sigma} \cdot \hat{\mathbf{e}}$ , where the inner product  $(\cdot)$  indicates the summation over the last index. Double notation over two indices, e.g. in Eq. 4.4, is denoted by  $(:)$ . The generalized Hooke's law (Eq. 4.4) then reads

$$\boldsymbol{\sigma} = \mathbf{C} : \boldsymbol{\epsilon} \quad (4.12)$$

or, employing symmetry relations (Eqs. 4.5–4.7),

$$\boldsymbol{\sigma} = \mathbf{C} : \nabla_{\mathbf{x}}\mathbf{u}. \quad (4.13)$$

#### 4.1.4 Elastodynamic wave equation

If a deformed crystal is at rest, i.e. in the case of a static equilibrium without body forces, the resulting conservation of momentum is expressed by  $\frac{\partial \sigma_{ij}}{\partial x_j} = 0$ . Acoustic vibrations and propagating elastic waves, however, imply that the evolving displacement gradient field becomes a function of time. Applying Newton's law, this leads to the fundamental *equation of motion* for a homogeneous anisotropic medium with material density  $\rho$  [284, Ch. 3.1.2; 282, Ch. 2.3.2]:

$$\begin{aligned} \rho \frac{\partial^2 u_i}{\partial t^2} &= \frac{\partial \sigma_{ij}}{\partial x_j}, \\ \rho \ddot{\mathbf{u}} &= \nabla_{\mathbf{x}} \cdot \boldsymbol{\sigma} = \text{div}_{\mathbf{x}} \boldsymbol{\sigma}. \end{aligned} \quad (4.14)$$

Note that in the absence of an externally applied torque, the stress tensor is symmetric and local rotations play no part in the equations of motion. Inserting the stress-strain relation given by the generalized Hooke's law (Eq. 4.4, see also Fig. 4.4), we obtain the *elastodynamic wave equation* that only depends on the spatiotemporal evolution of the displacement field  $\mathbf{u}(\mathbf{x}, t)$ :

$$\begin{aligned} \rho \frac{\partial^2 u_i}{\partial t^2} &= C_{ijkl} \frac{\partial^2 u_l}{\partial x_j \partial x_k}, \\ \rho \ddot{\mathbf{u}} &= \text{div}_{\mathbf{x}} \mathbf{C} : \nabla_{\mathbf{x}} \mathbf{u}. \end{aligned} \quad (4.15)$$

Since the stiffness tensor of isotropic media is fully defined by the two material-dependent Lamé constants  $\lambda$  and  $\mu$ , we obtain simplified forms of the constitutive equation (Eq. 4.4) and elastodynamic wave equation (Eq. 4.15):

$$\sigma_{ij} = \lambda \epsilon_{kk} + 2\mu \epsilon_{ij} \quad \text{and} \quad \rho \ddot{\mathbf{u}} = (\lambda + \mu) \nabla \text{div}_{\mathbf{x}} \mathbf{u} + \mu \Delta \mathbf{u}. \quad (4.16)$$

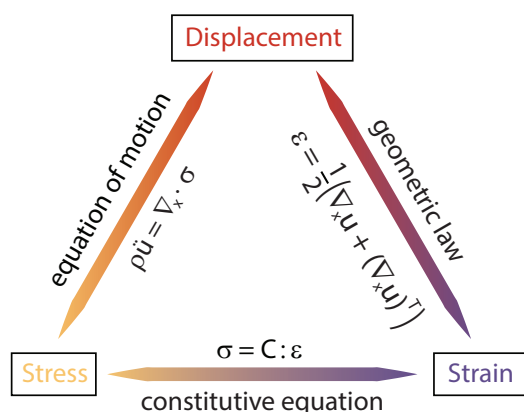


**Figure 4.4:** Relationships between stress, strain, and displacement. From the indicated pairwise related parameters, the wave equation can be derived.

Unlike exclusively transverse electromagnetic waves in vacuum and longitudinal waves in fluids, transverse and longitudinal waves can both propagate in elastic solids. As will be detailed in section 4.1.5, the corresponding wave velocities scale with the square-root of the stiffness components. To analyze the local structural distortion arising from vibrational motions (e.g. in optically excited heterostructures; see Chapter 7 and Refs. [72, 116]), it is insightful to retrieve the time-dependent evolution of the displacement gradient tensor  $\mathbf{F}(\Delta t) = \boldsymbol{\epsilon}(\Delta t) + \boldsymbol{\omega}(\Delta t) + \mathbf{1}$ .

#### 4.1.5 Bulk phonon dispersions

While the preceding sections featured an introduction into the basic concepts of strain and stress, motion and deformation, and into constitutive equations that make up elasticity theory, the microscopic structure of solids has been ignored. Due to interatomic distances of a few Å and sound velocities between  $10^3$  m/s and  $10^4$  m/s, we can anticipate that the continuum-mechanical picture only provides an accurate description of the lattice dynamics for a specific range of wavenumbers and wave frequencies. In order to derive the limiting values, we treat the elastic crystal as an assembly of atoms (mass  $m$ ) that are located at the nodes of a three-dimensional lattice (lattice constant  $a$ ) and connected by material-specific springs (spring constant  $K$ ). Once one atom is displaced, neighboring atoms are set in motion and the disturbance propagates through the solid. One general solution [291, Ch. 5.2.2] of the simplified one-dimensional equation of motion (derived from the combination of Hooke's law and Newton's law) describes the lattice dynamics as a propagating plane wave (wavenumber  $q$ ) with a dispersion relation given by

$$\omega = \sqrt{\frac{4K}{m}} \left| \sin \frac{qa}{2} \right|. \quad (4.17)$$

Due to the periodicity of the crystal, dispersion curves are usually shown for the first Brillouin zone only. At the zone borders, standing waves with group velocity  $v_{\text{gr}} = d\omega/dq = 0$  evolve. For small wavenumbers, such that  $qa \ll 1$ , the dispersion becomes the straight line

$$\omega \approx \sqrt{K/m} a q = v_{\text{ph}} q, \quad (4.18)$$

whose slope  $v_{\text{ph}}$  is the phase velocity. If the wavelength  $\lambda = 2\pi/q$  is comparable to the interatomic distance  $a$ , the medium is dispersive and the acoustic cut-off frequency  $f_c = \sqrt{K/(\pi^2 m)} = v_{\text{ph}}/(\pi a)$  is reached at the zone borders. For silicon with lattice constant  $a = 5.43 \text{ \AA}$  and longitudinal sound velocity  $v_L = 8432 \text{ m/s}$ , the cut-off frequency is  $f_c = 4943 \text{ GHz}$ . With increasing frequency, the wavelength becomes shorter: Traditional piezoelectric transducers operating in a broadband ultrasound regime (40 kHz–500 MHz, Ref. [285, App. A]), for example, launch acoustic phonons with wavelengths between a few centimeters and few tens of micrometers. By optically exciting thin crystalline membranes using short laser pulses, high-frequency acoustic phonons in the gigahertz-regime can be generated and observed, for example, through time-resolved diffraction patterns in UTEM. Here, the phonon wavelength approaches the sample thickness, but still remains larger than the crystal lattice constant. Thus, the solid appears continuous to the described lattice dynamics.

In addition to compression movements along the propagation direction of the wave, lattice atoms can also be displaced in perpendicular directions, which results in two transverse (shear) waves. Restoring forces will in general be different in all directions, so that three distinct dispersion curves are assigned to the individual polarizations [see blue curves in Figs. 4.5 d–f]. Independently from the atomic displacement relative to the wave propagation direction, all atoms oscillate in phase in the same way as for acoustic waves. The low-frequency branches of the dispersion relation are therefore called *acoustic*. In crystal lattices described by an  $N$ -atomic unit cell such as diamond silicon with  $N = 2$  (see crystal structure in Fig. 4.5 a), not only acoustic distortions of the entire basis occur, but atoms within the basis can oscillate out of phase. The resulting high-frequency dispersion branches are called *optical* in analogy to electromagnetic dipole oscillations. All types of atomic displacements relative to equilibrium positions and the propagation direction of the wave are shown in Fig. 4.5 c for a 1D crystal unit cell with two atoms. Characteristic features of the optical longitudinal and transverse modes (red curves in Figs. 4.5 d–f) include small group velocities over a broad range of wavenumbers  $q$  and a maximum phase difference of  $\pi$  between neighboring atoms in the small- $q$  region.

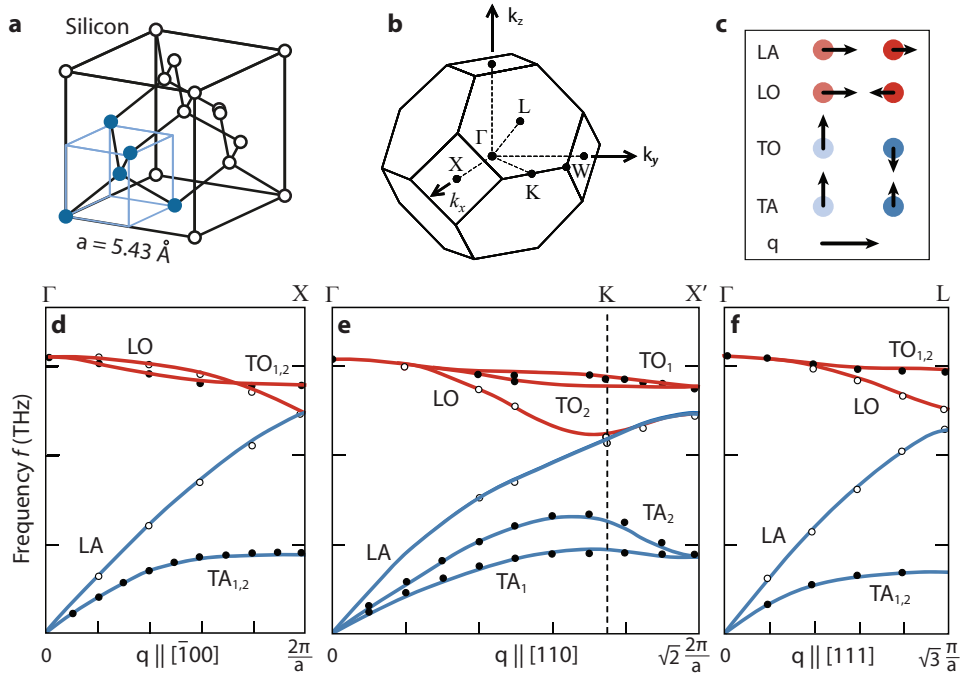


**Figure 4.5:** Phonon dispersion curves of bulk silicon. (a) Diamond structure of silicon with two-atomic unit cell. (b) Reciprocal space representation of the fcc Brillouin zone with characteristic points. Adapted from Ref. [292]. (c) Schematics of optical and acoustic longitudinal (LO, LA) and transverse (TO, TA) wave polarizations for a biatomic unit cell. (d–f) Silicon dispersion relations along different wave propagation directions obtained from calculations (lines) and experimentally (circles). While the three transverse optical/acoustic branches are split (e), they are degenerate for lattice vibrations in high-symmetry directions (d,f). Adapted from Ref. [293].

While the bulk dispersion relation generally has 3 acoustic phonon branches and  $3(N - 1)$  optical phonon branches (Fig. 4.5e), the transverse branches of each type can be degenerate along specific crystalline directions. This behavior is for example found along the  $\Gamma X$ -direction (corresponds to  $[\bar{1}00]$ , Fig. 4.5d) and along the  $\Gamma L$ -direction (corresponds to  $[111]$ , Fig. 4.5f). The location of the characteristic points  $\Gamma$ , X, L etc. in the first Brillouin zone is depicted in Fig. 4.5b. The degeneracy of transverse phonon branches can also be illustrated by so-called velocity surfaces, as explained in the following subsection.

#### 4.1.6 Velocity surfaces

A geometrical representation of a velocity surface is obtained from joining the tips of all polarization-specific phase-velocity vectors, drawn in spherical coordinates [294]. In isotropic media, the phase velocities of bulk waves are independent of the propagation direction, and the polarization vector is either parallel (longitudinal wave) or perpendicular

(transverse wave) to it. Hence, an isotropic crystal is fully described by two velocity spheres<sup>4</sup> of radii  $v_L$  and  $v_T$ , as illustrated in Fig. 4.6a for an arbitrary cross-sectional plane through the centre of the spheres. In anisotropic materials, however, the directional dependency of the generally three bulk phase velocities not only leads to non-spherical velocity surfaces, but also to the fact that atomic displacements are in most cases not exactly parallel or perpendicular to the propagation direction. Except for distortions along specific crystalline symmetry directions (pure mode directions according to Auld [281, Ch. 7I]), the different modes are designated with the prefix *quasi*.<sup>5</sup>

In order to explicitly calculate the phase velocity and polarization of bulk waves, we recall the elastodynamic equation of motion (Eq. 4.15) and seek a solution in form of a plane harmonic wave propagating along the direction  $\mathbf{n}$  in a crystal with stiffness  $C_{ijkl}$ . The resulting *Christoffel equation* [296, 297]

$$(C_{ijkl}n_jn_k - \rho v^2\delta_{il})u_l = 0 \quad (4.19)$$

with the Kronecker delta  $\delta_{il}$  shows that the polarization vector  $u_l$  is an eigenvector of the symmetric and positive-definite *Christoffel tensor*  $\Gamma_{il} = C_{ijkl}n_jn_k$ . Nontrivial solutions for the three phase velocities in a given direction are found from the secular determinant

$$|\Gamma_{il} - \rho v^2\delta_{il}| = 0, \quad (4.20)$$

in which  $\gamma = \rho v^2$  are the positive eigenvalues of the Christoffel tensor [284, Ch. 4.2.1]. The most straightforward solution of this eigenvalue problem is obtained for isotropic materials, for which the Christoffel tensor

$$\mathbf{\Gamma} = \begin{pmatrix} C_{44} & 0 & 0 \\ 0 & C_{44} & 0 \\ 0 & 0 & C_{11} \end{pmatrix} \quad (4.21)$$

yields the acoustic velocities  $v_L = \sqrt{C_{11}/\rho} = \sqrt{(\lambda + 2\mu)/\rho}$  and  $v_T = \sqrt{C_{44}/\rho} = \sqrt{\mu/\rho}$  of the bulk longitudinal and transverse waves. Since  $C_{11} > C_{44}$ , also  $v_L > v_T$  holds true for all isotropic solids.

As visualized in Fig. 4.6b, cross sections of the velocity surfaces of anisotropic materials

---

<sup>4</sup>Shear vertical and shear horizontal waves propagate in isotropic media with identical transverse velocity  $v_T$ , giving rise to only one common transverse velocity surface. The second velocity surface is

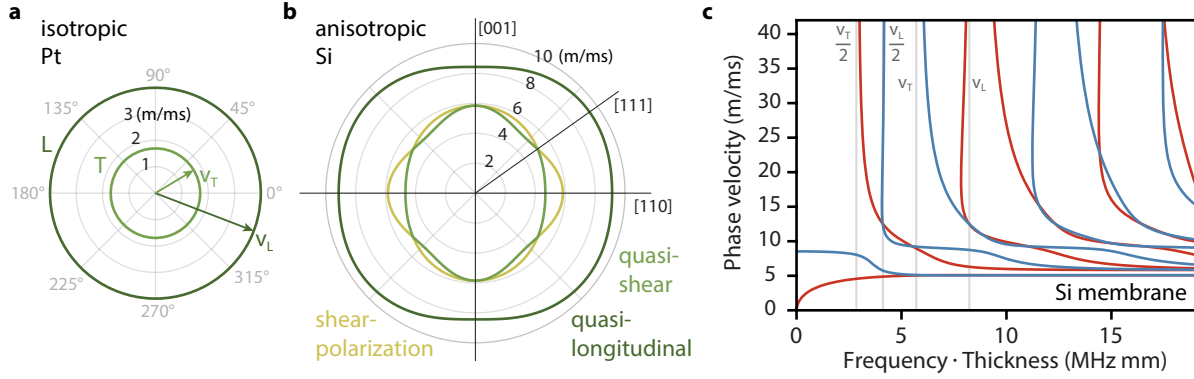


**Figure 4.6:** Sound velocities in bulk and confined media. (a) In isotropic platinum, bulk velocities  $v_L$  and  $v_T$  are independent of the wave propagation direction resulting in spherical velocity surfaces with radii  $v_L > v_T$ . (b) The velocity surface of silicon is given by three sound velocities, here shown for the  $(\bar{1}10)$ -plane, revealing the crystalline anisotropy. In  $[001]$ - and  $[111]$ -direction, the transverse phase velocities are degenerate. (c) Lamb phase-velocity curves for a 35-nm thin silicon membrane with  $k \parallel [110]$ , decoupled into symmetric (blue) and antisymmetric (red) modes. The asymptotic behavior of the phase velocities is related to cut-off frequencies given by multiples of the sound velocities, here  $v_L = 8432 \text{ m/s}$  and  $v_T = 5843 \text{ m/s}$ . All curves are traced using the free software suite *Dispersion Curve (DC)* [298].

are more complex.<sup>6</sup> The three curves shown for wave propagations in a diagonal plane of silicon are expressed in terms of the stiffness-tensor components  $C_{11}$ ,  $C_{12}$ , and  $C_{44}$  and are all non-circular. For the  $[001]$ - and  $[111]$ -directions, the two transverse phase velocities are equal, which corresponds to the degeneration of the dispersion curves of bulk silicon (see Figs. 4.5 d,f).

## 4.2 Guided acoustic waves in confined nanostructures

Spatial confinement of acoustic phonons in semi-infinite and (multilayered) plates<sup>7</sup> introduces restrictions on phonon polarizations, acoustic wave localizations, and superpositions of generated waves. The resulting guided waves have already been analytically studied in the late 19th and early 20th century and are named after the scientists who first discovered them, i.e. Rayleigh, Love, Lamb, and Stonely [39–41, 299]. Curiously, an infinite number of guided Lamb modes with distinct polarizations and (anti)symmetric displacement fields

associated with longitudinal waves.

<sup>5</sup>For details on the difference between pure modes and *quasi* modes, see also Refs. [295, Ch. 16; 284, Ch. 4.2.1].

<sup>6</sup>The reader is referred to Ref. [284, Ch. 4.2.5] for explicit expressions of the phase velocities as a function of the polar angle  $\theta$ .

<sup>7</sup>A plate can be any solid which is much thinner compared to the other two dimensions.

with respect to the center-plane is supported in elastic plates. Exploiting the latter fact, an elastic version of the quantum spin Hall effect [300, 301] in form of helical edge modes is experimentally achieved [302] supporting theoretical predictions [303].

### 4.2.1 Lamb waves in isotropic media

In order to arrive at an intuitive description of guided Lamb modes, we consider an acoustic wave propagating in an isotropic solid, which is characterized by two sound velocities that are independent of the propagation direction (Fig. 4.6a). As the wave impinges on the material-vacuum interface, boundary conditions of traction-free surfaces apply. For a transverse horizontal (TH) wave polarized parallelly to the free surface, this condition is inherently fulfilled and the wave will be totally reflected. Longitudinal (L) and transverse vertical (TV) waves, however, are coupled at the boundary: an incident L (TV) wave results in a reflected L (TV) wave and a converted TV (L) wave (see geometry in Fig. 4.7a). Similar to electromagnetic waves, the propagation directions of the partial waves are given by the acoustic Snell's law, and reflection coefficients as well as conversion coefficients can be deduced in analogy to Fresnel equations [284, Ch. 4.4; 281, Ch. 9B]. For the pure shear wave, the quasi-shear and the quasi-longitudinal wave in anisotropic media (see velocity surfaces in Fig. 4.6b), an analytical statement of Snell's law is difficult to derive, but it is possible to obtain scattering angles graphically from slowness surfaces (i.e. the inverse of the velocity surfaces) [284, Ch. 4.4; 281, Ch. 9C].

In plate-shaped waveguides with a uniform cross section and two plane-parallel surfaces, acoustic plane waves propagate along the waveguide axis  $\mathbf{n}$  by reflection from both surfaces (Fig. 4.7b), with the same propagation wavenumber  $k$  for all partial waves. In the direction  $\boldsymbol{\nu}$  perpendicular to the waveguide axis, the wave pattern is a function of resonant standing waves. These mode solutions are called *Lamb waves*.

The most general method for solving isotropic waveguide problems makes use of the Helmholtz decomposition [304], in which the displacement field is expressed by a divergence-free scalar related to dilations and a curl-free vector potential related to shear strains. In the case of Lamb waves, both surfaces of a plate with thickness  $2h$  are in contact with vacuum and traction-free. The out-of-plane wavevector components  $k_{\nu}^L$  and  $k_{\nu}^T$  for longitudinal and transverse acoustic waves are related to the common in-plane

wavevector  $k$ , the acoustic sound velocities  $v_L$  and  $v_T$ , and the angular frequency  $\omega$  by

$$(k_\nu^L)^2 = \frac{\omega^2}{v_L^2} - k^2 \quad \text{and} \quad (k_\nu^T)^2 = \frac{\omega^2}{v_T^2} - k^2. \quad (4.22)$$

With these definitions, one quickly arrives at the characteristic dispersion relation, called *Rayleigh-Lamb equation*:

$$\frac{\tan(hk_\nu^L + \alpha)}{\tan(hk_\nu^T + \alpha)} = \frac{k_\nu^T}{k_\nu^L} \left( 1 - \frac{\omega^4}{4k^2 (k_\nu^T)^2 v_T^4} \right). \quad (4.23)$$

The parameter  $\alpha$  classifies Lamb modes as symmetric ( $\alpha = 0$ ) or antisymmetric ( $\alpha = \pi/2$ ) in terms of the evolving displacement field with respect to the mid-plane of the plate. The corresponding dispersion curves – typically plotted using dimensionless parameters as shown in Fig. 4.7d – are designated  $S_n$  and  $A_n$  ( $n \in \mathbb{N}_0$ ). The dispersion equations for the Lamb wave modes are simple in appearance, but can only be solved by numerical algorithms. For more information on several dispersion-curve tracing routines, the reader is referred to Refs. [285, 305, 306].

The following paragraphs briefly discuss some essential features of the dispersion curves and their associated displacement fields, which are covered in more detail in most comprehensive books on elasticity theory. In opposite to the finite number of modes in bulk materials, an infinite number of guided Lamb modes exists in elastic plates. Two cases can be distinguished, depending on whether the frequency-thickness product approaches either zero or a cut-off value as  $kh/\pi \rightarrow 0$  (Fig. 4.7d). The two lowest-order modes, i.e. the symmetric mode  $S_0$  and the antisymmetric mode  $A_0$ , cover the full frequency range. Near the origin, the longitudinal  $S_0$ -mode behaves linearly, while the flexural  $A_0$ -mode becomes parabolic:  $\omega(k) = \frac{v_P}{\sqrt{3}} k^2 h$  [284, Ch. 5.5.2]. Here,  $v_P = v_L \sqrt{1 - C_{12}^2/C_{11}^2}$  is the plate velocity, that is approached by both zero-order modes for large in-plane wavenumbers. In contrast, higher order modes ( $n \in \mathbb{N}$ ) are counted in their sequence of increasing cut-off frequencies that scale with the sound velocities:

$$\begin{aligned} f_{c,S_{2n}} \cdot 2h = n v_T \quad \text{and} \quad f_{c,A_{2n}} \cdot 2h = n v_L \\ f_{c,S_{2n+1}} \cdot 2h = \left(n + \frac{1}{2}\right) v_L \quad \text{and} \quad f_{c,A_{2n+1}} \cdot 2h = \left(n + \frac{1}{2}\right) v_T. \end{aligned} \quad (4.24)$$

This characteristic frequency spectrum for small wavenumbers is similarly found for the phase velocities, as shown in Fig. 4.6c for anisotropic silicon. Hence, only for the

zero-order antisymmetric mode, vanishing phase velocities are observed as a result of the parabolic dispersion in the low- $k$  regime. Cut-off frequencies of Lamb modes with  $n \neq 0$  become vertical asymptotes.<sup>8</sup> With increasing sample thickness  $2h$ , the Lamb dispersion curves shift down to lower frequencies.

Remarkably, there are no intersections of Lamb modes of the same type ( $S_n$  with  $S_m$ , or  $A_n$  with  $A_m$ ,  $n \neq m$ ) in the entire  $k$ -range [307]. Near “intersections” (e.g., between the  $S_4$  and the  $S_6$  branch at around  $2fh = 5.5$  MHz·mm), avoided crossings are observed in analogy to level repulsions predicted by Wigner and von Neuman in 1929 for quantum-mechanical systems [308].

A physical picture of the displacement field associated with the two types of Lamb modes is best obtained by focusing on the small- $k$  region. As seen from Fig. 4.6c, the mode order indicates the number of zero-crossings in the displacement component perpendicular to the propagation direction (see black lines in Fig. 4.6c). In both sequences, pure shear and pure longitudinal types of standing waves alternate.

#### 4.2.2 Anisotropic Lamb wave description

The potential theory method used to derive the Rayleigh-Lamb equation (Eq. 4.23) is limited in that it cannot be applied to anisotropic problems. The partial wave technique, however, is suitable for any planar waveguide problem. The main idea is closely related to the introductory part of the previous subsection, as it arrives at the Lamb wave solutions using a linear homogeneous system of six superimposed partial waves. For the analysis of guided modes in multilayered composites, the partial wave approach is combined with the Thomson-Haskell transfer matrix method [309, 310], the global matrix method [311], or the stiffness matrix method [312, 313].

Although anisotropy and confinement introduce a high degree of complexity to nanophononic wave problems, an elegant mathematical formulation of the elastic wave equation can be derived to retrieve analytical solutions for the low-frequency limits of Lamb waves in homogeneous, stratified, and functionally graded anisotropic plates. Following Refs. [314–317], we analyze plane waves propagating in the  $n\nu$ -plane, i.e. displacement fields do not depend on the argument  $\mathbf{x} \cdot \boldsymbol{\omega} = \mathbf{x} \cdot (\mathbf{n} \times \boldsymbol{\nu})$ . Solutions to this acoustic wave

---

<sup>8</sup>For  $k \rightarrow 0$ , the limit values for the frequencies result equally for isotropic and anisotropic media according to Eq. 4.24.

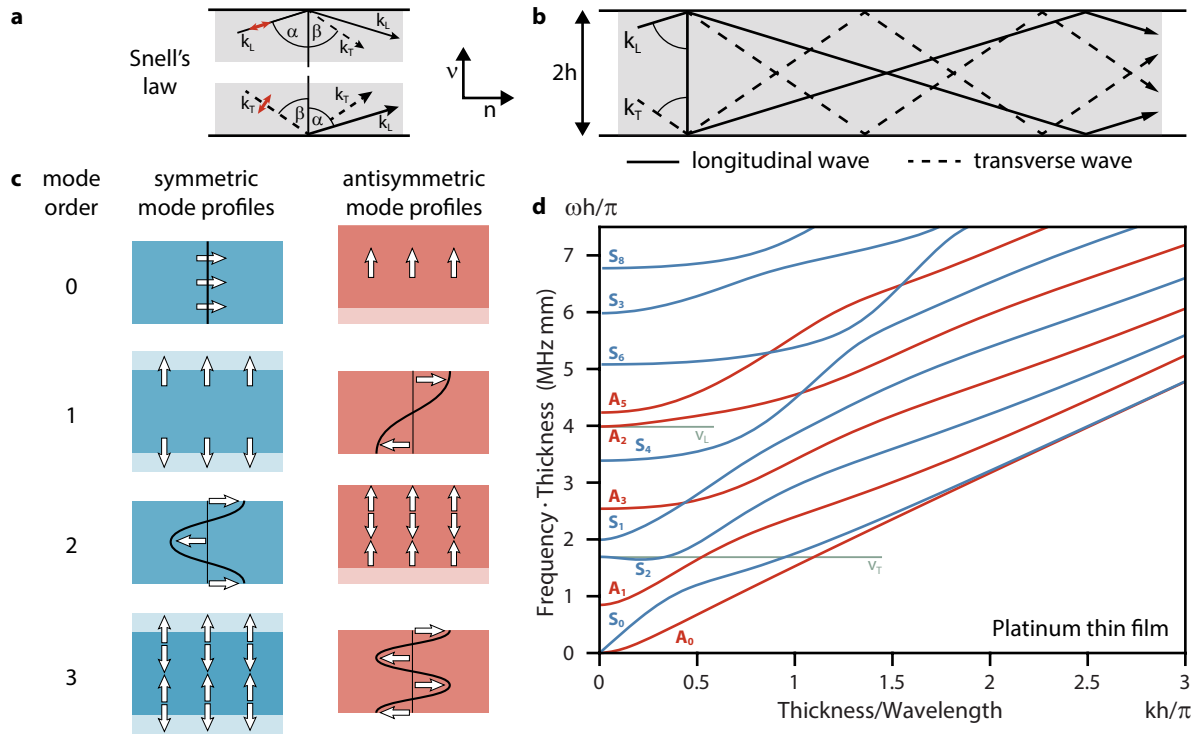


**Figure 4.7:** Lamb waves in acoustic waveguides. (a) Schematic drawing of acoustic wave reflection at oblique incidence and partial mode conversion between longitudinal and transverse waves at traction-free surfaces of an isotropic medium. (b) Due to the coupling of longitudinal and transverse waves in a plate-like waveguide, Lamb waves can evolve. (c) Displacement maps for the first four symmetric (blue) and antisymmetric (red) Lamb modes in the small- $k$  regime. As indicated by the arrows, shear and longitudinal types of transverse standing waves alternate in both sequences. (d) Symmetric  $S_n$  and antisymmetric  $A_n$  dispersion curves for isotropic platinum (10 nm) with sound velocities  $v_L = 3988$  m/s and  $v_T = 1693$  m/s. The curves are traced using the free software suite *Dispersion Curve* (DC) [298].

problem take the form [315]

$$\mathbf{u}(\mathbf{x}, t) = \mathbf{m}(\underbrace{ik \mathbf{x} \cdot \boldsymbol{\nu}}_{x'}) \exp[ik(\mathbf{x} \cdot \mathbf{n} - ct)], \quad (4.25)$$

where the exponential describes the propagation of the plane wave in the direction of unit vector  $\mathbf{n}$  with phase velocity  $c$  and wavenumber  $k = 2\pi/\lambda$ . Since sound velocities and deformation profiles strongly depend on the propagation direction in anisotropic materials, we choose the complex vector function  $\mathbf{m}$  to take an arbitrary wave polarization in transverse direction  $\mathbf{x} \cdot \boldsymbol{\nu}$  into account. Substituting this plane wave ansatz into the acoustic wave equation (Eq. 4.15), we obtain the displacement gradient

$$\begin{aligned} \nabla_{\mathbf{x}} \mathbf{u} &= ik \boldsymbol{\nu} \cdot \partial_{x'} \mathbf{m}(x') \exp[ik(\mathbf{x} \cdot \mathbf{n} - ct)] + ik \mathbf{n} \cdot \mathbf{m}(x') \exp[ik(\mathbf{x} \cdot \mathbf{n} - ct)] \\ &= ik(\boldsymbol{\nu} \partial_{x'} + \mathbf{n}) \cdot \mathbf{m}(x') \exp[ik(\mathbf{x} \cdot \mathbf{n} - ct)]. \end{aligned} \quad (4.26)$$

For the full spatial expression in Eq. 4.15, we get

$$\operatorname{div}_{\mathbf{x}} \mathbf{C} : \nabla_{\mathbf{x}} \mathbf{u} = ik(\boldsymbol{\nu} \partial_{x'} + \mathbf{n}) \cdot \mathbf{C} : ik(\boldsymbol{\nu} \partial_{x'} + \mathbf{n}) \cdot \mathbf{m}(x') \exp[ik(\mathbf{x} \cdot \mathbf{n} - ct)]. \quad (4.27)$$

Using the temporal derivative  $\rho \ddot{\mathbf{u}} = \rho c^2 \mathbf{u}$ , the wave equation in simplified and reorganized form reads

$$[(\boldsymbol{\nu} \cdot \mathbf{C} \cdot \boldsymbol{\nu}) \partial_{x'}^2 + (\boldsymbol{\nu} \cdot \mathbf{C} \cdot \mathbf{n} + \mathbf{n} \cdot \mathbf{C} \cdot \boldsymbol{\nu}) \partial_{x'} + (\mathbf{n} \cdot \mathbf{C} \cdot \mathbf{n}) - \rho c^2 \mathbf{1}] \cdot \mathbf{m}(x') = \mathbf{0} \quad (4.28)$$

or, in a more compact notation,

$$\left[ \mathbf{A}_1 \partial_{x'}^2 + (\mathbf{A}_2 + \mathbf{A}_2^T) \partial_{x'} + \mathbf{A}_3 \right] \cdot \mathbf{m}(x') = \mathbf{0}, \quad (4.29)$$

with  $3 \times 3$  matrices

$$\mathbf{A}_1 = \boldsymbol{\nu} \cdot \mathbf{C} \cdot \boldsymbol{\nu}; \quad \mathbf{A}_2 = \boldsymbol{\nu} \cdot \mathbf{C} \cdot \mathbf{n}; \quad \mathbf{A}_3 = \mathbf{n} \cdot \mathbf{C} \cdot \mathbf{n} - \rho c^2 \mathbf{1}. \quad (4.30)$$

Matrices  $\mathbf{A}_1$  and  $\mathbf{A}_3$  are symmetric and positive-definite guaranteeing the existence of their inverses. In analogy to the wave equation in bulk anisotropic solids described by the Christoffel tensor  $\Gamma_{il}$  (Eq. 4.19), Eq. 4.29 is called Christoffel equation. Note that the elasticity tensor  $\mathbf{C}$  and hence, the  $\mathbf{A}$  matrices strongly depend on the chosen coordinate system relative to crystallographic orientations. Choosing explicit unit vectors

$\mathbf{n} = (100)$  and  $\boldsymbol{\nu} = (010)$ , and recalling the subscript notation, the components  $(jk)$  of the  $\mathbf{A}$ -matrices in Eq. 4.30 become

$$\begin{aligned} A_1^{jk} &= \sum_{i,l} \nu_i C_{ijkl} \nu_l = C_{2jk2} \\ A_2^{jk} &= \sum_{i,l} \nu_i C_{ijkl} n_l = C_{1jk2} \\ A_3^{jk} + \rho c^2 \delta_{jk} &= \sum_{i,l} n_i C_{ijkl} n_l = C_{1jk1}. \end{aligned} \quad (4.31)$$

For the class of cubic materials with stiffness tensor components (Voigt notation)  $C_{11} = C_{22} = C_{33}$ ,  $C_{12} = C_{13} = C_{23}$ , and  $C_{44} = C_{55} = C_{66}$  [284, Ch. 3.2.3], the matrices read

$$\mathbf{A}_1 = \begin{pmatrix} C_{44} & 0 & 0 \\ 0 & C_{11} & 0 \\ 0 & 0 & C_{44} \end{pmatrix} \quad \mathbf{A}_2 = \begin{pmatrix} 0 & C_{12} & 0 \\ C_{44} & 0 & 0 \\ 0 & 0 & 0 \end{pmatrix} \quad \mathbf{A}_3 + \rho c^2 \mathbf{1} = \begin{pmatrix} C_{11} & 0 & 0 \\ 0 & C_{44} & 0 \\ 0 & 0 & C_{44} \end{pmatrix}. \quad (4.32)$$

As surfaces and interfaces in confined crystal structures impose boundary conditions on mechanical variables, the differential equation 4.29 turns into a Cauchy problem [318, 319]. The auxiliary vector function  $\mathbf{w}(x') = \partial'_x \mathbf{m}(x')$  transforms the second-order Christoffel equation into the following matrix equation of first order (Cauchy normal form) [314, 315, 317]:

$$\partial'_x \mathbf{Y}(x') = \mathbf{G} \cdot \mathbf{Y}(x'), \quad (4.33)$$

with the six-dimensional vector function

$$\mathbf{Y}(x') = \begin{pmatrix} \mathbf{m}(x') \\ \mathbf{w}(x') \end{pmatrix} \quad (4.34)$$

and  $6 \times 6$  matrix

$$\mathbf{G} = \begin{pmatrix} \mathbf{0} & \mathbf{1} \\ -\mathbf{A}_1^{-1} \cdot \mathbf{A}_3 & -\mathbf{A}_1^{-1} \cdot (\mathbf{A}_2 + \mathbf{A}_2^T) \end{pmatrix}. \quad (4.35)$$

Identifying matrix  $\mathbf{G}$  as a Jacobian, the general solution of Eq. 4.33 is

$$\mathbf{Y}(x') = \exp(\mathbf{G}x') \cdot \mathbf{Y}_0, \quad (4.36)$$

where  $\mathbf{Y}_0$  is a six-dimensional complex vector defined by boundary conditions. Specifically, to solve the acoustic wave problem for a thin plate with thickness  $2h$ , the traction-free

boundary condition (Neumann boundary condition) needs to be employed in the direction of the plate surface normal  $\boldsymbol{\nu}$ :

$$\mathbf{t}_\nu(\mathbf{x}, t) \equiv \boldsymbol{\nu} \cdot \mathbf{C} : \nabla_{\mathbf{x}} \mathbf{u}(\mathbf{x}, t)|_{\mathbf{x}=\pm h} = 0. \quad (4.37)$$

In terms of matrices, the boundary conditions are represented by

$$\left( \mathbf{A}_1 \frac{\partial}{\partial x'} + \mathbf{A}_2 \right) \cdot \mathbf{m}(x')|_{x'=\pm ikh} = 0. \quad (4.38)$$

At this point, we can draw on solution approaches developed by Ehselby *et al.* [320] and Stroh [321] for acoustic wave propagation problems in elastic materials with arbitrary anisotropy [283, 322, 323]. Within the so-called sextic formalism, Eq. 4.36 and Eq. 4.38 can be combined to incorporate Eq. 4.29 into a system of six linear differential equations in terms of polarizations and surface tractions. Specifically, we obtain the linear relationship

$$\begin{pmatrix} \mathbf{m}(\pm ikh) \\ \mathbf{t}_\nu(\pm ikh) \end{pmatrix} = \mathbf{Z} \cdot \exp(\pm ikh\mathbf{G}) \cdot \mathbf{B}, \quad (4.39)$$

where  $\mathbf{B}$  is a six-dimensional complex vector and  $\mathbf{Z} = \begin{pmatrix} \mathbf{1} & \mathbf{0} \\ \mathbf{A}_2 & \mathbf{A}_1 \end{pmatrix}$  is called impedance matrix. Furthermore, it can be shown that polarizations and tractions on both plate surfaces are coupled by a transfer matrix  $\mathbf{T} = \mathbf{Z} \cdot \exp(-2ikh\mathbf{G}) \cdot \mathbf{Z}^{-1}$  [314]. This coupling is expressed by a degenerate mapping  $\mathbf{R}$  finally yielding the Lamb dispersion equation for any anisotropic homogeneous plate with traction free boundaries. Nontrivial solutions for the phase velocity are found evaluating the characteristic equation [314, 315]

$$\det[\mathbf{R}] = \det \left[ (\mathbf{0}; \mathbf{1}) \cdot \mathbf{Z} \cdot \exp(-2ikh\mathbf{G}) \cdot \mathbf{Z}^{-1} \cdot (\mathbf{0}; \mathbf{1})^T \right] = 0. \quad (4.40)$$

In the limit of  $k \rightarrow 0$ , the phase velocity for the lowest order quasi-symmetric Lamb mode is obtained from the secular equation [315]

$$\det \left[ (\mathbf{0}; \mathbf{1}) \cdot \mathbf{Z} \cdot \mathbf{G} \cdot \mathbf{Z}^{-1} \cdot (\mathbf{0}; \mathbf{1})^T \right] = 0. \quad (4.41)$$

Validation of the presented general equations for a homogeneous plate with free surfaces can easily be shown for the simplest case of isotropic materials [315].

In Ref. [116] (reprinted in Chapter 7), the presented formalism was employed for  $k \rightarrow 0$

to calculate the asymptotic phase velocity of the  $S_0$  Lamb wave propagating along the crystallographic [110]-direction of anisotropic silicon.

In the case of multilayer plates with  $N$  layers, interface boundary conditions, i.e. continuity of surface tractions

$$\mathbf{m}^{(k)}(x')|_{x'=-ikh_k} = \mathbf{m}^{(k+1)}(x')|_{x'=+ikh_{k+1}} \quad k = 1, \dots, N - 1 \quad (4.42)$$

and displacements across corresponding interfaces

$$\left( \mathbf{A}_1^{(k)} \frac{\partial}{\partial x'} + \mathbf{A}_2^{(k)} \right) \cdot \mathbf{m}^{(k)}(x')|_{x'=-ikh_k} = \left( \mathbf{A}_1^{(k+1)} \frac{\partial}{\partial x'} + \mathbf{A}_2^{(k+1)} \right) \cdot \mathbf{m}^{(k+1)}(x')|_{x'=+ikh_{k+1}}, \quad (4.43)$$

extend the transfer matrix  $\mathbf{T}$  into a multiplication of the individual layer transfer matrices [315]. Numerical modelling of acoustic modes in complex stratified plates containing multiple layers with alternating contrast physical properties [315, 316] and functionally graded plates [324] is performed by a combination of the presented sextic Cauchy formalism and the Thomson-Haskell transfer matrix method. In comparison to results obtained for a single homogeneous plate, considerable differences in the dispersion relation of layered composites are theoretically predicted across a broad frequency range.

### 4.2.3 Transverse magnetic modes in a planar dielectric waveguide

Similar to nanophononic waveguides, guided-wave optic components serve as key building blocks of today's communication systems, medical equipment, as well as scientific and engineering instrumentation. Bearing in mind the previously discussed elasticity principles and properties of acoustic waveguides, the following section aims at gaining a broader perspective on waveguide concepts by covering an optical equivalent in form of a planar dielectric waveguide. Although differences between phononic and photonic systems are to be expected in the governing wave equations, required boundary conditions, and resulting dispersion relations, notable resemblances reflect the universality of the idea to confine propagating waves to a structure that supports an infinite number of guided modes.

In the simplest geometric form, an optical planar waveguide consists of three homogeneous dielectrics (refractive indices  $n_{1,2,3}$ ) of which the infinitely-extended core layer (large  $n_2$ ) with a thickness  $2a$  comparable to the operating wavelength  $\lambda_0$  is covered by a semi-infinite cladding (small  $n_1, n_3$ ) at both surfaces [325]. While dielectric waveguides

may contain anisotropic materials, most often isotropic, nonmagnetic materials are combined. In addition to this natural choice, we establish the analogy to Lamb waveguides on the basis of loss-less materials and a symmetric step-index profile ( $n_1 = n_3$ ) characterized by an abrupt change of the refractive index at the film-cladding interfaces.<sup>9</sup>

Similar to the subdivision of transverse acoustic waves in isotropic media into shear-horizontal (SH) and shear-vertical (SV) waves, this optical planar waveguide can also support two independent types of transverse waves. These are plane waves with electric field components either *normal* to or *in* the plane of incidence defined by the surface normal and the incident wave vector [326, Ch. 1]. The corresponding polarizations are referred to as *perpendicular/transverse electric* (TE) or *parallel/transverse magnetic* (TM), respectively.<sup>10</sup> In line with the discussion of the displacement-field component perpendicular to the propagation direction in the planar Lamb waveguide, we only consider the optical case of parallelly polarized TM waves, for which the incident, reflected, and transmitted electric fields  $\mathbf{E}$  have components in and normal to the propagation direction. The accompanying magnetic fields  $\mathbf{H}$  are normal to the plane of incidence and the propagation direction. Different from acoustics, the electromagnetic field is localized in the core layer of the waveguide by total internal reflections [327, Ch. 1.1], and not by mode conversions at interfaces and a superposition of differently polarized waves.

To find the electromagnetic modes guided by the thin-film waveguide, we have to solve Maxwell's equations with boundary conditions for individual field components. For TM modes propagating along the  $z$ -direction of the waveguide with the upper surface-normal along  $x$  and refractive indices independent of the cartesian coordinates, the region-specific wave equation expressed in terms of  $H_y$  read [327, Ch. 2.1]:

$$\frac{d^2 H_y(x)}{dx^2} + (k_0^2 n^2 - k^2) H_y(x) = 0 \quad (4.44)$$

$$E_y = H_x = H_z = 0.$$

Here,  $k_0 = 2\pi/\lambda_0$  is the wavenumber in vacuum and  $k$  is the propagation wavevector in the waveguide. Assuming that the guided electromagnetic fields are confined in the thin film (f) and exponentially decay in the cladding (c) ( $n_f > n_c$ , phase velocities:

---

<sup>9</sup>In contrast, most practical planar waveguides have a linear or exponential graded-index profile that is continuous along the surface normals [326, Ch. 3].

<sup>10</sup>As soon as the planar waveguide has a finite dimension in the direction perpendicular to the surface normals and the propagation direction, i.e. for a 3D rectangular waveguide, TE and TM modes are coupled [326, Ch. 5.2].

$v_{f,c} = c_0/n_{f,c}$ ), the magnetic field distribution is [327, Ch. 2.1.2] expressed as

$$H_y(x) = \begin{cases} A \cos(\kappa a - \phi) e^{-\xi(x-a)} & x > a \\ A \cos(\kappa x - \phi) & -a \leq x \leq a \\ A \cos(\kappa a + \phi) e^{-\xi(x+a)} & x < -a \end{cases} . \quad (4.45)$$

Similar to the normal wavevector components  $k_\nu^L$  and  $k_\nu^T$  for longitudinal and transverse acoustic waves (cf. Eq. 4.22), the optical wavevector components  $\kappa$  and  $\xi$  along the  $x$ -axis in the film and cladding regions are defined by

$$\kappa^2 = \frac{\omega^2}{v_f^2} - k^2 > 0 \quad \text{and} \quad \xi^2 = k^2 - \frac{\omega^2}{v_c^2} > 0 . \quad (4.46)$$

From the boundary conditions that the tangential components  $H_y$  and  $E_z$  are continuous across the planar interfaces ( $x = \pm a$ ) between the different dielectrics, the following dispersion equation for waves with frequency  $\omega$  and propagation wavevector  $k$  is obtained:

$$a\kappa = \frac{m\pi}{2} + \arctan\left(\frac{n_d^2 \xi}{n_c^2 \kappa}\right) . \quad (4.47)$$

The TM mode number  $m$  is the equivalent to the parameter  $\alpha$  that characterized symmetric and antisymmetric Lamb modes (cf. Eq. 4.23) in the previous section 4.2.1. Separating even and odd modes, we can rewrite the optical dispersion relation in the form [325–327]

$$\tan(a\kappa) = \begin{cases} + \left(\frac{n_d^2 \xi}{n_c^2 \kappa}\right) & (m \text{ even}) \\ - \frac{1}{\left(\frac{n_d^2 \xi}{n_c^2 \kappa}\right)} & (m \text{ odd}) , \end{cases} \quad (4.48)$$

which closely resembles the Rayleigh-Lamb equation (cf. Eq. 4.23) in its alternative version

$$\frac{\tan(hk_\nu^T)}{\tan(hk_\nu^L)} = \begin{cases} -\frac{4k^2 k_\nu^T k_\nu^L}{((k_\nu^T)^2 - k^2)^2} & (\text{symmetric}) \\ -\frac{((k_\nu^T)^2 - k^2)^2}{4k^2 k_\nu^T k_\nu^L} & (\text{antisymmetric}) . \end{cases} \quad (4.49)$$

Disregarding the change of sign in Eq. 4.48 compared to Eq. 4.49, these representations of the respective dispersion relations clearly reveal the common inverse relation between

the two types of modes in each waveguide. The even and odd mode numbers similarly correspond to symmetric and antisymmetric field profiles with respect to the mid-plane of the optic waveguide.

Another interesting commonality between these specific acoustic and optical waveguides is obtained from an explicit expression of the optical dispersion relation in terms of the angular frequency  $\omega$ . Such a formulation was previously given for the Rayleigh-Lamb equation (Eq. 4.23), which is repeated here for reasons of convenience:

$$\frac{\tan(hk_\nu^L + \alpha)}{\tan(hk_\nu^T + \alpha)} = \frac{k_\nu^T}{k_\nu^L} \left( 1 - \frac{\omega^4}{4k^2 (k_\nu^T)^2 v_T^4} \right). \quad (4.50)$$

Inserting the phase velocities and the full expressions for  $\kappa$  and  $\xi$  (Eq. 4.46) into the even branches of Eq. 4.48, we obtain

$$\tan(a\kappa) = \frac{v_c^2 k^2}{v_d^2 \xi \kappa} \left( 1 + \frac{\omega^2}{\kappa v_c^2} - \frac{\omega^4}{k^2 \kappa^2 v_c^2 v_d^2} \right) \quad (4.51)$$

for the optical waveguide.

As the transcendental equation can only be evaluated numerically, it is customary to use generalized parameters introduced by Kogelnik and Ramaswamy [328]. For the symmetric step-index waveguide two generalized parameters are sufficient [326, Ch. 2.2.2], which are

- (i) the generalized frequency or generalized film thickness  $V = 2k_0 a \sqrt{n_f^2 - n_c^2}$ , that includes all required parameters to fully characterize the vacuum wavelength and the symmetric planar waveguide, and
- (ii) the generalized guide index  $b = \frac{N^2 - n_c^2}{n_f^2 - n_c^2}$ , with the effective index  $N = k/k_0$ , spans from 0 to 1. Since  $n_c < N < n_f$ , the dispersion relations are limited to the region between the two light lines  $\omega = c_0/n_f k$  and  $\omega = c_0/n_c k$ .

In terms of these generalized parameters [326, Ch. 2.3.1], the dispersion relation for  $\text{TM}_m$  modes is

$$\frac{V}{2} \sqrt{1-b} = \frac{m\pi}{2} + \arctan \left( \frac{n_f^2}{n_c^2} \sqrt{\frac{b}{1-b}} \right). \quad (4.52)$$

As  $b$  (the propagation wavevector  $k$ ) becomes zero, all  $\text{TM}_m$  modes except for the  $\text{TM}_0$  mode approach nonzero cut-off frequencies at  $V_m = 2k_0 a \sqrt{n_f^2 - n_c^2} = m\pi$ . By the easily

achievable reformulation of this equation into

$$f \cdot 2a = m \frac{c_0}{2 \sqrt{n_f^2 - n_c^2}}, \quad (4.53)$$

a straightforward comparison of the optical cut-off frequencies with the Lamb cut-off frequencies (Eq. 4.24) can be drawn: For small  $k$ , both waveguides are characterized by cut-off frequencies  $f = \omega/(2\pi)$  that are counted in the mode index and linearly scale with bulk phase velocities.



### **Diffraction theory and diffractive probing of ultrafast structural dynamics**

---

While high-resolution imaging allows for the direct observation of the morphology of solid systems in real space, diffraction methods yield complementary structural information in reciprocal space. A comprehensive understanding of the investigated material can thus be gained from two different perspectives. Over the past decades, electron- and x-ray diffraction have become well-established techniques that are widely applied to thin films and thick crystals for composition, strain, and symmetry characterizations. Aside from a simple diffraction mode employing electron beam illumination, multiple different probing geometries using a range of probing energies, angles of incidence, and convergence angles are nowadays well-established and are being further developed these days. By harnessing the large range of diffraction methodologies, surface-sensitive measurements or the local probing of inhomogeneities have become accessible. Experimental access to temporal properties has been achieved by transferring these approaches to the ultrafast domain in pump-probe measurement schemes. By tracking the time-dependent evolution of the three main observables in an ultrafast diffraction experiment, i.e., diffraction intensity, scattering angle, and Bragg spot or line profiles, sensitivity to structural dynamics induced by pulsed excitation is gained. The straightforward connection between the scattering characteristics and the (transient) structure of the crystalline solid is described within the framework of scattering theory that is presented in this chapter.

After a brief overview of diffraction modes available in TEM with a particular focus on convergent beam electron diffraction (CBED), an introduction of the basic principles of scattering theory is provided. Furthermore, intensity variations arising from incoherent phonon dynamics are discussed. Although single elastic scattering covered by kinematical

scattering theory commonly suffices to understand fundamental structural signatures, only multiple scattering correctly predicts scattering intensities acquired for thick crystals and scattering profiles governed by inhomogeneous strain distributions along the probing beam path. The description of such (imperfect) crystals is therefore covered by dynamical scattering theory. The chapter closes with a few benchmarking results of recent ultrafast diffraction experiments.

## 5.1 Diffraction modes in TEM

Before discussing the mathematical description of diffraction, it is worth to briefly introduce a few diffraction modes typically used in TEM [329, Ch. 10.4]. Among those, selected area electron diffraction and convergent beam electron diffraction have been employed in ultrafast diffraction experiments presented in Chapter 7.

**Selected area electron diffraction (SAED)** Selected area electron diffraction is a very common technique used in TEM and is applied for the study of both amorphous and crystalline samples. Within this measurement scheme, the specimen is illuminated by a collimated electron beam. The region-of-interest is determined by an aperture inserted into the first image plane of the objective lens (see Fig. 2.2c). Typically, the probed specimen region is limited to diameters in the  $\mu\text{m}$ -range. The resulting electron diffractograms include structural information spatially averaged over the probed sample area. For polycrystalline materials, this diffraction technique allows to average over a large number of differently orientated nanoparticles, which gives rise to Debye-Scherrer rings (Fig. 5.1). From the analysis of the intensity in these rings, the temperature increase in response to an optical excitation of polycrystalline platinum deposited on a single-crystalline silicon membrane can be extracted (see Chapter 7.6.9).

**Nano-beam diffraction (NBD)** In SAED, the real-space resolution is determined by the illuminated circular region of interest chosen by the SAED aperture. In order to probe dynamics in inhomogeneous specimen on sub-micrometer length scales, the size of the diffracting area must be reduced to avoid averaging effects. For coherent electron sources, this is achieved with the electron optics system, which can be employed to illuminate nanometer-sized areas of a sample with nearly collimated electrons beams.

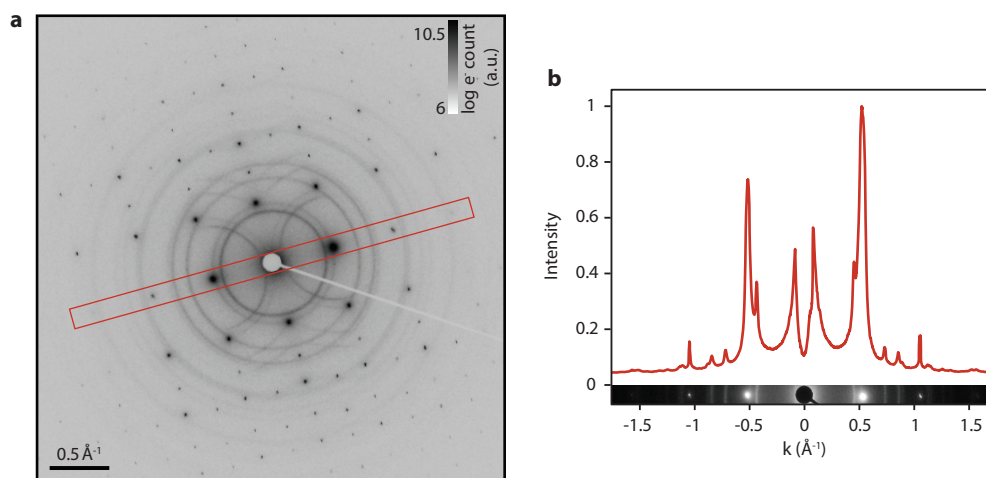


**Figure 5.1:** Diffraction of a Pt/Si heterostructure. (a) The diffraction pattern shows Bragg spots of a single-crystalline silicon membrane and Debye-Scherrer rings of a polycrystalline platinum stripe, which is deposited on the membrane. (b) Selected region (see red rectangle in a) and corresponding intensity profile from the diffraction pattern.

**Convergent beam electron diffraction (CBED)** Convergent beam electron diffraction is performed by focusing an electron beam with a convergence angle about ten times larger than in NBD mode at the specimen [329, Ch. 10.4.3]. Diffraction patterns recorded with this technique therefore contain information from nanoscale sample areas and strongly differ from images obtained with collimated, large-diameter electron beams.

In the focal plane of the objective lens, the transmitted and the diffracted electrons form discs (Fig. 5.2b), which are separated by reciprocal lattice vectors and define a family of conjugate diffraction spots where every spot corresponds to a particular incident beam direction. Consequently, the size of the CBED disks depends on the size of the condenser lens aperture and the excitation strength of the condenser mini lens (CM lens) which set the convergence angle of the electron illumination. The amount of accessible details, i.e., the magnification of reciprocal space, is given by the camera length of the imaging system.

Within the angular profile of the electron beam, the Bragg condition<sup>11</sup> is only fulfilled by particular angles of incidence, as illustrated in Fig. 5.2a for the simplified case that only one family of crystal planes fulfills the Bragg condition. The intersection of the cone-shaped electron beam (red) and the cone of the Bragg condition (black) results

<sup>11</sup>The Bragg condition states that electron waves, which are elastically scattered from equally spaced crystal lattice planes associated with a reciprocal lattice vector  $g$ , constructively interfere at specific scattering angles  $\theta_B$  and give rise to a diffraction pattern that critically depends on the orientation of the crystal, as well as on the electron energy (de Broglie-wavelength  $\lambda$ ). See section 5.2.2 for details.

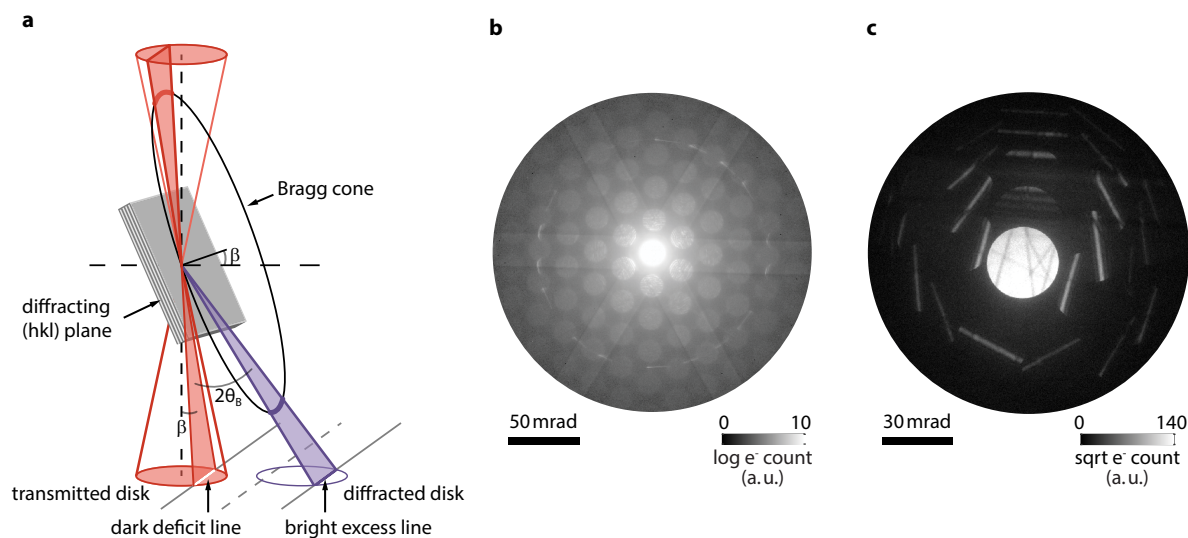


**Figure 5.2:** Basic principle of convergent beam electron diffraction. (a) Schematic representation of the formation of a CBED diffraction pattern. For small Bragg angles, the projection of the hyperbolic intersections of the electron beam cone (red) with the Bragg cone (black) on a flat screen/detector results in straight lines. (b) CBED diffraction pattern of a graphite flake along a high-symmetry direction, recorded at a small camera length (CBED mode CBD-553 of a JEOL F200 microscope). The three main visible features are CBED disks corresponding to the incident angular range of the electron beam, Kikuchi bands in the background, and a first-order-Laue-zone ring [330, Ch. 2.3]. (c) CBED diffraction pattern with deficit and excess Bragg lines for a tilted silicon membrane (CBED mode CBD-141 of a JEOL JEM-2100 microscope).

in a dark line called deficit line in the central disk (red) and a bright line, the excess line, in the diffracted disk (violet). Both lines fulfill the conservation of total intensity. As a consequence of the broad range of incident directions in the illumination cone in conjunction with the small electron wavelength, the Bragg condition is most often fulfilled simultaneously for several reciprocal lattice planes of a small region of the crystal (Fig. 5.2c). The resulting diffraction pattern consists of a transmitted disk surrounded by multiple diffracted disks. While each of the diffracted disks contains its own excess line, a combination of all different deficit lines is visible in the transmitted disk.

The convergence angle in the schematic drawing and the experimental data shown in Fig. 5.2 is chosen small enough so that the CBED disks are well-separated. Larger convergence angles lead to overlapping disks with more complex intensity distributions. For a highly-coherent electron beam, interference fringes within the overlaps of neighboring disks [331] can be analyzed to characterize phase shifts at lattice defects [332]. Furthermore, the continuous variation of incident beam directions results in additional intensity modulations. As will be discussed in section 5.2.3, CBED disks contain two-

dimensional rocking curves. In order to record these intensity profiles over a large angular range without disk overlap, an optimized coverage of the electron detector with scattered electrons is obtained by choosing a maximum incident angle that is twice the Bragg angle associated with the smallest reciprocal lattice vector of the material. Quantitative diffractive probing of structural dynamics at a metal/semiconductor bilayer heterostructure requires CBED patterns which contain many differently orientated, well-separated Bragg lines. As transient changes of line profiles are obtained by integrating the diffracted intensity along the individual line directions (see section 7.6.3), long and intense Bragg lines are beneficial.

The background between CBED disks is modulated by a set of Kikuchi bands passing through the center of the diffraction pattern and extending to large scattering angles. The intensity profile of these bands strongly depends on the crystal thickness. Generally, defect bands with an intensity lower than the surrounding background are obtained for thick crystals, whereas bright excess bands, as shown in Fig. 5.2b, are obtained for thin crystals [333; 130, Ch. 7.5.4]. In addition to Kikuchi bands, excess and defect Kikuchi lines can often be found. A Kikuchi diffraction pattern of a perfect crystal arises from a two-step scattering process: Electrons are first scattered inelastically within the sample into a wide cone and then elastically by crystal lattice planes. As a result, the Bragg reflections do not form diffraction spots but a pair of lines corresponding to  $\pm\theta_B$  [130, Ch. 7.5.4].

## **5.2 Kinematical scattering theory**

In order to fully appreciate the richness and complexity of measurements with diffraction contrast and extract the information linked to nanophononic wave fields, it is important to have a fundamental understanding of how crystal properties govern the formation mechanisms of diffraction patterns across a wide range of experimental parameters. Diffraction experiments focus on the interference of waves scattering from predominantly periodic arrangements of atoms, which leads to a conceptually similar mathematical description of elastic scattering for x-rays and wavefunctions of matter particles such as electrons and neutrons. As a first approach to describe the formation of electron diffraction patterns, kinematical scattering theory is applicable to cases of weak interaction between the incoming electron wave and the crystal potential such as in ultra thin-film samples studied in high-energy TEM.

### 5.2.1 First Born approximation for weak interaction potentials

For only weak wave interactions with the sample volume, the wave function  $\psi$  can be approximated by the incident wave function  $\psi_0$ . This approach corresponds to first-order perturbation theory and is known as the first Born approximation. Validity implies that the incident wave exhibits a single, direct scattering event (kinematic scattering approximation) in which spherical waves with a phase given by the incident wave emanate from the scattering potential. The scattered wave amplitude is much smaller compared to the incident beam amplitude rendering multiple scattering negligible.

Generally, for electrons interacting with a time-independent electrostatic potential field  $V(\mathbf{r})$  [329, Ch. 4.1], the electron wave function  $\psi$  satisfies the Schrödinger equation

$$\frac{1}{4\pi^2} \nabla^2 \psi(\mathbf{r}) + k_0^2 \psi(\mathbf{r}) = -U(\mathbf{r}) \psi(\mathbf{r}). \quad (5.1)$$

This linear differential equation contains the interaction potential  $U = -\frac{2m}{h} eV$  of the object and an energy term expressed by the vacuum wavenumber  $k_0 = \sqrt{2mE/h^2} = 2me\Phi/h^2$  which depends on the relativistic electron mass  $m = \gamma m_0$ , electron charge  $e$ , electron energy  $E$ , Planck constant  $h$ . The acceleration potential  $\Phi$  (typically between 80 keV and 300 keV in a TEM) enters in two ways: in the expression for the wave vector and in the interaction potential due to the relativistic factor  $\gamma = 1 + \frac{e\Phi}{m_0 c^2}$  in the electron mass. A convenient equivalence to the Schrödinger equation is the integral form

$$\psi(\mathbf{R}) = \psi_0(\mathbf{R}) - \int d^3\mathbf{r} G(\mathbf{R} - \mathbf{r}) U(\mathbf{r}) \psi(\mathbf{r}), \quad (5.2)$$

also known as the Lippmann-Schwinger equation [334; 329, Ch. 4.1]. Treating the incident electrons as a plane wave  $\psi_0 = \exp(2\pi i \mathbf{k}_0 \mathbf{r})$  with initial wave vector  $\mathbf{k}_0$  and wavelength  $\lambda_0 = 1/k_0$ , and employing the Green's function  $G(\mathbf{R}) = -\pi \frac{e^{2\pi i k R}}{R}$  for a distance  $\mathbf{R}$  from the interaction potential,<sup>12</sup> the Lippmann-Schwinger equation reads [329, Ch. 4.1]

$$\psi(\mathbf{R}) = e^{2\pi i \mathbf{k}_0 \mathbf{R}} + \pi \int d^3\mathbf{r} \frac{e^{2\pi i k |\mathbf{R} - \mathbf{r}|}}{|\mathbf{R} - \mathbf{r}|} U(\mathbf{r}) \psi(\mathbf{r}). \quad (5.3)$$

When the propagation distance in the exponent is large enough compared to the

---

<sup>12</sup>In the condensed matter notation in which  $k = \frac{2\pi}{\lambda}$ , the Schrödinger equation takes the form  $(\nabla^2 + k^2)\psi(\mathbf{r}) = -U(\mathbf{r})\psi(\mathbf{r})$ . The Green's function to be inserted in the Lippmann-Schwinger equation then is  $G(\mathbf{R}) = -\exp(ikR)/(4\pi R)$ . For a thorough derivation of Green's function, the reader is referred to Appendix B in Ref. [335].

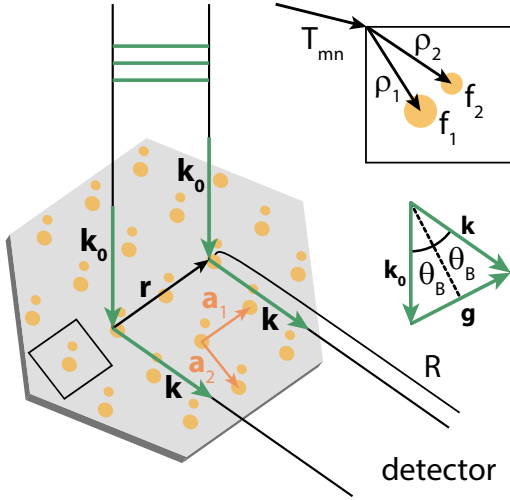


**Figure 5.3:** Diffraction of an incident plane wave with wave vector  $\mathbf{k}_0$  on periodic lattice with two-atomic basis described by base vectors  $\mathbf{a}_{1,2}$  and atom-specific scattering factors  $f_{1,2}$ . (Top right) Unit cell with a diatomic basis. (Bottom right) Momentum transfer upon scattering fulfilling the Laue condition  $\Delta\mathbf{k} = \mathbf{g}$ . Adapted from Ref. [339] with permission from the author.

scattering volume,  $|\mathbf{R} - \mathbf{r}|$  can be expanded into  $R - \frac{\mathbf{r} \cdot \mathbf{R}}{R}$  and the denominator in Eq. 5.3 can be replaced by  $|\mathbf{R}|$ . The scattered wave vector  $\mathbf{k}$  is directed along  $\mathbf{R}$  to the detector position:  $\mathbf{k} = k \frac{\mathbf{R}}{R}$  (see Fig. 5.3). Within the framework of kinematic scattering theory, the final wave function becomes

$$\psi(\mathbf{R}) \approx e^{2\pi i \mathbf{k}_0 \mathbf{R}} + f_s(\mathbf{k}, \mathbf{k}_0) \frac{e^{2\pi i \mathbf{k} \mathbf{R}}}{R}. \quad (5.4)$$

Importantly, the scattering amplitude is given by the Fourier transform of the interaction potential:

$$f_s(\mathbf{k}, \mathbf{k}_0) = \pi \int d^3\mathbf{r} e^{-2\pi i(\mathbf{k} - \mathbf{k}_0)\mathbf{r}} U(\mathbf{r}). \quad (5.5)$$

A relation of the electron scattering factor to the one for x-ray ratio is established by the Mott-Bethe formula [336–338]:

$$f_{\text{el}}^B(s) = \frac{1}{8\pi^2 a_H} \frac{Z - f^x(s)}{s^2} (\text{\AA}). \quad (5.6)$$

Therein,  $s = |\Delta\mathbf{k}| = |\mathbf{k} - \mathbf{k}_0|$  is the momentum change,  $Z$  is the atomic number,  $a_H$  is the Bohr radius, and  $(\frac{1}{8\pi^2 a_H}) \approx 0.0239 \text{\AA}^{-1}$ .

Numerical calculations commonly fit the x-ray scattering factor  $f^x$  with a sum of few Gaussian functions  $f^x(s) = \sum_{i=1}^4 a_i \exp(-b_i s^2) + c$ , with parameters  $a_i$  and  $b_i$ . Initially, the fit constants were retrieved by Doyle and Turner [340] for a range of  $s = 0$  to  $2 \text{\AA}^{-1}$  employing the Hartree-Fock method to calculate the charge density. Parametrization for all neutral atoms with  $s$  up to  $6 \text{\AA}^{-1}$  using five Gaussian functions is described and tabulated

by Peng et al. in Ref. [341] and in the International Tables for Crystallography [342]. In the far field, the scattering amplitude defines the partial cross section that depends on the scattering angle, atomic number, and beam energy  $E$  included in the relativistic constant  $\gamma$  [343, Ch. 3.1.4; 329, Ch. 4.3]:

$$\frac{d\sigma}{d\Omega} = \gamma^2 |f_{\text{el}}^B(s)|^2. \quad (5.7)$$

## 5.2.2 Diffraction of a perfect crystal

To complete the fundamentals of kinematical diffraction, an expression for the potential  $U(\mathbf{r})$  is missing. As a simple model system, we assume a perfect, infinite crystalline solid described by an underlying Bravais lattice. The periodic structure of smallest repeating units is defined by the translational vector  $\mathbf{T}_{m,n,o} = m\mathbf{a}_1 + n\mathbf{a}_2 + o\mathbf{a}_3$  with  $\mathbf{a}_{1,2,3}$  being linearly independent vectors of the crystal lattice in real-space [344, Ch. 4]. The electrostatic potential that the electrons scatter from has the same underlying translational periodicity. For a single unit cell with atomic potentials  $u_j$  of individual atoms at positions  $\boldsymbol{\rho}_j$  (see Fig. 5.3 for two-dimensional case), it is therefore possible to write the potential in the approximate form  $U_{\text{cell}} = \sum_j u_j(\boldsymbol{\rho}_j)$ . The total potential at a point  $\mathbf{r}$  is then obtained by convolving the Bravais lattice with the potential distribution inside the unit cell:  $U(\mathbf{r}) = \sum_{m,n,o} \sum_j u_j(\boldsymbol{\rho}_j - \mathbf{T}_{m,n,o})$ . Applying the first Born approximation, the amplitude of the scattered wave is given by

$$A(\Delta\mathbf{k}) = \mathcal{F}[U(\mathbf{r})] = \underbrace{\sum_j f_j(\Delta\mathbf{k}) e^{-2\pi i \boldsymbol{\rho}_j \Delta\mathbf{k}}}_{\text{structure factor } F} \cdot \underbrace{\sum_{m,n,o} e^{-2\pi i \mathbf{T}_{m,n,o} \Delta\mathbf{k}}}_{\text{lattice factor } G}. \quad (5.8)$$

The atom-specific scattering factor  $f_j$  is the Fourier transform of the atomic potential  $u_j$ . The structure factor  $F$  and lattice factor  $G$ , that will be discussed separately in the following, are independent from each other as they encode the scaling of the scattering amplitude and the arrangement of scattered reflexes in reciprocal space, respectively.

Non-vanishing contributions to the scattering intensity  $I = |A|^2$  are only obtained for reciprocal lattice vectors  $\Delta\mathbf{k}$ , for which  $\mathbf{a}_i \cdot \Delta\mathbf{k} = q$  with  $q \in \mathbb{Z}$  is independent of integers  $m, n, o$ . To find these specific vectors, we define the reciprocal lattice by a set of vectors  $\mathbf{G}_{hkl} = h\mathbf{b}_1 + k\mathbf{b}_2 + l\mathbf{b}_3$  in analogy to the real-space Bravais lattice constructed by lattice vectors  $\mathbf{T}_{m,n,o}$ . The basis vectors  $\mathbf{b}_i$  in reciprocal space can be constructed from

the real-space vectors  $\mathbf{a}_i$  employing the condition  $\mathbf{a}_i \mathbf{b}_j = \delta_{ij}$ . A possible solution to span the reciprocal space is given by the following set of primitive vectors:

$$\mathbf{b}_1 = \frac{\mathbf{a}_2 \times \mathbf{a}_3}{V_{\text{uc}}}; \quad \mathbf{b}_2 = \frac{\mathbf{a}_3 \times \mathbf{a}_1}{V_{\text{uc}}}; \quad \mathbf{b}_3 = \frac{\mathbf{a}_1 \times \mathbf{a}_2}{V_{\text{uc}}}, \quad (5.9)$$

where  $V_{\text{uc}} = \mathbf{a}_1 \cdot (\mathbf{a}_2 \times \mathbf{a}_3)$ . Constructive interference of electron waves occurs if  $\Delta \mathbf{k}$  coincides with a reciprocal lattice vector  $\mathbf{G}_{hkl}$  which is the Laue condition for scattering from a periodic three-dimensional crystal.

The lattice factor  $G$  can therefore also be written as a sum of Delta distributions  $\sum_{\mathbf{G}} \delta(\Delta \mathbf{k} - \mathbf{G})$ . When the Laue condition is satisfied, all terms in the lattice factor  $G$  are 1. For a specimen which is thin compared to its lateral dimensions, the peak intensity scales with  $N^2$ , where  $N$  is the number of unit cells in the lateral direction. The diffracted intensity integrated over  $\Delta \mathbf{k}$  increases with  $N$  and the peak width becomes narrower with  $1/N$ , as shown in Ref. [343, Ch. 5.2.1].

If the incident electron wave is only elastically scattered, i.e., for energy conservation expressed by  $\mathbf{k}_0^2 = \mathbf{k}^2$ , the incident and scattered wave vectors  $\mathbf{k}_0$  and  $\mathbf{k}$  lie on a sphere in reciprocal space as obtained by the geometrical Ewald construction. For 200-keV electrons with wavelength  $\lambda = 2.5 \cdot 10^{-3}$  nm [141, Ch. 1.5], the radius of the Ewald sphere is approximately two orders of magnitude larger than for typical x-ray wavelengths [345, Ch. 5.6]. In close proximity to reciprocal lattice points, the Ewald sphere of high-energy electrons translates into a flat surface allowing for the simultaneous detection of a large number of Bragg peaks.

While the reciprocal lattice vector  $\mathbf{G}_{hkl}$  is perpendicular to the corresponding real-space plane indexed with Miller indices  $h$ ,  $k$ , and  $l$ , its length is equal to the reciprocal of the interplanar spacing for those  $(hkl)$ -planes:  $|\mathbf{G}_{hkl}| = 1/d_{hkl}$ . Combining this relation with conservation of momentum,  $\mathbf{k} = \mathbf{k}_0 + \mathbf{G}$ , and energy  $|\mathbf{k}| = |\mathbf{k}_0|$ , one arrives at the real-space equivalence of the Laue condition, known as Bragg's law:

$$2d_{hkl} \sin(\theta_B) = n\lambda, \quad (5.10)$$

with integers  $n$  and Bragg angle  $\theta_B$  [344, Ch. 6].

The structure factor  $F$  in Eq. 5.8 describes the contribution to the scattering intensity of a single unit cell. It is expressed by the sum over the atomic form factors  $f_j$ , defined by the Fourier transform of the atom-specific potential  $u_j$ . Provided that no absorption effect

is important, the interaction potential  $U(\mathbf{r})$  can be described by a real function so that  $f(\Delta\mathbf{k}) = f^*(\Delta\mathbf{k})$  (cf. Eq. 5.5). Since  $I \propto |F(\Delta\mathbf{k})|^2 = |F(-\Delta\mathbf{k})|^2$ , inversion of a crystal through a center of symmetry does not change diffraction intensities in the kinematical approximation (Friedel's law) [345, Ch. 5.2.3]. The crystal symmetry is encoded in the positions of diffraction peaks. For all Bravais lattices, specific selection rules can be derived. While simple cubic crystals with one atom per unit cell show diffraction peaks for all integer combinations of Miller indices  $h$ ,  $k$ , and  $l$ , certain combinations are not allowed in crystals with more than one atom in the basis of the unit cell [343, Ch. 5.3.2]. Silicon, for example, belongs to the group of diamond cubic crystals set up by a simple cubic lattice with an eight-atom basis. The silicon structure factor  $F$  is expressed as a sum of eight terms and takes on two non-zero values. Diffraction peaks appear if all Miller indices are even and their sum is divisible by 4 or if all indices are odd integers.

### 5.2.3 Excitation error and shape function

So far, only infinite crystals were considered for which confined Bragg spots arise if the sample is homogeneously illuminated by a parallel electron beam and a reciprocal lattice point is in exact fulfillment of the Bragg condition. Consequently, the diffraction pattern of a crystal perfectly orientated in the zone-axis should not show any first-order diffraction spots. In contrast to this theoretical expectation, a large number of the diffraction spots is observed experimentally. Their origin lies in the finite scattering volume that leads to modulations in the scattering amplitude not yet included in the scattering theory for infinite crystals. Introducing the geometrical shape function  $s(\mathbf{r})$ , the scattering amplitude in general becomes  $A(\Delta\mathbf{k}) = \mathcal{F}[U(\mathbf{r}) \cdot s(\mathbf{r})] = \mathcal{F}[U(\mathbf{r})] \otimes \mathcal{F}[s(\mathbf{r})]$  [123, Ch. 2.6], Although the shape function can be a rather complex expression, e.g. for polyhedral particles [123, Ch. 9.8], the geometry of TEM thin films with a much smaller dimension along the electron beam direction compared to the lateral dimensions allows the simple approach to choose a rectangular function in  $\hat{z}$ -direction. Inserting the corresponding Fourier transform  $s(\Delta\mathbf{k}) = h\delta(\Delta k_x)\delta(\Delta k_y)\text{sinc}(\pi\Delta k_z h)$  into Eq. 5.8, the scattering amplitude in reciprocal space is given by

$$A(\Delta\mathbf{k}) = F \cdot \sum_{\mathbf{G}} \delta(\Delta\mathbf{k} - \mathbf{G}) \cdot h\delta(\Delta k_x)\delta(\Delta k_y)\text{sinc}(\pi\Delta k_z h). \quad (5.11)$$

Due to this softening of the Laue condition, the diffraction pattern is obtained by the intersection of the Ewald sphere with *reciprocal lattice rods* or “*relrods*” at each reciprocal

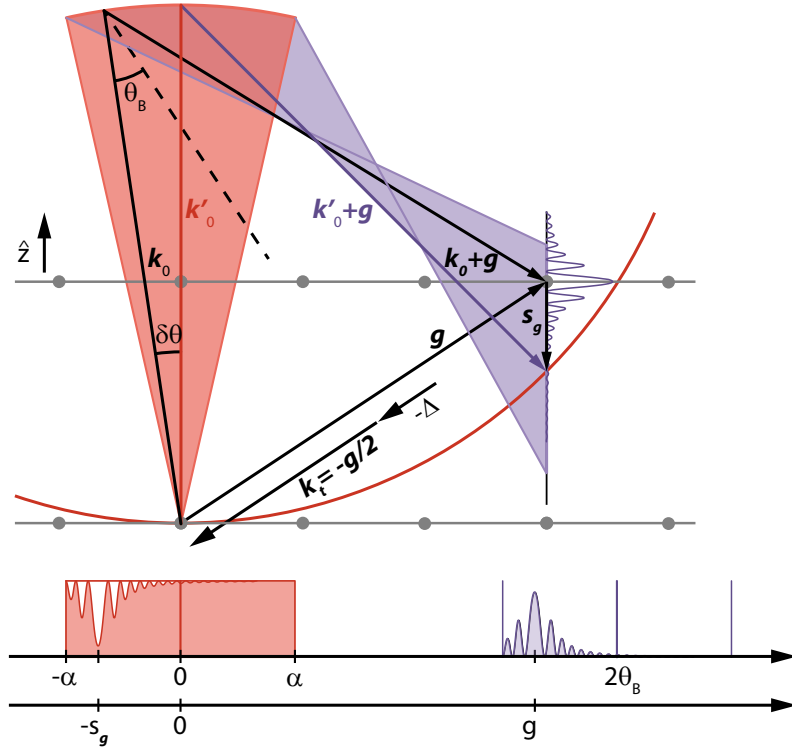


**Figure 5.4:** Schematic representation of the excitation error  $s_g$  in a CBED pattern. Bragg reflections lie on the intersection of the Ewald sphere with radius  $k_0$  (red circular segment) with reciprocal lattice points (grey dots). For a sample with finite thickness, diffraction intensity is also recorded if the incident beam not exactly fulfills the Bragg condition. Employing a convergent electron beam that contains a large range of incident beam directions (full convergence angle  $2\alpha$ ), the spatial variation of the excitation error is simultaneously probed in each CBED disk. The deficit and excess lines are not necessarily centered in the transmitted (red) and diffracted beams (violet). By relating the excitation error  $s_g$  with the transversal component  $k_t$  of the incident wave vector, Eq. 5.14 can be derived.

lattice point.

Vertically stacked thin films can be described by a sum of two periodic potentials, each convolved with a generally different rectangular shape function. Due to the linearity of the Fourier transform, the diffraction pattern contains the superposition of the two reciprocal lattices.

A quantification of the distance between the reciprocal lattice points and the exact Bragg orientation is based on the definition of the so-called excitation error  $s_g$  (see Fig. 5.4). This parameter is chosen such that it lies along the surface normal direction of the thin film sample surface in order to fulfill the condition of continuous momentum. Sign and amplitude, however, strongly change with the diffraction angle. As the cone of a convergent electron beam contains a large range of incident beam directions, this

variation of the excitation error is simultaneously probed in each disk. Following Ref. [329, Ch. 3.5], we consider an incident beam with wave vector  $\mathbf{k}_0$  and a diffracted beam given by  $\mathbf{k}_0 + \mathbf{g}$ , where  $\mathbf{g}$  is a reciprocal lattice vector. For a second incident beam  $\mathbf{k}'_0$  tilted to the right of  $\mathbf{k}_0$  by a small angle  $\delta\theta$ , the diffracted beam  $\mathbf{k}'_0 + \mathbf{g}$  appears tilted in the same direction, but does not intersect the Ewald sphere defined by  $k_0 = 1/\lambda$  anymore (Fig. 5.4). Due to energy conservation, the elastic scattering condition

$$|\mathbf{k}_0 + \mathbf{g} + \mathbf{s}_g|^2 = |\mathbf{k}_0|^2 \quad (5.12)$$

is fulfilled. Taking small Bragg angles and a surface normal perpendicular to the incident beam direction ( $\mathbf{k}_0 \perp \mathbf{g}$ ), and short  $|\mathbf{s}_g|$  into account, this equation can be approximated by

$$|\mathbf{k}_0 + \mathbf{g} + \mathbf{s}_g|^2 \approx |\mathbf{k}_0 + \mathbf{g}|^2 + 2k_0s_g. \quad (5.13)$$

The above equations combined yield  $s_g \approx (\mathbf{k}_0^2 - |\mathbf{k}_0 + \mathbf{g}|^2)/(2k_0)$ , which determines the sign convention for  $s_g$ : When the length of  $\mathbf{k}_0 + \mathbf{g}$  is shorter than  $k_0$  such that the Ewald sphere encloses the reciprocal lattice point, the excitation error is positive. If the reciprocal lattice lies outside of the sphere,  $s_g$  is negative. Separating the incident wave vector into components in direction as well as tangential to a zone-axis  $\mathbf{k}_0 = k_z\hat{z} + \mathbf{k}_t$  allows to calculate the excitation error without knowledge of the initial crystal orientation [329, Ch. 3.5]. Employing the Bragg condition  $k_t = -g/2$  or  $k'_t = -g/2 - \Delta$ , we derive  $s_g \approx (\mathbf{k}_t^2 + |\mathbf{k}_t + \mathbf{g}|^2)/(2k_0) = \lambda/2 \left( (-\frac{g}{2})^2 - (\frac{g}{2})^2 \right)$  or  $s_g \approx \lambda/2 \left( (-\frac{g}{2} - \Delta)^2 - (\frac{g}{2} - \Delta)^2 \right) = g\Delta/(1/\lambda)$ , respectively for both incident beams  $\mathbf{k}_0$  and  $\mathbf{k}'_0$ . As graphically obtained from Fig. 5.4, the deviation from the Bragg angle is related to the transversal vector component  $\Delta$  via  $\delta\theta \approx \Delta/(1/\lambda)$ . Therefore, we obtain the relation

$$s_g \approx g\delta\theta \quad (5.14)$$

between the excitation error, the lattice vector, and two Ewald sphere orientations differing by  $\delta\theta$ . Within the two-beam theory detailed in sections 5.3.2 and 5.3.4, these intensity variations across the CBED disk, known as rocking curves, provide an accurate method to determine the sample thickness.

### 5.3 Dynamical scattering theory

Kinematical scattering theory is very useful and valid for a wide range of diffraction experiments, albeit being limited to the assumption of independent diffracted beams as it describes the effect of the crystal potential by first-order perturbation theory. However, the rediffraction from the same crystal plane and the coherent interaction of multiple scattered waves, referred to as dynamical scattering, cannot always be neglected. Signatures of the coupling between different beams in a dynamical diffraction process are, for example, energy-dependent Bragg spot intensities and effective Debye temperatures, large intensity variations with the incident angle, the breakdown of Friedel's law, and the appearance of kinematically forbidden Bragg peaks [346, Ch. 4.8]. Also an analysis of CBED lines hints at failures of the Born approximation: Whereas line profiles within kinematical scattering theory show a characteristic main maximum and weak side-maxima, dynamical CBED lines may consist of two principle maxima and high-contrast side-maxima. Another dynamical feature observed in CBED patterns are splittings between superposed lines [347, 348].

Important quantities to determine whether the interaction of the probing beam with the crystal potential is dominated by single or multiple scattering are the sample thickness in relation to an extinction distance, and the scattering cross section [345, Ch. 8]. In contrast to x-rays that undergo weak scattering processes, the scattering cross section for electrons is much larger, in particular for low energy electrons [345, 349]. Consequently, the approximation of a weak interaction potential (first Born approximation) is no longer justified in this case and the scattering will violate the assumptions of neglecting higher-order Born approximations [343, Ch. 3.3.1; 345, Ch. 1.5.2].

Since the late 1920's, several mathematical formulations of dynamical diffraction theory have been developed, each with another perspective on the scattering problem and for another application [329, Ch. 5]. The two theories discussed below are based on solving the Schrödinger equation with an ansatz for the electron wave function that includes the periodic crystal potential expanded as a Fourier series. Following Bethe's original work [350], forward and diffracted beams coupled in the three-dimensional translational potential are described by a set of Bloch waves [351] that leads to an eigenvalue equation for the wave vectors and the Bloch coefficients. The focus of this description therefore lies on the dynamics inside a perfect crystal. In its important simplification to a two-beam problem, this theory can be used to estimate the specimen thickness. The second

formulation of dynamical scattering theory is based on a system of linear differential equations, known as the Howie-Whelan equations. The crystal is treated as an infinite number of successive planes of infinitesimal thickness, which renders this approach suitable for treating defects. Also different from the Bloch wave formulation, the Howie-Whelan equations address the scattering problem from the viewpoint of an external observer who is interested in the scattering angles and amplitudes after the electrons have left the crystal.

### 5.3.1 Bloch wave method

Within kinematical scattering theory for a perfect crystal, the periodicity of the crystal potential already plays an important role in the analysis of diffraction patterns as it is included in both the structure and the lattice factors (Eq. 5.8), which resulted from the application of the first Born approximation. However, the analytical result for the wave function was obtained by replacing the wave function on the right-hand side of the Schrödinger equation (Eq. 5.1) by the incident plane wave. As a consequence, the differential equations for the diffracted beams were independent of each other. For the discussion of the wave equation within dynamical scattering theory, which allows for a more quantitative electron diffraction intensity analysis, it is important to reconsider the three-dimensional crystal periodicity and its mathematical implications on unsimplified solutions of the Schrödinger equation. At this point, the question arises as to which wave vectors are allowed inside the crystal for a given energy determined by the incident wave vector. Since the potential can be expressed by an expansion into a Fourier series  $U(\mathbf{r}) = \sum_{\mathbf{g}} U_{\mathbf{g}} \exp(2\pi i \mathbf{g} \mathbf{r})$  with reciprocal lattice vectors  $\mathbf{g}$ , a complete set of eigenstates for the electron wave  $\Psi(\mathbf{r})$  inside the crystal is given by waves with Bloch wave vectors  $\mathbf{k}$ :

$$\psi(\mathbf{r}) = C(\mathbf{r}) \exp(2\pi i \mathbf{k} \mathbf{r}) = \sum_{\mathbf{h}} C_{\mathbf{h}} \exp(2\pi i \mathbf{k}_{\mathbf{h}} \mathbf{r}). \quad (5.15)$$

Therein,  $C(\mathbf{r})$  is a function with the periodicity of the lattice, and  $\mathbf{k}_{\mathbf{h}} = \mathbf{k} + \mathbf{h}$  defines a wave vector corresponding to the reciprocal lattice point  $\mathbf{h}$  [352]. The Bloch wave coefficients  $C_{\mathbf{h}}$  are independent of position, but depend on the Bloch wave vector. The set of equations

$$(k_0^2 + U_0 - (\mathbf{k} + \mathbf{h})^2) C_{\mathbf{h}} + \sum_{\mathbf{g} \neq \mathbf{h}} U_{\mathbf{h}-\mathbf{g}} C_{\mathbf{g}} = 0 \quad (5.16)$$

resulting from Eq. 5.1 is similar to the solid-state problem to calculate the band structure of a material. Hence, Eq. 5.16 defines a dispersion relation. The wave vector inside the medium of average potential is determined by  $\kappa^2 = k_0^2 + U_0$ , and hence, the kinetic energy of the electron increases slightly when the electron enters the solid as it is attracted by the positive nuclei. Using the equivalent matrix formulation

$$\begin{pmatrix} \kappa^2 - k^2 & \dots & U_{0h} & \dots & U_{0g} \\ \vdots & \ddots & \vdots & & \vdots \\ U_{h0} & \dots & \kappa^2 - k_h^2 & \dots & U_{hg} \\ \vdots & & \vdots & \ddots & \vdots \\ U_{g0} & \dots & U_{gh} & \dots & \kappa^2 - k_g^2 \end{pmatrix} \begin{pmatrix} C_0 \\ \vdots \\ C_h \\ \vdots \\ C_g \end{pmatrix} = 0 \quad (5.17)$$

with the abbreviation  $U_{hg} = U_{h-g}$ , we see that the first terms of Eq. 5.16 are represented by a diagonal matrix, already known from kinematical scattering theory, and off-diagonal matrix elements that describe the coupling between all beams inside the crystal. Note that the matrix is Hermitian ( $U_{gh} = U_{hg}^*$ ) in absence of absorption and real-symmetric ( $U_{gh} = U_{hg}$ ) for centro-symmetric crystals.

Non-trivial solutions of Eq. 5.17 require the determinant of the matrix to be zero, which means that  $2N$  roots of the corresponding polynomial equation have to be found for  $N$  beams, instead of a single wave as was the case in kinematical scattering theory. As originally proposed by Bethe [350] and discussed in detail by Metherell [353] and Humphreys [354], the electron wave inside the crystal is a superposition of all Bloch waves with individual amplitudes  $\alpha^{(j)}$ :

$$\psi(\mathbf{r}) = \sum_j \alpha^{(j)} \sum_{\mathbf{h}} C_{\mathbf{h}}^{(j)} \exp(2\pi i \mathbf{k}_{\mathbf{h}}^{(j)} \cdot \mathbf{r}). \quad (5.18)$$

The electron dispersion equation for Bloch wave  $j$  then reads

$$(\kappa^2 - |\mathbf{k}^{(j)} + \mathbf{h}|^2) C_{\mathbf{h}}^{(j)} + \sum_{g \neq h} U_{h-g} C_{\mathbf{g}}^{(j)} = 0. \quad (5.19)$$

The constants  $\alpha^{(j)}$  are determined by boundary conditions at the interface between vacuum and the entrance plane of the crystal: Since both, the incident wave and the wave inside the crystal are solutions to the Schrödinger equation, tangential components of the wave vectors  $\mathbf{k}_0$ ,  $\boldsymbol{\kappa}$ , and  $\mathbf{k}$  across this plane must be continuous. Consequently, the solution vectors  $\mathbf{k}^{(j)} = \boldsymbol{\kappa} + \gamma^{(j)} \mathbf{n}$  can only vary by the normal component  $\gamma^{(j)} \mathbf{n}$ .

In the high-energy approximation that allows to ignore the quadratic term in  $\gamma^{(j)}$ , the Bloch-wave description finally yields the eigenvalue equation of the form

$$\mathbf{A}\mathbf{C}^{(j)} = 2\mathbf{n} \cdot \mathbf{k}_0 \gamma^{(j)} \mathbf{C}^{(j)} \quad (5.20)$$

for all Bloch wave coefficients and wave vectors, as detailed in Refs. [123, 329, 354]. Solving the eigenvalue equation is a non-trivial problem that requires the use of numerical computation algorithms [355].

### 5.3.2 Two-beam approximation

Due to the small cross section of x-rays and neutron beams, it is, in most cases, allowed to assume the presence of the incident and only one strong diffracted beam while all other beams can be neglected. The strong scattering of electrons gives rise to many diffracted beams simultaneously. However, all but two beams may interfere destructively for particular crystal orientations [345, Ch. 8.1]. The two-beam theory, which follows naturally from the multi-beam case, is therefore relevant for several common experimental conditions with a tremendous advantage that it yields an analytical solution for the wave field, as explained in the following.

The matrix in Eq. 5.17 reduces to a  $2 \times 2$ -matrix with the characteristic equation

$$(\kappa^2 - k^2)(\kappa^2 - (k + g)^2) - U_g U_{-g} = 0 \quad (5.21)$$

for the matrix determinant. For large wave numbers  $\kappa$ ,  $k$  and  $|k + g|$  relative to their differences, Eq. 5.21 can be simplified to

$$(\kappa - k)(\kappa - |k + g|) = \left( \frac{|U_g|}{2\kappa} \right)^2, \quad (5.22)$$

which has four solutions for the wave vectors: Two plane waves given by  $\kappa - k^{(1)} = +|U_g|/(2\kappa)$  and  $(\kappa - k^{(2)}) = -|U_g|/(2\kappa)$  respectively propagate in the incident forward direction, while the other two waves are diffracted in the directions  $k^{(1)} + g$  and  $k^{(2)} + g$ . The difference  $\Delta k = |k^{(1)} - k^{(2)}| = |U_g|/\kappa$  is proportional to the Fourier component of the crystal potential and defines the extinction distance [329, Ch. 5.3]

$$\xi_g = \frac{\kappa}{|U_g|}. \quad (5.23)$$

In the approximation for high-energy electrons, only the  $z$ -components of the wave vector, which are (anti)parallel to the surface normal, need to be considered. Combining two waves corresponding to the same propagation direction [see Fig. 5.5(a)], we obtain

$$\begin{aligned}\varphi_0(z) &= C_0^{(1)} \exp\left(2\pi i k^{(1)} z\right) + C_0^{(2)} \exp\left(2\pi i k^{(2)} z\right) \\ \varphi_g(z) &= C_g^{(1)} \exp\left(2\pi i (\mathbf{k}^{(1)} + \mathbf{g})_z z\right) + C_g^{(2)} \exp\left(2\pi i (\mathbf{k}^{(2)} + \mathbf{g})_z z\right).\end{aligned}\quad (5.24)$$

An analysis of the coefficients  $C$  and relations between wave numbers as detailed in Ref. [352, Ch. 2] finally results in

$$\begin{aligned}\varphi_0(z) &= 2C_0 \exp(2\pi i K z) \cos(\pi \Delta k z) \\ \varphi_g(z) &= 2i C_0 \exp(2\pi i K z) \sin(\pi \Delta k z),\end{aligned}\quad (5.25)$$

so that the intensity for both beams exiting the crystal at  $z = t$ , where  $t$  is the sample thickness, is

$$\begin{aligned}I_0(t) &= 4C_0^2 \cos^2(\pi \Delta k t) = 4C_0^2 \cos^2\left(\frac{\pi}{\xi_g} t\right) \\ I_g(t) &= 4C_0^2 \sin^2(\pi \Delta k t) = 4C_0^2 \sin^2\left(\frac{\pi}{\xi_g} t\right).\end{aligned}\quad (5.26)$$

Through the sample, the intensity of the incoming wave oscillates between the wave in forward direction and the scattered beam [see Fig. 5.5(b)], which is analogous to the energy transfer between two coupled harmonic oscillators that have equal frequencies. This exchange of energy is one of the main features of dynamical diffraction, known as *Pendellösung* or thickness fringe oscillation.

Due to the finite sample thickness, the scattering intensity is further influenced by the excitation error  $s_g$ . Including these deviations from the Bragg condition ( $s_g \neq 0$ ) in the two-beam theory, the above equations for the intensities  $I_0(t)$  and  $I_g(t)$  as a function of sample thickness  $t$  become

$$I_g(t) = \frac{1}{1 + \omega^2} \sin^2\left(\frac{\pi t}{\xi_g} \sqrt{1 + \omega^2}\right) \quad (5.27)$$

and  $I_0 = 1 - I_g$  with the dimensionless parameter  $\omega = s_g \xi_g$  [329, Ch. 5.3b]. For  $s_g \gg 1/\xi_g$  and  $t \ll \xi_g$ , the kinematical approximation is recovered [343, Ch. 12.5].

In order to estimate whether kinematic scattering yields a good approximation for the nanoscale probing of structural distortion waves in a silicon membrane, we apply the

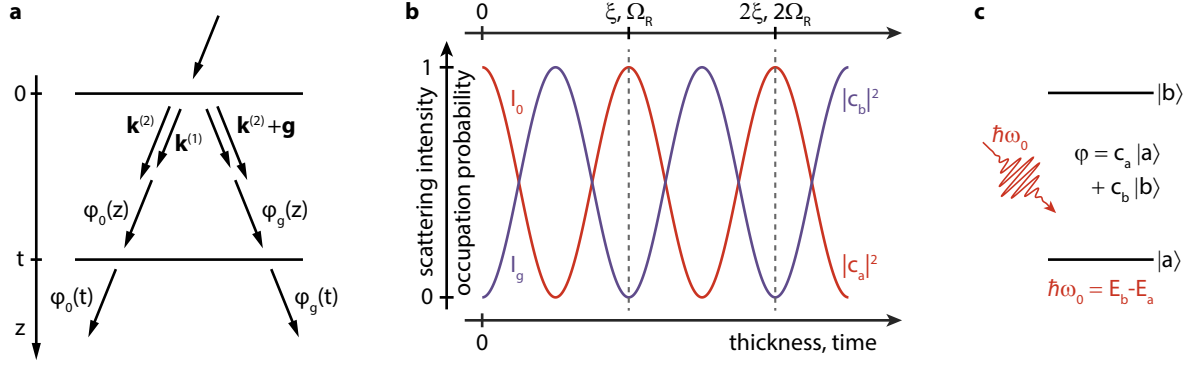


**Figure 5.5:** Two-beam approximation in scattering theory and analogous Rabi-oscillations in a coupled two-level system. (a) Combination of four coexisting waves in a sample of thickness  $t$ . Adapted from Ref. [352]. (b) Depths oscillations of the intensity between the forward and the scattered beam,  $I_0$  and  $I_g$ , respectively. (b,c) Excitation of a two-level system by an external field results in an equivalent temporal evolution of the occupation probabilities  $|c_b|^2$  and  $|c_a|^2$ .

definition for the extinction distance at temperature  $T = 0$  K given by

$$\xi_g = \frac{1}{\lambda|U_g|} = \frac{\pi V_c}{\lambda \gamma m f_{\text{el}}(s)} = \frac{\pi a_{\text{Si}}^3}{\lambda \gamma m \sum_{i=1}^5 a_i e^{-b_i \left(\frac{|G|}{2}\right)^2}}, \quad (5.28)$$

with the unit cell volume  $V_c$  and the atom-specific scattering factor  $f_{\text{el}}$  that depends on parameters  $a_i$  and  $b_i$  listed in Table 3 of Ref. [341] (see section 5.2.1.) The integer  $m$  depends on the Miller indices and takes into account the underlying Bravais lattice of the crystal. The parameters  $s = |\mathbf{G}|/2$  can be obtained from experimentally chosen reciprocal lattice vectors. Longer electron wavelengths at smaller acceleration voltages decrease the extinction length such that the transition from kinematical to dynamical scattering condition sets in earlier for similar sample thicknesses. The analysis of the ultrafast diffraction dynamics of high-quality 70-nm thin Si membranes probed with electron pulses accelerated to 45 keV has shown that dynamical diffraction theory is required to fit rocking curves and Bragg peak intensities at different sample orientations [356]. Best fit results are obtained for temperature-dependent extinction distances  $\xi_g'(T) = \xi_g(0 \text{ K})e^M$  [329, 356, 357] that take the Debye-Waller factor into account (see section 5.4) and thereby change the intensity profile of the rocking curves.

### 5.3.3 Analogy with Rabi-oscillations in two-level systems

Many important concepts of light-matter interaction discuss similar transitions between energy states and yield resonant modes characterized by oscillations of the population probability [358–361]. As detailed in the Appendix, the two states  $|a\rangle$  and  $|b\rangle$  of a quantum two-level system are resonantly coupled by a perturbation Hamiltonian that acts as a time-dependent interaction through the electric field  $E(t)$ . In a corresponding matrix formulation of the Hamiltonian, the dipole moments  $V_{ab}$  and  $V_{ba}$  of the transition arise as off-diagonal elements in analogy to the Fourier coefficients of the crystal potential in the Bloch wave method of scattering theory (cf. Eq. 5.17). The quantum dynamics of the two level system are then associated with a Rabi frequency  $\Omega_R$  (in place of the extinction distance  $\xi_g$ ) and follow the same trend as intensity oscillations between the forward and one strongly scattered beam in the two-beam approximation of scattering theory (cf. Eq. 5.26). These similar excitations are visualized in Fig. 5.5b.

### 5.3.4 Determination of sample thickness

The previously presented aspects of diffraction theory have shown that the sample thickness traversed by the electron beam significantly influences the image contrast, the width of CBED lines, and the validity of the first-order Born approximation. In order to determine the thickness of TEM specimens, several techniques of varying accuracy and applicability have been developed. As a first guidance, optical transparency measurements outside the TEM are suitable for exfoliated thin-film samples, such as graphite and transition metal dichalcogenides (TMDC) flakes. A common approach for in-situ characterizations relies on electron energy loss spectroscopy (EELS) spectra. Therein, the logarithmic ratio of the total and the zero-loss intensities is proportional to the ratio of the specimen thickness and the inelastic mean free path (MFP). Care must be taken that the MFP depends on the material and the specific experimental conditions, which yields results with an inaccuracy of about 20 % [141, Ch. 39]. Although this method is suitable for a wide range of (poly)crystalline and amorphous specimen, it has the major drawback that it assumes single scattering events.

A technique particularly precise for single-crystalline, thick membranes, harnesses the fact that the thickness-dependent intensity derived in the two-beam approximation (see Eq. 5.27) varies with the excitation error  $s_g$ : In diffraction patterns recorded with a convergent electron beam, the excitation error is simultaneously projected onto different

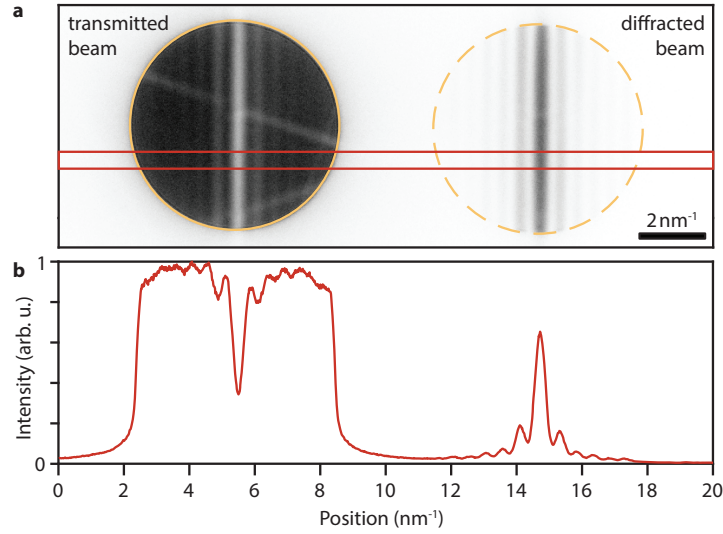


**Figure 5.6:** Thickness measurement of crystalline samples. (a) CBED pattern of a graphite flake containing the rocking curve of the strongly excited (100)-reflection. The central bright fringe in the (000)-disk is in the exact Bragg condition and is separated from the corresponding dark excess line in the (100)-disk by  $2\theta_B$ . (b) Intensity oscillations extracted from the rectangular area (red) across the diffraction pattern shown in (a). A specimen thickness of  $t = 344$  nm and an extinction length of  $\xi_{100} = 562$  nm is graphically retrieved by applying Eq. 5.29.

positions within the disks as it is related to the incident beam angle  $\theta$  through Eq. 5.14. This allows to calculate the membrane thickness by analyzing the Kossel-Möllenstedt fringes that appear in the form of alternating bright and dark fringes with a specific width and spacing [362]. Intensity minima of Eq. 5.27 occur if the following condition is fulfilled:

$$\frac{s_{g,i}^2}{n_i^2} + \frac{1}{\xi_g^2 n_i^2} = \frac{1}{t^2}. \quad (5.29)$$

Therein,  $s_{g,i}$  denotes the deviation parameter of the  $i^{\text{th}}$  minimum from the exact Bragg position ( $s_g = 0$ ). Graphically, the specimen thickness is obtained from the interception of this straight line with the  $y$ -axis at  $1/t^2$  [363, 364]. Values for  $s_{g,i}$  are obtained from the spacing of the fringe maxima, since  $s_{g,i} = \lambda g^2 \frac{\Delta\theta_i}{2\theta_B}$ , where  $\theta_B$  is the Bragg angle for the diffracting  $hkl$  plane,  $g = 1/d_{hkl}$ , and  $\theta_i$  are the distances of the  $i^{\text{th}}$  minimum from the exact Bragg condition [343].

### 5.3.5 Howie-Whelan equations

Instead of computing the allowed wave vectors inside a crystal as done in the Bloch wave description (section 5.3.1), the general derivation of the second approach to describe

dynamical scattering is based on Bragg's law, that supposes a superposition of plane waves depending on reciprocal lattice points from the beginning on [123, Ch. 5]. The general solution of the Schrödinger equation (Eq. 5.1) can therefore also be of the form

$$\psi(\mathbf{r}) = \sum_{\mathbf{g}} \psi_{\mathbf{g}} e^{2\pi i(\mathbf{k}_0 + \mathbf{g}) \cdot \mathbf{r}}. \quad (5.30)$$

Inserting this ansatz into Eq. 5.1 and ignoring absorption such that the potential is real, we obtain

$$\begin{aligned} \sum_{\mathbf{g}} \left[ \Delta \psi_{\mathbf{g}} + i4\pi(\mathbf{k}_0 + \mathbf{g}) \cdot \nabla \psi_{\mathbf{g}} + 4\pi^2(k_0^2 - (\mathbf{k}_0 + \mathbf{g})^2) \psi_{\mathbf{g}} \right] e^{2\pi i(\mathbf{k}_0 + \mathbf{g}) \cdot \mathbf{r}} \\ = -4\pi^2 \sum_{\mathbf{g}} U \psi_{\mathbf{g}} e^{2\pi i(\mathbf{k}_0 + \mathbf{g}) \cdot \mathbf{r}}. \end{aligned} \quad (5.31)$$

If the sample investigated by high-energy electrons has the shape of a planar slab, the first term of the above equation can be ignored [365] and the second term can be written in terms of the  $z$ -coordinate:

$$(\mathbf{k}_0 + \mathbf{g}) \cdot \nabla \psi_{\mathbf{g}} = |\mathbf{k}_0 + \mathbf{g}| \frac{d\psi_{\mathbf{g}}}{dz}. \quad (5.32)$$

At this point, it becomes clear that the approach presented here considers forward scattering by successive slices of infinitesimal thickness and is therefore useful to explain image contrast arising from lattice defects, which is in contrast to the Bloch wave method. Recalling the Fourier expansion of the crystal potential  $U = \sum_{\mathbf{q}} U_{\mathbf{q}} e^{2\pi i \mathbf{q} \cdot \mathbf{r}}$  and replacing the reciprocal lattice vector  $\mathbf{q}$  by  $\mathbf{q} = \mathbf{h} - \mathbf{g}$ , we obtain

$$\sum_{\mathbf{g}} \left[ \frac{d\psi_{\mathbf{g}}}{dz} - 2\pi \frac{k_0^2 - (\mathbf{k}_0 + \mathbf{g})^2}{2|\mathbf{k}_0 + \mathbf{g}|} \psi_{\mathbf{g}} \right] e^{2\pi i(\mathbf{k}_0 + \mathbf{g}) \cdot \mathbf{r}} = \sum_{\mathbf{g}} \left[ \pi i \sum_{\mathbf{h}} \frac{U_{\mathbf{g}\mathbf{h}}}{|\mathbf{k}_0 + \mathbf{h}|} \psi_{\mathbf{h}} \right] e^{2\pi i(\mathbf{k}_0 + \mathbf{h}) \cdot \mathbf{r}}, \quad (5.33)$$

which must be valid for each individual term of the summation. Using the definitions of the excitation error (Eq. 5.12) and the extinction distance (Eq. 5.23), the intensities of transmitted and diffracted waves at the exit surface of a crystalline specimen are given by the Howie-Whelan equations [366]:

$$\frac{d\psi_{\mathbf{g}}}{dz} = 2\pi i s_{\mathbf{g}} \psi_{\mathbf{g}} + \sum_{\mathbf{g} \neq \mathbf{h}} \frac{\pi i}{\xi_{\mathbf{g}}} \psi_{\mathbf{g}}. \quad (5.34)$$

## 5.4 Thermal effects on scattering intensities

Contributions to the scattering amplitude of a perfect crystal (Eq. 5.8) were derived on the assumption that the crystal is static with all atoms at fixed positions. However, this simplification neglects zero-point vibrations at  $T = 0$  K and vibrations of atoms around their equilibrium coordinates  $\boldsymbol{\rho}_j$  for  $T > 0$  K. Thermally induced structural disorder disrupts the phase coincidence in the constructive Bragg scattering, which is—within kinematic scattering theory—associated with two major effects: the intensity of Bragg reflections is reduced by the Debye-Waller factor (DWF) and thermal diffuse scattering (TDS) arises in the background. The development of the underlying theory has its origins in x-ray studies with early contributions from Debye [367], Waller [368], and Laval [369, 370]. Since then, the suppression of Bragg scattered intensity as a measure for incoherent elastic scattering and the complementary diffuse background scattering from correlated atomic motion has been investigated in a much broader field, particularly in ultrafast diffraction experiments.

In order to quantify the temperature influence on the scattering intensity, we focus on the structure factor  $F$  in which the atomic positions within the real-space unit cell are encoded. For the case of a time-dependent displacement field  $\mathbf{u}_j(t)$  and electron/atom interaction times much shorter than the atomic vibration period [371; 329, Ch. 4.7], the atomic coordinates are given by  $\boldsymbol{\rho}_j(t) = \boldsymbol{\rho}_{j,0} + \mathbf{u}_j(t)$ . Following Ref. [372, Ch. 3.4], the diffraction intensity  $I(\Delta\mathbf{k}) = |F|^2$  is then obtained from

$$I(t) = \sum_i f_i e^{-i\Delta\mathbf{k}\cdot(\boldsymbol{\rho}_{i,0} + \mathbf{u}_i)} \sum_j f_j^* e^{i\Delta\mathbf{k}\cdot(\boldsymbol{\rho}_{j,0} + \mathbf{u}_j)}. \quad (5.35)$$

The experimentally recorded time-averaged intensity  $\langle I(t) \rangle$  for components  $u_{\Delta\mathbf{k},i}(t) = \Delta\mathbf{k} \cdot \mathbf{u}_i(t)$  along the scattering vector reads

$$\langle I(t) \rangle = \sum_{i,j} f_i f_j^* e^{-i\Delta\mathbf{k}\cdot(\boldsymbol{\rho}_{i,0} - \boldsymbol{\rho}_{j,0})} \langle e^{-i\Delta\mathbf{k}\cdot(u_{\Delta\mathbf{k},i} - u_{\Delta\mathbf{k},j})} \rangle. \quad (5.36)$$

In case of small atomic displacements in harmonic approximation, the average in Eq. 5.36 can be expanded to second order [372, Ch. 3.4], yielding

$$\langle e^{i\Delta\mathbf{k}\cdot(u_{\Delta\mathbf{k},i} - u_{\Delta\mathbf{k},j})} \rangle \approx e^{-\frac{1}{2}\Delta k^2 \langle (u_{\Delta\mathbf{k},i} - u_{\Delta\mathbf{k},j})^2 \rangle} = e^{-\frac{1}{2}\Delta k^2 \langle u_{\Delta\mathbf{k},i}^2 \rangle} e^{-\frac{1}{2}\Delta k^2 \langle u_{\Delta\mathbf{k},j}^2 \rangle} e^{\Delta k^2 \langle u_{\Delta\mathbf{k},i} u_{\Delta\mathbf{k},j} \rangle}. \quad (5.37)$$

Using this expression and assuming identical scatterers  $f_i = f_j = f$ , Eq. 5.36 splits into

a term corresponding to the usual Bragg diffraction and a term expressing populated phonon modes:

$$\langle I(t) \rangle = f^2 e^{-2M} \sum_{i,j} e^{-i\Delta k \cdot (\rho_{i,0} - \rho_{j,0})} + f^2 e^{-2M} \sum_{i,j} e^{-i\Delta k \cdot (\rho_{i,0} - \rho_{j,0})} \left[ e^{\Delta k^2 \langle u_{\Delta k, i} u_{\Delta k, j} \rangle} - 1 \right]. \quad (5.38)$$

The abbreviation  $e^{-\Delta k^2 \langle u_{\Delta k}^2 \rangle} = e^{-2M}$  is the Debye-Waller factor DWF that reduces the Bragg diffraction intensity of an ideal static crystal without changing the width of the Bragg peak (Bragg line for CBED). The Debye-Waller factor is often rewritten using the Debye parameter  $M = B(T) s^2 = B(T) \left( \frac{\sin(\theta)}{\lambda} \right)^2$ , where  $B$  is defined by  $B = 8\pi^2 \langle u^2 \rangle$  [329, Ch. 4.7; 341].

#### 5.4.1 Debye-Waller factor in the Debye model

In ultrafast diffraction experiments, the DWF is typically calculated to analyze the optically induced temperature rise of the sample. To this end, the mean-square displacement  $\langle u^2 \rangle$  is expressed as a function of temperature  $T$  via the energy of the thermalized phonon distribution. Based on the quantum-mechanical description of harmonic oscillators, the mean total energy of phonons with phonon frequency  $\omega$  is related to the energy  $E(\omega, T) = [n(\omega, T) + 1/2] \hbar\omega$ , in which  $n(\omega, T) = 1/[\exp(\hbar\omega/k_B T) - 1]$  is the Boltzmann distribution [373, Ch. 2.4]. In the Debye model of thermal vibration, the mean-square displacement  $\langle u^2 \rangle$  becomes

$$\langle u^2 \rangle = \int_0^{\omega_D} \frac{E(\omega, T)}{m\omega^2} g(\omega) d\omega, \quad (5.39)$$

where  $g(\omega) = \frac{3\omega^2}{\omega_D^3}$  is the Debye density of states for three phonon branches [373, Ch. 2.4; 291]. The Debye frequency  $\omega_D$  is defined via the Debye temperature  $\Theta_D$  by  $\hbar\omega_D = k_B \Theta_D$  [344, Ch. 23]. Evaluating Eq. 5.39 with substitution  $z = \frac{\hbar\omega}{k_B T}$  finally yields [373, Ch. 2.9; 329, Ch. 4.7]

$$\langle u^2 \rangle = \frac{3\hbar^2}{mk_B \Theta_D} \left[ \frac{1}{4} + \frac{T^2}{\Theta_D^2} \int_0^{\Theta_D/T} \frac{1}{e^z - 1} z dz \right]. \quad (5.40)$$

The first temperature-independent term arises from the zero-point motion. For temperatures  $T \gg \Theta_D$ , the exponential in the integrand can be expanded in powers of  $z$  resulting

in the high-temperature approximation for the DWF [373, Ch. 2.9]

$$2M \rightarrow \frac{3\hbar^2 G^2 T}{mk_B \Theta_D}. \quad (5.41)$$

The suppressed diffraction intensity therefore scales linearly with temperature  $T$  and is strongly affected by reciprocal lattice vectors  $\mathbf{G}$  with large Miller indices. For thermalized phonon distributions, the relative intensity decrease at temperatures  $T_0$  and  $T_0 + \Delta T$  is  $I(T_0 + \Delta T)/I(T_0) = \exp[2(M(T_0) - M(T))]$ . It shall be noted, that the Debye temperature related to vibrational amplitudes is not necessarily equal to the Debye temperatures determined from specific-heat measurements [374; 372, Ch. 11.10]. While the differences are generally negligible, large deviations are in particular observed for germanium and silicon [374]. Also, different Debye temperatures for anisotropic crystals may be associated with in- and out-of-plane vibrations for example in graphite [155, 372, 375].

#### 5.4.2 Thermal diffuse scattering

The second term in Eq. 5.38 is associated with first-order thermal diffusive scattering (TDS) arising from correlated atomic motion [329, Ch. 13.2]. An approach for the atomic displacement  $\mathbf{u}$  is given by the superposition of all acoustic eigenmodes

$$\mathbf{u}(t) = \sum_{\mathbf{k},j} a_{\mathbf{k},j} \mathbf{e}_j \cos[\omega_j(\mathbf{k})t - \mathbf{k} \cdot \boldsymbol{\rho}_n + \phi_j(\mathbf{k})]. \quad (5.42)$$

$a_{\mathbf{k},j}$  is the vibrational amplitude of a phonon with polarization  $\mathbf{e}_j$ ,  $\omega_j(\mathbf{k})$  is the phonon dispersion relation, and  $\phi(\mathbf{k})$  is the initial phase. For the average  $\langle u_{\mathbf{k},n} u_{\mathbf{k},m} \rangle$ , we obtain the sum of contributions from all different lattice modes:

$$\langle u_{\mathbf{k},n} u_{\mathbf{k},m} \rangle = \frac{1}{2} \sum_{\mathbf{k},j} \langle a_{\mathbf{k},j}^2 \rangle (\Delta \mathbf{k} \cdot \mathbf{e}_j)^2 \cos(\mathbf{k} \cdot (\boldsymbol{\rho}_n - \boldsymbol{\rho}_m)). \quad (5.43)$$

Inserting this result into the second term in Eq. 5.38, the first-order thermal diffuse scattering contribution becomes

$$I_1 = \frac{f^2 N^2}{4} e^{-2M} \sum_{\mathbf{k},j} \langle a_{\mathbf{k},j}^2 \rangle (\Delta \mathbf{k} \cdot \mathbf{e}_j)^2 [\delta(\Delta \mathbf{k} + \mathbf{k} - \mathbf{G}) + \delta(\Delta \mathbf{k} - \mathbf{k} - \mathbf{G})]. \quad (5.44)$$

The amplitude squared for each wave  $\mathbf{k}, j$  is written as  $\langle a_{\mathbf{k},j}^2 \rangle$ , since thermal fluctuations are completely random so that only an average square can be discussed. Expressing

the amplitude in terms of quantum-mechanical phonon energy determined by the mode-specific Bose-Einstein population, we arrive at the large-temperature approximation [372, Ch. 11.4]

$$\langle a_{\mathbf{k},j}^2 \rangle = \frac{2kT}{Nm\omega_{\mathbf{k},j}^2}. \quad (5.45)$$

Besides an overall increase in the background scattered intensity due to the broad phonon spectrum, the delta-functions particularly give rise to satellite peaks at positions  $\mathbf{k} \pm \mathbf{G}$  around the reciprocal lattice points with major TDS intensity contributions from low-frequency modes. Since the mean-square amplitude directly depends on the phonon frequency  $\omega(\mathbf{k})$ , TDS is employed to investigate phonon band structures [376]. Furthermore, diffuse background analysis of individual phonon modes in time-dependent diffraction patterns has recently revealed electron-phonon and phonon-phonon couplings with energy relaxation times in the few-picosecond regime [377–380].

## 5.5 Structural dynamics studied by UTEM

Investigations of structural properties have a long tradition in the field of conventional TEM. By combining the versatile nanoscale imaging capabilities of TEM with the temporal resolution of ultrafast spectroscopy, ultrafast TEM (UTEM) has proven a valuable tool to study structural dynamics [42, 72, 119, 120, 381–384] on a broad spatial range from sub-nanometer to micrometer length- and with 100-femtosecond to microsecond time-scales. The purpose of this section is to provide a brief overview of some key experiments investigating ultrafast structural dynamics using UTEM.

A field of applications ideally suited for UTEM is the study of elastic deformations of nanoscale structures in response to optical excitation. Since typical acoustic sound velocities in condensed matter are on the order of 1 to 10 nm/ps, the spatio-temporal dynamics are well captured by ultrafast TEM. Nanoscale and microscale cantilevers, for example, exhibit resonances in the low megahertz range, which are directly visible in real space as longitudinal and transverse displacements from the at-rest position [385]. For single-crystalline stripes completely lying on top of an amorphous membrane, the observed motions are different: Due to the interaction with the substrate, top and bottom surfaces exhibit spatio-temporal dynamics that are governed by frictional forces. These forces result in static steady-sliding as well as periodic slip-stick motions [385].

A typical contrast enhancement technique in the real-space imaging of structural

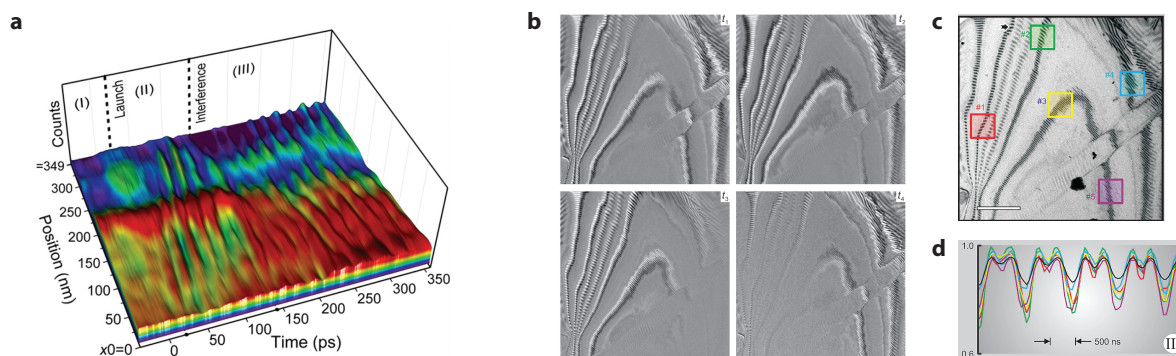


**Figure 5.7:** Bright-field imaging of strain waves in UTEM. **(a)** The surface contour plot shows the launching, propagation and interference of acoustic wave-trains in a MoS<sub>2</sub> membrane. Reprinted with permission from Ref. [386]. Copyright 2017 American Chemical Society. **(b)** Difference images of structural dynamics in a 75-nm thick graphite membrane for four different delay times with respect to a reference image recorded before optical excitation. **(c)** From the marked regions in the bright-field image of graphite (scale bar 1 μm), image contrast cross-correlation values are retrieved. **(d)** Cross-correlation for one representative time regime around 70 μs, for which a drumming mode at a resonance frequency of about 1 MHz can be observed. Figure panels b–d reprinted with permission from Ref. [100]. Copyright 2008 by American Chemical Society.

dynamics uses a SAED aperture (see Fig. 2.2) to select the undeflected electron beam or individual diffraction spots in the back focal plane of the objective lens. In the corresponding bright-field (BF) or dark-field (DF) images, contrast arises from local deviations from the Bragg condition or thickness variations within the sample [329]. Careful analysis of the complimentary imaging methods, acoustic phonon modes have been observed in graphite [100], as well as in TMDC thin-film samples [383, 386–388] (see e.g. Fig. 5.7). Spatial frequency maps obtained with this approach demonstrate the impact of structural defects on propagating wave fronts.

Due to the anisotropic bonding in TMDC materials, different lattice distortions have been observed along the *ab* crystallographic plane and along the out-of-plane *c*-direction, i.e. the layer-stacking direction [383, 389]. A layered material that additionally shows a strong in-plane anisotropic structure is black phosphorous. Following optical excitation of free-standing membranes of this material, DF images corresponding to zigzag and armchair directions therefore encode different structural dynamics. Aided by numerical simulations, the visualization of the nanosecond morphological dynamics reveals an anisotropic bulging which is driven by impulsive thermal stress, and anisotropic relaxations that also depend on the mechanical stiffnesses along specific axes [390].

Another prominent example of ultrafast imaging of structural dynamics is the time-resolved mapping of structural phase transitions. An ultrafast metal-insulator phase

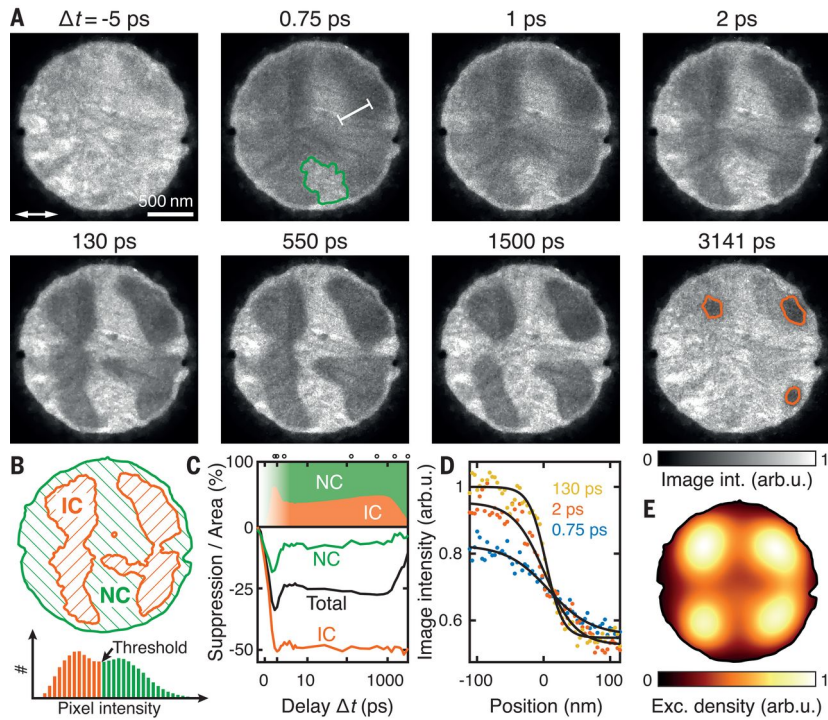


**Figure 5.8:** Ultrafast dark-field domain imaging of charge-density wave dynamics. (A) Ultrafast DF micrographs of transient domain configurations in the  $1T$ -TaS<sub>2</sub> film obtained in the laser pump-electron probe scheme ( $2.6\text{-mJ}/\text{cm}^2$  pump fluence, linear pump polarization indicated by white arrow). Pump-probe delay steps were chosen so as to capture all major stages of the dynamics [see black circles above (C)]. (B) (Top) Image segmentation at 130-ps delay time. (Bottom) The segmentation threshold is determined from the intensity histogram of the full image series within the circular aperture. (C) (Top) Area fractions of NC and IC regions after completed phase separation, as determined from the segmented images. (Bottom) Average intensity of the image series within the entire aperture (black curve), and average intensity in weakly and strongly pumped regions [green and orange curves, respectively; evaluated regions are indicated in (A) with corresponding colors]. (D) Exemplary profiles of NC/IC phase boundaries taken on the white line indicated in (A). (E) Spatial profile of the excitation density giving rise to the initial suppression pattern [see materials and methods available as supplementary materials and fig. S3]. Reprinted from Ref. [119] with permission from AAAS.

transition, for example, has been observed for polycrystalline VO<sub>2</sub> specimen, which change from a monoclinic room-temperature phase to the rutile high-temperature phase following optical excitation [381]. Couplings between structural and magnetic degrees of freedom have been demonstrated for organometallic nanoparticles. Based on diffraction patterns and corresponding DF images, a spin-crossover transition from a diamagnetic low-spin state to a paramagnetic high-spin state with associated unit cell deformations is followed for individual particles [382].

While the contrast enhancement by selecting intense diffraction order with an individual circular aperture certainly opened up novel experimental perspectives, the encountered

low-signal level in ultrafast DF images remains challenging. Recently, an array of small apertures tailored to filter the periodicities of a charge-density wave in  $1T$ -TaS<sub>2</sub> has been designed, delivering order parameter sensitivity in ultrafast nanoimaging of a structural phase transition [119]. As reported for the analysis of diffraction spot width in ULEED experiments, topological defects play a crucial role during the phase transition [74, 391]. In order to obtain diffraction from a sample region of sufficient homogeneity, the TEM capabilities to form a nearly collimated, but narrow electron beam can be harnessed. Combining sub-micrometer focus sizes with an electron beam tilt series, a three-dimensional hexatic phase ordering is found after optical excitation [120].

By further decreasing the electron probe size accompanied by large convergence angles, local deformations of the crystal unit cell can be tracked on nanometer length scales while providing access to multiple Bragg scattering conditions simultaneously (see section 5.1). Using this approach, the three-dimensional spatio-temporal reconstruction of the ultrafast lattice distortions triggered by optical pulses is achievable from Bragg line shifts as a function of temporal delay. Exemplary applications of the U-CBED method are presented in Chapter 7. In particular, the most recently reported experimental achievements in this field are presented as a central part of this thesis. The coherent response of a tailored source for acoustic breathing modes and local crystal rotations is demonstrated by locally probing the nanophononic wavefield with picosecond temporal resolution.

### **Ultrafast strain propagation and acoustic resonances in nanoscale bilayer systems**

---

In response to an optical excitation of a crystalline structure, a cascade of carrier and phonon relaxation processes occurs during which the lattice deforms thermoelastically and for example due to electronic and magnetic stress contributions [392]. A universal feature already extensively studied in a large variety of prototypical nanophonic systems is a homogeneous energy deposition in the depth of the sample, resulting in out-of-plane expansional breathing modes [43, 47, 95, 393–396]. As sound waves travel back and forth between free surfaces, the structure deforms in an oscillatory manner at discrete frequencies given by longitudinal sound velocities and thus determined by the material-specific elastic stiffness tensor and mass density (cf. section 4.1.6). However, for heterostructures consisting of several different material layers, this connection between material properties and acoustic resonances is significantly changed, leading to non-trivial temporal and spatial profiles of the strain dynamics.

In this chapter, we focus on an elastically mismatched metal/semiconductor bilayer system optically excited by femtosecond laser pulses in order to systematically advance toward an accurate, quantitative picture of UEM imaging of propagating acoustic-phonon dynamics. By performing discrete numerical linear chain simulations, we identify velocity ratios as one important parameter that causes the discrepancy from ultrafast strain dynamics in simple thin-film structures. A more ubiquitous analysis of the key dependencies of the acoustic phonon spectrum is based on an analytical phonon mode description within the field of continuum mechanics. In this general approach, a strong relation between the quantized phonon eigenmodes and the impedance ratio of both materials is revealed, which in limiting regimes can lead to wave localizations in individual layers. The following

article is therefore an important contribution to elucidate the complex coupling effects across bilayer interfaces and may form a profound theoretical basis for a large number of confined heterostructures studied in ultrafast electron or x-ray diffraction experiments.

The theoretical work of the second publication was conceived and directed by S. Schäfer. The analytical and numerical simulations were done by N. Bach in collaboration with S. Schäfer. N. Bach and S. Schäfer wrote the manuscript. Further non-author contributions are listed in the “Acknowledgments” section of Chapter 6.

N. Bach, S. Schäfer

*Structural Dynamics* **8**, 035101 (2021)

doi:10.1063/4.0000079

Ultrafast structural probing has greatly enhanced our understanding of the coupling of atomic motion to electronic and phononic degrees-of-freedom in quasi-bulk materials. In bi- and multilayer model systems, additionally, spatially inhomogeneous relaxation channels are accessible, often governed by pronounced interfacial couplings and local excitations in confined geometries. Here, we systematically explore the key dependencies of the low-frequency acoustic phonon spectrum in an elastically mismatched metal/semiconductor bilayer system optically excited by femtosecond laser pulses. We track the spatiotemporal strain wave propagation in the heterostructure employing a discrete numerical linear chain simulation and access acoustic wave reflections and interfacial couplings with a phonon mode description based on a continuum mechanics model. Due to the interplay of elastic properties and mass densities of the two materials, acoustic resonance frequencies of the heterostructure significantly differ from breathing modes in monolayer films. For large acoustic mismatch, the spatial localization of phonon eigenmodes is derived from analytical approximations and can be interpreted as harmonic oscillations in decoupled mechanical resonators.

## 6.1 Main text

Advanced technological applications ranging from heat management in nanoelectronics [252] to optomechanical resonators [254] are based on nanoscale systems with engineered thermal and acoustic interfaces [61, 244, 397, 398]. Nanostructures like gratings [276, 399, 400], semiconductor quantum wells [401] and superlattices [224, 402, 403] combined with sophisticated optical control strategies allow for achieving coherent phononic and photonic excitations, and tailored infrared optical near-fields [404, 405].

The complex microscopic mechanisms of pico- and femtosecond phononic processes are being uncovered by high-resolution optical spectroscopy and recently developed ultrafast methodologies. For example, phonon-phonon couplings, modified phonon dispersion relations, and dissipation times in nanoscale systems [243, 260, 406, 407] are accessible by all-optical technologies such as Brillouin scattering [260, 408, 409] and ultrafast pump-probe [95] and multidimensional [410, 411] spectroscopies. Experimental approaches explicitly capturing structural deformations within individual materials with high spatial resolution in reciprocal space include ultrafast electron [42–49, 157, 159, 412, 413] and x-ray diffraction [50–53, 414] techniques, extendable to time-resolved local diffractive probing using convergent electron beams [72, 105, 215]. Furthermore, real-space imaging of photoexcited localized vibrations, propagating strain waves, and structural phase transitions is provided by time-resolved scanning probe techniques [217, 221, 222] and ultrafast transmission electron microscopy (UTEM) [100, 119, 383, 386]. As prototypical nanophononic sample systems, ultrafast dynamics in bilayer films [54–56] and thin-films on semi-infinite substrates [57, 95, 415–419] were studied in detail, focussing on the influence of interfaces [54, 75, 420] and revealing unexpected interlayer electron-phonon interactions [58, 421, 422]. Ultrafast strain dynamics in these systems are typically modeled by numerical approaches including one-dimensional linear chain [33–36] and two-dimensional finite-element simulations [37, 38, 72]. Although complex strain dynamics are accurately recaptured in such approaches, analytical models offer an additional highly valuable and intuitive physical understanding [39–41], but were not systematically employed for analyzing the ultrafast structural response in nanoscale heterostructures.

Here, we apply an analytical acoustic mode description of ultrafast structural dynamics in a nanoscale bilayer system. Explicit expressions for the resonance frequencies are derived and compared to numerical results. The coupling of individual phononic modes in both layers is analyzed with respect to the acoustic mismatch and the emergence of

localized modes is demonstrated.

In order to arrive at a resonant acoustic mode description for bilayer films, we start off by considering a simple monolayer, as often investigated in ultrafast diffraction experiments [43, 47, 72, 229, 356, 395, 396, 414, 423]. In response to a homogeneous ultrashort laser excitation of such a sample, a transient stress gradient is induced in the depth of the film causing longitudinal strain waves to travel back and forth between the free surfaces. The resulting homogeneous compression and expansion of the film is often termed *breathing mode*. As an example, we depict in Fig. 6.1 b (top) the optically induced dynamics of a platinum thin film after excitation (see the supplementary material 6.2.1 for details). The resulting oscillatory change in film thickness occurs with a periodicity given by the strain pulse round trip time.

In an equivalent description, the traveling wave can be decomposed into a superposition  $\sum_n a_n u_n$  of resonant modes. For a simple thin film of thickness  $H$ , acoustic resonant modes with mode index  $n \in \mathbb{N}$  are given by  $u_n(z) = \cos(n\pi z/H)$  with mode frequencies  $f_n = nv/(2H)$ , in which  $v$  is the longitudinal sound velocity of the material. The base frequency  $f_1$  corresponds to the inverse round trip time of the strain wave. Mode amplitudes in the superposition depend on the effective time- and length-scale of the sample excitation. Specifically, for a homogenous excitation within the depth of the thin film and for a pump-induced stress with a rise time much larger than the considered resonance frequencies, one obtains  $-2\Delta H/(\pi^2 n^2)$  for the  $n$ th mode amplitude ( $n$  odd;  $\Delta H/H$ : average lattice strain after optical excitation), resulting in a saw-tooth-like temporal variation of the film strain.

In ultrafast diffraction experiments, the temporal evolution of the average strain along the probing direction is encoded in a periodic change of reciprocal lattice vectors leading to an angular displacement of the center-of-mass of Bragg scattering conditions. Only uneven higher harmonics of the fundamental breathing mode frequency are contributing to the average angular shift. Modes with even  $n$  result in zero average strain and therefore no shift in the average scattering condition. The superposition of all modes yields the strain distribution within the film and is thereby encoded in the profile of the Bragg spot (or Bragg line, for convergent beam electron diffraction). As an example, the modulation of the Bragg line width in laser-excited thin films was found to occur at twice the frequency of the breathing mode [72].

Although the modes in a monolayer material are directly obtained, in a two layer system, acoustic boundary conditions at the interface play a major role and require a

**Table 6.1:** Material properties of the Pt/Si-bilayer employed for the numerical and analytical simulations (see Refs. [284, 429]).

	$m$ (u)	$a$ (Å)	$\rho$ (kg/m <sup>3</sup> )	$v$ (m/s)	$Z$ (MPa·s/m)	$d$ (nm)
Silicon	28	5.43	2329	8433	19.4	35
Platinum	195	3.92	21450	3829	82.1	10

more detailed analysis. As an example, we numerically simulate the strain dynamics in a 10-nm thin polycrystalline platinum layer on top of a 35-nm thin single-crystalline silicon membrane ([001]-orientation along the  $z$ -direction) using a one-dimensional linear-chain model (detailed in supplementary material 6.2.1; for material parameters, see Tab. 6.1). In our model, we consider a homogeneous excitation of the top layer by an ultrashort optical pulse (see Fig. 6.1a) and assume an optically induced thermal stress due to locally equilibrated electron and lattice systems. More general cases could be included by additional transient stress contributions [392], such as thermoelastic electron-phonon coupling driven by hot carriers [416, 424–426], the deformation potential mechanism [95, 417], coupling between strain and macroscopic electric fields in non-centro symmetric materials [401, 427], and electrostriction in transparent solids [428].

Within the theoretical model, the obtained temporal evolution of the film thickness and interface positions after optical excitation is shown in Fig. 6.1b (bottom panel, displacements are amplified for better visibility). Although only platinum is optically excited, it is apparent that multifrequency strain dynamics are induced in both layers due to interlayer strain coupling, in contrast to the single platinum layer exhibiting only a breathing mode with a single frequency (with additional higher order harmonic contributions, Fig. 6.1b (top)). For a more detailed analysis of the strain dynamics, we extract the spatiotemporal structure of the strain field within the film, shown as a color-coded map in Fig. 6.1c. Following the optical excitation at  $t = 0$ , the metal layer expands and a positive strain builds up, leading, in turn, to a compression of the adjacent silicon membrane. Transmitted and reflected acoustic waves at the interfaces couple with the lattice dynamics in both layers.

Depending on the experimental geometry, ultrafast electron or x-ray diffraction experiments are sensitive to different components of the strain tensor and typically involve spatial averaging along the probing axis. In particular, for low-coherence probe beams, often only the mean strain of each layer is experimentally accessible. For the case of the

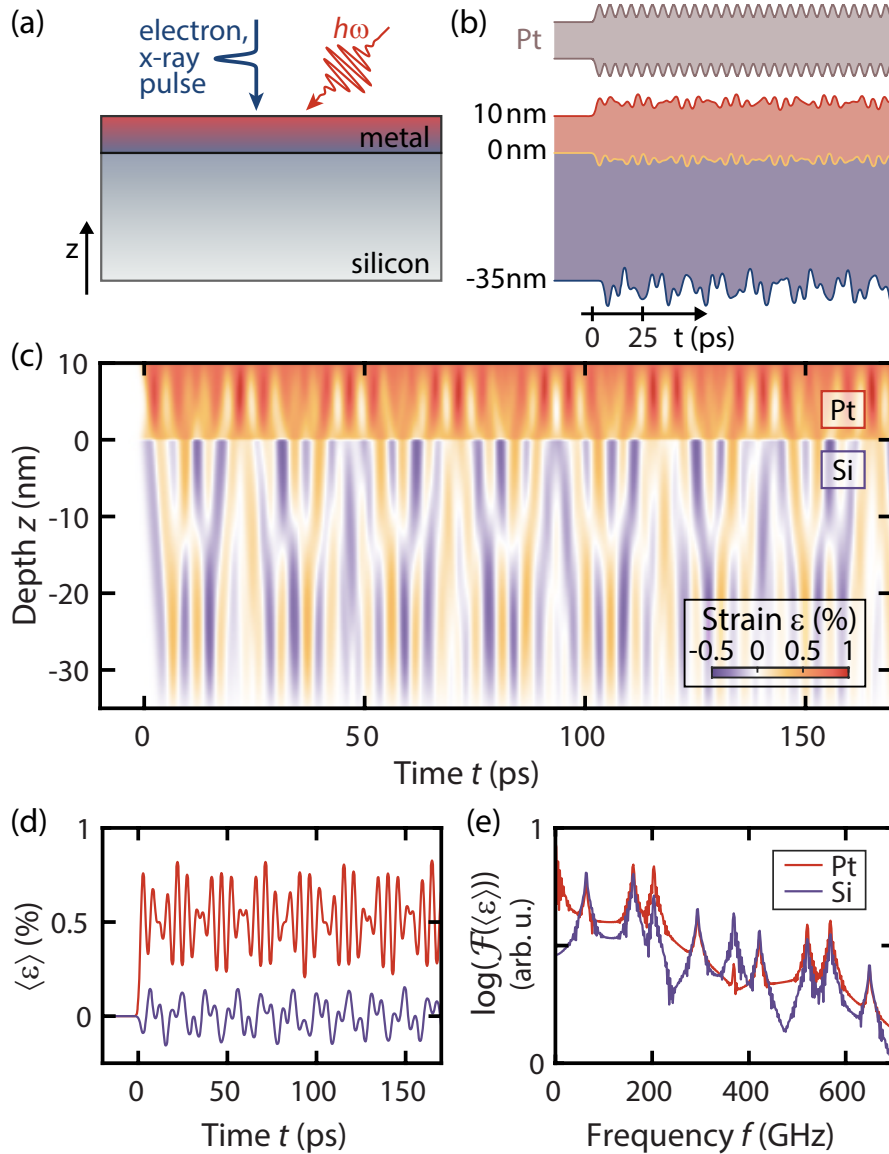


**Figure 6.1:** Strain dynamics in a nanoscale Pt/Si-bilayer film numerically simulated by a discrete one-dimensional linear chain model. (a) A bilayer membrane is optically excited by femtosecond laser pulses inducing a rapid lattice temperature increase and launching strain waves in both materials while silicon remains at room temperature. Structural dynamics are typically probed by ultrafast diffraction experiments harnessing the high spatial resolution in reciprocal space. (b) Temporal evolution of the surface and interface positions (displacements are amplified by a factor of 110 for better visibility) in single-layer platinum and the Pt/Si-bilayer. (c) Spatiotemporal strain map of structural dynamics induced by optical excitation at  $t = 0$ . (d) Mean strain  $\langle \epsilon \rangle$  in Pt (red) and Si (violet) obtained by spatially averaging the strain maps in panel (c). (e) Acoustic resonance frequencies obtained from Fourier transform of the temporal evolution of the mean strain shown in panel (d).

bilayer sample considered here, the evolution of the mean strain in both layers is shown in Fig. 6.1d. Heating of the platinum top layer leads to multifrequency oscillations around

an equilibrium positive strain of about 0.5%. The non-heated silicon is compressed by the adjacent expanding platinum layer and oscillates at smaller amplitudes around zero mean strain. Further insights into the temporal strain dynamics are obtained from a Fourier transform of the mean strain yielding layer-specific multiple resonance frequencies in the GHz-regime (Fig. 6.1e), with the most prominent peaks for the present case at  $f = 63.0$  GHz, 161.1 GHz, and 203.7 GHz. Curiously, none of these frequencies match acoustic round trip times,  $2l_{\text{Si}}/v_{\text{Si}} = 8.3$  ps (120.5 GHz) and  $2l_{\text{Pt}}/v_{\text{Pt}} = 5.2$  ps (192.3 GHz), for which  $l_{\text{Si(Pt)}}$  is the layer thickness and  $v_{\text{Si(Pt)}}$  the sound velocity for wave propagation in the  $z$ -direction.

To demonstrate that the origin of this apparent discrepancy is linked to the coupling of acoustic modes in both layers, we performed numerical strain dynamics simulations for metal layers with different sound velocities but a fixed mass density. The obtained frequency spectra of the mean strain, depending on the velocity ratio  $r_v = v_m/v_{\text{Si}}$ , are shown in Figs. 6.2a and 6.2b for the metal and silicon layer, respectively. For large velocity ratios and a fixed sound velocity of silicon, high-frequency modes are observed at frequencies related to the reciprocal round trip time in the silicon bottom layer (for details, see below). In contrast, resonance frequencies scale linearly with  $v_m$  in the limit of small velocity ratios. In the intermediate regime, strong couplings between both layers are apparent, showing avoided crossings of resonance frequency branches and a complex pattern of changes in the resonance amplitudes.

In the following, an analytical description is presented allowing for a more general discussion of strain propagation in coupled bilayer systems. For strongly mismatched bulk material properties, approximate solutions are found yielding insights into the origin of coupling mechanisms between adjacent layers. The acoustic wave field in the two quasi-isotropic elastic media, platinum and silicon, is described as a linear combination of back and forth propagating plane waves along the  $z$ -direction (see Tab. 6.1 for material properties and Fig. 6.1a for the coordinate system of the two-dimensional cross section). The relative wave amplitudes are determined by the acoustic boundary conditions at the interfaces between the materials and at the free surfaces, mathematically accumulated in a so-called global matrix  $D(\omega)$  (see the supplementary material 6.2.2 for details). Allowed acoustic mode frequencies  $\omega_n$  are obtained as the  $n$ th order root of the resulting characteristic function,  $\det [D(\omega)] = \sin\left(\omega \frac{H_{\text{Si}}}{v_{\text{Si}}}\right) \cos\left(\omega \frac{H_m}{v_m}\right) - \frac{Z_m}{Z_{\text{Si}}} \cos\left(\omega \frac{H_{\text{Si}}}{v_{\text{Si}}}\right) \sin\left(\omega \frac{H_m}{v_m}\right) \stackrel{!}{=} 0$ , in which  $H_{\text{Si}}$  and  $H_m$  are the positions of the silicon/vacuum and metal/vacuum interfaces. The impedances  $Z_{\text{Si,m}}$  are given by  $\rho_{\text{Si,m}}v_{\text{Si,m}}$ . The lowest-order roots  $f^{(n)} = \omega^{(n)}/(2\pi)$

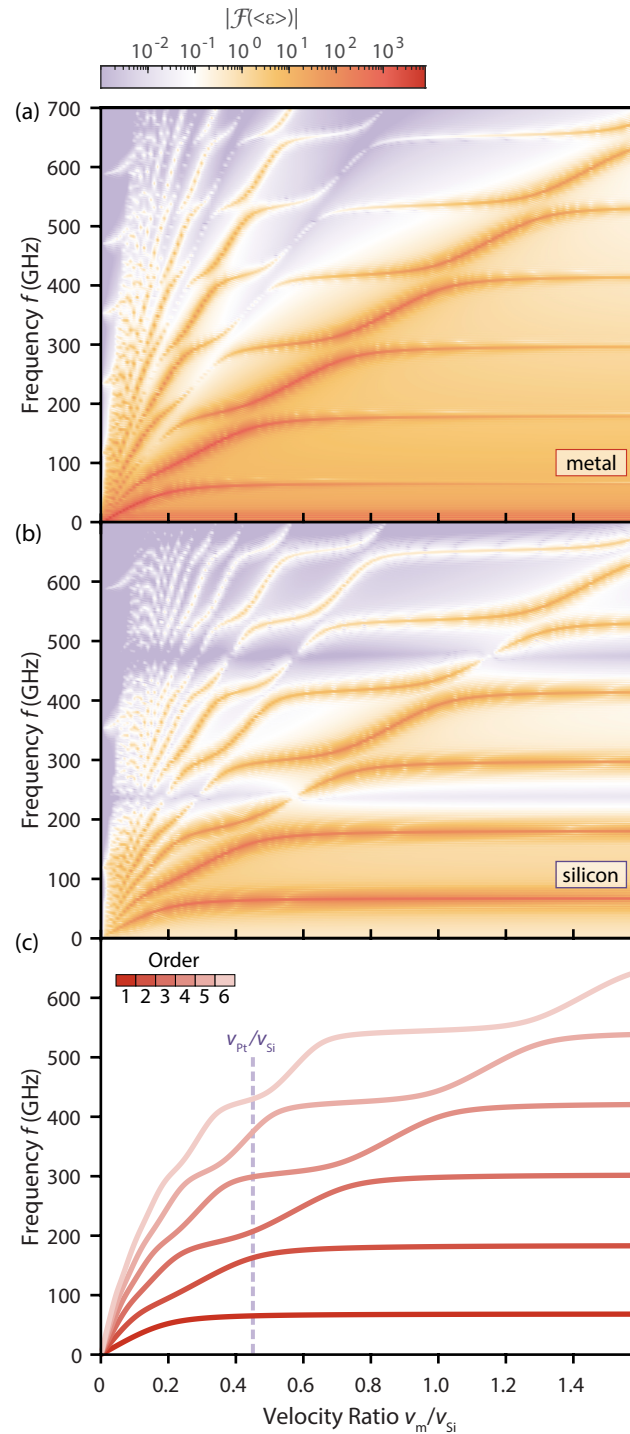


**Figure 6.2:** Acoustic resonance frequencies in a metal/silicon bilayer. (a) and (b) Fourier transform of the temporal evolution of the mean strain in the metal and silicon layers evaluated for different ratios of the sound velocities,  $r_v = v_m/v_{Si}$ . In the limits of small and large ratios, a linear scaling of the resonance frequencies or an equidistant ladder spectrum is observed, respectively. (c) Resonance frequencies derived from the roots of the characteristic function 6.1, in quantitative agreement with the peak locations of the Fourier spectra in panels (a) and (b).

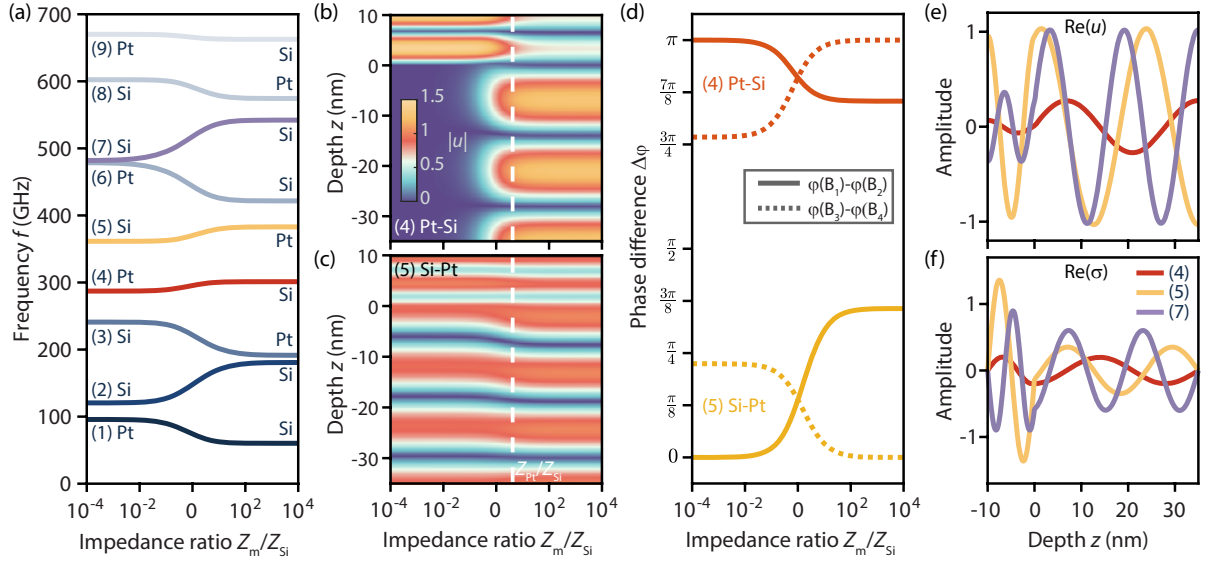


**Figure 6.3:** Acoustic mode profile and wave localization. (a)  $n$ th-order resonance frequencies depending on the impedance ratio  $r_Z = Z_m/Z_{Si}$  of the two materials. (b) and (c) Absolute value of the displacement field,  $|u|$ , for branches (5) and (4), respectively. (d) Phase difference of the amplitude coefficients within each layer separately, depending on the impedance ratio  $r_Z$  shown for branches (4) and (5) in red and yellow, respectively. (e) and (f) Instantaneous displacement  $u$  (e) and stress  $\sigma$  (f) for Pt/Si system with  $r_Z = 4.2$  as indicated by the white dashed line in (b) and (c). (d)-(f): Line colors are chosen consistently with (a).

for varying velocity ratios  $r_v$  are plotted in Fig. 6.2c for  $n \in 1, \dots, 6$ , reproducing the resonance branch structure retrieved from the linear-chain model.

The resonance frequencies in the limit of large ratios ( $v_m/v_{Si} \rightarrow \infty$ ) are understood by a first-order Taylor expansion of the characteristic function, yielding  $\tan\left(\omega \frac{H_{Si}}{v_{Si}}\right) = \frac{\rho_m}{\rho_{Si}} \frac{H_m}{v_{Si}} \omega$ . In this limit and for large frequencies  $\omega$ , solutions asymptotically approach the poles of the tangent functions located at  $f^{(n)} = (n - \frac{1}{2}) \frac{1}{T_{Si}}$  with  $T_{Si} = \frac{2H_{Si}}{v_{Si}}$ . The frequency branches of low mode order, particularly the first root of the characteristic function, significantly deviate from the frequency expected from the round trip time in silicon. Similarly for small velocity ratios ( $v_m/v_{Si} \rightarrow 0$ ),  $f^{(n)} = (n - \frac{1}{2}) \frac{v_m}{2H_m}$  is obtained.

A change in  $r_v$  results in both a varying round trip time and a change in the mode coupling. To disentangle both contributions, we consider in the following a density variation in the metal layer, keeping its sound velocity constant. Thereby, the round trip time in the metal layer is constant but the relative acoustic impedance  $r_Z$  of both layers changes. The resulting roots  $f^{(n)}(r_Z)$  of the characteristic function are plotted in Fig. 6.3a. For impedance matched layers, i.e.,  $\log(Z_m/Z_{Si}) = 0$ , the acoustic wave propagates without reflection at the interface yielding equal wave amplitudes in both layers.

In this case, the characteristic function simplifies to  $\sin\left[\left(\frac{|H_{\text{Si}}|}{v_{\text{Si}}} + \frac{H_{\text{m}}}{v_{\text{m}}}\right)\omega\right] = 0$ , resulting in resonance frequencies  $f^{(n)} = \frac{n}{T_{\text{m}}+T_{\text{Si}}}$  with  $n \in \mathbb{N}$ . In the limiting cases of small and large impedance ratios, the roots of the characteristic function can be also analytically obtained (see supplementary material 6.2.2 for corresponding Taylor expansions). Specifically, for  $r_Z \rightarrow 0$ , the resonance frequencies are given by  $nT_{\text{Si}}$  and  $(n - \frac{1}{2})T_{\text{m}}$ , so that the frequency spectrum is formed by two equidistant ladder spectra, indicated as (n)-Si and (n)-Pt in Fig. 6.3a, with different frequency spacing. In the opposite case of  $r_Z \rightarrow \infty$ , a similar spectral structure is obtained but with the roles of the respective layers interchanged.

Solving for the wave amplitudes at a given resonance frequency  $f^{(n)}(r_Z)$  (see the supplementary material 6.2.2) yields the corresponding displacement field, with the absolute wave amplitude shown in Figs. 6.3b and 6.3c for the resonance branches (4)-Pt-Si and (5)-Si-Pt. Both branches exhibit remarkably different spatial distributions of the wave amplitude. For the case shown in (c), atomic displacements of comparable amplitudes are observed in both layers for all impedance ratios. In contrast, for (4)-Pt-Si (Fig. 6.3b), the acoustic wave is localized in the upper material for small impedance ratios, shifting to the silicon layer with increasing impedance ratios.

The differences in the exemplary wave structures are caused by the acoustic boundary conditions [see Eq. (6.6) in the supplementary material] at the interface ( $z = 0$ ), which result in a relation between the impedance ratio and the strain in both materials:  $r_Z = \frac{Z_{\text{m}}}{Z_{\text{Si}}} = \frac{v_{\text{Si}} \epsilon_{zz}^{\text{Si}}}{v_{\text{m}} \epsilon_{zz}^{\text{m}}}$ . Specifically, the strain  $\epsilon_{zz}^{\text{Si}}$  ( $\epsilon_{zz}^{\text{m}}$ ) at the interface vanishes for  $Z_{\text{m}} \rightarrow 0$  ( $Z_{\text{m}} \rightarrow \infty$ ) at constant acoustic sound velocity ratios. For resonance frequencies governed by the material layer with a lower acoustic impedance, a sinusoidal standing wave with zero displacement at the layer interface and a displacement maximum at the open boundary is formed (as expected from the expression for the wave round trip times). For  $r_Z \rightarrow 0$  and  $r_Z \rightarrow \infty$ , this effect leads to wave localizations in the metal layer and the silicon layer, respectively, as shown for branch (4) in Fig. 6.3b. Similarly, wave localization is observed for all other (n)-Pt-Si branches (e.g.,  $n = 1$ ; see Fig. 6.5b in supplementary material). In contrast, for (n)-Si-Pt branches (e.g. for  $n = 5$ , shown in Fig. 6.3c) cosine-like standing waves are formed in silicon (metal) for  $r_Z \rightarrow 0$  ( $r_Z \rightarrow \infty$ ). As a consequence of the (partial) wave transmission into the other layer, no distinct localization of the acoustic wave is observed.

The sinus- and cosine-like standing waves in the bilayer (in the limits of small/large  $r_Z$ ) become also evident from the phase difference of the forward and backward propagating wave components. As shown in Fig. 6.3d, the sinusoidal behavior of (4) Pt-Si is apparent

in the phase difference  $\Delta\varphi = \pi$  between the wave components in one of the layers. In contrast,  $\Delta\varphi = 0$  is observed for (5)-Si-Pt, as expected for a cosine-like standing wave field. Finally, equal phase angles occur in both layers in the impedance-matched case ( $\log(r_Z) = 0$ ). For the specific case of the experimental Pt-Si-bilayer system (impedance mismatch  $r_Z = 4.2$ ), the instantaneous acoustic displacement and stress field at a chosen time  $t$  for selected resonance frequencies are shown in Figs. 6.3e and 6.3f, respectively.

With the analytical acoustic mode description in mind, we now come back to the discussion of individual features apparent in the frequency maps shown in Fig. 6.2a and 6.2b. First, the regions of vanishing mean strain (inclined/horizontal line-like features in Figs. 6.2a and 6.2b, respectively), occur if integer multiples of the acoustic wavelength match the layer thickness. As shown in Fig. 6.2b, such decreased mean strain amplitudes are found in the silicon layer for frequencies  $f_{\text{Si}} = n \cdot \frac{v_{\text{Si}}}{H_{\text{Si}}} = n \cdot \frac{8433 \text{ m/s}}{35 \text{ nm}} = n \cdot 240.9 \text{ GHz}$ ,  $n \in \mathbb{N}$  being independent of the metal sound velocity and therefore visible as violet shaded horizontal lines. For the metal layer (see Fig. 6.2a), the mean strain vanishes along diagonals with slopes proportional to the varied metal sound velocity.

Finally, the overall structure of the frequency maps can be understood by considering the resonances of the individual decoupled layers, corresponding to the horizontal and inclined lines in Figs. 6.2a and 6.2b. Coupling of the resonances results in the appearance of avoided crossings, associated with a change in the resonance slope and in the character of the resonant mode structure. Such a behavior is strongly reminiscent of the coupling of diabatic quantum states and additionally has a close analogy to the resonance structure of an optical bilayer Fabry-Pérot interferometer (see the supplementary material 6.2.4).

For macroscopic acoustic resonators, a resonant mode picture is well established. In the case of localized nanoscale acoustic fields, a series of questions arises, for example, regarding the validity of continuum-theory boundary conditions at small length scales, the importance of the material interface for acoustic and electronic coupling or the impact of nanocrystallinity. The mode analysis presented here may serve as a reference model to gauge potential deviations arising from the nanoscale dimensions involved.

In conclusion, we determined the acoustic response of a nanoscale metal/semiconductor bilayer system upon femtosecond optical excitation, calculating the strain dynamics from linear-chain simulations and describing the acoustic field in terms of superimposed counter-propagating harmonic waves perpendicular to the sample surface. In the confined heterostructure and due to elastic boundary conditions, quantized phonon eigenmodes

arise with frequencies in the gigahertz range, exhibiting strong couplings across the bilayer interface.

### **Supplementary Material**

See the supplementary material for further details on numerical and analytical models discussed in the main text.

### **Acknowledgements**

We acknowledge financial support by the Volkswagen Foundation as part of the Lichtenberg Professorship "Ultrafast nanoscale dynamics probed by time-resolved electron imaging" and the Collaborative Research Center Atomic Scale Control of Energy Conversion (No. DFG-SFB 1073, project A05). N.B. acknowledges a scholarship by the German Academic Scholarship Foundation. The authors thank Claus Ropers for helpful discussion.

### **Data Availability**

The data that support the findings of this study are available from the corresponding author upon reasonable request.

## 6.2 Supplementary material

### 6.2.1 Atomic displacement dynamics in a linear chain model

Focussing only on longitudinal acoustic waves propagating perpendicular to the surface of the Pt/Si-system allows to consider a simple one-dimensional linear chain of  $N$  Pt- and Si-masses linked by springs with force constant  $K_i = m_i(v_i/a_i)^2$ , where  $v_i$  is the longitudinal sound velocity,  $m_i$  is the atomic mass and  $a_i$  is the lattice constant [284] with  $i = 1$  (Si) and  $i = 2$  (Pt) (see Fig. 6.4a for schematic of the linear-chain). For single-crystalline silicon, the longitudinal sound velocity is calculated from  $v = \sqrt{C_{11}/\rho}$ , where  $C_{11} = 165.64$  GPa is the elastic constant in [001]-direction [284, 430] and  $\rho$  is the volumetric mass density. For the platinum layer, we consider a polycrystalline film with an isotropic sound velocity [279, 284]  $v = \sqrt{(\lambda + 2\mu)/\rho}$  given by Lamé constants  $\lambda = 192.8$  GPa and  $\mu = 60.9$  GPa (for material constants inserted in the linear chain model see Table 6.1). For the results shown in Fig. 6.2 in the main text, the sound velocity of the metal layer is varied at a fixed mass density. At the material interface, the two adjacent atoms of platinum and silicon are connected by a spring with  $K_2$ . For the chosen layer thicknesses of 35 nm and 10 nm and given the respective lattice constants  $a_1 = 5.43$  Å and  $a_2 = 3.92$  Å [429], the chain is set up taking  $N_1 = 66$  and  $N_2 = 26$  Si- and Pt-masses. For simplicity, the optical excitation of the metal layer is modeled by assuming an exponential temperature profile within the layer according to the platinum absorption coefficient  $\alpha_c = 7.8 \cdot 10^7/\text{m}$  at 800 nm-optical wavelength [431]. Temporally, the temperature increase follows an error function behavior with a rise time of 1 ps. For the peak temperature increase, we consider  $\Delta T = 857$  K (initial temperature  $T_0 = 293$  K). For the simulation discussed in the main text, the silicon layer is chosen to remain at  $T_0$ . The resulting thermal stress in platinum is implemented by adapting the equilibrium length of the corresponding springs according to the platinum thermal expansion coefficient of  $\alpha_{\text{th}} = 8.8 \cdot 10^{-6}$  1/K [429]. The induced atomic displacement dynamics are calculated employing a Verlet algorithm with 20-fs time-steps. Frequency components of the layer specific mean strain are obtained by numerical Fourier transformation applying a super-gaussian window (window width about 270 ps centered at 150 ps). For the numerical description of acoustic strain dynamics in a single platinum layer (shown in Fig. 6.1b in the main text), an equivalent model is applied.

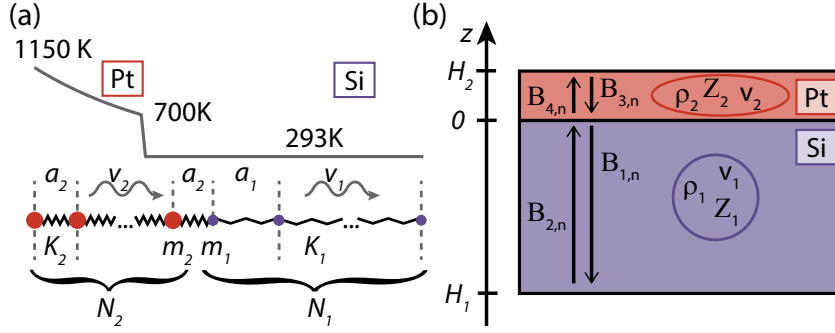


**Figure 6.4:** Schematic drawing of bilayer system in the one-dimensional linear-chain model (a) and as an acoustic resonator described by continuum elasticity theory (b).

## 6.2.2 Analytical model for the description of resonant strain modes

For the description of the acoustic modes in an elastic bilayer system, we implement a global matrix formalism [285, 305, 311, 432], originally developed for the analysis of seismic waves [285]. In this continuum mechanical approach the acoustic modes at angular frequency  $\omega$  are expressed as a superposition of forward and backward propagating plane waves with material-specific wave vectors. Due to the transversely homogeneous acoustic excitation in the experiment and quasi-isotropic materials, only wave vectors in the  $z$ -direction (i.e. perpendicular to the layer surfaces) and with a longitudinal polarization are considered (i.e. plane strain configuration; see Fig. 6.4 for the definition of the coordinate system). The displacement field  $u_z$  in the elastic media is obtained as

$$\begin{aligned} u_z^{(1)} &= B_1 e^{ik_1(z-v_1t)} + B_2 e^{-ik_1(z+v_1t)} \\ u_z^{(2)} &= B_3 e^{ik_2(z-v_2t)} + B_4 e^{-ik_2(z+v_2t)}. \end{aligned} \quad (6.1)$$

$k_{1,2} = \omega/v_{1,2}$  is the wave number at a specific angular frequency  $\omega$ ,  $v_{1,2}$  is the material dependent acoustic (phase) velocity and  $B = (B_1, B_2, B_3, B_4)^T$  is the coefficient vector of the wave superposition. The relevant component of the stress tensor,  $\sigma_{zz}$ , is obtained from elasticity [279] theory using the acoustic wave equation (excluding body forces)

$$\rho \frac{\partial^2 u_z}{\partial t^2} = \frac{\partial \sigma_{zz}}{\partial z}. \quad (6.2)$$

Furthermore, for isotropic solids the stress-strain relation is given by

$$\sigma_{zz} = \lambda(\epsilon_{xx} + \epsilon_{yy} + \epsilon_{zz}) + 2\mu\epsilon_{zz} \quad (6.3)$$

with the Lamé constants  $\lambda$  and  $\mu$ , and the strain  $\epsilon$  is related to the displacement field via

$$\epsilon_{ij} = \frac{1}{2} \left( \frac{\partial u_i}{\partial x_j} + \frac{\partial u_j}{\partial x_i} \right) \quad (6.4)$$

for which  $i, j = (x, y, z)$ . For the present case, equation 6.3 can be further simplified, yielding

$$\begin{aligned} \sigma_{zz}^{(1)} &= (\lambda_1 + 2\mu_1) \frac{\partial u_z^{(1)}}{\partial z} \\ \sigma_{zz}^{(2)} &= (\lambda_2 + 2\mu_2) \frac{\partial u_z^{(2)}}{\partial z}. \end{aligned} \quad (6.5)$$

Considering traction free surfaces at the top and bottom of the bilayer, and perfect bonding conditions (i.e. continuity in displacement and stress) at the interface, the boundary conditions are as follows:

$$\begin{aligned} \sigma_{zz}^{(1)} &= 0 & \text{at } z = H_1 \\ \sigma_{zz}^{(2)} &= 0 & \text{at } z = H_2 \\ u_z^{(1)} &= u_z^{(2)} & \text{at } z = 0 \\ \sigma_{zz}^{(1)} &= \sigma_{zz}^{(2)} & \text{at } z = 0. \end{aligned} \quad (6.6)$$

Assembling the four boundary conditions and using equations 6.1 and 6.5, the coefficient vector  $B$  is required to fulfill the characteristic equation  $DB = 0$ , with

$$D(\omega) = \begin{pmatrix} e^{i\omega \frac{H_1}{v_1}} & -e^{-i\omega \frac{H_1}{v_1}} & 0 & 0 \\ 0 & 0 & e^{i\omega \frac{H_2}{v_2}} & -e^{-i\omega \frac{H_2}{v_2}} \\ 1 & 1 & -1 & -1 \\ \omega \frac{\lambda_1 + 2\mu_1}{v_1} & -\omega \frac{\lambda_1 + 2\mu_1}{v_1} & -\omega \frac{\lambda_2 + 2\mu_2}{v_2} & \omega \frac{\lambda_2 + 2\mu_2}{v_2} \end{pmatrix} \quad (6.7)$$

being the coefficient matrix. Nontrivial solutions of the coefficient vector  $B$  are obtained for frequencies for which  $\det [D(\omega)] = 0$ . At these frequencies, standing waves are formed in the acoustic cavity. The corresponding characteristic function follows as

$$\begin{aligned} \xi &= Z_1 \omega \left\{ \sin \left( \omega \left( \frac{H_1}{v_1} + \frac{H_2}{v_2} \right) \right) + \sin \left( \omega \left( \frac{H_1}{v_1} - \frac{H_2}{v_2} \right) \right) \right\} \\ &\quad + Z_2 \omega \left\{ \sin \left( \omega \left( \frac{H_1}{v_1} - \frac{H_2}{v_2} \right) \right) - \sin \left( \omega \left( \frac{H_1}{v_1} + \frac{H_2}{v_2} \right) \right) \right\} = 0. \end{aligned} \quad (6.8)$$

Here, the relations  $\lambda_i + 2\mu_i = \rho_i \cdot v_i^2$  and  $Z_i = \rho_i \cdot v_i$  between the Lamé constants, mass density  $\rho$  and acoustic impedance  $Z$  have been used. For  $\omega \neq 0$ , equation 6.8 can also be

formulated as

$$\sin\left(\omega \frac{H_1}{v_1}\right) \cos\left(\omega \frac{H_2}{v_2}\right) - \underbrace{\frac{Z_2}{Z_1}}_{r_Z} \cos\left(\omega \frac{H_1}{v_1}\right) \sin\left(\omega \frac{H_2}{v_2}\right) = 0. \quad (6.9)$$

The resulting mode frequencies  $\omega_n$ , i.e. the  $n$ th order roots of the characteristic function, depend both on the layer thicknesses and sound velocities but also the acoustic impedance ratio of the bilayer system. From  $D(\omega_n)B_n = 0$  the mode-specific coefficient vector  $B_n$  is calculated.  $B_n$  is defined up to an arbitrary complex factor, which we choose by requiring  $|B_n| = 1$  and  $B_{3,n}$  to be a real number. Thereby, we obtain:

$$\begin{aligned} B_{1,n} &= B_{3,n} \cdot \frac{2 Z_2}{Z_1 \left(1 - e^{2i\omega_n \frac{H_1}{v_1}}\right) + Z_2 \left(1 + e^{2i\omega_n \frac{H_1}{v_1}}\right)} \\ B_{2,n} &= B_{1,n} \cdot e^{2i\omega_n \frac{H_1}{v_1}} \\ B_{3,n} &= 1 \\ B_{4,n} &= B_{1,n} + B_{2,n} - B_{3,n}. \end{aligned} \quad (6.10)$$

For each resonant mode  $n$ , the layer specific displacement and stress fields  $u_z$  and  $\sigma_{zz}$  can be calculated by inserting the resonance frequencies  $\omega_n$  and coefficients  $B_{1-4,n}$  into Eqs. 6.1 and 6.5.

For resonance frequencies  $\omega_{n,\text{ref}}$  at a given  $r_{Z,\text{ref}}$ , small changes in  $r_Z$  (at constant  $v_{1,2}$ ) result in shifted frequencies given by:

$$(\omega - \omega_n(r_{Z,\text{ref}})) \cdot \left. \frac{\partial \xi}{\partial \omega} \right|_{\substack{\omega_n(r_{Z,\text{ref}}) \\ r_{Z,\text{ref}}}} + (r_Z - r_{Z,\text{ref}}) \cdot \left. \frac{\partial \xi}{\partial r_Z} \right|_{\substack{\omega_n(r_{Z,\text{ref}}) \\ r_{Z,\text{ref}}}} = 0. \quad (6.11)$$

Specifically, for  $r_{Z,\text{ref}} = 0$ , two sets of resonance frequencies are obtained at small  $r_Z$ , given by

$$\begin{aligned} -\frac{r_Z}{b} \tan\left(\frac{b}{a} \pi n\right) + \frac{\pi n}{a} \quad \text{and} \\ \frac{r_Z}{b} \cot\left(\frac{a}{b} \left(\pi n - \frac{\pi}{2}\right)\right) + \frac{\pi n - \frac{\pi}{2}}{b}, \end{aligned} \quad (6.12)$$

in which  $a = \frac{|H_1|}{v_1}$  and  $b = \frac{H_2}{v_2}$ .

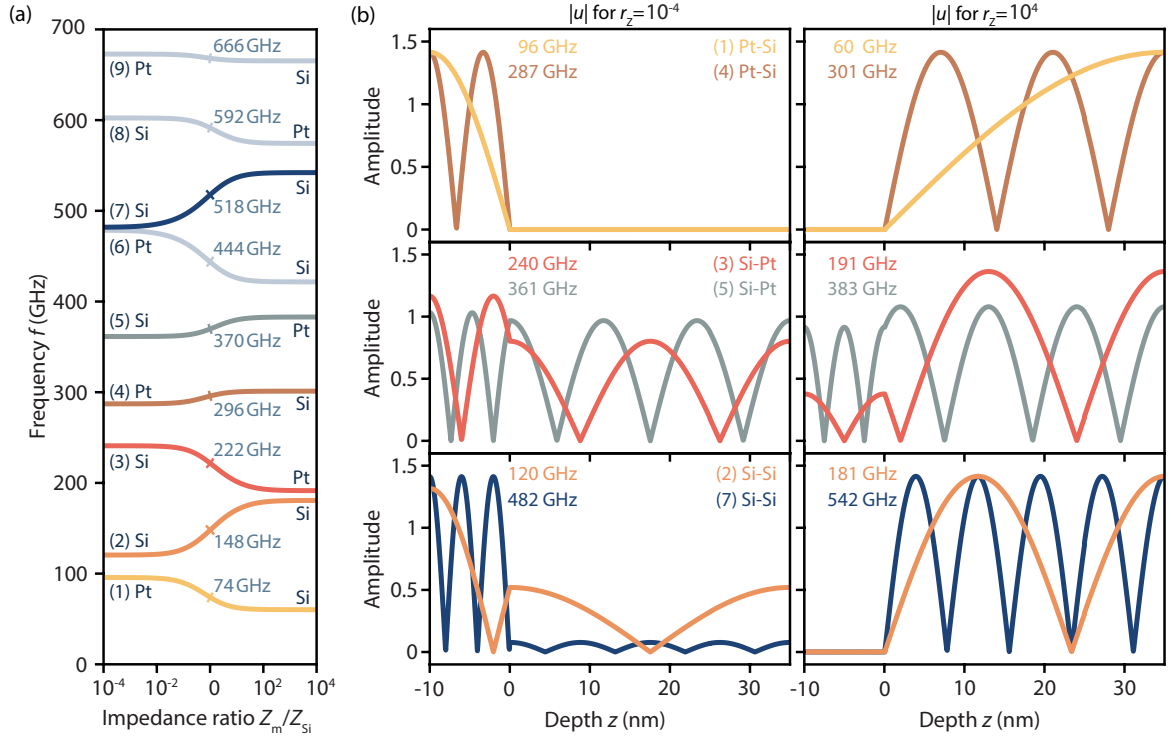


**Figure 6.5:** Resonance frequencies for the metal/semiconductor bilayer system with corresponding maximum displacement  $|u|$  for selected frequency branches. (a) The frequency spectrum is formed by two equidistant ladder spectra, indicated as  $(n)$  Si and  $(n)$  Pt. In the impedance-matched case ( $\log(r_Z) = 0$ ), frequencies result from round-trip times in both layers. (b) Maximum displacement  $|u|$  in the limits of small and large impedance ratios, showing wave localizations in the metal layer and the silicon layer for sinusoidal standing waves and comparable amplitudes in both layers if cosine-like waves form in one layer. Colors coincide with colors chosen for the  $n$ th order frequency branches in (a).

Similarly, for large  $r_Z$ , the frequencies are approximated by

$$\begin{aligned}
 & -\frac{1}{r_Z \cdot b} \tan\left(\frac{a}{b}\pi n\right) + \frac{\pi n}{b} \quad \text{and} \\
 & \frac{1}{r_Z \cdot a} \cot\left(\frac{b}{a}\left(\pi n - \frac{\pi}{2}\right)\right) + \frac{\pi n - \frac{\pi}{2}}{a},
 \end{aligned} \tag{6.13}$$

and, for  $r_Z$  close to one (impedance matched case), by

$$\frac{r_Z - 1}{a + b} \cdot \frac{\sin\left(\frac{a-b}{a+b}\pi n\right)}{2 \cos(\pi n)} + \frac{\pi n}{a + b} \tag{6.14}$$

as shown in Fig. 6.6a for mode orders  $n \in 1, \dots, 4$ . Corresponding maximum displacements  $|u|$  in the limits of small and large impedance ratios are shown in Fig. 6.5b.

### 6.2.3 Acoustic Impedances and Sound Velocities for common materials

For illustrating the variability in acoustic impedance and isotropic sound velocity, we compiled both quantities for common materials employed in multilayer systems. The isotropic sound velocities are defined as  $v_{\text{iso}} = \sqrt{(\lambda + 2\mu)/\rho}$ , in which the Lamé constants  $\lambda$  and  $\mu$  are calculated from

$$\lambda = \frac{\nu}{(1 + \nu)(1 - 2\nu)} E$$

$$\mu = \frac{1}{2 \cdot (1 + \nu)} E$$
(6.15)

with Young's modulus  $E$  and Poisson's ratio  $\nu$  (values taken from Refs. [429] and [433]).

As apparent in Fig. 6.6b, the impedances and sound velocities vary independently across the selected set of materials, changing by about one order of magnitude in both cases.

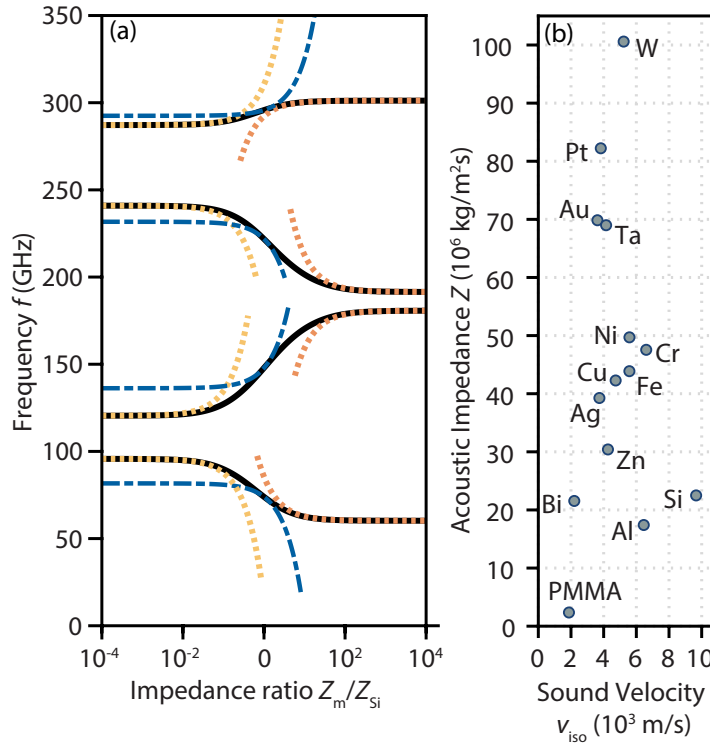


**Figure 6.6:** Resonance frequencies for the metal/semiconductor bilayer and common values for acoustic impedances and sound velocities. (a) Approximate resonance frequencies in the limit of small (dashed, yellow lines) and large (dashed, orange lines) impedance ratios, as well as for impedance matching (dot-dashed, blue lines) are given by Taylor functions according to Eq. 6.12 – 6.14. (b) Theoretical acoustic impedances covering several orders of magnitude and isotropic sound velocities for typically investigated thin films. Values are calculated as explained in supplementary material 6.2.3.

### 6.2.4 Optical bilayer Fabry-Pérot interferometer

In analogy to acoustic waves in a bilayer resonator, the optical field in a double Fabry-Perot interferometer can be described using a similar global matrix approach if only vertically incident light is considered. In particular, for a high-quality optical cavity close to resonance, the electromagnetic field outside the cavity can be neglected and, as in the acoustic case, the following linear system of four equations is obtained:

$$\begin{pmatrix} e^{i\omega \frac{n_1 H_1}{c}} & e^{-i\omega \frac{n_1 H_1}{c}} & 0 & 0 \\ 0 & 0 & e^{i\omega \frac{n_2 H_2}{c}} & -e^{-i\omega \frac{n_2 H_2}{c}} \\ 1 & 1 & -1 & -1 \\ n_1 & -n_1 & -n_2 & n_2 \end{pmatrix} \begin{pmatrix} E_1 \\ E_2 \\ E_2 \\ E_4 \end{pmatrix} = 0. \quad (6.16)$$

Here, the acoustic displacement and stress boundary conditions at the bilayer interface (at  $z = 0$ ) and the two surfaces (at  $z = H_1$  and  $z = H_2$ ) are replaced by continuous tangential components of electric and magnetic field vectors [27].  $n_{1,2}$  denotes the refractive index of each layer with thicknesses  $H_1 < 0$  and  $H_2 > 0$  and  $c$  is the light velocity in vacuum such that  $k_i = \frac{\omega n_i}{c}$  within the Fabry-Perot interferometer.

The characteristic function is again given by the determinant of the 4-by-4-matrix, simplifying to  $n_1 \sin\left(\omega \frac{n_2 H_2}{c}\right) \cos\left(\omega \frac{n_1 H_1}{c}\right) - n_2 \cos\left(\omega \frac{n_2 H_2}{c}\right) \sin\left(\omega \frac{n_1 H_1}{c}\right)$  and is in close resemblance to the function found for the acoustic bilayer system (cf. Eq. 6.9). For fixed  $n_1 = 2$  and layer thicknesses  $|H_1| = 0.35 \mu\text{m}$  and  $H_2 = 0.10 \mu\text{m}$ , the resonance spectrum  $f(r_n) = 2\pi\omega(r_n)$  in the visible light regime is plotted in Fig. 6.7 for varying ratios  $r_n = n_1/n_2$  of refractive indices.

We note that the characteristic function of the double Fabry-Perot interferometer can be mapped to the acoustic bilayer case for equal mass densities of both layers.

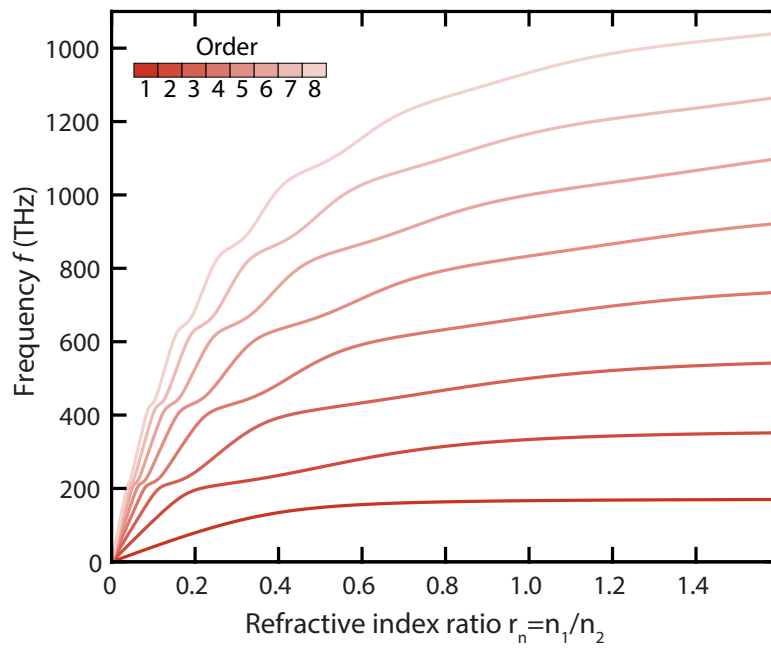


**Figure 6.7:** Optical resonance spectrum of a bilayer Fabry-Perot interferometer upon vertical incident light as a function of varying refractive index  $n_2$  for fixed  $n_1 = 2$  and layer thicknesses  $|H_1| = 0.35 \mu\text{m}$  and  $H_2 = 0.10 \mu\text{m}$ .



### **Tailored nanophononic wavefield in a patterned bilayer system probed by ultrafast convergent beam electron diffraction**

---

For time-resolved investigations of structural dynamics in spatially homogeneous materials, ultrafast diffraction experiments with electron and x-ray pulses have provided essential insights in the past two decades [54, 75, 393]. In spatially inhomogeneous systems like thin film samples or nanostructured semiconductor membranes, however, a variety of non-local relaxation processes play a role. For example, ballistic and diffusive charge carrier and phonon transport both within the individual phases and across interfaces are relevant relaxation processes in heterostructures. For the spatio-temporal imaging and separation of the individual contributions, methods that allow the dynamics to be mapped locally are essential. Time-resolved electron energy loss spectroscopy and electron holography with a focused electron beam provide information on charge carrier dynamics, while convergent beam electron diffraction (CBED) is employed to gain access to structural dynamics through the simultaneous probing with different angles of incidence of the electron beam.

In initial optical-pump/electron-probe experiments, Yurtsever et al. resolved coherent strain dynamics at a single probing position of a silicon wedge by quantitatively analyzing the time-dependent shift of Kikuchi lines [106, 434]. Due to the linear increase in the thickness of the wedge-shaped structure, this motion is attributed to strain waves originating from the laser-driven thermal expansion at the tip of the wedge and propagating in the lateral direction.

As an extension of this method, ultrafast convergent beam electron diffraction (U-CBED) was implemented at the Göttingen UTEM. In a first experiment, the successful application of strongly focused short electron pulses to study ultrafast dynamics on the nanometer

scale has been demonstrated by imaging optically triggered lattice distortions in a single-crystalline 120 nm-thick graphite membrane. The local structural distortions could be quantitatively extracted from the motion of selected Bragg lines. Following the optical excitation near the membrane edge, a breathing mode of the flake is excited homogeneously, as well as a shock wave that starts propagating at the edge and subsequently triggers an acoustic shear mode. This complex distortion field could be tracked with spatial and temporal resolutions of 28 nm and 700-fs, respectively.

The origin of the light-driven coherent shear motions in both the wedge-shaped silicon structure and the graphite membrane is the mesoscopically broken symmetry. This already hints at the possibility to tailor nanoacoustic wave fields by heterogeneous structures with extreme excitation gradients. In this context, patterned semiconductor membranes are an ideal platform for optically inducing different nanoscale acoustic waveforms. By two-dimensional scanning the focused electron beam with 15-nm-spatial and 2-ps temporal resolution, Nakumara et al. recently demonstrated that a 100-nm-thick silicon membrane with a small tungsten nanodisk (diameter: 700 nm, thickness: 100 nm) deposited at the center acts as a single point-like source of the photoinduced strain which propagates as a radial acoustic wave through the membrane [384].

A key aspect of nanophononics is the scattering of high-frequency acoustic waves that is influenced by the size and shape of scattering objects and the phonon wavelength [435, 436]. In order to quantitatively evaluate the resulting strain fields using the high spatial resolution of focused electron pulses, the second model system investigated in Ref. [384] consists of a tungsten stripe acting as a line-source of strain waves and an array of asymmetrically shaped voids in a distance of approximately 3600 nm. Depending on the orientation of the tungsten voids, the amplitude of shear acoustic phonon modes can be significantly suppressed (Fig. 7.1).

Fully harnessing the effect of amplitude modulations by advanced patterned geometries might enable nm-sized phonon foci causing tightly localized, large-amplituded lattice distortions. In order to make progress in this research direction, a spatiotemporal Fourier decomposition of the multi-modal distortion wave launched at the structured area and subsequently propagating through the membrane is required. In the recent publication reprinted in the following chapter, U-CBED (FWHM focal spot size about 15 nm, 1-ps temporal resolution) is used for local investigations of the nanoscale structural dynamics in a well-defined model system that consists of a platinum stripe deposited on a silicon membrane. Kinematic scattering theory is applied to the analysis of local

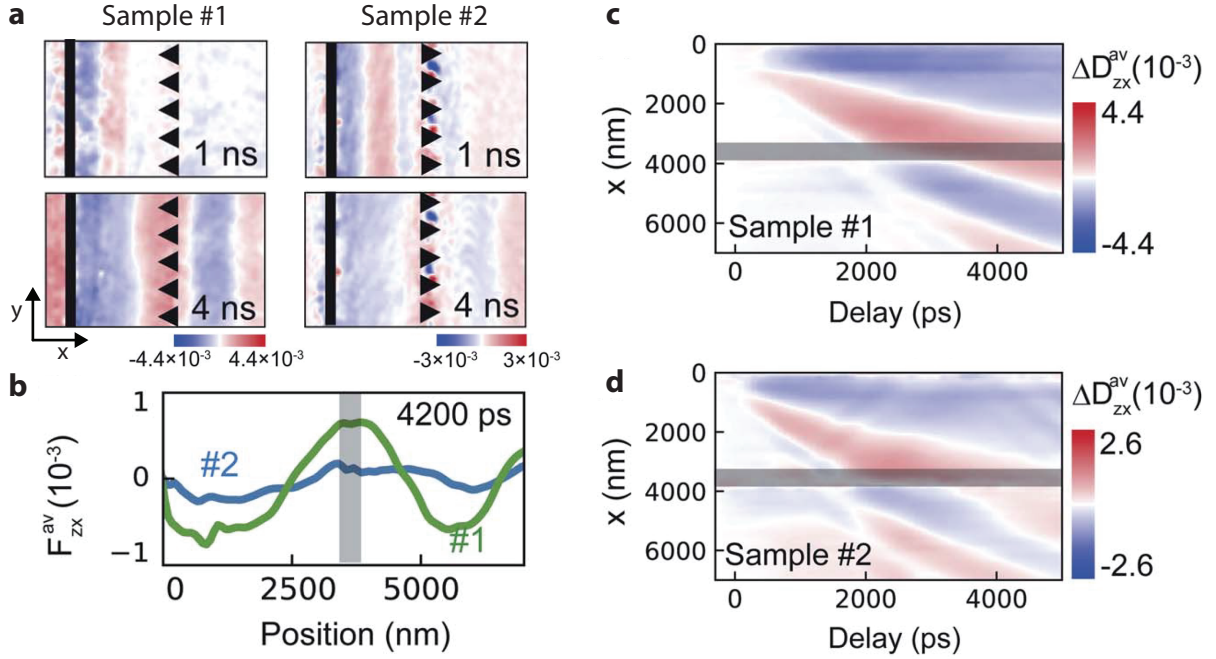


**Figure 7.1:** Strain dynamics in a silicon membrane patterned with tungsten bars (400 nm width) and void-arrays. (a) Temporal dynamics of the displacement gradient tensor component  $\Delta D_{zx}(x, y, t)$  reconstructed from the CBED-analysis of acoustic waves launched at the metal bar (black line) and propagating through the void-arrays of different orientations (black triangles). (b)  $\Delta D_{zx}^{av}(x, t)$  at a delay time of 4200 ps for both samples, obtained by averaging  $\Delta D_{zx}(x, y, t)$  along the  $y$ -direction. The amplitude of the acoustic wave in sample #2 is significantly suppressed in comparison to that in sample #1. (c, d) Spatiotemporal maps of the tensor component  $\Delta D_{zx}^{av}$  for both samples. The gray shaded regions in panels b–d denote the position of the void-arrays. Figure adapted from Ref. [384]. Licensed under CC BY 3.0.

lattice deformations, explains the influence of a finite crystal size on the scattering intensity, and furthermore allows to quantify the optically induced temperature rise of the 2- $\mu\text{m}$  wide polycrystalline platinum stripe on the silicon membrane. By a quantitative retrieval of the time-dependent local deformation gradient tensor, we identify the dominant acoustic longitudinal and shear horizontal acoustic modes consistent with Rayleigh-Lamb dispersion relations applying for wave propagation in thin plates (see previous Chapter 6 and Ref. [277]). The presented experimental and numerical work therefore provides a microscopic understanding of nanoscale processes in strongly inhomogeneous materials and guides the design of future energy devices that can exploit phonon properties and interactions by material composition and tailored responses to an optical excitation.

The experimental work described in the third publication of the present cumulative thesis was conceived and directed by S. Schäfer. M. Möller prepared the sample. CBED measurements were conducted by N. Bach and analyzed in collaboration with S. Schäfer,

M. Möller, A. Feist, C. Ropers. N. Bach implemented the finite-element numerical simulations with support from S. Schäfer. N. Bach and S. Schäfer wrote the manuscript. A. Feist, M. Möller, and C. Ropers participated in the improvement of the manuscript. Further non-author contributions are listed in the “Acknowledgments” section of Chapter 7.

N. Bach, A. Feist, M. Möller, C. Ropers, S. Schäfer

*Structural Dynamics* **9**, 034301 (2022)

10.1063/4.0000144

Optically excited nanostructures provide a versatile platform for the generation of confined nanophononic fields with potential (non-)linear interactions between different degrees of freedom. Control of resonance frequencies and the selective excitation of acoustic modes still remains challenging due to the interplay of nanoscale geometries and interfacial coupling mechanisms. Here, we demonstrate that a semiconductor membrane patterned with a platinum stripe acts as a tailored source for high-frequency strain waves generating a multi-modal distortion wave propagating through the membrane. To locally monitor the ultrafast structural dynamics at a specific distance from the deposited metal stripe, we employ ultrafast convergent beam electron diffraction in a laser-pump/electron-probe scheme. Experimentally observed acoustic deformations are reproduced by numerical simulations in a continuous medium model, revealing a spatiotemporal evolution of the lattice dynamics dominated by local rotations with minor strain and shear contributions.

## 7.1 Introduction

In recent years, non-equilibrium excitations in solids were utilized to trigger phase transitions on ultrafast time-scales and led to the discovery of novel transient phases and phase transition pathways [437, 438]. Efficient steering of solid-state systems into (meta-) stable states is typically achieved through direct coupling to the electronic subsystem [42, 49, 74, 119, 159, 223, 228, 412, 439–443].

Light-driven optical [444–446] and acoustic phonons [119, 444], as well as inhomogeneous nanoscale strain distributions [447, 448] have also been demonstrated to induce and modulate ultrafast phase transitions. However, it remains challenging to achieve detailed control of the spatiotemporal evolution of nanophononic wavefields. The underlying mechanisms of the optical excitation of acoustic phonons in nanoscale geometries [243] can be revealed by experimental approaches that capture the ultrafast structural dynamics with a sufficient spatial and temporal resolution. Aside from the recent progress in ultrafast x-ray [391, 449–452] and extreme-ultraviolet scattering techniques [61, 453], ultrafast electron probing approaches have been established for the investigation of structural dynamics. In particular, ultrafast transmission electron microscopy (UTEM) maps nanophononic fields [100, 151, 382, 386, 389, 390, 454] harnessing diffraction contrast in bright- and dark-field imaging. A quantitative access to local structural distortions on fs- and ps-time scales is gained by ultrafast convergent beam electron diffraction (U-CBED), simultaneously probing the electron diffraction intensity at different incident angles. Previous U-CBED experiments explored phonon excitations in simple geometries [72, 105, 106, 215], but lacked the capability for spatially tailored sample excitations.

Here, we resolve the optically induced structural response of a thin silicon membrane in close proximity to a patterned platinum stripe by employing ultrafast convergent beam electron diffraction. A multi-modal crystal distortion wave is launched at the silicon/platinum interface and propagates through the silicon membrane. Time-resolved changes in the electron diffraction patterns are quantitatively reproduced in a continuous medium model. The evolution of the inhomogeneous distortion field is governed by a superposition of Lamb waves frequency-matched to local strain resonances in the bilayer region.

## 7.2 Ultrafast convergent beam electron diffraction

For a controlled generation of ultrafast structural distortion waves, we utilize optically excited nano-patterned semiconductor thin films. In such an approach, the geometry of deposited metal structures is expected to have a strong influence on the evolving spatiotemporal distortion field. In the present work, we prepared 2  $\mu\text{m}$  wide platinum stripes (10-nm thickness) on a (100)-oriented single-crystalline silicon membrane (35-nm thickness). Excitation of platinum by optical pulses (800-nm center wavelength) induces thermal stress within the stripe and initiates a strain wave propagating away from the platinum edge. The structural distortion is probed by focused ultrashort electron pulses (120-keV electron energy, sub-picosecond temporal duration [71]) in a distance of about 170 nm from the platinum stripe edge (Figs. 7.2a and 7.2b). Specifically, we stroboscopically record diffraction patterns locally on the silicon membrane using a convergent electron beam (32-mrad full convergence angle, FWHM focal spot size of about 15 nm) for varying optical-pump/electron-probe delay times  $\Delta t$ . The incident cone of the incoming electron beam is represented by an intense central disk in the diffraction patterns. Owing to the broad angular distribution, multiple Bragg scattering conditions are fulfilled simultaneously [330]. Exemplarily for a specific sample orientation, deficit intensity lines within and excess Bragg lines around the disk are displayed in Figs. 7.2c and 7.2d. To obtain a larger set of distinct Bragg lines, the sample is tilted with respect to the electron beam direction. The position of each Bragg line is linked to a reciprocal lattice vector  $\mathbf{G}_{hkl}$  of the local (distorted) crystal structure of the silicon membrane. Thereby,  $\mathbf{G}_{hkl}$  is also related to the shape and orientation of the local real-space unit cell of silicon. Considering conservation of momentum and elastic scattering [345], as well as applying a paraxial approximation, the diffraction excess line positions in the detector plane are given by

$$r_G = \frac{-G_{hkl}^2/2 + k_0 G_Z}{\sqrt{G_X^2 + G_Y^2}} + \sqrt{G_X^2 + G_Y^2}. \quad (7.1)$$

Here,  $k_0$  is the incident electron wave vector (oriented along the  $Z$ -direction) and  $G_{hkl}$  is the reciprocal lattice vector in the laboratory-fixed coordinate system with Miller indices  $h$ ,  $k$ , and  $l$  (see supplementary material 7.6.4 for details). The inclination of the lines is characterized by an angle  $\phi$ , given by  $\tan(\phi) = G_X/G_Y$ . Based on the given scattering conditions [329], each Bragg line in the CBED pattern can be labeled with corresponding Miller indices (see Figs. 7.2c and 7.2d).

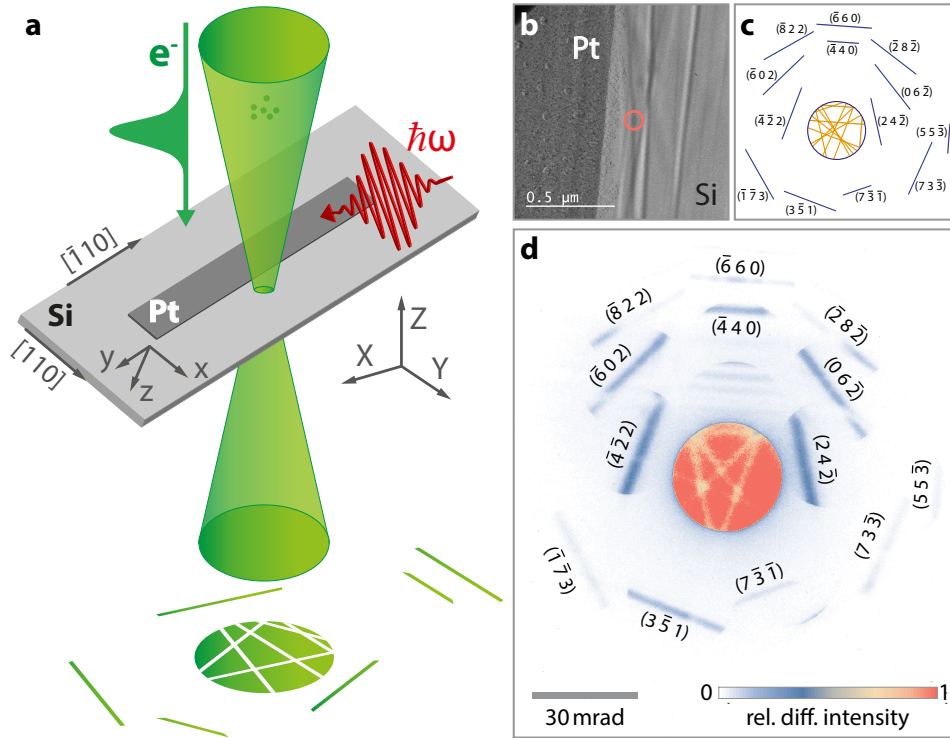


**Figure 7.2:** Ultrafast convergent beam electron diffraction on a Pt/Si heterostructure. (a) Experimental geometry of nanoscale diffractive electron probing on a single-crystalline silicon membrane (see arrows at membrane edges for crystalline orientation) in close vicinity to a polycrystalline platinum stripe. Inhomogeneous structural dynamics are induced by pulsed optical excitation of the platinum stripe. Laboratory- and sample-fixed coordinate systems are indicated by capital letters  $X$ ,  $Y$ , and  $Z$  and lowercase letters  $x$ ,  $y$ , and  $z$ , respectively. (b) Bright-field electron micrograph of the platinum stripe on the silicon membrane with the electron probing position (marked by red circle) in a distance of about 170 nm to the platinum stripe edge. (c) Calculated deficit (orange) and excess (blue) Bragg lines (labeled by Miller indices) for the employed sample orientation. (d) CBED pattern before optical excitation recorded at the probing position.

Selected Bragg line profiles extracted from the ultrafast CBED patterns are shown in Fig. 7.3 as a function of the optical-pump/electron-probe delay time  $\Delta t$ . The transient changes of Bragg line profiles are obtained by integrating the diffracted intensity along the individual line directions. All profiles are background corrected and normalized to the intensity within the disk, as detailed in supplementary material 7.6.3. Depending on the Miller indices, the Bragg lines show varying delay-dependent angular shifts  $\Delta\theta$  of up to 2 mrad. In all cases, shifts are only observed after an initial delay of about 40 ps due to the propagation time between the strain wave source and the electron probing position. The precise relative timing of electron pulse arrival at the sample and optical excitation was independently characterized by inelastic electron-light scattering [110, 238]. On a 500-ps time scale, the absolute shifts exhibit an overall decrease with an

additional complex temporal modulation containing multiple frequencies in the gigahertz range. These reproducibly observable small-amplitude oscillations become more evident from the delay-dependent central position, extracted from fitting Lorentz-profiles to each Bragg line cross section (see Fig. 7.3g, for details of the analysis see supplementary material 7.6.3). After the zero-crossing of most line shifts at around 600 ps, further low-frequency oscillations are observed. Bragg lines corresponding to reciprocal lattice vectors pointing along the stripe, such as  $(\bar{4}40)$  and  $(3\bar{5}1)$  (see Figs. 7.3c and 7.3f), show a largely reduced angular shift. This selective behavior is expected due to the translational-symmetric strain field along the long stripe ( $[\bar{1}10]$ -direction). A further peculiar feature in the line profiles is the decrease in the scattering intensity maximum in most selected lines around 80 ps. This intensity change indicates an inhomogeneous strain profile within the depth of the silicon membrane as previously observed in similar studies for an optically excited graphite flake [72].

### 7.3 Numerical simulation of nanophononic distortion field

To identify the origin and analyze the spatiotemporal evolution of the strain dynamics in the Pt/Si heterostructure, we numerically solve the anisotropic elastodynamic wave equation using a finite-element approach. Due to the symmetry of the problem we implement a two-dimensional  $x$ - $z$  cross section with an infinitely extended platinum stripe in the  $y$ -direction (for coordinate system, see Fig. 7.2a). Considering the stripe length (100  $\mu\text{m}$ ), probing position (approximate distance from stripe corners 50  $\mu\text{m}$ ), and silicon strain wave velocities [284] ( $v_1 = 8432 \text{ m/s}$ ), lattice distortions from the stripe corners do not affect the structural dynamics in the sub-6-ns range. The optical excitation of the platinum stripe is implemented as a depth-dependent heat source adapted to the absorbed local optical power in the experiment. The thermal coupling between the platinum layer and the silicon membrane is determined by the thermal boundary resistance (see supplementary material 7.6.7 for details).

Generally, the local lattice distortion can be described by a time-dependent deformation gradient tensor [329]  $\mathbf{F}(\Delta t) = \boldsymbol{\epsilon}(\Delta t) + \boldsymbol{\omega}(\Delta t) + \mathbf{1}$ , where  $\boldsymbol{\epsilon}$  and  $\boldsymbol{\omega}$  are the symmetric strain and antisymmetric rotation tensors, respectively. Due to the effective symmetry of the problem,  $\mathbf{F}$  can be represented by a  $2 \times 2$  matrix with components  $F_{ij}$  [ $i, j \in (x, z)$ ]. The diagonal entries  $F_{xx}$  and  $F_{zz}$  signify compression or dilatation along the respective directions. The off-diagonal components  $F_{xz}$  and  $F_{zx}$  describe a shearing

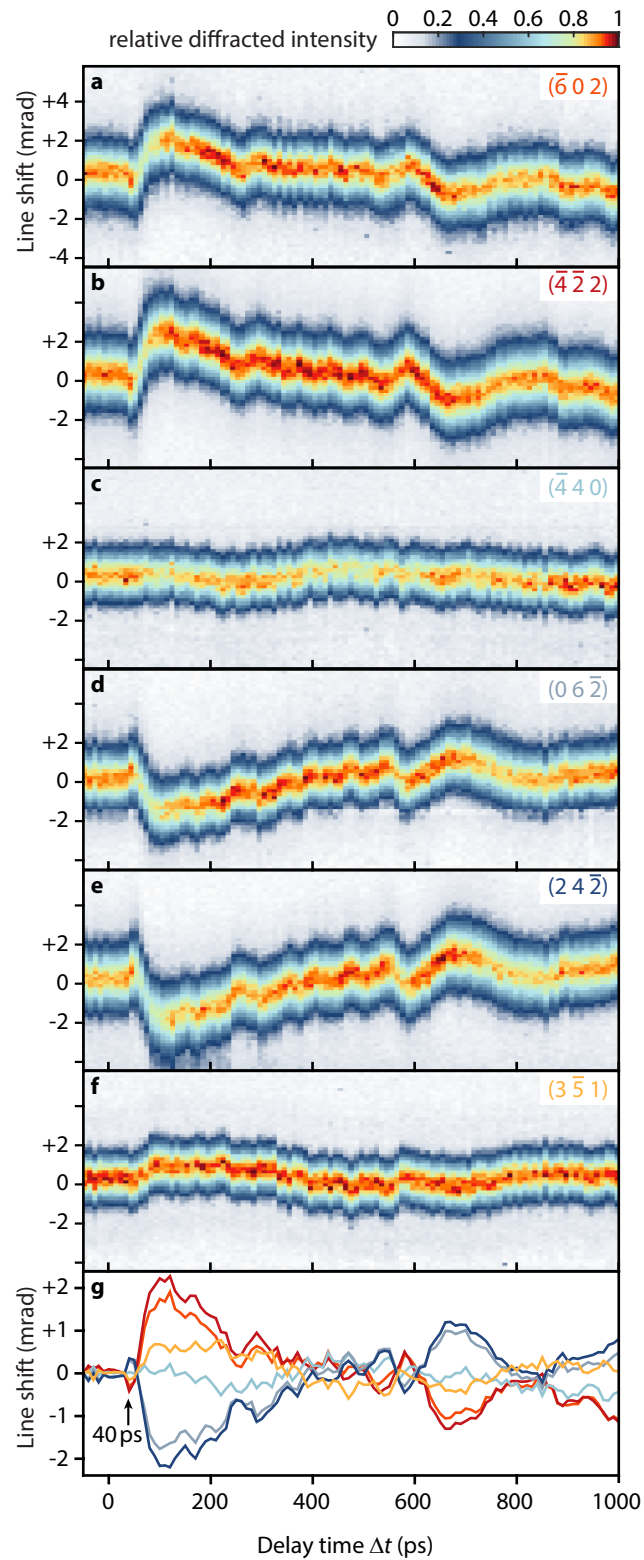


**Figure 7.3:** Transient Bragg line profiles. Delay-dependent profiles of selected Bragg lines recorded in the U-CBED experiment (a-f) and extracted peak shifts of Lorentz-profiles fitted to each Bragg line cross section (g). Each Bragg line map is normalized to its signal maximum.

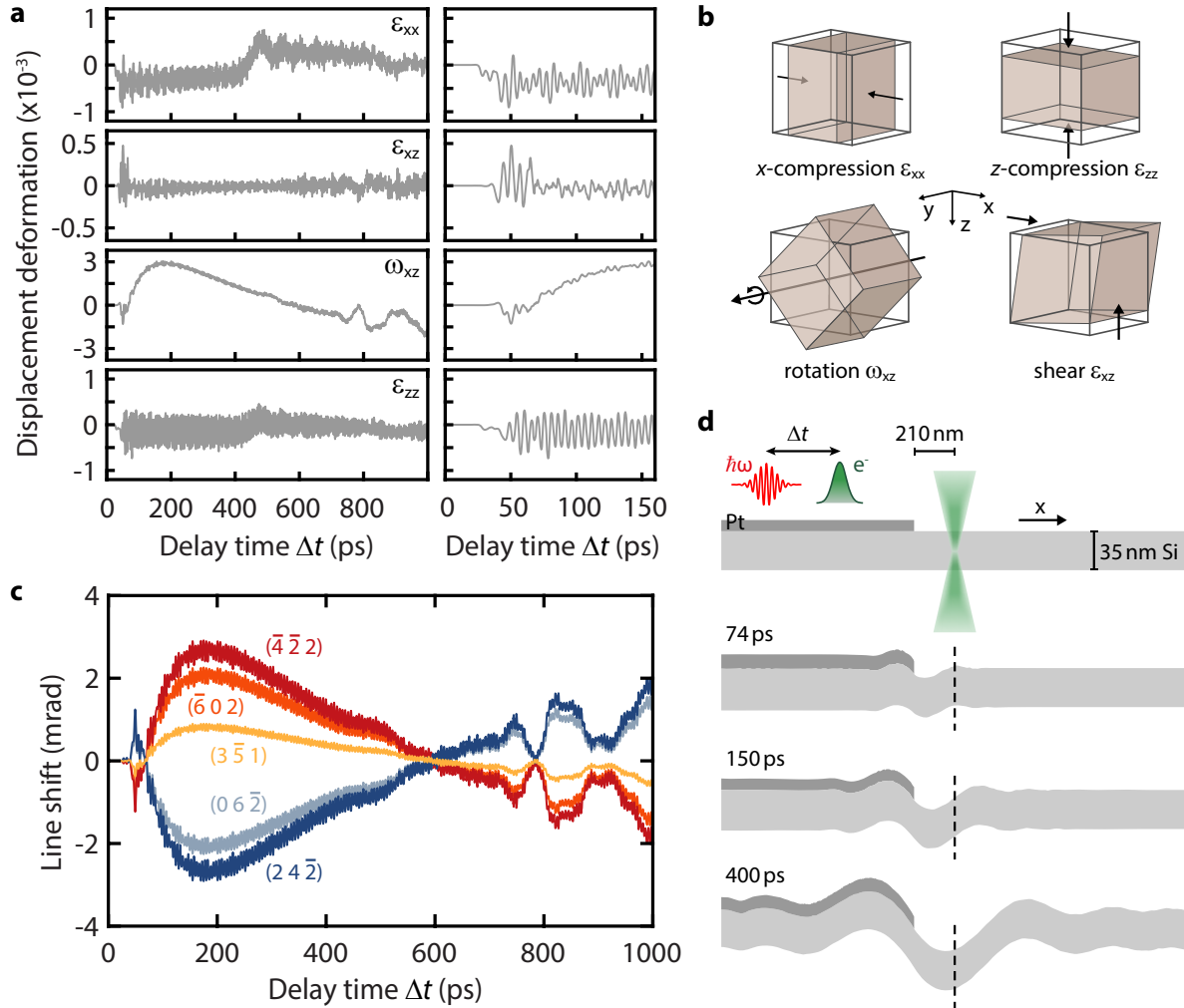


**Figure 7.4:** Simulated acoustic wave dynamics close to the Pt-stripe/Si-membrane heterostructure. (a) Temporal dynamics of selected strain and rotation tensor components extracted at a distance of 210 nm from the Pt stripe edge. Each component is averaged along the  $z$ -direction. Close-ups for early delay times (displayed in the right column) reveal multi-frequency oscillations. (b) Schematic representation of lattice distortions associated with the selected deformation gradient tensor components shown in (a). (c) Predicted Bragg line shifts based on the simulated wave dynamics taking into account the four symmetry-allowed tensor components. (d) Real-space distortion of silicon and platinum surfaces before and after optical excitation at different delay times. For better visibility, the surface displacements are scaled by a factor of 250. A large wavelength overall membrane bending is superimposed by additional high-frequency oscillations with small amplitudes.

$[\epsilon_{xz} = (F_{xz} + F_{zx})/2]$  and a rotation  $[\omega_{xz} = (F_{xz} - F_{zx})/2]$  of the unit cell. A schematic representation of the associated lattice distortions is given in Fig. 7.4b. From the numerically simulated temporal evolution of the tensor components for our sample system (see Fig. 7.4a), it is apparent that the main lattice distortion induced by the optically illuminated platinum stripe consists of a local rotation of the unit cell and only smaller contributions from the strain tensor. High-frequency oscillations are observed in all components, as visible in the right panels of Fig. 7.4a.

For visualizing the optically induced membrane dynamics, we extracted the time-dependent displacement vector component  $u_z$  at each point of the material layer surfaces and the interface of the Pt/Si heterostructure and constructed the displaced surfaces at four delay times in Fig. 7.4d. For enhanced visibility, the displacement is scaled by a factor of 250. Two mechanisms are responsible for the observed deformation of the membrane, both linked to the optically induced heating of the platinum stripe. First, thermal expansion of the stripe in the transverse ( $x$ -) direction results in a bimetal-like bending of the underlying silicon membrane (Fig. 7.4d). The detailed shape of the resulting membrane bending wave is expected to be governed by the time-scale of the platinum expansion and the mechanical coupling between platinum and silicon. Second, additional fast small-amplitude displacement oscillations (Fig. 7.4a) are induced by local resonances in the bilayer region resulting in a superposition of symmetric and antisymmetric Lamb waves with a range of frequencies  $\omega$  as discussed below. At the electron probe position next to the platinum stripe, the main displacement results from the overall bending of the membrane encoded in the rotation tensor  $\omega_{xz}$ .

From the numerically obtained tensor components  $F_{ij}$ , the temporal shift of the expected Bragg line positions  $r_G$  can be calculated (see supplementary material 7.6.4). Choosing the experimentally selected Bragg lines and time-dependent tensor components at a distance of 210 nm to the platinum stripe (similar to the experimental probe position of about 170 nm) yields the results shown in Fig. 7.4c. The numerical line shifts closely resemble the experimental findings with few-percent deviations particularly in the first 160 ps (see Fig. 7.9 in the supplementary material for details), providing a close link between the simulation and the experiment. Only the dynamics of the  $(\bar{4}40)$  and  $(\bar{6}60)$  lines are not recovered, indicating a dependence on omitted tensor components containing deformations along the  $y$ -axis. Deviations from the behavior expected for reasons of symmetry may result either from an overall deformation occurring during the deposition of the platinum stripe or from local membrane distortions induced by the mechanical contact with the

polycrystalline stripe.

Whereas the simulated tensor components can be used to predict Bragg line shifts (see Eq. 7.1 and supplementary material 7.6.4), the full reconstruction of the tensor components from the experimental data is generally not achievable. For a detailed analysis of the tensor component subspace which is experimentally accessible, we consider a linearized relation between the Bragg line positions and the tensor components. The corresponding derivatives  $\frac{\partial r_G}{\partial F_{ij}}$  are collected in a sensitivity matrix  $A$  (see supplementary material 7.6.5). A singular value decomposition of  $A$  reveals three linear combinations of tensor components which the U-CBED experiment is most sensitive to. In the lab coordinate system, the eigenvectors correspond to displacement gradients along the direction of the incoming electron probe pulses. For the chosen sample orientation and the selected Bragg-scattered lines, we obtain a high sensitivity to two shear-rotational motions perpendicular to the  $z$ -axis and to vibrations along the  $z$ -axis. This result is consistent with the general sensitivity of line shifts in CBED experiments to changes of reciprocal lattice vectors along the electron beam direction (see supplementary material 7.6.5).

## 7.4 Lamb wave decomposition

Apart from the transient shift of selected Bragg-scattered lines, most lines exhibit a pronounced drop in the intensity maximum in the line profile around 80 ps. For a detailed analysis of the profiles, we recorded an additional delay scan with 2-ps time steps. Cross sections through the  $(\bar{4}\bar{2}2)$  line are shown in Fig. 7.5 a. The line profiles in CBED patterns are related to the inhomogeneity of the displacement field, both within the electron spot diameter and along the depth of the thin film [329, 449]. The strained crystal imprints a phase modulation on the electron exit wave resulting in a diffracted intensity  $I_{hkl} \propto |\mathcal{F}[\exp\{(2\pi i \mathbf{G}_{hkl} \cdot \mathbf{u}(r))\}]|^2$ . Due to the different length scales involved, we chose two approaches to include the effects in our calculations. While we treat the displacement inhomogeneity within the depth of the membrane explicitly, we assume a spatial average for the transverse variations of the electron probe.

In the limit of a perfectly localized electron probe, the simulated line profiles, as shown in Fig. 7.5 b, largely reproduce the experimentally observed linewidth and the temporal variations in the maximum line amplitude and line position. Interestingly, and different from the experiment, the maximum intensity in the line profiles oscillates with a period of 2.4 ps, visible particularly for delay times above 60 ps. Within the oscillation, the

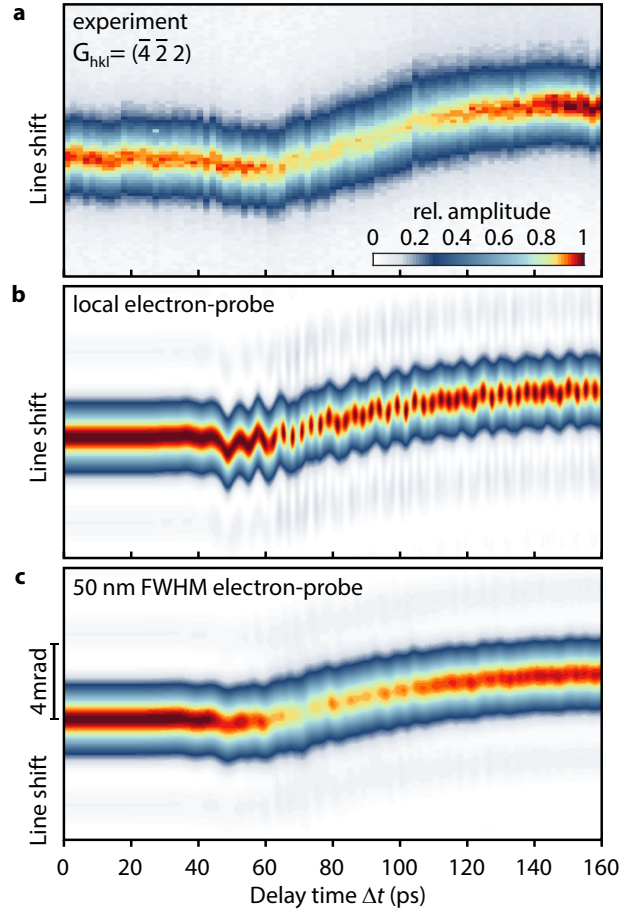


**Figure 7.5:** Temporal evolution of Bragg line profile. (a) Experimental time-dependent cross sections of the  $(\bar{4}\bar{2}2)$  line show a decrease of the scattered intensity maximum between 70 and 100 ps. (b,c) Calculated line profiles using numerically simulated displacement fields for (b) a local electron probe with negligible spatial extension and (c) considering spatial averaging due to an electron beam focused to 50 nm FWHM.

associated intensity is relocated to the diffraction sidebands at angular distances similar to the first maximum of the thin-film shape function (see supplementary material 7.6.6 for details). Considering, additionally, the incoherent averaging due to a 50 nm FWHM lateral size of the electron probe beam, the oscillatory features are averaged out, as shown in Fig. 7.5c, and a closer match with the experimental results is obtained. We note that the experimental line profiles do not show scattering sidebands that clearly exceed the background level (except for the partially visible  $(\bar{2}20)$ -disk in Fig. 7.2d). This effect arises from an additional line blurring by diffuse and inelastic scattering processes.

Finally, we discuss the microscopic origin of the overall membrane bending and the high-frequency oscillations obtained in the finite-element simulation. Generally, the

acoustic spectrum in a planar wave guide consists of an infinite number of propagating waves, each characterized by the in-plane wave vector  $\mathbf{k}$ , a vectorial mode profile and dispersion relations  $\omega(\mathbf{k})$ . For the single-crystalline silicon membrane studied here with lattice distortions restricted to the  $x$ - $z$ -plane (spanned by the [110]- and [001]-crystalline directions, i.e., sagittal polarization), acoustic modes decouple into pure Lamb modes [40, 276, 455]. They are designated  $S_n$  and  $A_n$  based on the associated displacements which are symmetric or antisymmetric relative to the mid-plane of the membrane. The corresponding dispersion curves for the current geometry are displayed in Fig. 7.6a (see supplementary material 7.6.8 for details on dispersion curve tracing and calculation of displacements). The mode index  $n \in \mathbb{N}_0$  signifies the number of nodes of the displacements along the out-of-plane  $z$ -direction. Figure 7.6d depicts an example for the displacement field for both an  $A_1$  and  $S_1$  wave at a frequency of 163.4 GHz and corresponding wavenumbers as extracted from the dispersion relation.

In Figs. 7.6b and 7.6c, we show the decomposition of the numerically simulated strain wave profile into Lamb wave amplitudes revealing a strong excitation of the  $A_0$  (flexural) Lamb mode in the low-frequency regime ( $< 40$  GHz). Additional local maxima in the amplitude of the zero-order branches, as well as on  $S_n$  and  $A_n$  branches with mode order  $n > 0$ , appear at specific higher frequencies. These frequencies are linked to quasi-standing acoustic resonances in the Pt/Si bilayer region which acts as the source of the Lamb wave field. Within an analytical acoustic mode description of resonant longitudinal strain modes [277], the lowest resonance frequencies in the Pt/Si bilayer system are located at 65.2, 163.4 and 208.0 GHz (horizontal lines in Fig. 7.6a). These distinct resonances are in good agreement with the excitation spectrum observed in Figs. 7.6b and 7.6c. Similarly, for delay times above 60 ps, the bilayer resonance frequency at 208 GHz is also visible in the tensor component  $F_{xz}$ , as shown in Fig. 7.7a, as well as in the simulated diffraction line profiles in Fig. 7.5b. In accordance with these results, the complete displacement wave field can be well reproduced by just considering a superposition of Lamb waves at the bilayer resonance frequencies and an additional low-frequency component taken from the average of the simulated displacement field at each delay time (for the  $u_x$  component see Figs. 7.7b and 7.7c,  $u_z$ : Fig. 7.10). For an alternative representation of the obtained displacement field, see Fig. 7.6e.

The characteristics of the induced acoustic wave field can be tuned by the metal/semiconductor bilayer structure. In particular changing the impedance matching or the individual thicknesses allows for tuning of frequency components in the wave field. Furthermore,

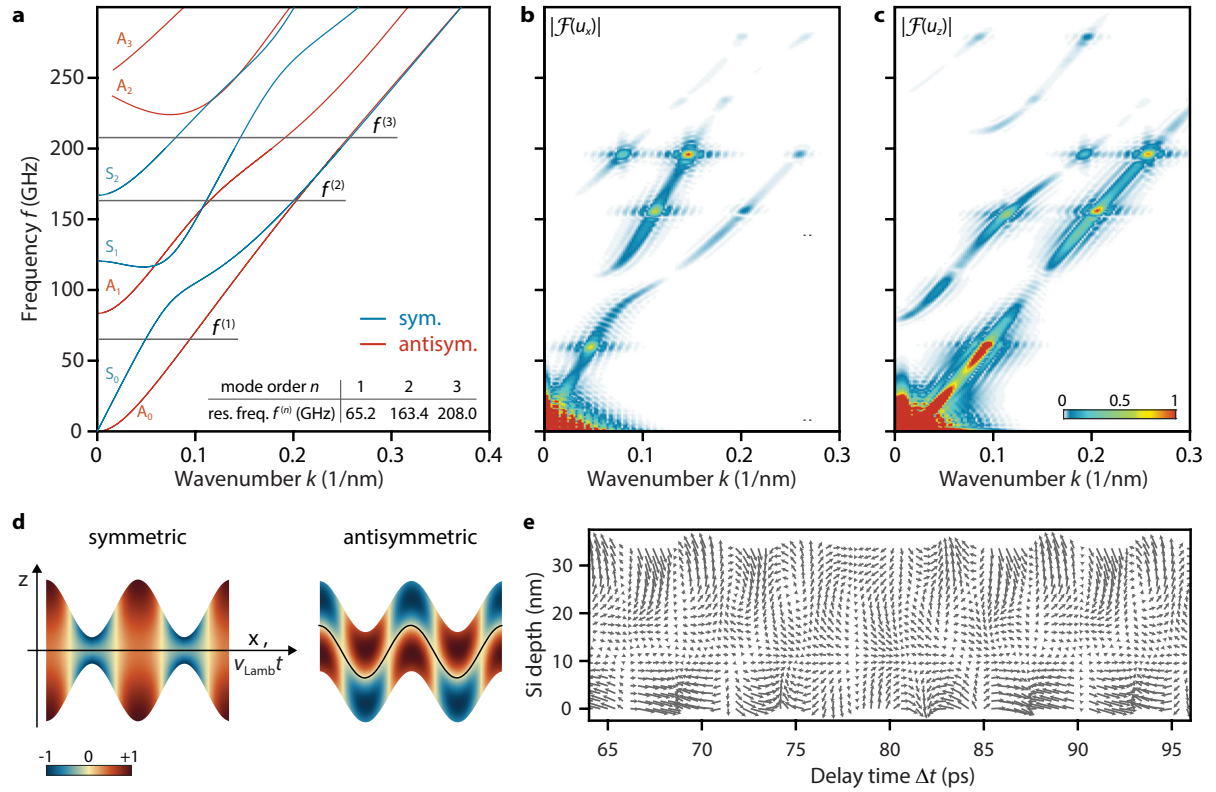


**Figure 7.6:** Mode decomposition of the acoustic wave field. (a) Lamb dispersion curves for a 35-nm thin silicon membrane with  $\mathbf{k} \parallel [110]$ , decoupled into symmetric  $S_n$  and antisymmetric  $A_n$  modes. As a reference, the three lowest resonance frequencies  $f^{(n)}$  in a homogeneous Pt/Si bilayer system are given. (b, c) Spatiotemporal Fourier decomposition of the mean displacements  $u_x$  (b) and  $u_z$  (c), obtained from finite-element simulations. Prominent amplitude maxima appear at the resonance frequencies of the Pt/Si bilayer system. (d) Schematics of displacement field for the symmetric  $S_1$  and antisymmetric  $A_1$  Lamb modes at  $f^{(2)} = 163.4$  GHz. ( $u_{z, \text{Lamb}}$  is indicated as a scaled surface displacement. Color-coding corresponds to  $u_{x, \text{Lamb}}$ ). (e) Vector field representation of the superposition of selected Lamb modes qualitatively reproducing the numerically simulated displacement fields (cf. Fig. 7.7).

while in the current geometry Lamb waves with a broad range of wavevectors along the  $x$ -direction are excited, tailored coupling schemes of the acoustic wave source to the membrane may lead to the generation of Lamb wave superpositions with a narrowband wavevector distribution.

## 7.5 Conclusion

Our results demonstrate that patterned semiconductor membranes are a versatile platform for optically inducing nanoscale acoustic waveforms. The propagating wave, as experimentally probed by ultrafast convergent beam electron diffraction, is composed

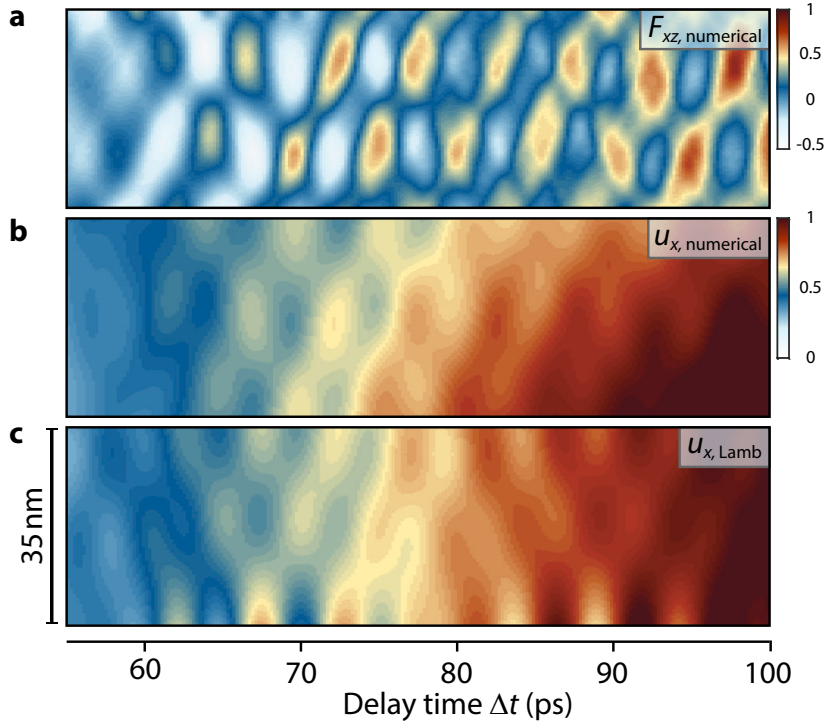


**Figure 7.7:** Spatiotemporal dynamics of the acoustic wave field. (a, b) Calculated evolution of the shear-rotation tensor component  $F_{xz}$  and corresponding displacement field  $u_x$  at a distance of 210 nm from the platinum stripe edge. (c) Displacement field obtained from a Lamb mode superposition in  $x$ -direction with additional contributions from the numerical through-thickness averaged displacement, qualitatively reproducing the results in (b).

of Lamb waves triggered by local resonances in the structured area of the membrane. The presence of small-amplitude symmetry-forbidden distortions already points to the importance of local membrane defects and inhomogeneous nanoscale pre-straining.

Since the explicit patterned geometry and its coupling to the homogeneous membrane have a strong impact on the generated acoustic wavefield, the chosen model heterostructure offers various opportunities for further tailoring and locally enhancing the structural response via acoustic wave interferences. In particular, acoustic foci may allow for an ultrafast control of local strain-driven phase transitions.

### Supplementary Material

See the supplementary material for further details on the sample preparation and experimental setup, data collection and analysis, the finite-element simulation, and the acoustic Lamb wave description discussed in the main text. Matlab source code on the singular

value decomposition of the sensitivity matrix together with corresponding data-files is provided as supplemental data.

### **Acknowledgements**

We acknowledge the financial support by the Volkswagen Foundation as part of the Lichtenberg Professorship “Ultrafast nanoscale dynamics probed by time-resolved electron imaging” and the Collaborative Research Center “Atomic Scale Control of Energy Conversion” (DFG-SFB 1073, project A05). N.B. acknowledges a scholarship by the German Academic Scholarship Foundation. The authors thank V. Gusev for helpful discussions on the formation of Lamb eigenmodes and propagation of Lamb waves in crystalline plates.

### **Conflict of Interest**

The authors have no conflicts to disclose.

### **Data Availability**

The data that support the findings of this study are available from the corresponding author upon reasonable request.

---

The supplemental data is available on the *Structural Dynamics* website at the following link:  
[aca.scitation.org/doi/suppl/10.1063/4.0000144](https://doi.org/10.1063/4.0000144).

## 7.6 Supplementary material

### 7.6.1 Sample system

The sample is based on a single-crystalline, 35-nm thin silicon membrane (Plano GmbH) (approximate dimension:  $100 \times 100 \mu\text{m}^2$ ) on which a single 2- $\mu\text{m}$  wide platinum stripe is fabricated using electron beam lithography and a thermal evaporation process. The stripe is centered within the membrane and has a length of 100  $\mu\text{m}$ , a film thickness of 10 nm and an edge sharpness of approximately 10 nm. A 1-nm thin chromium adhesion layer deposited between the membrane and the platinum layer is neglected in the analysis of laser-induced structural dynamics. The long side of the Pt stripe is orientated along the  $[\bar{1}10]$ -direction of the silicon membrane (see Fig. 7.2a).

### 7.6.2 Ultrafast transmission electron microscope in CBED mode

All experimental data were acquired with the Göttingen Ultrafast Transmission Electron Microscope (UTEM), based on a JEOL JEM-2100F Schottky field emission electron microscope. The instrument is modified to allow for ultrashort electron pulse generation from a ZrO/W Schottky field emitter tip using 400-nm ultrashort laser pulses yielding low-emittance electron pulses with down to 200-fs duration [71]. The laser-driven electron gun was operated at an acceleration potential of 120 kV. For laser-pump/electron-probe experiments, the sample is illuminated by p-polarized 800-nm optical pump pulses with 1-ps pulse duration at a 250-kHz repetition rate and an incidence angle of  $55^\circ$  relative to the electron beam. The optical beam is focused down to 50  $\mu\text{m}$  full-width-at-half-maximum (FWHM). Diffraction patterns for the ultrafast convergent beam electron diffraction (U-CBED) experiment were recorded with a focused electron beam with a full convergence angle of 32 mrad (condenser lens aperture 200- $\mu\text{m}$  diameter). The minimal focal spot for these TEM settings was about 15 nm. For the effective electron spot diameters during the U-CBED experiment, additional contributions such as beam defocussing, and sample and beam drifts need to be considered. The specimen was mounted in a JEOL double-tilt holder, which was rotated by about  $-34^\circ$  around the holder axis (i.e., laboratory-fixed  $X$ -axis) and  $3^\circ$  around the rotated  $Y$ -axis. All diffraction patterns were recorded on a charge-coupled device camera (Gatan UltraScan 4000), binned to  $1024 \times 1024$  pixels (0.164 mrad per pixel angular resolution) with an indicated projection camera length of 25 cm. Images are acquired with 60-s exposure time and  $4 \times 4$  binning in 2 or 10 ps

time steps for the 160-ps long and 1000-ps long delay scan, respectively. Similar probe positions in a distance of approximately 170 nm from the long platinum edge are chosen in both delay scans.

### 7.6.3 Extraction of Bragg-scattered line profiles

For the analysis of the Bragg-scattered line profiles in the ultrafast convergent beam electron diffraction experiments, each single diffraction image is centered with respect to the central disk. Rectangular regions of interest (ROI) around the Bragg lines with one edge parallel to the respective Bragg line are defined. Afterwards, the scattered intensity across the full Bragg line, the line position, and spatial width are extracted from each ROI using a Lorentzian fit that includes a linear offset. The linear background is subtracted from the experimental Bragg-scattered line profiles. Fluctuations in the electron beam current over time are compensated by normalization to the spatially integrated intensity in the central disk of each diffractogram. Although we only present the results of a single measurement, the Bragg line shifts were highly reproducible, as shown in Fig. 7.8. No averaging over scans is performed in the data analysis.

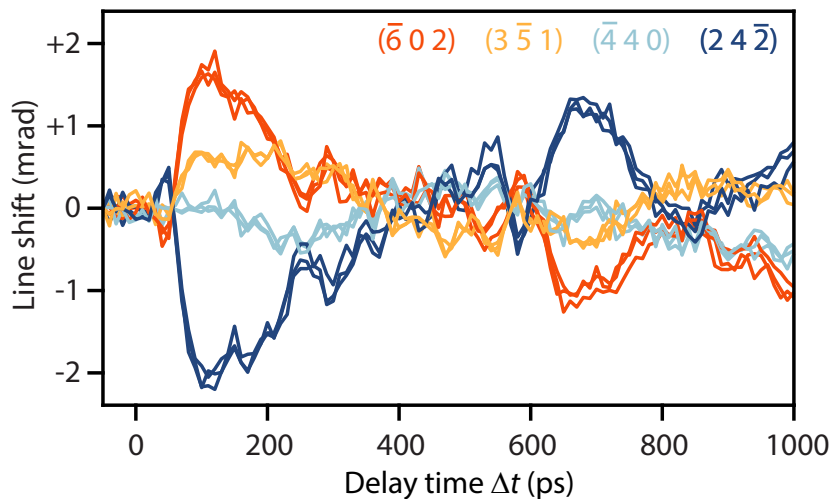


**Figure 7.8:** Delay-dependent angular shifts of exemplary Bragg lines shown for three repetitions of 1000-ps long delay scans (typical measurement time of each scan about 2 h). Both, the overall behavior and small-amplitude high-frequency oscillations are well reproduced across the different delay scans.

### 7.6.4 Convergent beam electron diffraction pattern

The positions and inclination angles of deficit and excess Bragg lines in a diffraction pattern obtained with a convergent electron beam are linked to the size, shape, and orientation of the local crystal unit cell at the electron probing position. The real-space basis  $\mathbf{B}_u^{\text{sample}} = (\mathbf{a}_1 \ \mathbf{a}_2 \ \mathbf{a}_3)$  of the silicon unit cell in the sample-fixed coordinate system ( $x$ ,  $y$ , and  $z$ ) (cf. Fig. 7.2a) is defined by unit vectors  $\mathbf{a}_1 = \frac{a_{\text{Si}}}{\sqrt{2}} (1 \ 1 \ 0)^T$ ,  $\mathbf{a}_2 = \frac{a_{\text{Si}}}{\sqrt{2}} (1 \ -1 \ 0)^T$ , and  $\mathbf{a}_3 = a_{\text{Si}} (0 \ 0 \ 1)^T$ , with the silicon lattice constant [429]  $a_{\text{Si}} = 5.43 \text{ \AA}$ . To account for a tilted sample orientation, a rotation matrix  $\mathbf{R} = \mathbf{R}_X(\alpha) \cdot \mathbf{R}_Y(\beta) \cdot \mathbf{R}_Z(\gamma)$  is applied that is constructed from individual matrices  $\mathbf{R}_X$ ,  $\mathbf{R}_Y$ , and  $\mathbf{R}_Z$  corresponding to rotations around the laboratory-fixed  $X$ ,  $Y$ , and  $Z$  coordinate axes<sup>2</sup>. For the orientation of the coordinate system relative to the microscope column, see Fig. 7.2a. The rotated real-space unit cell basis in the laboratory-fixed coordinate system is given by  $\mathbf{B}_u^{\text{lab}} = \mathbf{R}\mathbf{B}_u^{\text{sample}}$ . The reciprocal basis  $\mathbf{G}_u^{\text{lab}}$  is obtained from the identity  $\mathbf{G}_u^{\text{lab}}\mathbf{B}_u^{\text{lab}} = \mathbf{1}$  (in the  $1/\lambda$ -convention). Reciprocal lattice vectors  $\mathbf{G}$  with Miller indices  $h$ ,  $k$ , and  $l$  are consequently expressed as  $\mathbf{G} = \mathbf{G}_u(hkl)^T$ . Bragg diffraction [345] is observed if the incident and scattered electron wavevectors  $\mathbf{k}_0$  and  $\mathbf{k}$  differ by a reciprocal lattice vector of the diffracting crystal, i.e.,  $\mathbf{G} = \mathbf{k} - \mathbf{k}_0$ . Employing elastic scattering and assuming small scattering angles, the expression  $-G^2/2 = k_0G = k_{0,X}G_X + k_{0,Y}G_Y + k_{0,Z}G_Z$  between the components of  $k_0$  and  $G$  is obtained. Applying  $k_{0,X}$ ,  $k_{0,Y} \ll k_0$  and  $k_X$ ,  $k_Y \ll k$  (paraxial approximation for the optical axis oriented along  $Z$ ), the scattering condition can be linearized, yielding

$$-\frac{G^2}{2} = k_X G_X + k_Y G_Y + k_0 G_Z \quad (7.2)$$

with  $G^2 = G_X^2 + G_Y^2 + G_Z^2$ .  $[k_X, k_Y]$  describe straight lines in the transverse  $k$ -space for each  $G$ , along which incident electron intensity is scattered out to larger angles. The resulting excess Bragg lines have a distance

$$r_G = \frac{-G^2/2 + k_0 G_Z}{\sqrt{G_X^2 + G_Y^2}} + \sqrt{G_X^2 + G_Y^2} \quad (7.3)$$

<sup>2</sup>The sample orientation is retrieved from a comparison between recorded and simulated diffraction patterns as follows:

160 ps delay scan:  $\alpha = 25.09^\circ$ ,  $\beta = -0.30^\circ$  and  $\gamma = -4.66^\circ$ ;

1000 ps delay scan:  $\alpha = 25.18^\circ$ ,  $\beta = -0.63^\circ$  and  $\gamma = -5.41^\circ$ .

from the center of the diffraction pattern. Angular line shifts are retrieved by division of Eq. (7.3) with the wavenumber  $k_0$  of the incident electron beam.

In the present work, we quantify the optically induced structural distortion of the silicon membrane by a deformation gradient tensor  $F$  with spatiotemporal dependency [329]. Within linear elasticity theory, the application of  $F(\Delta t) = \boldsymbol{\epsilon}(\Delta t) + \boldsymbol{\omega}(\Delta t) + \mathbf{1}$ , where  $\boldsymbol{\epsilon}$  and  $\boldsymbol{\omega}$  are the symmetric shear and antisymmetric rotation tensors, respectively, leads to a deformed unit cell basis of the form  $\mathbf{B}_F^{\text{lab}} = \mathbf{R} \cdot \mathbf{F}^{\text{sample}} \cdot \mathbf{B}_u^{\text{sample}}$  and a new reciprocal lattice basis  $\mathbf{G}_F^{\text{lab}} = (\mathbf{B}_F^{\text{lab}})^{-1}$ . The tensors are a function of the displacement gradients of the displacement vector  $u$  along the coordinate axes. In linear approximation, we write:

$$\epsilon_{ij} = \frac{1}{2} \left( \frac{\partial u_i}{\partial x_j} + \frac{\partial u_j}{\partial x_i} \right), \quad \omega_{ij} = \frac{1}{2} \left( \frac{\partial u_i}{\partial x_j} - \frac{\partial u_j}{\partial x_i} \right),$$

with  $i, j \in (x, y, z)$ .

### 7.6.5 Line sensitivity to specific tensor components and reciprocal lattice vector components

Generally, the Bragg line positions  $r_G$  depend nonlinearly on the reciprocal lattice vector and tensor components. Assuming only small tensor components  $F_{ij}$ , the relation can be linearized in the form

$$\Delta r_G = \sum_{i,j} \frac{\partial r_G}{\partial F_{ij}} \Delta F_{ij}, \quad (7.4)$$

considering components  $F_{ij} = \delta_{ij} + \Delta F_{ij}$ , where  $\delta_{ij}$  is the Kronecker delta and  $\Delta F_{ij}$  is a small number in each tensor component separately. The difference quotients  $\frac{\partial r_G}{\partial F_{ij}}$  can be computed either analytically or approximated numerically. The results  $\frac{\partial r_G}{\partial F_{ij}}$  for  $n$  selected Bragg lines and  $m$  tensor components can be aggregated in a  $n \times m$  matrix  $\mathbf{A}$ . Inserting numerically calculated tensor components (cf. supplementary material 7.6.7) in Eq. (7.4), the time-dependent shift of selected Bragg lines can be predicted, as shown in Fig. 7.4c.

Extracting, in turn, the time-dependent displacement gradient tensor  $F$  from the experimentally observed angular Bragg line shifts would require matrix  $\mathbf{A}$  to have a numerically stable inverse. However, it is found that even small variations in the line shift on the order of 0.05 mrad already have a strong impact on the retrieved tensor, indicating that a full reconstruction of the tensor  $F$  from the experimental line shifts is not possible based on diffraction data recorded for a single sample orientation. To construct the tensor component subspace to which the experiment is still sensitive, we perform a singular

value decomposition  $\mathbf{A} = \mathbf{U} \cdot \mathbf{S} \cdot \mathbf{V}^T$  of the matrix  $\mathbf{A}$ , with unitary matrices  $\mathbf{U}$  and  $\mathbf{V}$ , and the diagonal matrix  $\mathbf{S}$  (see supplemental source code for numerical results).  $\mathbf{V}$  contains a set of  $m$  basis vectors of the tensor component vector space, which by the action of  $\mathbf{A}$  are stretched by a factor  $S_{mm}$ . Thereby, basis vectors with small  $S_{mm}$  do not result in an appreciable Bragg line shift and cannot be accurately reconstructed from the experimental line shift. Considering an experimental accuracy of the recorded shifts of about  $\Delta r_{\min} = 0.05$  mrad, only two basis vectors in  $\mathbf{V}$  correspond to distortions for which the experiment yields a sensitivity of better than  $r_{\min}/S_{11,22} < 10^{-5}$ . For a third vector, a sensitivity of about  $6.4 \times 10^{-4}$  is found, and worse than  $3.1 \times 10^{-3}$  for all other basis vectors. For a comparison of these tensor sensitivities to the magnitude of the expected tensor components, see Fig. 7.4a.

An intuitive interpretation of the basis vectors, to which the experiment is most sensitive, is gained by transforming the calculated base vectors in  $\mathbf{V}$  into the laboratory coordinate system, using the rotation matrix  $\mathbf{R}$ . It is observed that line shifts are predominantly governed by the gradient displacement components  $F_{XZ}$ ,  $F_{YZ}$ , and, to a lesser extent, also by  $F_{ZZ}$ . These tensor components  $F_{iZ} = \delta_{iZ} + \frac{\partial u_i}{\partial Z}$  correspond to changes in the displacement vector along the  $Z$ -axis, i.e., parallel to the electron beam.

A general picture on the sensitivity of line shifts in U-CBED is obtained by considering their response to changes in the reciprocal lattice vectors:

$$\Delta r = \sum_{i=X,Y,Z} \frac{\partial r}{\partial G_i} \Delta G_i. \quad (7.5)$$

Here,  $\Delta G_i = G_{i,F} - G_{i,0}$  is the difference of the reciprocal lattice vector component  $i$  after and before the application of the deformation gradient tensor  $F$ . From Eq. (7.3) for the excess Bragg line positions, the following partial derivatives are obtained:

$$\begin{aligned} \frac{\partial r}{\partial G_X} &= \frac{(G^2/2 - k_0 G_Z) \cdot G_X}{(G_X^2 + G_Y^2)^{3/2}} \\ \frac{\partial r}{\partial G_Y} &= \frac{(G^2/2 - k_0 G_Z) \cdot G_Y}{(G_X^2 + G_Y^2)^{3/2}} \\ \frac{\partial r}{\partial G_Z} &= \frac{-G_Z + k_0}{\sqrt{G_X^2 + G_Y^2}}. \end{aligned} \quad (7.6)$$

Since  $(G^2/2) \approx k_0 G_Z$ ,  $\frac{\partial r}{\partial G_{X,Y}}$  can be neglected and line shifts  $\Delta r$  are dominated by  $\partial r / \partial G_Z$ .

Due to the deformation given by  $\mathbf{F}$ , the reciprocal basis matrix  $\mathbf{G}_u^{\text{lab}}$  changes to

$\mathbf{G}_F^{\text{lab}} = \mathbf{G}_u^{\text{lab}} (\mathbf{F}^{\text{lab}})^{-1}$ . Therefore,  $\Delta G_Z$  is only influenced by the last column of  $\mathbf{F}^{\text{lab}}$ , which may contain a dilatational component along the  $Z$ -direction ( $F_{ZZ}$ ) or shear-rotational components perpendicular to the  $Z$ -axis ( $F_{XZ}$  and  $F_{YZ}$ ). For the case of static residual strains in heterogeneous materials, it was demonstrated that an unambiguous tensor measurement can be obtained by CBED tomography using three independent projection axes [456].

### 7.6.6 Theoretical description of Bragg line profiles

Considering only single scattering events (kinematical approximation) and a monochromatic, spatially coherent incident electron wave, the wavefield  $\hat{\psi}(k)$  after sample interaction can be approximated by a superposition of wave components with wave vectors  $\mathbf{k}$ , each with an amplitude proportional to  $f(\Delta\mathbf{k}) = \pi \int d^3r e^{-2\pi i \Delta\mathbf{k}r} \rho(\mathbf{r})$  [329]. Here,  $\rho(\mathbf{r})$  is the interaction potential experienced by the electron when transversing the crystal, and  $\Delta\mathbf{k} = \mathbf{k} - \mathbf{k}_0$  is the momentum change between the incident and the scattered electron wave.

For an idealized crystal, the potential  $\rho(\mathbf{r})$  is given by the product of a function describing the infinite lattice  $l(\mathbf{r})$  and a shape function  $s(\mathbf{r})$  which defines the shape and extent of the nanocrystal (e.g., the finite Si membrane thickness):  $\rho(\mathbf{r}) = s(\mathbf{r})l(\mathbf{r})$ . Local displacements  $u(\mathbf{r})$ , arising for example from propagating Lamb waves, change the lattice function into  $l(\mathbf{r} + \mathbf{u}(\mathbf{r}))$  such that  $f(\Delta\mathbf{k})$  in the vicinity of reciprocal lattice vectors  $\mathbf{k} \approx \mathbf{G}$  is modulated by an additional phase factor  $\exp\{i\phi\}$  containing the projection of the displacement field onto  $\mathbf{G}$  [449]. The strained crystal therefore imprints a phase modulation on the electron exit wave, resulting in diffracted intensities  $I(\Delta\mathbf{k} - \mathbf{G}) \propto |\mathcal{F}(\exp\{i\mathbf{G} \cdot \mathbf{u}(\mathbf{r})\})|^2$ .

### 7.6.7 Numerical simulation of structural dynamics in Pt-stripe/Si-membrane heterostructure

To obtain a better understanding of the spatiotemporal acoustic wave propagation, we numerically solve the two-dimensional elastodynamic wave equation using finite-element simulations in COMSOL Multiphysics [457]. For the sample geometry, we consider an infinitely extending Pt-stripe on a Si-membrane imposing a plane strain ansatz and a mirror symmetry plane ( $xz$ -plane) along the platinum stripe. The membrane and stripe thickness and stripe width are adopted according to the experimental dimensions.

The presence of the nominally 1-nm thin chromium adhesion layer is neglected. In order to reduce computation time, the silicon membrane is truncated 6  $\mu\text{m}$  away from platinum stripe instead of 100  $\mu\text{m}$ . For the given sound velocities and the chosen geometry dimensions, no acoustic wave reflections from the simulation box boundaries are expected within the first nanosecond.

Since acoustic sound velocities in silicon depend on the wave propagation direction, we employ a symmetry-adapted stiffness tensor. Specifically, the rotated stiffness tensor  $C_{\text{rot}}$  in Voigt-notation (with the  $x$  and  $y$  coordinates pointing along the  $[110]$ - and  $[\bar{1}10]$ -directions) is obtained from the conventional stiffness tensor by a basis change  $C_{\text{rot}} = K \cdot C \cdot K^T$ . For silicon, the standard components in  $C$  are  $C_{11} = 166$  GPa,  $C_{12} = 64$  GPa,  $C_{44} = 80$  GPa [429, 430]. For the definition of  $K$ , see Ref. [458]. For platinum, isotropic elasticity properties [429] are assumed, governed by Young’s modulus  $E = 168$  GPa, Poisson’s ratio  $\nu = 0.38$  and mass density  $\rho = 21\,450$  kg/m<sup>3</sup>.

The simulation is carried out using a combination of the COMSOL “Solid State” and “Heat Transfer in Solids” modules to solve for the time-dependent heat transfer and structural dynamics in the heterogeneous system. The absorbed laser power per unit volume at a pump wavelength of 800 nm is modeled as a depth- and time-dependent heat source  $Q$  in the platinum layer. The parameters of the heat source are defined by the optical absorption coefficient of platinum [459] ( $a_c = 1.2688 \cdot 10^6/\text{cm}$ ), the optical reflectivity ( $R_{\text{Pt}} = 0.97$ , p-polarized) at the employed wavelength and incidence angle, a laser fluence of 8.5 mJ/cm<sup>2</sup> estimated from experimental parameters, and considering a laser pulse duration of 100 fs (FWHM). The thermal coupling between the two media is defined by the Kapitza thermal boundary resistance [460]  $R_{\text{th}} = 1.1 \cdot 10^{-8}$  m<sup>2</sup>·K/W. For the adopted thermal resistance, the initial temperature difference between platinum and silicon in the bilayer region drops to 10 % after about 500 ps. During the simulation time of 1 ns, a substantial lateral temperature gradient persists within the silicon membrane. For matching the amplitude of the simulated structural dynamics with the experimental data, the displacement field was scaled by a factor of 5.4 (cf. Fig. 7.9). This scaling factor may account for an increased absorbed energy in the bilayer system due to optical interferences not included in the numerical simulation. The scaled maximum temperature increase of about 300 K as obtained in the simulation is in reasonable agreement with the temperature change extracted from the Debye Waller analysis (cf. supplementary material 7.6.9). Additional effects such as the detailed mechanical coupling of the two material layers and a potential (non-)thermal hot electron distribution in the silicon membrane are

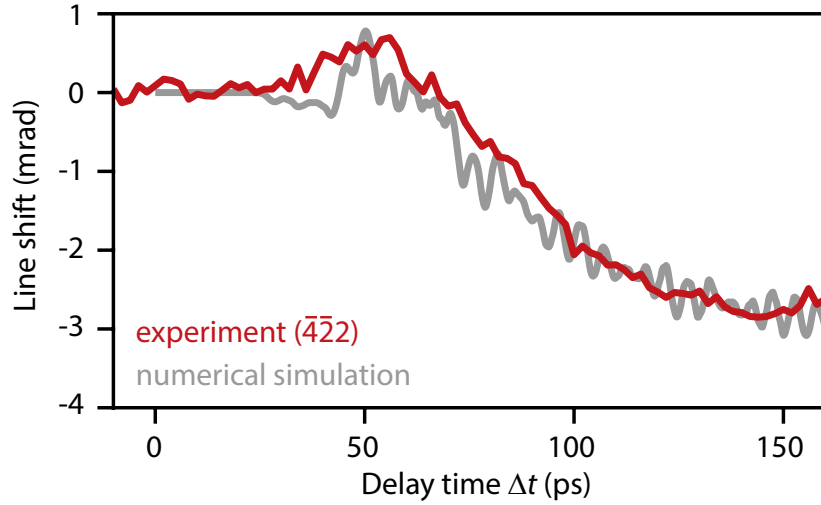


**Figure 7.9:** Determining scaling factor of the numerical results. For matching the experimental Bragg line shifts, the calculated displacement fields are scaled by a factor of 5.4. A comparison between experimental and scaled calculated results is shown for the  $(\bar{4}\bar{2}\bar{2})$  Bragg line shift.

expected to affect the time-dependent distortion to some extent but are not considered in detail here.

Experimentally, it was found that the silicon membrane in the vicinity to the platinum stripe is bent by about  $5^\circ$  due to the preparation process. Including a corresponding initial stress distribution in the structural dynamics simulation did not substantially influence the predicted Bragg line shifts.

The numerically obtained strain field can be decomposed into a superposition of propagating waves by performing a spatial and temporal Fast Fourier transform (FFT) of the simulated displacement field. Specifically, the mean value of the displacement components  $u_x$  and  $u_z$  along the  $z$ -axis is calculated for the first 1000 nm next to the platinum stripe and the first 400 ps after optical excitation. For evaluating the Fourier transform, the obtained spatiotemporal displacement maps are smoothed by a supergaussian window centered at a distance of 500 nm and a temporal delay of 200 ps. The signal of the individual FFTs is normalized to the maximum amplitude found in localized high-frequency resonances, yielding the results shown in Figs. 7.5b and 7.5c.

### 7.6.8 Acoustic Lamb wave description for anisotropic silicon

To derive the dispersion of acoustic waves in a crystalline thin film, the elastodynamic equation of motion with traction free mechanical boundary conditions at the membrane

surfaces needs to be solved [284, 285]. For single-layer isotropic media or high symmetry directions in anisotropic materials (as in the chosen silicon membrane), the solutions of this guided wave problem are so-called Lamb waves [40, 282] which are superpositions of quasi-longitudinal and -transverse bulk waves and are classified as symmetric (S), antisymmetric (A), and shear-horizontal (SH) waves. Symmetric Lamb waves are also termed dilatational waves, and antisymmetric waves flexural waves, due to their overall impact on the membrane deformation.

The corresponding dispersion relations for the generally infinite number of symmetric and antisymmetric modes are in the isotropic case given by an explicit characteristic function called Rayleigh-Lamb equation [284, 285]:

$$\frac{\tan(hk_z^l + \alpha)}{\tan(hk_z^t + \alpha)} = \frac{k_z^t}{k_z^l} \left( 1 - \frac{\omega^4}{4k^2 (k_z^t)^2 \cdot v_t^4} \right), \quad (7.7)$$

with parameters

$$(k_z^l)^2 = \frac{\omega^2}{v_l^2} - k^2 \quad \text{and} \quad (k_z^t)^2 = \frac{\omega^2}{v_t^2} - k^2. \quad (7.8)$$

Here,  $k_z^l$  and  $k_z^t$  are the out-of-plane wavevector components for longitudinal and transverse acoustic waves given for an angular wave frequency  $\omega = 2\pi f$ , in-plane wave vector  $\mathbf{k}$ , and acoustic sound velocities  $v_l$  and  $v_t$ . The sample thickness  $d$  is included in variable  $h = d/2$ . Symmetric and antisymmetric modes are separated by choosing  $\alpha = 0$  and  $\alpha = \pi/2$ , respectively. Since no analytic expression for the various branches of the dispersion curve exists, numerical root-finding algorithms need to be implemented to solve for the Lamb in-plane wavenumber at a given frequency.

For anisotropic materials, however, the quasi-longitudinal and -transverse bulk sound velocities depend on the propagation direction. Similar expressions as the Rayleigh-Lamb wave dispersion equations for isotropic media are in particular obtained for mode propagation in symmetry directions [461]:

$$\frac{\tan(hk_z^l)}{\tan(hk_z^t)} = Q. \quad (7.9)$$

$Q$  is an explicit expression containing  $k_z^t$  and  $k_z^l$ , and the elastic properties of the medium.

For the silicon membrane with Lamb wave propagation along the [110]-direction discussed in the main text, we used the free software suite *Dispersion Curve* (DC) [298] developed by Armin Huber to trace the dispersion curves of the decoupled symmetric

and antisymmetric Lamb modes (for details see also Ref. [306]). Dispersion curves for frequencies  $f$  up to 300 GHz and corresponding wavenumbers  $k$  up to 0.4/nm are displayed in Fig. 7.6a. It is confirmed that the expected limiting behavior [284] of the Lamb wave dispersion is recovered, such as

1. the cut-off frequency  $\times$  plate thickness products are equal to even or odd multiples of half of the sound velocities [284]  $v_l = 8433$  m/s and  $v_t = 5843$  m/s,
2. phase velocities  $c_p = \frac{\omega}{k}$  of the  $A_0$  and  $S_0$  branch in the large- $k$  region approach the Rayleigh wave velocity  $v_R = v_t \cdot (0.718 - (v_t/v_l)^2)/(0.75 - (v_t/v_l)^2) = 5150$  m/s (approximation by Viktorov, Ref. [462]),
3. the phase velocity of the  $S_0$  branch in the small- $k$  region [315] reaches  $\sqrt{(C_{11}^2 + C_{11}C_{12} - 2C_{12}^2 + 2C_{11}C_{44})/(2C_{11} \cdot \rho)} = 8533$  m/s.

For comparison of numerically solved displacement fields with a Lamb wave superposition, through-thickness profiles at the bilayer resonance frequencies were extracted from the DC software, considering all dispersion branches shown in Fig. 7.5a. These profiles with individual propagation-induced phase terms are superimposed and the mean displacements extracted from the numerical simulations are added. Excluding the lowest-order 65.2 GHz resonance frequency, the dispersion field  $u_x$  in Fig. 7.6b is qualitatively in good agreement with the Lamb displacement superposition in Fig. 7.6c in the main text. Following the same procedure for  $u_z$ , a further simplification to only five displacement fields is possible, i.e., selecting the wavenumbers for frequencies 163.4 GHz on the  $A_0$ ,  $S_0$ ,  $A_1$ , and  $S_1$  branches and 208.0 GHz on  $A_0$ . The result is displayed in Fig. 7.10. We note that generally the Lamb wave dispersion depends on the static stress exerted on the membrane [274], which could lead to small changes in the observed  $k/f$ -dependence.

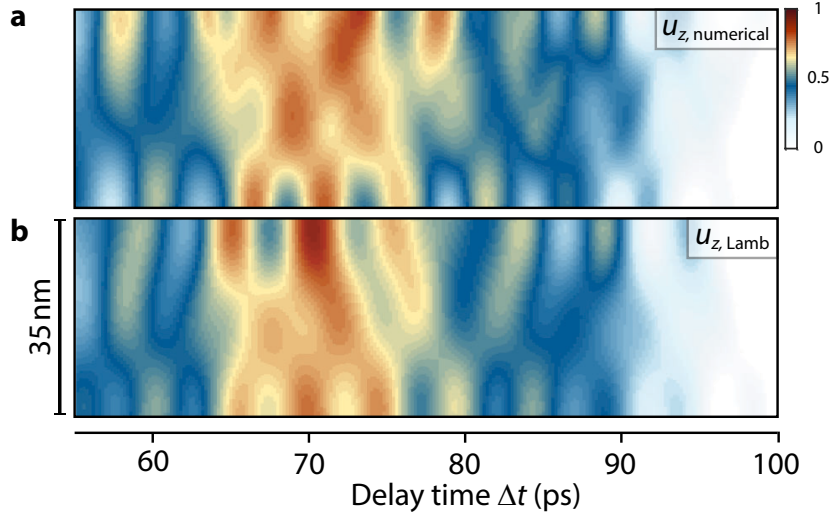


**Figure 7.10:** Comparison of the numerically obtained displacement field (a) within the silicon membrane along the  $z$ -direction with corresponding results based on a Lamb wave superposition (b). Choosing a selection of Lamb modes at the specific resonance frequencies of the Pt/Si bilayer system (as indicated in Fig. 7.6a), the analytical superposition is in good agreement with the numerical results regarding spatial inhomogeneity and displacement oscillations.

### 7.6.9 Debye Waller analysis

In order to extract the optically induced temperature rise of the 2- $\mu\text{m}$  wide polycrystalline platinum stripe on the silicon membrane, the decrease of the integrated diffraction intensity  $I$  in the Debye-Scherrer rings is acquired with a collimated electron beam (approx. 2.4- $\mu\text{m}$  spot diameter). For the (113)-ring, a total diffracted intensity change by 7.5% is observed at the same incident optical fluence as applied in the U-CBED experiment (see Fig. 7.11). To differentiate the temperature-dependent Bragg peak intensity and a broader diffuse background, we only consider a small scattering angle width around the (113)-ring for determining the diffracted intensity. The observed intensity drop corresponds to an optically induced increase of the lattice temperature from 300 K to about 506 K. Up to 70 ps after optical excitation, we did not observe a recovery of the ring intensity, in agreement with 500-ps-scale cooling time obtained numerically. The extracted effective electron-phonon coupling constant of 1.3 ps is in reasonable agreement with previous pump-probe experiments [416, 424, 463], given the chosen delay steps of 1 ps and 700-fs electron pulse length. Furthermore, we confirmed that no irreversible structural changes occur up to an incident optical fluence of 14 mJ/cm<sup>2</sup>.

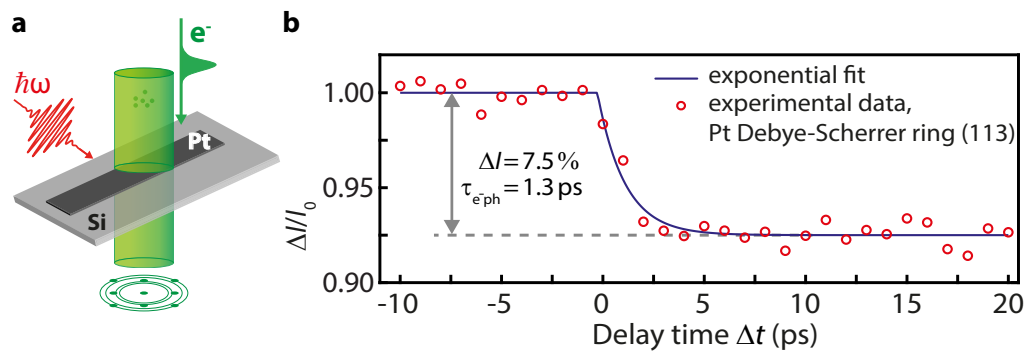


**Figure 7.11:** Debye Waller analysis for the Pt/Si bilayer region. (a) Sketch of the experimental geometry for recording ultrafast parallel electron beam diffraction on the Pt/Si bilayer region. The diffraction pattern consists of a superposition of Bragg spots and Debye-Scherrer rings originating from silicon and platinum, respectively. (b) Delay-dependent intensity of the Pt (113) Debye-Scherrer ring after optical excitation. Adapting a single-exponential transient yields a platinum temperature increase of about 200 K. Within the first 20 ps, no subsequent temperature decrease is observed demonstrating that heat transfer to the underlying silicon membrane occurs on longer time scales.

### Summary and perspectives

---

The work performed in this thesis addressed challenges in UTEM imposed by nanoscale electron pulses containing high charge densities (Chapter 3) and tackled the complexity of ultrafast structural dynamics in confined heterostructures (Chapters 6 and 7). Enabled by both mathematical models and experimental investigations of Coulomb interactions and nanophononic wavefields, we have reported on the following main achievements:

1. We have demonstrated the control over longitudinal and transverse properties of electron pulses photoemitted from a laser-driven Schottky field emitter and have presented a guideline for optimizing electron source parameters in similar nanoscale photocathodes.
2. By patterning a semiconductor membrane, we have established a tailored source with a well-defined excitation gradient for launching nanoscale acoustic wavefronts.
3. Applying an analytical mode description in the framework of linear elasticity theory, we have derived universal expressions for explicitly predicting acoustic resonance frequencies in elastically mismatched metal/semiconductor bilayer systems.
4. We have successfully complemented nanoscale diffractive probing with a sensitivity analysis of experimentally accessible strain field components and identified the macroscopic origin of the spatiotemporal strain dynamics in our model heterostructure. We have validated the origin of inhomogeneous structural dynamics as a superposition of Rayleigh-Lamb modes at the resonance frequencies of the bilayer system.

In the remaining part of the conclusion, more details on these four principle milestones are given.

**Details on work presented in Chapter 3** By exploiting the key advantage of utilizing a localized single-photon photoemission process (section 3.2), we have quantitatively accessed the impact of Coulomb interactions on spatial, spectral, and temporal pulse properties, and disentangled stochastic and mean-field effects (milestone 1). We have shown that transverse electron properties are governed by a stochastic emittance growth (section 3.4), whereas Coulomb-induced spectral broadening (section 3.4) is a mean-field space-charge effect. The experimentally observed linear growth of focal spot sizes and energy widths with an increasing number of electrons per pulse is corroborated by multiparticle simulations (section 3.6). Stretching optical photoemission pulses, small electron foci from the low-charge regime are recovered. As obtained from simulations, considerable Coulomb forces act only within the first 4  $\mu\text{m}$  of the propagation distance (section 3.7): 80 % of the spectral broadening is gained in about 1 % of the total distance in the emitter assembly. Since this is much shorter than length scales of temporal pulse broadening depending slightly sub-linearly on the imprinted energy width (section 3.5), the spectral broadening can be treated as quasi-instantaneous. For the limit of large energy widths, the pulse duration depends linearly on the energy width and the chirp is obtained as the inverse shear, which is well-described by an analytical model (section 3.7).

**Details on work presented in Chapter 6** In the second part of the work (milestone 3), we have explored the impact of boundary conditions on optically induced strain fields, which has led to the following important findings for our reference model: Different from breathing modes in homogeneous monolayer materials at a single resonance frequency, multifrequency strain dynamics are optothermally induced in both layers due to interlayer strain coupling. Changing the impedance matching or the individual thicknesses allows for tuning of frequency components in the wave field. For strongly mismatched bulk material properties, we demonstrated the emergence of spatially localized phonon eigenmodes.

**Details on work presented in Chapter 7** In the third part of the work (milestones 2 and 4), we demonstrated that U-CBED serves as a unique tool in the field of nanophononics by giving quantitative access to optically induced coherent lattice dynamics with nm/ps spatiotemporal resolution. Applied to a Pt/Si-heterostructure (section 7.2), U-CBED has delivered the following main results supported by numerical simulations: We conclude that the lattice dynamics in our heterostructure are governed by local rotations with minor strain and shear contributions (section 7.3). An analysis of linear combination of tensor

components (section 7.3) revealed an experimental sensitivity to two shear-rotational motions perpendicular to the  $z$ -axis and to vibrations along the  $z$ -axis along the electron beam direction. Bragg-scattered line profiles indicated inhomogeneous structural dynamics within the depth of the membrane. By analyzing the Fourier-amplitude of the mean spatiotemporal displacement field, we verified that these microscopically originate from acoustic resonance frequencies of the Pt/Si bilayer system. Accordingly, a reconstruction of the complete displacement field is achieved by a superposition of the Rayleigh-Lamb modes (section 7.4).

In the section that follows, a few topics are discussed that address unresolved challenges with laser-driven electron sources and viewpoints on future UTEM experiments in the field of nanophononics.

## 8.1 Future developments of laser-driven electron sources

Based on the systematically characterized pulse properties (see Refs. [71, 173] and Chapter 3), several source optimization aspects are relevant for further improvement of time-resolved electron microscopy. These include ongoing development work on the laser-driven ZrO/W emitter, but also new designs of photoemission sources based on electrically biased (311)-oriented tungsten emitters, yielding longer transverse coherence lengths and possibly longer longitudinal coherence lengths. Furthermore, the gained sound understanding of the mechanism of pulse broadening allows for active pulse compression schemes that result in lower final electron pulse durations and chirp.

### 8.1.1 Perspectives for laser-driven ZrO/W emitters

For the laser-driven Schottky emitter, we suggest the following improvement pathways:

**Nanoscale facets:** The geometric shape of the ZrO/W emitter affects the effective field strength at the tip and is a significant parameter in the characterization of the electron source through beam emittance and brightness as a figure-of-merit. The shape of the tip, and thus the electron emission generally changes over time. Especially at high temperatures, where diffusion processes take place, the shape of the tip can change significantly if large electrostatic fields are applied. By optimization of established conditioning procedures, variations of the size and shape of the facets are feasible, which would maximize the emission current and lead to a high beam brightness at small emittance values that remain stable at reduced temperatures.

**Stable photoemission:** Stroboscopic investigations of reversible dynamics with low-dose electron pulses require a long temporal stability of the photoemission current at low temperatures of the Schottky emitter operated in photoemission mode. The presented time-resolved diffraction data has been acquired with unchanged focusing of the laser beam on the tip at 250-kHz repetition rate. All diffractograms were integrated for 60 s. The delay time scans consisted of 85 (160-ps delay scan) to 105 (1000-ps delay scan) data points resulting in a measurement time of about 2 h each. Within the first two hours of the long delay scan, a 35-% decrease in emissions has been observed, which can be attributed to the shortening of the tip during cooling. Thereafter, the emission current still dropped about 20 % with each further full delay scan, which can be explained by the persistent length change of the tip and a changing work function of the emitter due to adsorbates. For future two-dimensional strain mappings requiring a better long-term stability, the

emitter should therefore be operated in excellent vacuum conditions ( $p < 10^{-10}$  mbar), as is the case for cold field emitters.

**Wavelength for photoemission pulses:** In the linear photoemission process, the initial kinetic energy spread of the electron pulses is mainly governed by the maximal excess energy. Assuming a work function of 2.7 eV for the W(100) front facet (see Chapter 2), UV laser pulses at a central wavelength of 400 nm yield an initial energy spread of 0.4 eV between electrons emitted from the Fermi level or emitted from lower states. This spread can consequently be minimized by illuminating the Schottky tip apex with longer central wavelengths closer to the work function. Since the detailed mechanisms of the work-function changes are unclear, a tunable laser system to vary the wavelength of the photoemission pulses is useful. An investigation of the number of emitted electrons and the energy width of the electron pulses for varying extraction fields might yield deeper insights and operation schemes for future laser-driven electron sources. This has already been done for a few field variations at the Göttingen UTEM (see [113]), but a deeper analysis promises a more comprehensive understanding.

### 8.1.2 Novel pulsed electron sources based on tungsten tips

While the development of the laser-driven Schottky field emitter has allowed to perform unique time-resolved experiments [110, 111, 116, 119, 120, 234] which would not have been possible on the previous generation of UTEMs, advanced phase-sensitive imaging techniques, such as electron holography, urgently need a further improvement in electron coherence towards fully coherent electron pulses. To this end, cold-field emission guns (CFEGs) which are based on quantum mechanical tunneling of electrons through a static potential barrier into vacuum (see Chapter 2) are a promising candidate due to record brightness values and the low energy spread in conventional operation mode [130, Ch. 4.1]. For the first implemented laser-driven cold-field field emitter, ultrashort electron pulses with a duration of 400 fs and an energy spread close to 1 eV have been achieved for nanometer-size foci [80]. Although contaminations of the tip can drastically change the emission current, well-defined flashing procedures to elevated temperatures of about 2500 K have been developed and are now routinely used, which also overcome conditioning challenges of laser-driven ZrO/W tip emitters.

Outside TEM, laser-driven electron emission from tungsten nanotips [82–84, 108, 172, 464, 465] has in the past already been employed in ultrafast electron diffraction [75]

and in femtosecond point projection microscopy [207]. In contrast to single-photon photoemission from Schottky field emitters, different photoemission regimes have been studied for tungsten tips. For nonlinear photoemission, the confined electron emission is discussed in terms of multiphoton electron emission [83, 84, 108, 465, 466] or optical field emission [82, 464]. Recent work on highly-biased tungsten photocathodes with 400-nm photoemission pulses demonstrated that tungsten tips can also be operated in the linear photoemission regime, yielding highly coherent photoelectron bunches with a negligible dc tunneling component [153]. Different from conventional operation mode, in which electrons are emitted from the tungsten [310] front facet with the lowest work function (4.32 eV) among crystal planes typical for tungsten [231], photoemission over the Schottky-lowered barrier was attributed to crystal planes with work functions up to 4.8 eV. Despite of resulting larger emission angles, a back-projected source size below 1 nm was achieved in photoemission mode, which is close to previously published values for dc field emission from tungsten tips [467] and significantly smaller than the geometrical tip radius. By employing the tungsten tip emitter at moderate Schottky-induced work function reduction and at photoemission photon energies of about 3.5 to 4 eV, a pulsed electron source with predominant emission from the [310] crystallographic plane yielding transverse beam properties comparable to continuous cold-field electron emitters should be achievable.

### 8.1.3 Pulse compression schemes

As already outlined in Chapters 2 and 3, the dispersive propagation of electron pulses with higher electron densities leads to a temporal spreading and spectral broadening of the electron pulses. This close correlation can be explained by Coulomb forces that lead to a shearing of the electron pulse in longitudinal phase space. Maintaining short pulse durations at increased pulse charges therefore requires high acceleration fields and schemes to recompress the longitudinal phase-space distribution. Indeed, by applying a time-dependent electric field in the longitudinal direction, fast electrons at the front of the pulse are decelerated, and slow electrons at the back of the pulse are accelerated. As a result of this velocity-bunching scheme, the electron chirp can be compensated. Afterwards, the dispersive propagation of the electron pulse in field-free space leads to a temporal focus at a distance controlled through the chirp. In accordance with Liouville's theorem (preservation of the populated phase space volume [180]), the energy spread increases proportionally with the compression in time.

Conventional recompression strategies for UED setups often employ radio-frequency cavities that generate a few-GHz oscillatory field synchronized with the photoemission laser pulse (cf. designs and numerical simulations reported in Refs. [185, 203, 468, 469]). As demonstrated in experimental work, single-electron pulses have been compressed to 30 fs [470], while the compression technique applied to electron pulses containing high-bunch charges yields minimal pulse durations between 160 and 400 fs [86, 198, 471]. Despite improved synchronization technologies [472–474] it remains challenging to achieve few-fs electron pulses over long acquisition times. An approach that adopts the concept of oscillatory fields for electron pulse compression but avoids synchronization problems relies on all-optical setups using terahertz cavities [200]. Recently, THz-fields have enabled a temporal compression of single-electron pulses down to 28 fs [475]. Considering spatial restrictions in a TEM column, this all-optical technique also paves the way for expanding the range of applications in nanoscale time-resolved electron microscopy.

## 8.2 Ultrafast nanodiffraction in UTEM

Upcoming nanodiffraction experiments will in particular continue to profit from the general technical development of the UTEM methodology. As it will be briefly introduced in the following, these include probe aberration correctors that allow for sub-nm spatial resolution and CBED experiments with large convergence angles, as well as energy filters for disentangling elastic and inelastic scattering contributions. Of particular interest in future experiments exploring Lamb waves could be mode couplings, further tailoring and locally enhancing nanophononic wavefields via different model heterostructures and acoustic wave interferences, and nonlinear dynamical phenomena in nanoscale systems optothermally driven into resonance. These aspects will be discussed in the last part of this thesis.

### 8.2.1 Advanced local probing with probe aberration correctors

For mapping the local lattice distortions in the Pt/Si heterostructure [116], a focal spot size was characterized as about 15 nm.<sup>13</sup> However, a larger effective electron spot diameter of about 50 nm was extracted by comparing experimentally observed line profiles with

<sup>13</sup>TEM illumination condition: CBD-141, i.e. weakest excitation of first condenser lens possible (*spot 1*), large convergence angle (*alpha 4*) and 200- $\mu$ m condenser lens aperture (*CLA 1*); high coherence setting at 120 kV acceleration.

numerically calculated linewidths and temporal variations within the lines. This difference has been attributed to incoherent averaging effects arising from a defocused electron beam, as well as sample- and beam-drifts, prompting the development of drift correction schemes.

Ultimate resolution in nanodiffraction, which depends on the formation of small electron probes, requires careful tuning of the experimental parameters, such that few-nm to sub-Angstrom focal spot sizes are achieved. As reported in an earlier publication on the performance capabilities and applications of the Göttingen UTEM [71], the smallest spot diameter for a convergence angle of 6.7 mrad is 0.89 nm,<sup>14</sup> which yields a normalized emittance of 1.73 nm·mrad and a degree of coherence of 11 %. Since all beam properties have been measured at the sample position, they contain contributions from both intrinsic source properties and aberrations from the imaging optics.

In particular at large convergence angles  $\alpha$ , for example 32 mrad and 50 mrad as previously used in strain analysis [72, 116], the spherical aberration of the objective lens strongly affects the spot diameter, which increases with  $1/2 C_s \alpha^3$  [130, Ch. 4.2.2]. The corresponding aberration coefficient  $C_s$  is on the order of the focal length of the objective lens. In geometrical optics, a positive spherical aberration is based on the principle that marginal rays at large angles with respect to the optical axis are deflected more strongly than paraxial rays.<sup>15</sup> Decreasing the electron wavelength or the focal length of the objective lens are two strategies to achieve an enhanced resolution in a TEM. However, irradiation with high energy electrons causes specimen damage and a small focal length comes at the expense of tilt angles feasible in the gap between the pole pieces. These limitations therefore raise the question of how positive spherical aberration can be technically overcome by other means, such as correction elements.

As proven in a fundamental work by Scherzer in 1936 [478], any electron-optical system suffers from spherical aberration if simultaneously the lens fields are rotationally

---

<sup>14</sup>TEM illumination condition: CBD-193, i.e. *spot 1*, largest *alpha* setting possible (*alpha 9*) and 40- $\mu$ m condenser lens aperture (*CLA 3*); high coherence setting at 200 kV acceleration voltage

<sup>15</sup>Alternatively, a wave aberration can be defined [476, Ch. 5.1]. Here, the *geometrical* deviations of an aberrated wave surface from a non-aberrated Gaussian wave front as a function of the angle to the optical axis is related to a phase change across the image plane and can be described by an aberration function (see section 2.2). Names and symmetries of aberrations up to the seventh order are listed in Table 7.2 of Ref. [477]. For example, a first-order aberration describes a defocus that is linear in angle and spherical aberration is a third-order effect (cubic in angle). Both geometrical aberrations are symmetry-allowed for a perfectly rotationally symmetric electromagnetic field. A second-order astigmatism, however, is a *parasitic* aberration induced by mechanical imperfections of a lens [477, Ch. 7.3.2].

symmetric, space-charge free along the optical axis, static, and the system produces a real image of the object. The last three aspects of Scherzer's theorem are associated with enormous experimental drawbacks regarding the correction of spherical aberrations, while rotationally asymmetric electron optics, such as stigmators for compensating the axial astigmatism [130, Ch. 2.4.1], allow for high-resolution imaging and local probing methods. The correction of spherical aberration – if not removed by image post-processing – relies on inducing a negative spherical aberration with such corrector elements. Eventually, the total resulting aberration of the objective lens and the correction device can be eliminated. Two main sorts of asymmetric multipole correctors for imprinting a negative spherical aberration to the electron beam have been developed in the field of scanning TEM (STEM) and conventional TEM: quadrupole-octupole correctors [479–482] and hexapole correctors [483–488] (for more historical and technical details see e.g. the review by Hawkes and Kasper [239] and Ref. [477]).

The successful correction of spherical aberrations has drastically pushed the resolution limit in electron microscopy below 50 pm at 300 kV [489] and enables high-contrast imaging of lattice fringes of radiation-sensitive samples at low voltages (20 kV) [128]. Recently even at 60 kV, sub-Ångstrom resolution has been demonstrated for a silicon single crystal [490]: Bragg reflections of the silicon sample were acquired with 73 pm spatial resolution by employing a CEOS ASCOR corrector [488, 491] in a CFEG-equipped JEOL NEOARM.

Besides achieving minimal spot sizes using aberration corrected probe systems, another advantage of performing CBED with a probe corrector is the realization of larger convergence angles (e.g. 38-mrad semi-angle in Ref. [490]). Due to the advanced coherence properties of the probing electron beam in a JEOL 2200FS with a CEOS spherical aberration probe corrector [482], interference patterns have been observed for overlapping CBED disks [492].

While  $C_s$ -STEM allows for high-contrast imaging of the amplitude of the object exit wave, phase information is still missing. Employing electron beam holography, both contributions to image contrast are simultaneously recorded and an aberration-corrected object exit wave can be reconstructed by an *a posteriori* deconvolution from aberrations according to transfer theory (section 2.2) [142]. An *a priori* aberration correction therefore seems redundant. However, as shown by Geiger et. al [493], both the fringe contrast in electron beam holograms and the spatial-frequency limit are improved in a probe-corrected TEM [486] by a factor of about 2. Such a signal/noise improvement would facilitate the usage of low-dose electron pulses which is vital for non-equilibrium investigations with

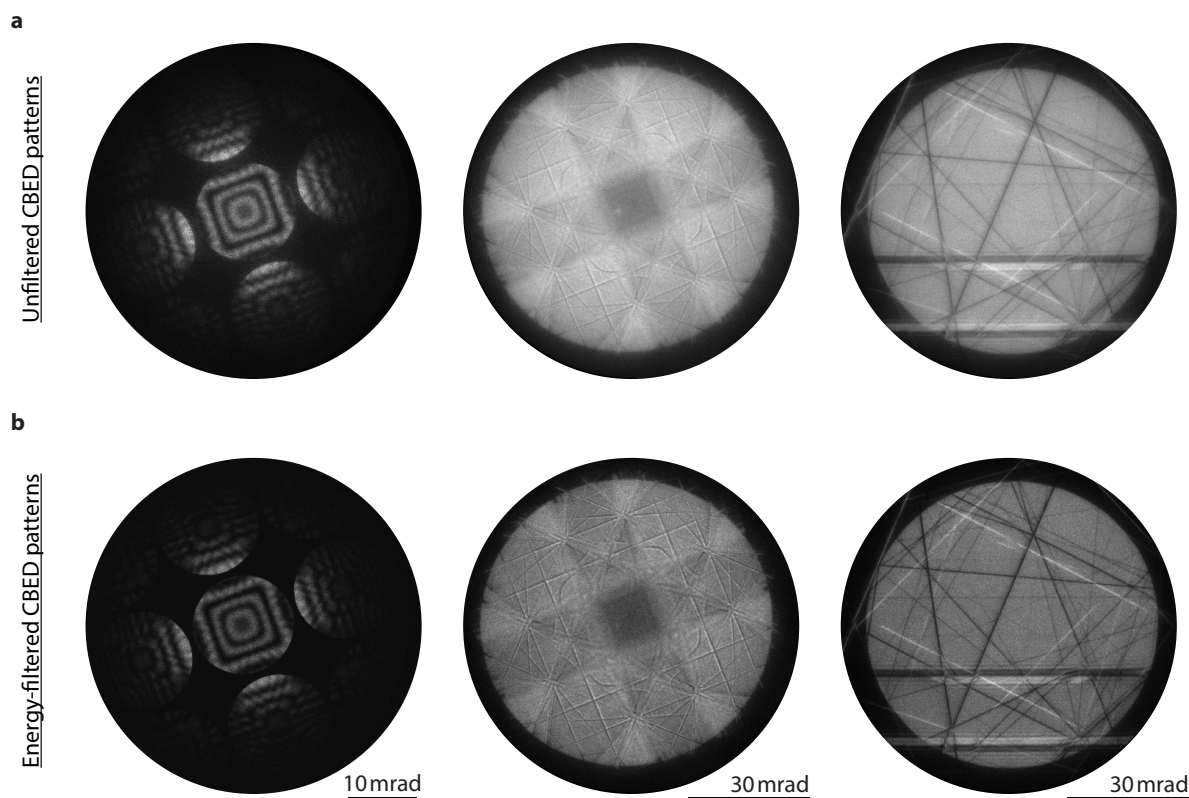


**Figure 8.1:** CBED patterns of a (100)-oriented 200-nm thick silicon membrane pre (a) and after (b) energy-filtering. (a) Left to right: Diffraction images showing bright pendellösung fringes, defect Kikuchi bands, and deficit and excess Bragg lines. (b) Corresponding energy-filtered diffraction patterns with a zero-loss peak width (FWHM) of about 1 eV. All patterns are recorded at 200 kV with a JEOL F200 microscope equipped with a CFEG and a “CEOS Energy Filtering and Imaging Device”.

photoemission pulses in UTEM.

## 8.2.2 Inelastic scattering effects and energy filtering

The description of the diffraction pattern formation in Chapters 5 and 7 was restricted to the assumption of purely elastic scattering which gives rise to diffraction peaks (or lines) when the Bragg condition is fulfilled. Additionally, however, electrons scatter inelastically and contribute to a diffuse background intensity in the diffraction pattern. The momentum transfer and the energy loss involved in the inelastic scattering depend on the type and localization of inelastic interactions. For high-energy electrons, these interactions can be single-electron, collective plasmon, and phonon scattering processes, as well as multiple coupled scattering effects [329, Ch.10.6]. Coulomb repulsion by inner- or outer-shell crystal electrons, which are excited to higher energy states, typically

leads to a scattering of the fast electron by about 10 mrad or 1–2 mrad, respectively (for  $E_0 \approx 100$  keV) [138, Ch. 1.1]. Inelastic scattering involving plasmons (collective oscillation of the valence electron density) are visible in an energy spectrum as a peak in the range of 5–30 eV with a smoothly decreasing intensity at larger energy losses [138, Ch. 1.1]. About 80 % of the plasmonic scattering intensity is concentrated at small scattering angles below 7 mrad [494]. Thermal diffuse scattering (TDS) from phonons causes only small (meV) energy losses, so that it is contained within the so-called zero-loss peak of the energy spectrum. In a diffraction pattern, thermal diffuse scattering produces satellite peaks around Bragg spots and extends to large angles (see section 5.4.2). In essence, recording full electron energy spectra (for varying electron probe positions) allows for a reconstruction of local sample properties like the chemical composition and the phononic band structure.

By performing energy-filtered TEM (see section 2.1), spatially resolved information on the electron energy loss distribution for certain parts of the spectrum can be retrieved. This approach has, for example, recently allowed to quantitatively map electron-light interactions at microresonators for individual photon sideband populations with an energy window of 800 meV [495]. Zero-loss filtering of diffraction patterns removes the plasmonic component, thereby making faint TDS more visible and enhancing contributions from coherent elastic diffraction: For lattice strain measurements, energy filtering significantly improves the visibility of Bragg lines in a CBED pattern (Fig. 8.1, see also Ref. [496] displaying various examples of CBED patterns revealing the effectiveness of energy filtering), rendering energy-filtered U-CBED an ideal method for future investigations of ultrafast structural dynamics.

### 8.2.3 Lamb wave interactions and phonon confinement

Ultrafast nanoscale dynamics are influenced by the atomic-scale structure of interfaces, nanoscale morphologies, and local defect structures. The presence of small-amplitude symmetry-forbidden dynamics in the patterned silicon membrane (see Chapter 7 and Ref. [116]), for example, is possibly a signature of local membrane distortions and inhomogeneous nanoscale pre-straining.

When a Lamb wave encounters an interface (which can be the membrane edge or a change in membrane thickness), mode conversion can occur that is consistent with traction-free boundary conditions. Generally, not only propagating modes with real

wavevectors are generated during refractions but also evanescent modes with complex or purely imaginary wavevectors [497, 498], while the frequency of the incident wave is maintained. As experimentally shown for Lamb waves interacting at the interface between two regions of different thicknesses [275, 499] and at free edges of homogeneous membranes [500, 501], mode conversion may involve the same mode type  $S_n$  [275, 499], two different types of modes (e.g. incident mode  $S_2$ , reflected mode  $S_1$ ) [501] or take place between modes corresponding to two different regions of the same dispersion curve (incident and reflected mode e.g.  $S_1$ ) [500]. For small wavenumbers, the  $S_1$  mode always has a negative group velocity and a positive phase velocity (see Fig. 7.6), which gives rise to so-called backward wave propagating.<sup>16</sup> Through mode conversion between a forward and backward propagating mode, negative reflection<sup>17</sup> can be observed: Waves with equal wavenumbers on both sides of the interface are characterized by incident and refraction angles equal in magnitude but propagate on the same side of the interface normal. Exploiting this effect, Lamb wave focusing has been achieved [275, 499, 501, 506], opening new pathways to manipulate wave fields in unprecedented and nonintuitive ways.

The negative-refraction-based generation of phonon foci strongly depends on mode conversion efficiencies [498] and has so far been discussed for macroscopic (mm-scale) systems. An interesting approach for phonon confinement to nanoscale volumes relies on spatially tailored phonon excitations in nano-patterned semiconductor membranes. As discussed in Chapter 7, these well-defined heterostructures serve as Lamb-wave sources with a discrete spectrum according to local resonances of the bilayer system. Apart from the importance of elastic properties and layer thicknesses in such nanoscale systems, also the explicit geometry has a strong impact on the acoustic wavefield. By changing the current geometry from metal stripes that launch plane waves (see Chapter 7) to arc structures, it is expected that the induced strain field forms an acoustic focus at the center of such lenses due to wave interferences. Ideally, sub-wavelength focus sizes are achieved. For the 10-nm thin platinum layer on a 35-nm thin silicon membrane, for example, a strong resonance was found for the  $A_0$  mode at a wavenumber of  $0.09 \text{ nm}^{-1}$  (Fig. 7.6), which could yield a focus size below 100 nm. The high spatial resolution of U-CBED would be perfectly suitable for the mapping of the evolving displacement field at such nanometer length-scales. In future UTEM experiments, the extreme strain profile of tightly localized lattice distortions may enable the investigation of elastically driven

---

<sup>16</sup>Except for the three lowest modes  $A_0$ ,  $S_0$ , and  $A_1$ , backward waves exist for all Lamb modes over some range of Poisson's ratio [502, 503].

<sup>17</sup>See also the optical equivalent of negative-index materials [504, 505].

phase transitions [447, 448].

### 8.2.4 Nonlinear phononics

The quantitative discussion of propagating acoustic waves and localized oscillations in the metal-/semiconductor heterostructure (Chapters 6 and 7) was based on linear elasticity theory (Chapter 4), since only small displacement deformations below 1% were observed. However, large amplitude distortions in phonon foci might require an analysis within the framework of nonlinear phononics. In the past decade, insights into nonlinear effects have in particular been obtained by studying 2D materials [4, 507–509]. When exfoliated into ultra-thin membranes, unique mechanical properties arise [510–512], among which mechanical flexibility and tuneable stiffness transfer the description of the membrane motion into the nonlinear regime at already small external excitation forces [513]. Also by scaling down the membrane radius  $R$ , different regimes of motion can be reached, as shown in Fig. 8.2a for circular graphene membranes [17]. Whereas large membranes ( $R = 100 \mu\text{m}$ ) exhibit a linear motion over a large range of out-of-plane amplitudes (two orders of magnitude), the harmonic region becomes smaller for decreasing membrane sizes (about one order of magnitude for  $R = 2.5 \mu\text{m}$ ) and eventually disappears completely ( $R = 50 \text{nm}$ ), so that the membrane exhibits a nonlinear response at amplitudes of less than 10 nm. Driving the graphene nanodrum optothermally using laser pulses [514], a variety of nonlinear phenomena can be observed (Fig. 8.2b).

Typically, the nonequilibrium dynamics are described by the Duffing equation

$$m_i \ddot{q}_i + c_i \dot{q}_i + k_i q_i + \gamma q_i^3 = F_{\text{ext},i0} \cos(\omega t - \Phi) + \tilde{F}. \quad (8.1)$$

Here,  $q_i(t)$  represents the maximum deflection of an acoustic mode  $i$ ,  $\tilde{F}$  is a constant force term,  $m_i$ ,  $c_i$ , and  $k_i$  describe the mode-dependent linear modal mass, damping coefficient, and linear stiffness, respectively. The primary cause for nonlinear effects is geometric nonlinearity, described by the nonlinear stiffness term of the form  $\gamma q_i^3$ . As a result, the system exhibits a spring hardening, which leads to an amplitude increase and a shift of the resonance frequency to higher values. When the driving frequency  $\omega$  is further increased, the frequency-response-function (FRF) becomes unstable, entering a bi-stable regime also observed experimentally [1, 515, 516]. The parametric term  $k_i(t)q_i$  introduces additional resonance at twice the fundamental frequency and slightly larger frequencies [517, 518]. as well as mode-couplings [514, 519]. The combination of high frequencies in the MHz-regime

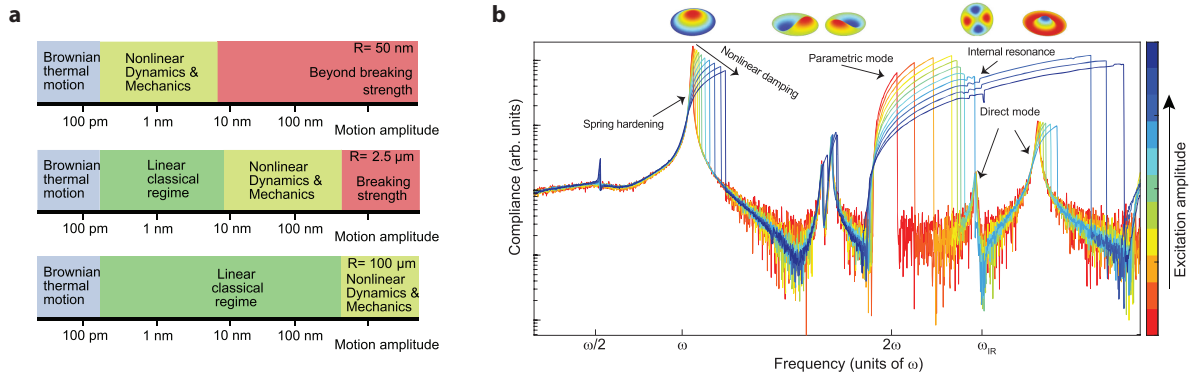


**Figure 8.2:** Nonlinear dynamical phenomena in 2D material resonators. **(a)** Schematic indicating ranges of dynamic motion exhibited by circular graphene membranes of different radii  $R$  at room temperature. **(b)** Measured nonlinear dynamic frequency response curves of a multi-layer graphene nanodrum (10 nm thick and 5  $\mu\text{m}$  in diameter); from the red to the blue curves the drive level increases (color bar on the right hand side). In a single set of measurements the Duffing response, nonlinear damping, parametric resonance and internal resonance (mode-coupling) are observed, by simultaneous application of both direct and parametric drive. The linear  $x$ -axis indicates the detection frequency in terms of the fundamental resonance frequency  $\omega = \omega_1$ , the logarithmic  $y$ -axis shows the measured mechanical compliance  $|\text{FRF}(\omega)|$ . At a frequency  $\omega_{IR}$  an internal resonance between a direct and parametric mode is observed. Reprinted from Ref. [17]. Licensed under CC BY 4.0. Mode shapes are reprinted from Ref. [514]. Licensed under CC BY 4.0.

and small membrane sizes, however, poses central challenges for quantitatively mapping the evolving strain fields. In addition to optical, transconductive and capacitive readout schemes [17], U-CBED could yield valuable insights by directly accessing both in-plane strain and out-of-plane motions.

---

### Short introduction into Rabi-oscillations

---

The linear response of a two-level quantum-mechanical system [520, Ch. 5.2] with states  $|a\rangle$  and  $|b\rangle$  (see Fig. 5.5 c) coupled by an external field can be modeled by writing the corresponding wavefunction as

$$|\varphi(t)\rangle = C_a(t) |a\rangle + C_b(t) |b\rangle, \quad (\text{A.1})$$

with two complex coefficients  $C_a$  and  $C_b$  such that  $|C_a|^2 + |C_b|^2 = 1$  normalizes the wavefunction. The Hamiltonian  $H$  of the time-dependent Schrödinger equation  $H\varphi = i\hbar \frac{\partial \varphi}{\partial t}$  is given by

$$\begin{aligned} H &= H^0 + H'(t) \\ &= E_a |a\rangle \langle a| + E_b |b\rangle \langle b| + (V_{ab} |a\rangle \langle b| + V_{ba} |b\rangle \langle a|) E(t), \end{aligned} \quad (\text{A.2})$$

with level energies  $E_a = \hbar\omega_a$  and  $E_b = \hbar\omega_b$ .  $H'(t)$  is the perturbation Hamiltonian that depends on the dipole-matrix element  $V_{ab}$  of the transition driven by an electric field  $E(t)$ . In the dipole approximation [ $E(\mathbf{r}, t) \approx E(t)$ ], the electric field is

$$E(t) = E_0 \cos(\omega_0 t), \quad (\text{A.3})$$

with constant field amplitude  $E_0$  and frequency  $\omega_0$ . For this system, the Schrödinger equation yields

$$\begin{aligned} \dot{C}_a &= -i\omega_a C_a - 2i\Omega_R e^{i\phi} \cos(i\omega_a t) C_b \\ \dot{C}_b &= -i\omega_b C_b - 2i\Omega_R e^{i\phi} \cos(i\omega_a t) C_a, \end{aligned} \quad (\text{A.4})$$

with  $\phi$  the complex phase of  $V_{ab} = |V_{ab}|e^{i\phi}$ . The Rabi frequency

$$\Omega_R = \frac{|V_{ab}E_0|}{2\hbar} \quad (\text{A.5})$$

is at resonance proportional to the amplitude of the light field and to the dipole moment  $V_{ab}$ . In the rotating wave approximation taking into account only the slow coupling dynamics, we redefine

$$c_a = C_a e^{i\omega_a t} \quad \text{and} \quad c_b = C_b e^{i\omega_b t}, \quad (\text{A.6})$$

and introduce the detuning  $\Delta = \omega_0 - (\omega_b - \omega_a)$ , which yields the solution

$$\begin{aligned} \dot{c}_a(t) &= e^{i\frac{\Delta}{2}t} \left[ (\cos \Omega t) - i\frac{\Delta}{2\Omega} \sin(\Omega t) \right] c_a(t) - i\frac{\Omega_R}{\Omega} \sin(\Omega t) c_b(t) \\ \dot{c}_b(t) &= e^{i\frac{\Delta}{2}t} \left[ (\cos \Omega t) - i\frac{\Delta}{2\Omega} \sin(\Omega t) \right] c_b(t) - i\frac{\Omega_R}{\Omega} \sin(\Omega t) c_a(t). \end{aligned} \quad (\text{A.7})$$

Here,  $\Omega = \sqrt{\Omega_R^2 + \left(\frac{\Delta}{2}\right)^2}$  is the generalized Rabi frequency. Assuming  $c_a(0) = 1$  and  $c_b(0) = 0$ , the probability to find the system in the excited state at time  $t$  is

$$P_b(t) = |c_b|^2 = \left(\frac{\Omega_R}{\Omega}\right)^2 \sin^2(\Omega t) \stackrel{\Delta=0}{=} \sin^2(\Omega_R t). \quad (\text{A.8})$$

---

## Bibliography

---

1. C. Chen, S. Rosenblatt, K. I. Bolotin, W. Kalb, P. Kim, I. Kymissis, H. L. Stormer, T. F. Heinz, J. Hone, Performance of Monolayer Graphene Nanomechanical Resonators with Electrical Readout. *Nature Nanotechnology* **4**, 861–867 (2009) (cit. on pp. 1, 169).
2. J. S. Bunch, A. M. van der Zande, S. S. Verbridge, I. W. Frank, D. M. Tanenbaum, J. M. Parpia, H. G. Craighead, P. L. McEuen, Electromechanical Resonators from Graphene Sheets. *Science* **315**, 490–493 (2007) (cit. on p. 1).
3. A. Castellanos-Gomez, R. van Leeuwen, M. Buscema, H. S. J. van der Zant, G. A. Steele, W. J. Venstra, Single-Layer MoS<sub>2</sub> Mechanical Resonators. *Advanced Materials* **25**, 6719–6723 (2013) (cit. on p. 1).
4. J. Lee, Z. Wang, K. He, J. Shan, P. X.-L. Feng, High Frequency MoS<sub>2</sub> Nanomechanical Resonators. *ACS Nano* **7**, 6086–6091 (2013) (cit. on pp. 1, 169).
5. D. W. Carr, S. Evoy, L. Sekaric, H. G. Craighead, J. M. Parpia, Measurement of Mechanical Resonance and Losses in Nanometer Scale Silicon Wires. *Applied Physics Letters* **75**, 920–922 (1999) (cit. on p. 1).
6. H.-Y. Chiu, P. Hung, H. W. C. Postma, M. Bockrath, Atomic-Scale Mass Sensing Using Carbon Nanotube Resonators. *Nano Letters* **8**, 4342–4346 (2008) (cit. on p. 1).
7. Q. P. Unterreithmeier, T. Faust, J. P. Kotthaus, Damping of Nanomechanical Resonators. *Physical Review Letters* **105**, 027205 (2010) (cit. on p. 1).
8. M. Bückle, V. C. Hauber, G. D. Cole, C. Gärtner, U. Zeimer, J. Grenzer, E. M. Weig, Stress Control of Tensile-Strained In<sub>1-x</sub>Gasub>xP Nanomechanical String Resonators. *Applied Physics Letters* **113**, 201903 (2018) (cit. on p. 1).

9. J. Doster, S. Hoenl, H. Lorenz, P. Paulitschke, E. M. Weig, Collective Dynamics of Strain-Coupled Nanomechanical Pillar Resonators. *Nature Communications* **10**, 5246 (2019) (cit. on p. 1).
10. P. Paulitschke, N. Seltner, A. Lebedev, H. Lorenz, E. M. Weig, Size-Independent Young's Modulus of Inverted Conical GaAs Nanowire Resonators. *Applied Physics Letters* **103**, 261901 (2013) (cit. on p. 1).
11. D. V. Scheible, R. H. Blick, Silicon Nanopillars for Mechanical Single-Electron Transport. *Applied Physics Letters* **84**, 4632–4634 (2004) (cit. on p. 1).
12. H. G. Craighead, Nanoelectromechanical Systems. *Science* **290**, 1532–1535 (2000) (cit. on p. 1).
13. K. L. Ekinci, M. L. Roukes, Nanoelectromechanical Systems. *Review of Scientific Instruments* **76**, 061101 (2005) (cit. on pp. 1, 51).
14. L. Wei, X. Kuai, Y. Bao, J. Wei, L. Yang, P. Song, M. Zhang, F. Yang, X. Wang, The Recent Progress of MEMS/NEMS Resonators. *Micromachines* **12**, 724 (2021) (cit. on p. 1).
15. G. Langfelder, M. Bestetti, M. Gadola, Silicon MEMS Inertial Sensors Evolution over a Quarter Century. *Journal of Micromechanics and Microengineering* **31**, 084002 (2021) (cit. on p. 1).
16. O. Brand, I. Dufour, S. M. Heinrich, F. Josse, Eds., *Resonant MEMS: Fundamentals, Implementation and Application* (Wiley, Weinheim, 2015); ISBN: 978-3-527-67636-1 (cit. on p. 1).
17. P. G. Steeneken, R. J. Dolleman, D. Davidovikj, F. Alijani, H. S. J. van der Zant, Dynamics of 2D Material Membranes. *2D Materials* **8**, 042001 (2021); doi:10.1088/2053-1583/ac152c (cit. on pp. 1, 169, 170).
18. S. Pairis, F. Donatini, M. Hocevar, D. Tumanov, N. Vaish, J. Claudon, J.-P. Poizat, P. Verlot, Shot-Noise-Limited Nanomechanical Detection and Radiation Pressure Backaction from an Electron Beam. *Physical Review Letters* **122**, 083603 (2019) (cit. on p. 1).
19. A. D. O'Connell, M. Hofheinz, M. Ansmann, R. C. Bialczak, M. Lenander, E. Lucero, M. Neeley, D. Sank, H. Wang, M. Weides, J. Wenner, J. M. Martinis, A. N. Cleland, Quantum Ground State and Single-Phonon Control of a Mechanical Resonator. *Nature* **464**, 697–703 (2010) (cit. on pp. 1, 51).

- 
20. J. D. Teufel, T. Donner, D. Li, J. W. Harlow, M. S. Allman, K. Cicak, A. J. Sirois, J. D. Whittaker, K. W. Lehnert, R. W. Simmonds, Sideband Cooling of Micromechanical Motion to the Quantum Ground State. *Nature* **475**, 359–363 (2011) (cit. on p. 1).
  21. S. Stassi, I. Cooperstein, M. Tortello, C. F. Pirri, S. Magdassi, C. Ricciardi, Reaching Silicon-Based NEMS Performances with 3D Printed Nanomechanical Resonators. *Nature Communications* **12**, 6080 (2021) (cit. on p. 1).
  22. K. Jensen, K. Kim, A. Zettl, An Atomic-Resolution Nanomechanical Mass Sensor. *Nature Nanotechnology* **3**, 533–537 (2008) (cit. on pp. 1, 51).
  23. Y. T. Yang, C. Callegari, X. L. Feng, K. L. Ekinci, M. L. Roukes, Zeptogram-Scale Nanomechanical Mass Sensing. *Nano Letters* **6**, 583–586 (2006) (cit. on p. 1).
  24. J. Chaste, A. Eichler, J. Moser, G. Ceballos, R. Rurali, A. Bachtold, A Nanomechanical Mass Sensor with Yoctogram Resolution. *Nature Nanotechnology* **7**, 301–304 (2012) (cit. on pp. 1, 51).
  25. H. J. Mamin, D. Rugar, Sub-Attonewton Force Detection at Millikelvin Temperatures. *Applied Physics Letters* **79**, 3358–3360 (2001) (cit. on pp. 1, 51).
  26. J. Moser, J. Güttinger, A. Eichler, M. J. Esplandiu, D. E. Liu, M. I. Dykman, A. Bachtold, Ultrasensitive Force Detection with a Nanotube Mechanical Resonator. *Nature Nanotechnology* **8**, 493–496 (2013) (cit. on p. 1).
  27. B. E. A. Saleh, M. C. Teich, *Fundamentals of Photonics* (Wiley, Weinheim, 2007); ISBN: 978-81-265-3774-7 (cit. on pp. 1, 124).
  28. J. Cuffe, O. Ristow, E. Chávez, A. Shchepetov, P.-O. Chapuis, F. Alzina, M. Hettich, M. Prunnila, J. Ahopelto, T. Dekorsy, C. M. Sotomayor Torres, Lifetimes of Confined Acoustic Phonons in Ultrathin Silicon Membranes. *Physical Review Letters* **110**, 095503 (2013) (cit. on pp. 1, 52).
  29. M. Grossmann, M. Klingele, P. Scheel, O. Ristow, M. Hettich, C. He, R. Waitz, M. Schubert, A. Bruchhausen, V. Gusev, E. Scheer, T. Dekorsy, Femtosecond Spectroscopy of Acoustic Frequency Combs in the 100-GHz Frequency Range in Al/Si Membranes. *Physical Review B* **88**, 205202 (2013) (cit. on p. 1).
  30. A. Bartels, R. Cerna, C. Kistner, A. Thoma, F. Hudert, C. Janke, T. Dekorsy, Ultrafast Time-Domain Spectroscopy Based on High-Speed Asynchronous Optical Sampling. *Review of Scientific Instruments* **78**, 035107 (2007) (cit. on p. 1).

31. F. Hudert, A. Bruchhausen, D. Issenmann, O. Schecker, R. Waitz, A. Erbe, E. Scheer, T. Dekorsy, A. Mlayah, J.-R. Huntzinger, Confined Longitudinal Acoustic Phonon Modes in Free-Standing Si Membranes Coherently Excited by Femtosecond Laser Pulses. *Physical Review B* **79**, 201307 (2009) (cit. on pp. 1, 52).
32. M. Schubert, M. Grossmann, C. He, D. Brick, P. Scheel, O. Ristow, V. Gusev, T. Dekorsy, Generation and Detection of Gigahertz Acoustic Oscillations in Thin Membranes. *Ultrasonics* **56**, 109–115 (2015) (cit. on pp. 1, 2).
33. C. Colvard, T. A. Gant, M. V. Klein, R. Merlin, R. Fischer, H. Morkoc, A. C. Gossard, Folded Acoustic and Quantized Optic Phonons in (GaAl)As Superlattices. *Physical Review B* **31**, 2080–2091 (1985) (cit. on pp. 2, 108).
34. J. Li, R. Clinite, X. Wang, J. Cao, Simulation of Ultrafast Heating Induced Structural Dynamics Using a One-Dimensional Spring Model. *Physical Review B* **80**, 014304 (2009) (cit. on pp. 2, 108).
35. M. Herzog, D. Schick, P. Gaal, R. Shayduk, C. v. Korff Schmising, M. Bargheer, Analysis of Ultrafast X-ray Diffraction Data in a Linear-Chain Model of the Lattice Dynamics. *Applied Physics A* **106**, 489–499 (2012) (cit. on pp. 2, 108).
36. D. Schick, A. Bojahr, M. Herzog, R. Shayduk, C. von Korff Schmising, M. Bargheer, udkm1DsimA Simulation Toolkit for 1D Ultrafast Dynamics in Condensed Matter. *Computer Physics Communications* **185**, 651–660 (2014) (cit. on pp. 2, 108).
37. R. M. Karl, G. F. Mancini, J. L. Knobloch, T. D. Frazer, J. N. Hernandez-Charpak, B. Abad, D. F. Gardner, E. R. Shanblatt, M. Tanksalvala, C. L. Porter, C. S. Bevis, D. E. Adams, H. C. Kapteyn, M. M. Murnane, Full-Field Imaging of Thermal and Acoustic Dynamics in an Individual Nanostructure Using Tabletop High Harmonic Beams. *Science Advances* **4**, eaau4295 (2018) (cit. on pp. 2, 108).
38. F. Medeghini, A. Crut, M. Gandolfi, F. Rossella, P. Maioli, F. Vallée, F. Banfi, N. Del Fatti, Controlling the Quality Factor of a Single Acoustic Nanoresonator by Tuning Its Morphology. *Nano Letters* **18**, 5159–5166 (2018) (cit. on pp. 2, 108).
39. L. Rayleigh, On Waves Propagated along the Plane Surface of an Elastic Solid. *Proceedings of the London Mathematical Society* **s1-17**, 4–11 (1885) (cit. on pp. 2, 63, 108).

- 
40. H. Lamb, On Waves in an Elastic Plate. *Proceedings of the Royal Society of London. Series A, Containing Papers of a Mathematical and Physical Character* **93**, 114–128 (1917) (cit. on pp. 2, 63, 108, 141, 153).
  41. R. Stoneley, H. F. Baker, Elastic Waves at the Surface of Separation of Two Solids. *Proceedings of the Royal Society of London. Series A, Containing Papers of a Mathematical and Physical Character* **106**, 416–428 (1924) (cit. on pp. 2, 63, 108).
  42. P. Baum, D.-S. Yang, A. H. Zewail, 4D Visualization of Transitional Structures in Phase Transformations by Electron Diffraction. *Science* **318**, 788–792 (2007) (cit. on pp. 2, 101, 108, 132).
  43. F. Carbone, P. Baum, P. Rudolf, A. H. Zewail, Structural Preablation Dynamics of Graphite Observed by Ultrafast Electron Crystallography. *Physical Review Letters* **100** (2008) (cit. on pp. 2, 105, 108, 109).
  44. M. Eichberger, H. Schäfer, M. Krumova, M. Beyer, J. Demsar, H. Berger, G. Moriena, G. Sciaini, R. J. D. Miller, Snapshots of Cooperative Atomic Motions in the Optical Suppression of Charge Density Waves. *Nature* **468**, 799–802 (2010) (cit. on pp. 2, 38, 108).
  45. S. Schäfer, W. Liang, A. H. Zewail, Primary Structural Dynamics in Graphite. *New Journal of Physics* **13**, 063030 (2011) (cit. on pp. 2, 38, 108).
  46. A. Hanisch-Blicharski, A. Janzen, B. Krenzer, S. Wall, F. Klasing, A. Kalus, T. Frigge, M. Kammler, M. Horn-von Hoegen, Ultra-Fast Electron Diffraction at Surfaces: From Nanoscale Heat Transport to Driven Phase Transitions. *Ultramicroscopy* **127**, 2–8 (2013) (cit. on pp. 2, 15, 108).
  47. R. P. Chatelain, V. R. Morrison, B. L. M. Klarenaar, B. J. Siwick, Coherent and Incoherent Electron-Phonon Coupling in Graphite Observed with Radio-Frequency Compressed Ultrafast Electron Diffraction. *Physical Review Letters* **113** (2014) (cit. on pp. 2, 38, 105, 108, 109).
  48. L. Waldecker, R. Bertoni, R. Ernstorfer, J. Vorberger, Electron-Phonon Coupling and Energy Flow in a Simple Metal beyond the Two-Temperature Approximation. *Physical Review X* **6**, 021003 (2016) (cit. on pp. 2, 38, 108).
  49. J. G. Horstmann, H. Böckmann, B. Wit, F. Kurtz, G. Storeck, C. Ropers, Coherent Control of a Surface Structural Phase Transition. *Nature* **583**, 232–236 (2020) (cit. on pp. 2, 28, 108, 132).

50. K. Sokolowski-Tinten, C. Blome, J. Blums, A. Cavalleri, C. Dietrich, A. Tarasevitch, I. Uschmann, E. Förster, M. Kammler, M. Horn-von-Hoegen, D. von der Linde, Femtosecond X-ray Measurement of Coherent Lattice Vibrations near the Lindemann Stability Limit. *Nature* **422**, 3 (2003) (cit. on pp. 2, 108).
51. A. M. Lindenberg, J. Larsson, K. Sokolowski-Tinten, K. J. Gaffney, C. Blome, O. Synnergren, J. Sheppard, C. Caleman, A. G. MacPhee, D. Weinstein, D. P. Lowney, T. K. Allison, T. Matthews, R. W. Falcone, A. L. Cavalieri, D. M. Fritz, S. H. Lee, P. H. Bucksbaum, D. A. Reis, J. Rudati, P. H. Fuoss, C. C. Kao, D. P. Siddons, R. Pahl, J. Als-Nielsen, S. Duesterer, R. Ischebeck, H. Schlarb, H. Schulte-Schrepping, T. Tschentscher, J. Schneider, D. von der Linde, O. Hignette, F. Sette, H. N. Chapman, R. W. Lee, T. N. Hansen, S. Techert, J. S. Wark, M. Bergh, G. Huldt, D. van der Spoel, N. Timneanu, J. Hajdu, R. A. Akre, E. Bong, P. Krejcik, J. Arthur, S. Brennan, K. Luening, J. B. Hastings, Atomic-Scale Visualization of Inertial Dynamics. *Science* **308**, 392–395 (2005) (cit. on pp. 2, 38, 108).
52. T. Huber, S. O. Mariager, A. Ferrer, H. Schäfer, J. A. Johnson, S. Grübel, A. Lübcke, L. Huber, T. Kubacka, C. Dornes, C. Laulhe, S. Ravy, G. Ingold, P. Beaud, J. Demsar, S. L. Johnson, Coherent Structural Dynamics of a Prototypical Charge-Density-Wave-to-Metal Transition. *Physical Review Letters* **113**, 026401 (2014) (cit. on pp. 2, 108).
53. M. J. Neugebauer, T. Huber, M. Savoini, E. Abreu, V. Esposito, M. Kubli, L. Rettig, E. Bothschafter, S. Grübel, T. Kubacka, J. Rittmann, G. Ingold, P. Beaud, D. Dominko, J. Demsar, S. L. Johnson, Optical Control of Vibrational Coherence Triggered by an Ultrafast Phase Transition. *Physical Review B* **99**, 220302 (2019) (cit. on pp. 2, 108).
54. W. Liang, S. Schäfer, A. H. Zewail, Ultrafast Electron Crystallography of Heterogeneous Structures: Gold-graphene Bilayer and Ligand-Encapsulated Nanogold on Graphene. *Chemical Physics Letters* **542**, 8–12 (2012) (cit. on pp. 2, 16, 52, 108, 127).
55. K. Sokolowski-Tinten, X. Shen, Q. Zheng, T. Chase, R. Coffee, M. Jerman, R. K. Li, M. Ligges, I. Makasyuk, M. Mo, A. H. Reid, B. Rethfeld, T. Vecchione, S. P. Weathersby, H. A. Dürr, X. J. Wang, Electron-Lattice Energy Relaxation in Laser-Excited Thin-Film Au-insulator Heterostructures Studied by Ultrafast MeV Electron Diffraction. *Structural Dynamics* **4**, 054501 (2017) (cit. on pp. 2, 108).

- 
56. M. Z. Mo, V. Becker, B. K. Ofori-Okai, X. Shen, Z. Chen, B. Witte, R. Redmer, R. K. Li, M. Dunning, S. P. Weathersby, X. J. Wang, S. H. Glenzer, Determination of the Electron-Lattice Coupling Strength of Copper with Ultrafast MeV Electron Diffraction. *Review of Scientific Instruments* **89**, 10C108 (2018) (cit. on pp. 2, 16, 108).
57. V. Tinnemann, C. Streubühr, B. Hafke, A. Kalus, A. Hanisch-Blicharski, M. Ligges, P. Zhou, D. von der Linde, U. Bovensiepen, M. Horn-von Hoegen, Ultrafast Electron Diffraction from a Bi(111) Surface: Impulsive Lattice Excitation and DebyeWaller Analysis at Large Momentum Transfer. *Structural Dynamics* **6**, 035101 (2019) (cit. on pp. 2, 108).
58. A. von Reppert, L. Willig, J.-E. Pudell, S. P. Zeuschner, G. Sellge, F. Ganss, O. Hellwig, J. A. Arregi, V. Uhlí, A. Crut, M. Bargheer, Spin Stress Contribution to the Lattice Dynamics of FePt. *Science Advances* **6**, eaba1142 (2020) (cit. on pp. 2, 108).
59. S. M. Falke, C. A. Rozzi, D. Brida, M. Maiuri, M. Amato, E. Sommer, A. D. Sio, A. Rubio, G. Cerullo, E. Molinari, C. Lienau, Coherent Ultrafast Charge Transfer in an Organic Photovoltaic Blend. *Science* **344**, 1001–1005 (2014) (cit. on p. 2).
60. E. Turgut, C. La-o-vorakiat, J. M. Shaw, P. Grychtol, H. T. Nembach, D. Rudolf, R. Adam, M. Aeschlimann, C. M. Schneider, T. J. Silva, M. M. Murnane, H. C. Kapteyn, S. Mathias, Controlling the Competition between Optically Induced Ultrafast Spin-Flip Scattering and Spin Transport in Magnetic Multilayers. *Physical Review Letters* **110** (2013) (cit. on p. 2).
61. M. E. Siemens, Q. Li, R. Yang, K. A. Nelson, E. H. Anderson, M. M. Murnane, H. C. Kapteyn, Quasi-Ballistic Thermal Transport from Nanoscale Interfaces Observed Using Ultrafast Coherent Soft X-ray Beams. *Nature Materials* **9**, 26–30 (2010) (cit. on pp. 2, 51, 108, 132).
62. O. Bostanjoglo, T. Rosin, Resonance oscillations of magnetic domain walls and bloch lines observed by stroboscopic electron microscopy. *physica status solidi (a)* **57**, 561–568 (1980) (cit. on pp. 2, 7).
63. A. H. Zewail, Four-Dimensional Electron Microscopy. *Science* **328**, 187–193 (2010) (cit. on pp. 2, 15, 38).
64. D. J. Flannigan, A. H. Zewail, 4D Electron Microscopy: Principles and Applications. *Accounts of Chemical Research* **45**, 1828–1839 (2012) (cit. on pp. 2, 38).

65. T. LaGrange, B. W. Reed, D. J. Masiel, Movie-Mode Dynamic Electron Microscopy. *MRS Bulletin* **40**, 22–28 (2015) (cit. on p. 2).
66. L. Piazza, D. J. Masiel, T. LaGrange, B. W. Reed, B. Barwick, F. Carbone, Design and Implementation of a Fs-Resolved Transmission Electron Microscope Based on Thermionic Gun Technology. *Chemical Physics* **423**, 79–84 (2013) (cit. on pp. 2, 38).
67. E. Kieft, K. B. Schliep, P. K. Suri, D. J. Flannigan, Communication: Effects of Thermionic-Gun Parameters on Operating Modes in Ultrafast Electron Microscopy. *Structural Dynamics* **2**, 051101 (2015) (cit. on p. 2).
68. G. Cao, S. Sun, Z. Li, H. Tian, H. Yang, J. Li, Clocking the Anisotropic Lattice Dynamics of Multi-Walled Carbon Nanotubes by Four-Dimensional Ultrafast Transmission Electron Microscopy. *Scientific Reports* **5**, 8404 (2015) (cit. on p. 2).
69. K. Bücke, M. Picher, O. Crégut, T. LaGrange, B. W. Reed, S. T. Park, D. J. Masiel, F. Banhart, Electron Beam Dynamics in an Ultrafast Transmission Electron Microscope with Wehnelt Electrode. *Ultramicroscopy* **171**, 8–18 (2016) (cit. on pp. 2, 38).
70. F. Houdellier, G. M. Caruso, P. Abeilhou, A. Arbouet, “Design and Realization of an Ultrafast Cold Field Emission Source Operating under High Voltage” in *European Microscopy Congress 2016: Proceedings*, European Microscopy Society, Ed. (Wiley, Weinheim, 2016), pp. 316–317; ISBN: 978-3-527-80846-5 (cit. on p. 2).
71. A. Feist, N. Bach, N. Rubiano da Silva, T. Danz, M. Möller, K. E. Priebe, T. Domröse, J. G. Gatzmann, S. Rost, J. Schauss, S. Strauch, R. Bormann, M. Siviş, S. Schäfer, C. Ropers, Ultrafast Transmission Electron Microscopy Using a Laser-Driven Field Emitter: Femtosecond Resolution with a High Coherence Electron Beam. *Ultramicroscopy* **176**, 63–73 (2017) (cit. on pp. 2, 3, 9, 10, 15, 16, 18, 19, 23, 35, 38–42, 133, 145, 160, 164).
72. A. Feist, N. Rubiano da Silva, W. Liang, C. Ropers, S. Schäfer, Nanoscale Diffractive Probing of Strain Dynamics in Ultrafast Transmission Electron Microscopy. *Structural Dynamics* **5**, 014302 (2018) (cit. on pp. 3, 9, 38, 52, 59, 101, 108, 109, 132, 135, 164).

- 
73. A. Arbouet, G. M. Caruso, F. Houdellier, “Chapter One - Ultrafast Transmission Electron Microscopy: Historical Development, Instrumentation, and Applications” in *Advances in Imaging and Electron Physics*, P. W. Hawkes, Ed. (Elsevier, 2018), vol. 207, pp. 1–72 (cit. on pp. 3, 15, 35).
  74. S. Vogelgesang, G. Storeck, J. G. Horstmann, T. Diekmann, M. Sivilis, S. Schramm, K. Rossnagel, S. Schäfer, C. Ropers, Phase Ordering of Charge Density Waves Traced by Ultrafast Low-Energy Electron Diffraction. *Nature Physics* **14**, 184–190 (2018) (cit. on pp. 3, 28, 38, 104, 132).
  75. M. Gulde, S. Schweda, G. Storeck, M. Maiti, H. K. Yu, A. M. Wodtke, S. Schäfer, C. Ropers, Ultrafast Low-Energy Electron Diffraction in Transmission Resolves Polymer/Graphene Superstructure Dynamics. *Science* **345**, 200–204 (2014) (cit. on pp. 3, 38, 108, 127, 161).
  76. T. Ishikawa, S. A. Hayes, S. Keskin, G. Corthey, M. Hada, K. Pichugin, A. Marx, J. Hirscht, K. Shionuma, K. Onda, Y. Okimoto, S.-y. Koshihara, T. Yamamoto, H. Cui, M. Nomura, Y. Oshima, M. Abdel-Jawad, R. Kato, R. J. D. Miller, Direct Observation of Collective Modes Coupled to Molecular Orbital-Driven Charge Transfer. *Science* **350**, 1501–1505 (2015) (cit. on pp. 3, 38).
  77. W. J. Engelen, M. A. van der Heijden, D. J. Bakker, E. J. D. Vredenburg, O. J. Luiten, High-Coherence Electron Bunches Produced by Femtosecond Photoionization. *Nature Communications* **4**, 1693 (2013) (cit. on pp. 3, 38).
  78. A. J. McCulloch, D. V. Sheludko, M. Junker, R. E. Scholten, High-Coherence Picosecond Electron Bunches from Cold Atoms. *Nature Communications* **4**, 1692 (2013) (cit. on p. 3).
  79. T. Li, B. L. Rickman, W. A. Schroeder, Emission Properties of Body-Centered Cubic Elemental Metal Photocathodes. *Journal of Applied Physics* **117**, 134901 (2015) (cit. on pp. 3, 38).
  80. G. M. Caruso, F. Houdellier, S. Weber, M. Kociak, A. Arbouet, High Brightness Ultrafast Transmission Electron Microscope Based on a Laser-Driven Cold-Field Emission Source: Principle and Applications. *Advances in Physics: X* **4**, 1660214 (2019) (cit. on pp. 3, 9, 15, 20, 161).

81. C. Zhu, D. Zheng, H. Wang, M. Zhang, Z. Li, S. Sun, P. Xu, H. Tian, Z. Li, H. Yang, J. Li, Development of Analytical Ultrafast Transmission Electron Microscopy Based on Laser-Driven Schottky Field Emission. *Ultramicroscopy* **209**, 112887 (2020) (cit. on pp. 3, 35).
82. P. Hommelhoff, C. Kealhofer, M. A. Kasevich, Ultrafast Electron Pulses from a Tungsten Tip Triggered by Low-Power Femtosecond Laser Pulses. *Physical Review Letters* **97**, 247402 (2006) (cit. on pp. 3, 9, 15, 16, 35, 38, 161, 162).
83. C. Ropers, D. R. Solli, C. P. Schulz, C. Lienau, T. Elsaesser, Localized Multiphoton Emission of Femtosecond Electron Pulses from Metal Nanotips. *Physical Review Letters* **98**, 043907 (2007) (cit. on pp. 3, 9, 16, 35, 38, 161, 162).
84. B. Barwick, C. Corder, J. Strohaber, N. Chandler-Smith, C. Uiterwaal, H. Batelaan, Laser-Induced Ultrafast Electron Emission from a Field Emission Tip. *New Journal of Physics* **9**, 142–142 (2007) (cit. on pp. 3, 9, 16, 161, 162).
85. B. J. Siwick, J. R. Dwyer, R. E. Jordan, R. J. D. Miller, Ultrafast Electron Optics: Propagation Dynamics of Femtosecond Electron Packets. *Journal of Applied Physics* **92**, 1643–1648 (2002) (cit. on pp. 3, 23, 27, 28, 39, 41).
86. T. van Oudheusden, P. L. E. M. Pasmans, S. B. van der Geer, M. J. de Loos, M. J. van der Wiel, O. J. Luiten, Compression of Subrelativistic Space-Charge-Dominated Electron Bunches for Single-Shot Femtosecond Electron Diffraction. *Physical Review Letters* **105** (2010) (cit. on pp. 3, 25, 47, 163).
87. P. Musumeci, J. T. Moody, C. M. Scoby, M. S. Gutierrez, H. A. Bender, N. S. Wilcox, High Quality Single Shot Diffraction Patterns Using Ultrashort Megaelectron Volt Electron Beams from a Radio Frequency Photoinjector. *Review of Scientific Instruments* **81**, 013306 (2010) (cit. on pp. 3, 38, 39).
88. M. Kuwahara, Y. Nambo, K. Aoki, K. Sameshima, X. Jin, T. Ujihara, H. Asano, K. Saitoh, Y. Takeda, N. Tanaka, The Boersch Effect in a Picosecond Pulsed Electron Beam Emitted from a Semiconductor Photocathode. *Applied Physics Letters* **109**, 013108 (2016) (cit. on pp. 3, 23, 32, 38, 39).
89. O. J. Luiten, S. B. van der Geer, M. J. de Loos, F. B. Kiewiet, M. J. van der Wiel, How to Realize Uniform Three-Dimensional Ellipsoidal Electron Bunches. *Physical Review Letters* **93** (2004); doi:10.1103/PhysRevLett.93.094802 (cit. on pp. 3, 25–27, 41, 47).

- 
90. S. Collin, M. Merano, M. Gatri, S. Sonderegger, P. Renucci, J.-D. Ganière, B. Deveaud, Transverse and Longitudinal Space-Charge-Induced Broadenings of Ultrafast Electron Packets. *Journal of Applied Physics* **98**, 094910 (2005) (cit. on pp. 3, 23, 39).
  91. A. M. Michalik, J. E. Sipe, Analytic Model of Electron Pulse Propagation in Ultrafast Electron Diffraction Experiments. *Journal of Applied Physics* **99**, 054908 (2006) (cit. on pp. 3, 23, 39).
  92. B. W. Reed, Femtosecond Electron Pulse Propagation for Ultrafast Electron Diffraction. *Journal of Applied Physics* **100**, 034916 (2006) (cit. on pp. 3, 23, 39).
  93. A. Gahlmann, S. Tae Park, A. H. Zewail, Ultrashort Electron Pulses for Diffraction, Crystallography and Microscopy: Theoretical and Experimental Resolutions. *Physical Chemistry Chemical Physics* **10**, 2894 (2008) (cit. on pp. 3, 23, 29, 39).
  94. A. Paarmann, M. Gulde, M. Müller, S. Schäfer, S. Schweda, M. Maiti, C. Xu, T. Hohage, F. Schenk, C. Ropers, R. Ernstorfer, Coherent Femtosecond Low-Energy Single-Electron Pulses for Time-Resolved Diffraction and Imaging: A Numerical Study. *Journal of Applied Physics* **112**, 113109 (2012) (cit. on pp. 3, 23, 39).
  95. C. Thomsen, H. T. Grahn, H. J. Maris, J. Tauc, Surface Generation and Detection of Phonons by Picosecond Light Pulses. *Physical Review B* **34**, 4129–4138 (1986) (cit. on pp. 7, 105, 108, 110).
  96. G. C. Cho, W. Kütt, H. Kurz, Subpicosecond Time-Resolved Coherent-Phonon Oscillations in GaAs. *Physical Review Letters* **65**, 764–766 (1990) (cit. on p. 7).
  97. E. D. Potter, J. L. Herek, S. Pedersen, Q. Liu, A. H. Zewail, Femtosecond Laser Control of a Chemical Reaction. *Nature* **355**, 66–68 (1992) (cit. on p. 7).
  98. A. H. Zewail, Femtochemistry: Atomic-Scale Dynamics of the Chemical Bond †. *The Journal of Physical Chemistry A* **104**, 5660–5694 (2000) (cit. on p. 7).
  99. P. Nuernberger, G. Vogt, T. Brixner, G. Gerber, Femtosecond Quantum Control of Molecular Dynamics in the Condensed Phase. *Physical Chemistry Chemical Physics* **9**, 2470–2497 (2007) (cit. on p. 7).
  100. O.-H. Kwon, B. Barwick, H. S. Park, J. S. Baskin, A. H. Zewail, Nanoscale Mechanical Drumming Visualized by 4D Electron Microscopy. *Nano Letters* **8**, 3557–3562 (2008); doi:10.1021/nl8029866 (cit. on pp. 7, 102, 108, 132).

101. M. K. Santala, B. W. Reed, S. Raoux, T. Topuria, T. LaGrange, G. H. Campbell, Irreversible Reactions Studied with Nanosecond Transmission Electron Microscopy Movies: Laser Crystallization of Phase Change Materials. *Applied Physics Letters* **102**, 174105 (2013) (cit. on p. 7).
102. B. Barwick, H. S. Park, O.-H. Kwon, J. S. Baskin, A. H. Zewail, 4D Imaging of Transient Structures and Morphologies in Ultrafast Electron Microscopy. *Science* **322**, 1227–1231 (2008) (cit. on pp. 8, 38).
103. U. J. Lorenz, A. H. Zewail, Observing Liquid Flow in Nanotubes by 4D Electron Microscopy. *Science* **344**, 1496–1500 (2014) (cit. on p. 8).
104. H. S. Park, J. S. Baskin, A. H. Zewail, 4D Lorentz Electron Microscopy Imaging: Magnetic Domain Wall Nucleation, Reversal, and Wave Velocity. *Nano Letters* **10**, 3796–3803 (2010) (cit. on p. 8).
105. A. Yurtsever, A. H. Zewail, 4D Nanoscale Diffraction Observed by Convergent-Beam Ultrafast Electron Microscopy. *Science* **326**, 708–712 (2009) (cit. on pp. 8, 108, 132).
106. A. Yurtsever, A. H. Zewail, Kikuchi Ultrafast Nanodiffraction in Four-Dimensional Electron Microscopy. *Proceedings of the National Academy of Sciences* **108**, 3152–3156 (2011) (cit. on pp. 8, 127, 132).
107. O. F. Mohammed, D.-S. Yang, S. K. Pal, A. H. Zewail, 4D Scanning Ultrafast Electron Microscopy: Visualization of Materials Surface Dynamics. *Journal of the American Chemical Society* **133**, 7708–7711 (2011) (cit. on p. 8).
108. R. Bormann, M. Gulde, A. Weismann, S. V. Yalunin, C. Ropers, Tip-Enhanced Strong-Field Photoemission. *Physical Review Letters* **105**, 147601 (2010) (cit. on pp. 9, 16, 35, 38, 161, 162).
109. G. Herink, D. R. Solli, M. Gulde, C. Ropers, Field-Driven Photoemission from Nanostructures Quenches the Quiver Motion. *Nature* **483**, 190–193 (2012) (cit. on pp. 9, 16).
110. A. Feist, K. E. Echternkamp, J. Schauss, S. V. Yalunin, S. Schäfer, C. Ropers, Quantum Coherent Optical Phase Modulation in an Ultrafast Transmission Electron Microscope. *Nature* **521**, 200–203 (2015) (cit. on pp. 9, 35, 40, 134, 161).
111. K. E. Echternkamp, A. Feist, S. Schäfer, C. Ropers, Ramsey-Type Phase Control of Free-Electron Beams. *Nature Physics* **12**, 1000–1004 (2016) (cit. on pp. 9, 161).

- 
112. K. E. Priebe, C. Rathje, S. V. Yalunin, T. Hohage, A. Feist, S. Schäfer, C. Ropers, Attosecond Electron Pulse Trains and Quantum State Reconstruction in Ultrafast Transmission Electron Microscopy. *Nature Photonics* **11**, 793–797 (2017) (cit. on pp. 9, 38).
  113. T. Rittmann, “Attosecond Beam Shaping in Ultrafast Electron Microscopy,” Master Thesis, Georg-August Universität, 2022 (cit. on pp. 9, 24, 161).
  114. A. Feist, S. V. Yalunin, S. Schäfer, C. Ropers, High-Purity Free-Electron Momentum States Prepared by Three-Dimensional Optical Phase Modulation. *Physical Review Research* **2**, 043227 (2020) (cit. on p. 9).
  115. O. Kfir, H. Lourenço-Martins, G. Storeck, M. Sivis, T. R. Harvey, T. J. Kippenberg, A. Feist, C. Ropers, Controlling Free Electrons with Optical Whispering-Gallery Modes. *Nature* **582**, 46–49 (2020) (cit. on p. 9).
  116. N. Bach, A. Feist, M. Möller, C. Ropers, S. Schäfer, Tailored Nanophononic Wavefield in a Patterned Bilayer System Probed by Ultrafast Convergent Beam Electron Diffraction. *Structural Dynamics* **9**, 034301 (2022) (cit. on pp. 9, 52, 59, 70, 161, 163, 164, 167, 227).
  117. M. Möller, J. H. Gaida, S. Schäfer, C. Ropers, Few-Nm Tracking of Current-Driven Magnetic Vortex Orbits Using Ultrafast Lorentz Microscopy. *Communications Physics* **3**, 1–7 (2020) (cit. on pp. 9, 13).
  118. M. Möller, J. H. Gaida, C. Ropers, Pinning and Gyration Dynamics of Magnetic Vortices Revealed by Correlative Lorentz and Bright-Field Imaging. *Physical Review Research* **4**, 013027 (2022) (cit. on p. 9).
  119. T. Danz, T. Domröse, C. Ropers, Ultrafast Nanoimaging of the Order Parameter in a Structural Phase Transition. *Science* **371**, 371–374 (2021); doi:10.1126/science.abd2774 (cit. on pp. 9, 101, 103, 104, 108, 132, 161).
  120. T. Domröse, T. Danz, S. F. Schaible, K. Rosnagel, S. V. Yalunin, C. Ropers, Light-Induced Hexatic State in a Layered Quantum Material. *Nature Materials* (2023) (cit. on pp. 9, 101, 104, 161).
  121. F. Houdellier, G. M. Caruso, S. Weber, M. Kociak, A. Arbouet, Development of a High Brightness Ultrafast Transmission Electron Microscope Based on a Laser-Driven Cold Field Emission Source. *Ultramicroscopy* **186**, 128–138 (2018) (cit. on pp. 9, 38).

122. T. R. Harvey, J.-W. Henke, O. Kfir, H. Lourenço-Martins, A. Feist, F. J. García de Abajo, C. Ropers, Probing Chirality with Inelastic Electron-Light Scattering. *Nano Letters* **20**, 4377–4383 (2020) (cit. on p. 9).
123. M. De Graef, *Introduction to Conventional Transmission Electron Microscopy* (Cambridge University Press, Cambridge, 2003); ISBN: 978-0-521-62995-9 (cit. on pp. 10, 14, 86, 92, 97).
124. W. Graves, L. DiMauro, R. Heese, E. Johnson, J. Rose, J. Rudati, T. Shaftan, B. Sheehy, presented at the PACS2001. Proceedings of the 2001 Particle Accelerator Conference (Cat. No.01CH37268), vol. 3, pp. 2227–2229, ISBN: 978-0-7803-7191-0 (cit. on p. 10).
125. B. L. Rickman, J. A. Berger, A. W. Nicholls, W. A. Schroeder, Intrinsic Electron Beam Emittance from Metal Photocathodes: The Effect of the Electron Effective Mass. *Physical Review Letters* **111**, 237401 (2013) (cit. on p. 10).
126. N. Bach, “Charakterisierung Eines Laser-getriebenen Schottky-Emitters,” Master Thesis, Georg-August Universität, 2016 (cit. on pp. 10, 17, 22).
127. M. Haider, P. Hartel, H. Müller, S. Uhlemann, J. Zach, Information Transfer in a TEM Corrected for Spherical and Chromatic Aberration. *Microscopy and Microanalysis: The Official Journal of Microscopy Society of America, Microbeam Analysis Society, Microscopical Society of Canada* **16**, 393–408 (2010) (cit. on p. 11).
128. U. Kaiser, J. Biskupek, J. C. Meyer, J. Leschner, L. Lechner, H. Rose, M. Stöger-Pollach, A. N. Khlobystov, P. Hartel, H. Müller, M. Haider, S. Eyhusen, G. Benner, Transmission Electron Microscopy at 20 kV for Imaging and Spectroscopy. *Ultramicroscopy* **111**, 1239–1246 (2011) (cit. on pp. 11, 165).
129. T. C. Danz, “Ultrafast Transmission Electron Microscopy of a Structural Phase Transition,” Doctoral Thesis, Georg-August-University Göttingen, 2021 (cit. on p. 11).
130. L. Reimer, H. Kohl, *Transmission Electron Microscopy: Physics of Image Formation* (Springer New York, New York, NY, 5., th ed. Softcover version of original hardcover edition 2008, 2010); ISBN: 978-1-4419-2308-0 (cit. on pp. 12, 14, 81, 161, 164, 165).

- 
131. H. Tietz, Design and Characterization of 64 MegaPixel Fiber Optic Coupled CMOS Detector for Transmission Electron Microscopy. *Microscopy and Microanalysis* **14**, 804–805 (2008) (cit. on p. 12).
  132. R. Clough, A. Kirkland, “Direct Digital Electron Detectors” in *Advances in Imaging and Electron Physics* (Elsevier, 2016), vol. 198, pp. 1–42; ISBN: 978-0-12-804810-8 (cit. on p. 12).
  133. A.-C. Milazzo, P. Leblanc, F. Duttweiler, L. Jin, J. C. Bouwer, S. Peltier, M. Ellisman, F. Bieser, H. S. Matis, H. Wieman, P. Denes, S. Kleinfelder, N.-H. Xuong, Active Pixel Sensor Array as a Detector for Electron Microscopy. *Ultramicroscopy* **104**, 152–159 (2005) (cit. on p. 12).
  134. A. Feist, G. Huang, G. Arend, Y. Yang, J.-W. Henke, A. S. Raja, F. J. Kappert, R. N. Wang, H. Lourenço-Martins, Z. Qiu, J. Liu, O. Kfir, T. J. Kippenberg, C. Ropers, Cavity-Mediated Electron-Photon Pairs. *Science* **377**, 777–780 (2022) (cit. on p. 12).
  135. T. WeSSels, S. Däster, Y. Murooka, B. Zingsem, V. Migunov, M. Kruth, S. Finizio, P.-H. Lu, A. Kovács, A. Oelsner, K. Müller-Caspary, Y. Acremann, R. E. Dunin-Borkowski, Continuous Illumination Picosecond Imaging Using a Delay Line Detector in a Transmission Electron Microscope. *Ultramicroscopy* **233**, 113392 (2022) (cit. on p. 12).
  136. D. Jannis, C. Hofer, C. Gao, X. Xie, A. Béch e, T. J. Pennycook, J. Verbeeck, Event Driven 4D STEM Acquisition with a Timepix3 Detector: Microsecond Dwell Time and Faster Scans for High Precision and Low Dose Applications. *Ultramicroscopy* **233**, 113423 (2022) (cit. on p. 12).
  137. Y. Auad, M. Walls, J.-D. Blazit, O. St ephane, L. H. Tizei, M. Kociak, F. De la Pe na, M. Tenc e, Event-Based Hyperspectral EELS: Towards Nanosecond Temporal Resolution. *Ultramicroscopy* **239**, 113539 (2022) (cit. on p. 12).
  138. R. Egerton, *Electron Energy-Loss Spectroscopy in the Electron Microscope* (Springer US, Boston, MA, 2011); ISBN: 978-1-4419-9582-7 (cit. on pp. 12, 167).
  139. F. Kahl, V. Gerheim, M. Linck, H. M uller, R. Schillinger, S. Uhlemann, “Chapter Three - Test and Characterization of a New Post-Column Imaging Energy Filter” in *Advances in Imaging and Electron Physics*, P. W. Hawkes, M. Hytch, Eds. (Elsevier, 2019), vol. 212, pp. 35–70 (cit. on p. 12).

140. GIF Continuum and Continuum S | Gatan, Inc. <https://www.gatan.com/products/tem-imaging-spectroscopy/gif-continuum-and-continuum-s> (cit. on p. 12).
141. D. B. Williams, C. B. Carter, *Transmission Electron Microscopy* (Springer US, Boston, MA, 2009); ISBN: 978-0-387-76501-3 (cit. on pp. 12–14, 19, 85, 95).
142. H. Lichte, M. Lehmann, Electron Holography Basics and Applications. *Reports on Progress in Physics* **71**, 016102 (2007) (cit. on pp. 13, 14, 165).
143. F. Zernike, Das Phasenkontrastverfahren Bei Der Mikroskopischen Beobachtung. *Z. techn. Physik* **16**, 454–457 (1935) (cit. on p. 13).
144. F. Zernike, How I Discovered Phase Contrast. *Science* **121**, 345–349 (1955) (cit. on p. 13).
145. L. Zhang, J. P. Hoogenboom, B. Cook, P. Kruit, Photoemission Sources and Beam Blankers for Ultrafast Electron Microscopy. *Structural Dynamics* **6**, 051501 (2019) (cit. on pp. 15, 22).
146. M. Aeschlimann, E. Hull, J. Cao, C. A. Schmuttenmaer, L. G. Jahn, Y. Gao, H. E. Elsayed-Ali, D. A. Mantell, M. R. Scheinfein, A Picosecond Electron Gun for Surface Analysis. *Review of Scientific Instruments* **66**, 1000–1009 (1995) (cit. on p. 15).
147. M. Eichberger, N. Erasmus, K. Haupt, G. Kassier, A. von Flotow, J. Demsar, H. Schwoerer, Femtosecond Streaking of Electron Diffraction Patterns to Study Structural Dynamics in Crystalline Matter. *Applied Physics Letters* **102**, 121106 (2013) (cit. on p. 15).
148. M. Gao, Y. Jiang, G. H. Kassier, R. J. Dwayne Miller, Single Shot Time Stamping of Ultrabright Radio Frequency Compressed Electron Pulses. *Applied Physics Letters* **103**, 033503 (2013) (cit. on p. 15).
149. B. J. Siwick, J. R. Dwyer, R. E. Jordan, R. J. D. Miller, An Atomic-Level View of Melting Using Femtosecond Electron Diffraction. *Science* **302**, 1382–1385 (2003) (cit. on p. 15).
150. L. Piazza, C. Ma, H. X. Yang, A. Mann, Y. Zhu, J. Q. Li, F. Carbone, Ultrafast Structural and Electronic Dynamics of the Metallic Phase in a Layered Manganite. *Structural Dynamics* **1**, 014501 (2014) (cit. on p. 15).

- 
151. D. R. Cremons, D. A. Plemmons, D. J. Flannigan, Femtosecond Electron Imaging of Defect-Modulated Phonon Dynamics. *Nature Communications* **7**, 11230 (2016) (cit. on pp. 15, 38, 132).
152. M. J. Fransen, M. H. F. Overwijk, P. Kruit, Brightness Measurements of a ZrO/W Schottky Electron Emitter in a Transmission Electron Microscope. *Applied Surface Science* **146**, 357–362 (1999) (cit. on pp. 15, 38).
153. D. Ehberger, J. Hammer, M. Eisele, M. Krüger, J. Noe, A. Högele, P. Hommelhoff, Highly Coherent Electron Beam from a Laser-Triggered Tungsten Needle Tip. *Physical Review Letters* **114**, 227601 (2015) (cit. on pp. 15, 38, 162).
154. J. Vogelsang, J. Robin, B. J. Nagy, P. Dombi, D. Rosenkranz, M. Schiek, P. GroSS, C. Lienau, Ultrafast Electron Emission from a Sharp Metal Nanotaper Driven by Adiabatic Nanofocusing of Surface Plasmons. *Nano Letters* **15**, 4685–4691 (2015) (cit. on pp. 15, 16, 28, 38).
155. S. Schäfer, W. Liang, A. H. Zewail, Structural Dynamics of Surfaces by Ultrafast Electron Crystallography: Experimental and Multiple Scattering Theory. *The Journal of Chemical Physics* **135**, 214201 (2011) (cit. on pp. 16, 100).
156. S. Wall, B. Krenzer, S. Wippermann, S. Sanna, F. Klasing, A. Hanisch-Blicharski, M. Kammler, W. G. Schmidt, M. Horn-von Hoegen, Atomistic Picture of Charge Density Wave Formation at Surfaces. *Physical Review Letters* **109**, 186101 (2012) (cit. on p. 16).
157. T. Frigge, B. Hafke, T. Witte, B. Krenzer, C. Streubühr, A. Samad Syed, V. Miki Trontl, I. Avigo, P. Zhou, M. Ligges, D. von der Linde, U. Bovensiepen, M. Horn-von Hoegen, S. Wippermann, A. Lücke, S. Sanna, U. Gerstmann, W. G. Schmidt, Optically Excited Structural Transition in Atomic Wires on Surfaces at the Quantum Limit. *Nature* **544**, 207–211 (2017) (cit. on pp. 16, 38, 108).
158. D.-S. Yang, N. Gedik, A. H. Zewail, Ultrafast Electron Crystallography. 1. Nonequilibrium Dynamics of Nanometer-Scale Structures. *The Journal of Physical Chemistry C* **111**, 4889–4919 (2007) (cit. on p. 16).
159. E. J. Sie, C. M. Nyby, C. D. Pemmaraju, S. J. Park, X. Shen, J. Yang, M. C. Hoffmann, B. K. Ofori-Okai, R. Li, A. H. Reid, S. Weathersby, E. Mannebach, N. Finney, D. Rhodes, D. Chenet, A. Antony, L. Balicas, J. Hone, T. P. Devereaux, T. F. Heinz, X. Wang, A. M. Lindenberg, An Ultrafast Symmetry Switch in a Weyl Semimetal. *Nature* **565**, 61–66 (2019) (cit. on pp. 16, 108, 132).

160. M. Krüger, C. Lemell, G. Wachter, J. Burgdörfer, P. Hommelhoff, Attosecond Physics Phenomena at Nanometric Tips. *Journal of Physics B: Atomic, Molecular and Optical Physics* **51**, 172001 (2018) (cit. on p. 16).
161. M. S. Bronsgeest, “Physics of Schottky Electron Sources,” PhD thesis, Technische Universiteit Delft, 2009 (cit. on pp. 16, 17).
162. L. W. Swanson, G. A. Schwind, “Review of ZrO/W Schottky Cathode” in *Handbook of Charged Particle Optics* (CRC Press, Second, 2009); ISBN: 978-1-315-21988-2 (cit. on p. 17).
163. P. R. Thornton, “Electron Physics in Device Microfabrication. I General Background and Scanning Systems” in *Advances in Electronics and Electron Physics*, L. Marton, Ed. (Academic Press, 1979), vol. 48, pp. 271–380 (cit. on p. 17).
164. J. E. Wolfe, Operational Experience with Zirconiated TF Emitters. *Journal of Vacuum Science and Technology* **16**, 1704–1708 (1979) (cit. on p. 17).
165. S. Horiuchi, *Fundamentals of High-Resolution Transmission Electron Microscopy* (North-Holland, Amsterdam; New York, 1994); ISBN: 978-0-444-88744-3 (cit. on p. 17).
166. L. R. Danielson, L. W. Swanson, High Temperature Coadsorption Study of Zirconium and Oxygen on the W(100) Crystal Face. *Surface Science* **88**, 14–30 (1979) (cit. on pp. 17, 35).
167. L. R. Danielson, The Zr-O-W(100) Emitter and Coadsorption of Zirconium and Carbon Monoxide on W(100). *Journal of Applied Physics* **52**, 6769–6776 (1981) (cit. on pp. 17, 35).
168. S. C. Lee, Y. Irokawa, M. Inoue, R. Shimizu, Behavior of Zirconium in the ZrO/W(100) System at High Temperature, Studied by ISS, AES and Work-Function Measurements. *Surface Science* **330**, 289–296 (1995) (cit. on p. 17).
169. H. Satoh, H. Nakane, H. Adachi, Behavior of Zirconium on ZrO/W(100) Surface. *Applied Surface Science* **100–101**, 216–221 (1996) (cit. on p. 17).
170. H. Tanaka, H. Nakayama, K. Watanabe, Ab Initio Calculation of Work Functions of ZrO/W(100) and YO/W(100) Surfaces. *Japanese Journal of Applied Physics* **44**, 7518 (2005) (cit. on p. 17).

- 
171. N. Bach, A. Feist, T. Domröse, M. Moller, N. Rubiano da Silva, T. Danz, S. Schafer, C. Ropers, presented at the 2017 30th International Vacuum Nanoelectronics Conference (IVNC), pp. 80–81; doi:10.1109/IVNC.2017.8051554 (cit. on p. 18).
  172. R. Bormann, S. Strauch, S. Schäfer, C. Ropers, An Ultrafast Electron Microscope Gun Driven by Two-Photon Photoemission from a Nanotip Cathode. *Journal of Applied Physics* **118**, 173105 (2015) (cit. on pp. 18, 19, 38, 161).
  173. N. Bach, T. Domröse, A. Feist, T. Rittmann, S. Strauch, C. Ropers, S. Schäfer, Coulomb Interactions in High-Coherence Femtosecond Electron Pulses from Tip Emitters. *Structural Dynamics* **6**, 014301 (2019) (cit. on pp. 18, 23, 26–28, 30, 32, 160, 227).
  174. W. Schottky, Über Den Einfluss von Strukturwirkungen, Besonders Der Thomson-schen Bildkraft, Auf Die Elektronenemission Der Metalle. *Physikalische Zeitschrift* **15**, 872–878 (1914) (cit. on p. 19).
  175. H. D. Beckey, H. Krone, F. W. Roellgen, Comparison of Tips, Thin Wires and Sharp Metal Edges as Emitters for Field Ionization Mass Spectrometry. *Journal of Physics E: Scientific Instruments* **1**, 118 (1968) (cit. on pp. 19, 29, 48).
  176. H. Kawano, Effective Work Functions for Ionic and Electronic Emissions from Mono- and Polycrystalline Surfaces. *Progress in Surface Science* **83**, 1–165 (2008) (cit. on p. 19).
  177. R. H. Fowler, L. Nordheim, Electron Emission in Intense Electric Fields. *Proceedings of the Royal Society of London. Series A, Containing Papers of a Mathematical and Physical Character* **119**, 173–181 (1928) (cit. on p. 19).
  178. R. Haindl, K. Köster, A. Feist, C. Ropers, presented at the 2021 34th International Vacuum Nanoelectronics Conference (IVNC), pp. 1–2, ISBN: 978-1-66542-589-6 (cit. on p. 20).
  179. P. W. Hawkes, E. Kasper, *Principles of Electron Optics* (Academic Press, San Diego, 2014); ISBN: 978-0-12-333340-7 (cit. on pp. 20, 21, 32).
  180. F. Schwabl, *Statistische Mechanik*; ISBN: 978-3-540-31095-2 (cit. on pp. 20, 162).
  181. M. Reiser, *Theory and Design of Charged Particle Beams* (Wiley, 2008); ISBN: 978-3-527-62205-4 (cit. on pp. 21, 38, 40, 41).

182. J. C. H. Spence, *High-Resolution Electron Microscopy* (Oxford University Press, Oxford, United Kingdom ; New York, NY, Fourth edition, 2017); ISBN: 978-0-19-879583-4 (cit. on p. 22).
183. R. Burge, J. Dainty, J. Thom, The Spatial Coherence of Electron Beams. *Proc EMAG*, 221 (1975) (cit. on p. 22).
184. B. E. A. Saleh, M. C. Teich, *Grundlagen Der Photonik* (Wiley, Weinheim, 2008); ISBN: 978-3-527-40677-7 (cit. on pp. 22, 41).
185. T. van Oudheusden, E. F. de Jong, S. B. van der Geer, W. P. E. M. O. 't Root, O. J. Luiten, B. J. Siwick, Electron Source Concept for Single-Shot Sub-100 Fs Electron Diffraction in the 100 keV Range. *Journal of Applied Physics* **102**, 093501 (2007) (cit. on pp. 23, 25, 39, 163).
186. P. Baum, On the Physics of Ultrashort Single-Electron Pulses for Time-Resolved Microscopy and Diffraction. *Chemical Physics* **423**, 55–61 (2013) (cit. on p. 23).
187. S. Passlack, S. Mathias, O. Andreyev, D. Mittnacht, M. Aeschlimann, M. Bauer, Space Charge Effects in Photoemission with a Low Repetition, High Intensity Femtosecond Laser Source. *Journal of Applied Physics* **100**, 024912 (2006) (cit. on pp. 23, 27, 28).
188. G. H. Jansen, Coulomb Interactions in Particle Beams. *Nuclear Instruments and Methods in Physics Research Section A: Accelerators, Spectrometers, Detectors and Associated Equipment* **298**, 496–504 (1990) (cit. on pp. 23, 24, 31, 39).
189. A. H. V. van Veen, C. W. Hagen, J. E. Barth, P. Kruit, Reduced Brightness of the ZrO/W Schottky Electron Emitter. *Journal of Vacuum Science & Technology B: Microelectronics and Nanometer Structures* **19**, 2038 (2001) (cit. on p. 23).
190. M. S. Bronsgeest, J. E. Barth, G. A. Schwind, L. W. Swanson, P. Kruit, Extracting the Boersch Effect Contribution from Experimental Energy Spread Measurements for Schottky Electron Emitters. *Journal of Vacuum Science & Technology B: Microelectronics and Nanometer Structures Processing, Measurement, and Phenomena* **25**, 2049–2054 (2007) (cit. on pp. 23, 24, 31, 32, 39).
191. P. Denham, P. Musumeci, Space-Charge Aberrations in Single-Shot Time-Resolved Transmission Electron Microscopy. *Physical Review Applied* **15**, 024050 (2021) (cit. on p. 23).

- 
192. L. A. DuBridge, Theory of the Energy Distribution of Photoelectrons. *Physical Review* **43**, 727–741 (1933) (cit. on p. 24).
  193. W. W. Roehr, The Effect of Temperature on the Energy Distribution of Photoelectrons. II. Total Energies. *Physical Review* **44**, 866–871 (1933) (cit. on p. 24).
  194. M. Aidelsburger, F. O. Kirchner, F. Krausz, P. Baum, Single-Electron Pulses for Ultrafast Diffraction. *Proceedings of the National Academy of Sciences* **107**, 19714–19719 (2010) (cit. on p. 24).
  195. H. Boersch, Experimentelle Bestimmung der Energieverteilung in thermisch ausgelösten Elektronenstrahlen. *Zeitschrift für Physik* **139**, 115–146 (1954) (cit. on pp. 24, 39).
  196. K. H. Loeffler, Energy-Spread Generation in Electron-Optical Instruments. *Zeitschrift für Angewandte Physik*, 145 (1969) (cit. on pp. 25, 39).
  197. B. Cook, T. Verduin, C. W. Hagen, P. Kruit, Brightness Limitations of Cold Field Emitters Caused by Coulomb Interactions. *Journal of Vacuum Science & Technology B, Nanotechnology and Microelectronics: Materials, Processing, Measurement, and Phenomena* **28**, C6C74–C6C79 (2010) (cit. on pp. 25, 39).
  198. R. P. Chatelain, V. R. Morrison, C. Godbout, B. J. Siwick, Ultrafast Electron Diffraction with Radio-Frequency Compressed Electron Pulses. *Applied Physics Letters* **101**, 081901 (2012) (cit. on pp. 25, 163).
  199. J. Maxson, D. Cesar, G. Calmasini, A. Ody, P. Musumeci, D. Alesini, Direct Measurement of Sub-10 Fs Relativistic Electron Beams with Ultralow Emittance. *Physical Review Letters* **118**, 154802 (2017) (cit. on pp. 25, 39).
  200. C. Kealhofer, W. Schneider, D. Ehberger, A. Ryabov, F. Krausz, P. Baum, All-Optical Control and Metrology of Electron Pulses. *Science* **352**, 429–433 (2016) (cit. on pp. 25, 39, 163).
  201. P. Musumeci, J. T. Moody, R. J. England, J. B. Rosenzweig, T. Tran, Experimental Generation and Characterization of Uniformly Filled Ellipsoidal Electron-Beam Distributions. *Physical Review Letters* **100**, 244801 (2008) (cit. on p. 25).
  202. D. Filippetto, P. Musumeci, R. K. Li, B. J. Siwick, M. R. Otto, M. Centurion, J. P. F. Nunes, Ultrafast electron diffraction: Visualizing dynamic states of matter. *Rev. Mod. Phys.* **94**, 045004 (2022) (cit. on p. 25).

203. S. B. van der Geer, M. J. de Loos, T. van Oudheusden, W. P. E. M. op 't Root, M. J. van der Wiel, O. J. Luiten, Longitudinal Phase-Space Manipulation of Ellipsoidal Electron Bunches in Realistic Fields. *Physical Review Special Topics - Accelerators and Beams* **9**, 044203 (2006) (cit. on pp. 26, 163).
204. M. Otto, “Advancements in Electron Pulse Compression Technology Applied to Ultrafast Electron Scattering,” PhD thesis, McGill University, 2020 (cit. on p. 27).
205. B. Cook, P. Kruit, Coulomb Interactions in Sharp Tip Pulsed Photo Field Emitters. *Applied Physics Letters* **109**, 151901 (2016) (cit. on pp. 27, 39).
206. M. Müller, A. Paarmann, R. Ernstorfer, Femtosecond Electrons Probing Currents and Atomic Structure in Nanomaterials. *Nature Communications* **5**, 5292 (2014) (cit. on pp. 28, 38).
207. E. Quinonez, J. Handali, B. Barwick, Femtosecond Photoelectron Point Projection Microscope. *Review of Scientific Instruments* **84**, 103710 (2013) (cit. on pp. 28, 162).
208. G. Storeck, S. Vogelgesang, M. Siviş, S. Schäfer, C. Ropers, Nanotip-Based Photoelectron Microgun for Ultrafast LEED. *Structural Dynamics* **4**, 044024 (2017) (cit. on p. 28).
209. G. Storeck, J. G. Horstmann, T. Diekmann, S. Vogelgesang, G. von Witte, S. V. Yalunin, K. Rossnagel, C. Ropers, Structural Dynamics of Incommensurate Charge-Density Waves Tracked by Ultrafast Low-Energy Electron Diffraction. *Structural Dynamics* **7**, 034304 (2020) (cit. on p. 28).
210. S. T. Park, O.-H. Kwon, A. H. Zewail, Chirped Imaging Pulses in Four-Dimensional Electron Microscopy: Femtosecond Pulsed Hole Burning. *New Journal of Physics* **14**, 053046 (2012) (cit. on pp. 31, 40, 48).
211. J. Orloff, Ed., *Handbook of Charged Particle Optics* (CRC Press/Taylor & Francis, Boca Raton, 2nd ed, 2009); ISBN: 978-1-4200-4554-3 (cit. on pp. 31, 32).
212. M. Fransen, T. L. Van Rooy, P. Tiemeijer, M. Overwijk, J. Faber, P. Kruit, “On the Electron-Optical Properties of the ZrO/W Schottky Electron Emitter” in *Advances in Imaging and Electron Physics* (Elsevier, 1999), vol. 111, pp. 91–166; ISBN: 978-0-12-014753-3 (cit. on p. 31).

- 
213. S. Meier, P. Hommelhoff, Coulomb Interactions and the Spatial Coherence of Femtosecond Nanometric Electron Pulses. *ACS Photonics* **9**, 3083–3088 (2022); doi:10.1021/acsp Photonics.2c00839 (cit. on pp. 32, 33).
214. G. H. Jansen, Trajectory Displacement Effect in Particle Projection Lithography Systems: Modifications to the Extended Two-Particle Theory and Monte Carlo Simulation Technique. *Journal of Applied Physics* **84**, 4549–4567 (1998) (cit. on p. 32).
215. D. J. Flannigan, D. R. Cremons, D. T. Valley, Multimodal Visualization of the Optomechanical Response of Silicon Cantilevers with Ultrafast Electron Microscopy. *Journal of Materials Research* **32**, 239–247 (2017) (cit. on pp. 35, 108, 132).
216. G. M. Caruso, F. Houdellier, P. Abeilhou, A. Arbouet, Development of an Ultrafast Electron Source Based on a Cold-Field Emission Gun for Ultrafast Coherent TEM. *Applied Physics Letters* **111**, 023101 (2017) (cit. on p. 35).
217. Y. Terada, S. Yoshida, O. Takeuchi, H. Shigekawa, Real-Space Imaging of Transient Carrier Dynamics by Nanoscale PumpProbe Microscopy. *Nature Photonics* **4**, 869–874 (2010) (cit. on pp. 38, 108).
218. M. Wagner, A. S. McLeod, S. J. Maddox, Z. Fei, M. Liu, R. D. Averitt, M. M. Fogler, S. R. Bank, F. Keilmann, D. N. Basov, Ultrafast Dynamics of Surface Plasmons in InAs by Time-Resolved Infrared Nanospectroscopy. *Nano Letters* **14**, 4529–4534 (2014) (cit. on p. 38).
219. M. A. Huber, M. Plankl, M. Eisele, R. E. Marvel, F. Sandner, T. Korn, C. Schüller, R. F. Haglund, R. Huber, T. L. Cocker, Ultrafast Mid-Infrared Nanoscopy of Strained Vanadium Dioxide Nanobeams. *Nano Letters* **16**, 1421–1427 (2016) (cit. on p. 38).
220. V. Kravtsov, R. Ulbricht, J. M. Atkin, M. B. Raschke, Plasmonic Nanofocused Four-Wave Mixing for Femtosecond near-Field Imaging. *Nature Nanotechnology* **11**, 459–464 (2016) (cit. on p. 38).
221. T. L. Cocker, V. Jelic, M. Gupta, S. J. Molesky, J. A. J. Burgess, G. D. L. Reyes, L. V. Titova, Y. Y. Tsui, M. R. Freeman, F. A. Hegmann, An Ultrafast Terahertz Scanning Tunnelling Microscope. *Nature Photonics* **7**, 620–625 (2013) (cit. on pp. 38, 108).

222. T. L. Cocker, D. Peller, P. Yu, J. Repp, R. Huber, Tracking the Ultrafast Motion of a Single Molecule by Femtosecond Orbital Imaging. *Nature* **539**, 263–267 (2016) (cit. on pp. 38, 108).
223. P. Beaud, A. Caviezel, S. O. Mariager, L. Rettig, G. Ingold, C. Dornes, S.-W. Huang, J. A. Johnson, M. Radovic, T. Huber, T. Kubacka, A. Ferrer, H. T. Lemke, M. Chollet, D. Zhu, J. M. Glowina, M. Sikorski, A. Robert, H. Wadati, M. Nakamura, M. Kawasaki, Y. Tokura, S. L. Johnson, U. Staub, A Time-Dependent Order Parameter for Ultrafast Photoinduced Phase Transitions. *Nature Materials* **13**, 923–927 (2014) (cit. on pp. 38, 132).
224. M. Bargheer, N. Zhavoronkov, Y. Gritsai, J. C. Woo, D. S. Kim, M. Woerner, T. Elsaesser, Coherent Atomic Motions in a Nanostructure Studied by Femtosecond X-ray Diffraction. *Science* **306**, 1771–1773 (2004) (cit. on pp. 38, 108).
225. R. J. D. Miller, Femtosecond Crystallography with Ultrabright Electrons and X-rays: Capturing Chemistry in Action. *Science* **343**, 1108–1116 (2014) (cit. on p. 38).
226. S. P. Weathersby, G. Brown, M. Centurion, T. F. Chase, R. Coffee, J. Corbett, J. P. Eichner, J. C. Frisch, A. R. Fry, M. Gühr, N. Hartmann, C. Hast, R. Hettel, R. K. Jobe, E. N. Jongewaard, J. R. Lewandowski, R. K. Li, A. M. Lindenberg, I. Makasyuk, J. E. May, D. McCormick, M. N. Nguyen, A. H. Reid, X. Shen, K. Sokolowski-Tinten, T. Vecchione, S. L. Vetter, J. Wu, J. Yang, H. A. Dürr, X. J. Wang, Mega-Electron-Volt Ultrafast Electron Diffraction at SLAC National Accelerator Laboratory. *Review of Scientific Instruments* **86**, 073702 (2015) (cit. on p. 38).
227. C. Gerbig, A. Senftleben, S. Morgenstern, C. Sarpe, T. Baumert, Spatio-Temporal Resolution Studies on a Highly Compact Ultrafast Electron Diffractometer. *New Journal of Physics* **17**, 043050 (2015) (cit. on p. 38).
228. K. Haupt, M. Eichberger, N. Erasmus, A. Rohwer, J. Demsar, K. Rossnagel, H. Schwoerer, Ultrafast Metamorphosis of a Complex Charge-Density Wave. *Physical Review Letters* **116**, 016402 (2016) (cit. on pp. 38, 132).
229. M. Harb, W. Peng, G. Sciaini, C. T. Hebeisen, R. Ernstorfer, M. A. Eriksson, M. G. Lagally, S. G. Kruglik, R. J. D. Miller, Excitation of Longitudinal and Transverse Coherent Acoustic Phonons in Nanometer Free-Standing Films of (001) Si. *Physical Review B* **79** (2009) (cit. on pp. 38, 109).

- 
230. L. W. Swanson, G. A. Schwind, “Review of ZrO/W Schottky Cathode” in *Handbook of Charged Particle Optics, Second Edition*, J. Orloff, Ed. (CRC Press, 2017); ISBN: 978-1-4200-4555-0 (cit. on p. 38).
231. A. V. Crewe, J. Wall, L. M. Welter, A High-Resolution Scanning Transmission Electron Microscope. *Journal of Applied Physics* **39**, 5861–5868 (1968) (cit. on pp. 38, 162).
232. T. Ishikawa, T. Urata, B. Cho, E. Rokuta, C. Oshima, Y. Terui, H. Saito, A. Yonezawa, T. T. Tsong, Highly Efficient Electron Gun with a Single-Atom Electron Source. *Applied Physics Letters* **90**, 143120 (2007) (cit. on p. 38).
233. H. Zhang, J. Tang, J. Yuan, Y. Yamauchi, T. T. Suzuki, N. Shinya, K. Nakajima, L.-C. Qin, An Ultrabright and Monochromatic Electron Point Source Made of a LaB<sub>6</sub> Nanowire. *Nature Nanotechnology* **11**, 273–279 (2016) (cit. on p. 38).
234. N. Rubiano da Silva, M. Möller, A. Feist, H. Ulrichs, C. Ropers, S. Schäfer, Nanoscale Mapping of Ultrafast Magnetization Dynamics with Femtosecond Lorentz Microscopy. *Physical Review X* **8**, 031052 (2018) (cit. on pp. 38, 161).
235. M. Merano, S. Collin, P. Renucci, M. Gatri, S. Sonderegger, A. Crottini, J. D. Ganière, B. Deveaud, High Brightness Picosecond Electron Gun. *Review of Scientific Instruments* **76**, 085108 (2005) (cit. on p. 39).
236. L. Wimmer, O. Karnbach, G. Herink, C. Ropers, Phase Space Manipulation of Free-Electron Pulses from Metal Nanotips Using Combined Terahertz near Fields and External Biasing. *Physical Review B* **95** (2017) (cit. on p. 39).
237. B. Piglosiewicz, S. Schmidt, D. J. Park, J. Vogelsang, P. GroSS, C. Manzoni, P. Farinello, G. Cerullo, C. Lienau, Carrier-Envelope Phase Effects on the Strong-Field Photoemission of Electrons from Metallic Nanostructures. *Nature Photonics* **8**, 37–42 (2014) (cit. on p. 39).
238. B. Barwick, D. J. Flannigan, A. H. Zewail, Photon-Induced near-Field Electron Microscopy. *Nature* **462**, 902–906 (2009) (cit. on pp. 40, 134).
239. P. W. Hawkes, E. Kasper, *Principles of Electron Optics* (Academic Press, 1996); ISBN: 978-0-12-333341-4 (cit. on pp. 41, 165).

240. N. Browning, M. Bonds, G. Campbell, J. Evans, T. LaGrange, K. Jungjohann, D. Masiel, J. McKeown, S. Mehraeen, B. Reed, M. Santala, Recent Developments in Dynamic Transmission Electron Microscopy. *Current Opinion in Solid State and Materials Science* **16**, 23–30 (2012) (cit. on p. 41).
241. L. Verlet, Computer "Experiments" on Classical Fluids. I. Thermodynamical Properties of Lennard-Jones Molecules. *Physical Review* **159**, 98–103 (1967) (cit. on p. 46).
242. J. S. Kim, T. LaGrange, B. W. Reed, M. L. Taheri, M. R. Armstrong, W. E. King, N. D. Browning, G. H. Campbell, Imaging of Transient Structures Using Nanosecond in Situ TEM. *Science* **321**, 1472–1475 (2008) (cit. on p. 47).
243. S. Volz, J. Ordonez-Miranda, A. Shchepetov, M. Prunnila, J. Ahopelto, T. Pezeril, G. Vaudel, V. Gusev, P. Ruello, E. M. Weig, M. Schubert, M. Hettich, M. Grossman, T. Dekorsy, F. Alzina, B. Graczykowski, E. Chavez-Angel, J. Sebastian Reparaz, M. R. Wagner, C. M. Sotomayor-Torres, S. Xiong, S. Neogi, D. Donadio, Nanophononics: State of the Art and Perspectives. *The European Physical Journal B* **89** (2016) (cit. on pp. 51, 108, 132).
244. D. G. Cahill, W. K. Ford, K. E. Goodson, G. D. Mahan, A. Majumdar, H. J. Maris, R. Merlin, S. R. Phillpot, Nanoscale Thermal Transport. *Journal of Applied Physics* **93**, 793–818 (2002) (cit. on pp. 51, 108).
245. P. E. Hopkins, C. M. Reinke, M. F. Su, R. H. Olsson, E. A. Shaner, Z. C. Leseman, J. R. Serrano, L. M. Phinney, I. El-Kady, Reduction in the Thermal Conductivity of Single Crystalline Silicon by Phononic Crystal Patterning. *Nano Letters* **11**, 107–112 (2011) (cit. on p. 51).
246. M. Nomura, J. Nakagawa, Y. Kage, J. Maire, D. Moser, O. Paul, Thermal Phonon Transport in Silicon Nanowires and Two-Dimensional Phononic Crystal Nanostructures. *Applied Physics Letters* **106**, 143102 (2015) (cit. on p. 51).
247. D. M. Moss, A. V. Akimov, B. A. Glavin, M. Henini, A. J. Kent, Ultrafast Strain-Induced Current in a GaAs Schottky Diode. *Physical Review Letters* **106**, 066602 (2011) (cit. on p. 51).
248. C. L. Poyser, A. V. Akimov, A. G. Balanov, R. P. Champion, A. J. Kent, A Weakly Coupled Semiconductor Superlattice as a Harmonic Hypersonic-Electrical Transducer. *New Journal of Physics* **17**, 083064 (2015) (cit. on p. 51).

- 
249. M. Eichenfield, J. Chan, R. M. Camacho, K. J. Vahala, O. Painter, Optomechanical Crystals. *Nature* **462**, 78–82 (2009) (cit. on p. 51).
250. E. Verhagen, S. Deléglise, S. Weis, A. Schliesser, T. J. Kippenberg, Quantum-Coherent Coupling of a Mechanical Oscillator to an Optical Cavity Mode. *Nature* **482**, 63–67 (2012) (cit. on p. 51).
251. R. Van Laer, B. Kuyken, D. Van Thourhout, R. Baets, Interaction between Light and Highly Confined Hypersound in a Silicon Photonic Nanowire. *Nature Photonics* **9**, 199–203 (2015) (cit. on p. 51).
252. E. Pop, Energy Dissipation and Transport in Nanoscale Devices. *Nano Research* **3**, 147–169 (2010) (cit. on pp. 51, 108).
253. T. J. Kippenberg, K. J. Vahala, Cavity Optomechanics: Back-Action at the Mesoscale. *Science* **321**, 1172–1176 (2008) (cit. on p. 51).
254. M. Aspelmeyer, T. J. Kippenberg, F. Marquardt, Cavity Optomechanics. *Reviews of Modern Physics* **86**, 1391–1452 (2014) (cit. on pp. 51, 108).
255. I. Favero, K. Karrai, Optomechanics of Deformable Optical Cavities. *Nature Photonics* **3**, 201–205 (2009) (cit. on p. 51).
256. J. L. Arlett, E. B. Myers, M. L. Roukes, Comparative Advantages of Mechanical Biosensors. *Nature Nanotechnology* **6**, 203–215 (2011) (cit. on p. 51).
257. B. Lassagne, Y. Tarakanov, J. Kinaret, D. Garcia-Sanchez, A. Bachtold, Coupling Mechanics to Charge Transport in Carbon Nanotube Mechanical Resonators. *Science* **325**, 1107–1110 (2009) (cit. on p. 51).
258. G. A. Steele, A. K. Hüttel, B. Witkamp, M. Poot, H. B. Meerwaldt, L. P. Kouwenhoven, H. S. J. van der Zant, Strong Coupling Between Single-Electron Tunneling and Nanomechanical Motion. *Science* **325**, 1103–1107 (2009) (cit. on p. 51).
259. D. Rugar, R. Budakian, H. J. Mamin, B. W. Chui, Single Spin Detection by Magnetic Resonance Force Microscopy. *Nature* **430**, 329–332 (2004) (cit. on p. 51).
260. J. Cuffe, E. Chávez, A. Shchepetov, P.-O. Chapuis, E. H. El Boudouti, F. Alzina, T. Kehoe, J. Gomis-Bresco, D. Dudek, Y. Pennec, B. Djafari-Rouhani, M. Prunnila, J. Ahopelto, C. M. Sotomayor Torres, Phonons in Slow Motion: Dispersion Relations in Ultrathin Si Membranes. *Nano Letters* **12**, 3569–3573 (2012) (cit. on pp. 51, 52, 108).

261. A. A. Balandin, Nanophononics: Phonon Engineering in Nanostructures and Nanodevices. *Journal of Nanoscience and Nanotechnology* **5**, 1015–1022 (2005) (cit. on p. 51).
262. A. A. Balandin, Phononics of Graphene and Related Materials. *ACS Nano* **14**, 5170–5178 (2020) (cit. on p. 51).
263. C. Jean, L. Belliard, T. W. Cornelius, O. Thomas, M. E. Toimil-Molares, M. Cassinelli, L. Becerra, B. Perrin, Direct Observation of Gigahertz Coherent Guided Acoustic Phonons in Free-Standing Single Copper Nanowires. *The Journal of Physical Chemistry Letters* **5**, 4100–4104 (2014) (cit. on p. 51).
264. Y. Cang, Y. Jin, B. Djafari-Rouhani, G. Fytas, Fundamentals, Progress and Perspectives on High-Frequency Phononic Crystals. *Journal of Physics D: Applied Physics* **55**, 193002 (2022) (cit. on p. 51).
265. M. Miniaci, R. K. Pal, Design of Topological Elastic Waveguides. *Journal of Applied Physics* **130**, 141101 (2021) (cit. on p. 51).
266. J. Gomis-Bresco, D. Navarro-Urrios, M. Oudich, S. El-Jallal, A. Griol, D. Puerto, E. Chavez, Y. Pennec, B. Djafari-Rouhani, F. Alzina, A. Martínez, C. M. S. Torres, A One-Dimensional Optomechanical Crystal with a Complete Phononic Band Gap. *Nature Communications* **5**, 4452 (2014) (cit. on p. 51).
267. L. M. Nash, D. Kleckner, A. Read, V. Vitelli, A. M. Turner, W. T. M. Irvine, Topological Mechanics of Gyroscopic Metamaterials. *Proceedings of the National Academy of Sciences* **112**, 14495–14500 (2015) (cit. on p. 51).
268. P. Wang, L. Lu, K. Bertoldi, Topological Phononic Crystals with One-Way Elastic Edge Waves. *Physical Review Letters* **115**, 104302 (2015) (cit. on p. 51).
269. M. Z. Hasan, C. L. Kane, Colloquium: Topological Insulators. *Reviews of Modern Physics* **82**, 3045–3067 (2010) (cit. on p. 51).
270. G. Ma, M. Xiao, C. T. Chan, Topological Phases in Acoustic and Mechanical Systems. *Nature Reviews Physics* **1**, 281–294 (2019) (cit. on p. 51).
271. K. v. Klitzing, G. Dorda, M. Pepper, New Method for High-Accuracy Determination of the Fine-Structure Constant Based on Quantized Hall Resistance. *Physical Review Letters* **45**, 494–497 (1980) (cit. on p. 51).

- 
272. A. Bruchhausen, R. Gebs, F. Hudert, D. Issenmann, G. Klatt, A. Bartels, O. Schecker, R. Waitz, A. Erbe, E. Scheer, J.-R. Huntzinger, A. Mlayah, T. Dekorsy, Subharmonic Resonant Optical Excitation of Confined Acoustic Modes in a Free-Standing Semiconductor Membrane at GHz Frequencies with a High-Repetition-Rate Femtosecond Laser. *Physical Review Letters* **106**, 077401 (2011) (cit. on p. 52).
273. A. V. Osetrov, H.-J. Fröhlich, R. Koch, E. Chilla, Acoustoelastic Effect in Anisotropic Layered Structures. *Physical Review B* **62**, 13963–13969 (2000) (cit. on p. 52).
274. B. Graczykowski, J. Gomis-Bresco, F. Alzina, J. S. Reparaz, A. Shchepetov, M. Prunnila, J. Ahopelto, C. M. S. Torres, Acoustic Phonon Propagation in Ultra-Thin Si Membranes under Biaxial Stress Field. *New Journal of Physics* **16**, 073024 (2014) (cit. on pp. 52, 154).
275. S. Bramhavar, C. Prada, A. A. Maznev, A. G. Every, T. B. Norris, T. W. Murray, Negative Refraction and Focusing of Elastic Lamb Waves at an Interface. *Physical Review B* **83**, 014106 (2011) (cit. on pp. 52, 168).
276. M. Grossmann, O. Ristow, M. Hettich, C. He, R. Waitz, E. Scheer, V. Gusev, T. Dekorsy, M. Schubert, Time-Resolved Detection of Propagating Lamb Waves in Thin Silicon Membranes with Frequencies up to 197 GHz. *Applied Physics Letters* **106**, 171904 (2015) (cit. on pp. 52, 108, 141).
277. N. Bach, S. Schäfer, Ultrafast Strain Propagation and Acoustic Resonances in Nanoscale Bilayer Systems. *Structural Dynamics* **8**, 035101 (2021) (cit. on pp. 52, 129, 141, 227).
278. B. Graczykowski, M. Sledzinska, M. Placidi, D. Saleta Reig, M. Kasprzak, F. Alzina, C. M. Sotomayor Torres, Elastic Properties of Few Nanometers Thick Polycrystalline MoS<sub>2</sub> Membranes: A Nondestructive Study. *Nano Letters* **17**, 7647–7651 (2017) (cit. on p. 52).
279. K. F. Graff, *Wave Motion in Elastic Solids* (Dover Publications, New York, 1991); ISBN: 978-0-486-66745-4 (cit. on pp. 52, 54, 56, 57, 118, 119).
280. I. S. Sokolnikoff, *Mathematical Theory of Elasticity* (McGraw-Hill Inc., US, 2nd edition, 1956); ISBN: 978-0-07-059629-0 (cit. on pp. 52, 56).

281. B. A. Auld, *Acoustic Fields and Waves in Solids* (Wiley, New York, 1973); ISBN: 978-0-471-03702-6 (cit. on pp. 52, 57, 62, 64).
282. J. D. Achenbach, *Wave Propagation in Elastic Solids* (North Holland Pub. Co. ; American Elsevier Pub. Co., Amsterdam; New York, 1984) (cit. on pp. 52, 58, 153).
283. T. C. T. Ting, *Anisotropic Elasticity: Theory and Applications* (Oxford University Press, New York, 1996); ISBN: 978-0-19-507447-5 (cit. on pp. 52, 55, 56, 70).
284. D. Royer, E. Dieulesaint, *Elastic Waves in Solids* (Springer, Berlin ; New York, 2000); ISBN: 978-3-540-65932-7 (cit. on pp. 52–55, 57, 58, 62–65, 69, 110, 118, 135, 153, 154).
285. J. L. Rose, *Ultrasonic Guided Waves in Solid Media* (Cambridge University Press, Cambridge, 2014); ISBN: 978-1-107-04895-9 (cit. on pp. 52, 60, 65, 119, 153).
286. A. Einstein, Die Grundlage Der Allgemeinen Relativitätstheorie. *Annalen der Physik* **354**, 769–822 (1916) (cit. on p. 53).
287. M. Moakher, “The Algebra of Fourth-Order Tensors with Application to Diffusion MRI” in *Visualization and Processing of Tensor Fields*, G. Farin, H.-C. Hege, D. Hoffman, C. R. Johnson, K. Polthier, M. Rumpf, D. Laidlaw, J. Weickert, Eds. (Springer Berlin Heidelberg, Berlin, Heidelberg, 2009), pp. 57–80; ISBN: 978-3-540-88377-7 (cit. on p. 55).
288. W. Voigt, *Lehrbuch der kristallphysik (mit ausschluss der kristalloptik)* (B.G. Teubner, Leipzig; Berlin, 1910) (cit. on p. 56).
289. P. Curie, Sur La Symétrie Dans Les Phénomènes Physiques, Symétrie d’un Champ Électrique et d’un Champ Magnétique. *Journal de Physique Théorique et Appliquée* **3**, 393–415 (1894) (cit. on p. 56).
290. J. Wilson, A. Yoffe, The Transition Metal Dichalcogenides Discussion and Interpretation of the Observed Optical, Electrical and Structural Properties. *Advances in Physics* **18**, 193–335 (1969) (cit. on p. 56).
291. R. Gross, A. Marx, *Festkörperphysik* (Walter de Gruyter GmbH & Co KG, 2018); ISBN: 978-3-11-055928-6 (cit. on pp. 59, 99).
292. M. Fox, *Optische Eigenschaften von Festkörpern*; ISBN: 978-3-11-066913-8 (cit. on p. 61).
293. S. Hunklinger, *Festkörperphysik* (De Gruyter, Berlin ; Boston, 5. Auflage, 2018); ISBN: 978-3-11-056774-8 (cit. on p. 61).

- 
294. D. F. Winterstein, Velocity Anisotropy Terminology for Geophysicists. *GEO-PHYSICS* **55**, 1070–1088 (1990) (cit. on p. 61).
295. F. I. Fedorov, *Theory of Elastic Waves in Crystals* (Springer, Berlin, 1968); ISBN: 978-1-4757-1275-9 (cit. on p. 63).
296. E. B. Christoffel, Untersuchungen über die mit dem Fortbestehen linearer partieller Differentialgleichungen verträglichen Unstetigkeiten. *Annali di Matematica Pura ed Applicata* **8**, 81–112 (1877) (cit. on p. 62).
297. E. B. Christoffel, Ueber die Fortpflanzung von Stößen durch elastische feste Körper. *Annali di Matematica Pura ed Applicata* **8**, 193–243 (1877) (cit. on p. 62).
298. Center for Lightweight-Production-Technology - The Dispersion Calculator: A Free Software for Calculating Dispersion Curves of Guided Waves in Multilayered Composites, [https://www.dlr.de/zlp/en/desktopdefault.aspx/tabid-14332/24874\\_read-61142/](https://www.dlr.de/zlp/en/desktopdefault.aspx/tabid-14332/24874_read-61142/) (cit. on pp. 63, 67, 153).
299. A. E. H. Love, *Some Problems of Geodynamics: Being an Essay to Which the Adams Prize in the University of Cambridge Was Adjudged in 1911*. (Univ. Press, Cambridge, 1911) (cit. on p. 63).
300. C. L. Kane, E. J. Mele, Z<sub>2</sub> Topological Order and the Quantum Spin Hall Effect. *Physical Review Letters* **95**, 146802 (2005) (cit. on p. 64).
301. C. L. Kane, E. J. Mele, Quantum Spin Hall Effect in Graphene. *Physical Review Letters* **95**, 226801 (2005) (cit. on p. 64).
302. M. Miniaci, R. K. Pal, B. Morvan, M. Ruzzene, Experimental Observation of Topologically Protected Helical Edge Modes in Patterned Elastic Plates. *Physical Review X* **8**, 031074 (2018) (cit. on p. 64).
303. S. H. Mousavi, A. B. Khanikaev, Z. Wang, Topologically Protected Elastic Waves in Phononic Metamaterials. *Nature Communications* **6**, 8682 (2015) (cit. on p. 64).
304. P. M. Morse, H. Feshbach, *Methods of Theoretical Physics* (McGraw-Hill, Boston, Mass, 1953); ISBN: 978-0-07-043316-8 (cit. on p. 64).
305. M. Lowe, Matrix Techniques for Modeling Ultrasonic Waves in Multilayered Media. *IEEE Transactions on Ultrasonics, Ferroelectrics, and Frequency Control* **42**, 525–542 (1995) (cit. on pp. 65, 119).

306. A. Huber, “Numerical Modeling of Guided Waves in Anisotropic Composites with Application to Air-coupled Ultrasonic Inspection,” PhD thesis, Universität Augsburg, 2021 (cit. on pp. 65, 154).
307. A. G. Every, Intersections of the Lamb Mode Dispersion Curves of Free Isotropic Plates. *The Journal of the Acoustical Society of America* **139**, 1793–1798 (2016) (cit. on p. 66).
308. J. Neumann, E. Wigner, Über Merkwürdige Diskrete Eigenwerte. *Physikalische Zeitschrift* (1929) (cit. on p. 66).
309. W. T. Thomson, Transmission of Elastic Waves through a Stratified Solid Medium. *Journal of Applied Physics* **21**, 89–93 (1950) (cit. on p. 66).
310. N. A. Haskell, The Dispersion of Surface Waves on Multilayered Media. *Bulletin of the Seismological Society of America* **43**, 17–34 (1953) (cit. on p. 66).
311. L. Knopoff, A Matrix Method for Elastic Wave Problems. *Bulletin of the Seismological Society of America* **54**, 431–438 (1964) (cit. on pp. 66, 119).
312. S. I. Rokhlin, L. Wang, Stable Recursive Algorithm for Elastic Wave Propagation in Layered Anisotropic Media: Stiffness Matrix Method. *The Journal of the Acoustical Society of America* **112**, 822–834 (2002) (cit. on p. 66).
313. L. Wang, S. I. Rokhlin, Stable Reformulation of Transfer Matrix Method for Wave Propagation in Layered Anisotropic Media. *Ultrasonics* **39**, 413–424 (2001) (cit. on p. 66).
314. S. V. Kuznetsov, Lamb Waves in Anisotropic Plates (Review). *Acoustical Physics* **60**, 95–103 (2014) (cit. on pp. 66, 69, 70).
315. S. V. Kuznetsov, Low Frequency Limits for Lamb Waves in Homogeneous, Stratified and Functionally Graded Anisotropic Plates. *Mechanics of Advanced Materials and Structures*, 1–7 (2021) (cit. on pp. 66, 68–71, 154).
316. S. V. Kuznetsov, Abnormal Dispersion of Lamb Waves in Stratified Media. *Zeitschrift für angewandte Mathematik und Physik* **70**, 175 (2019) (cit. on pp. 66, 71).
317. S. V. Kuznetsov, Cauchy Six-Dimensional Formalism for Lamb Waves in Multilayered Plates. *ISRN Mechanical Engineering* **2013**, 1–11 (2013) (cit. on pp. 66, 69).

- 
318. A.-L. Cauchy, Mémoire Sur Un Théorème Fondamental, Dans Le Calcul Intégral. *Comptes Rendus de l'Académie des sciences* **14**, 1020–1026 (1842) (cit. on p. 69).
319. J. Hadamard, *Lectures on Cauchy's Problem in Linear Partial Differential Equations* (Dover Publications, Mineola, N.Y, 2003); ISBN: 978-0-486-49549-1 (cit. on p. 69).
320. J. Eshelby, W. Read, W. Shockley, Anisotropic Elasticity with Applications to Dislocation Theory. *Acta Metallurgica* **1**, 251–259 (1953) (cit. on p. 70).
321. A. N. Stroh, Steady State Problems in Anisotropic Elasticity. *Journal of Mathematics and Physics* **41**, 77–103 (1962) (cit. on p. 70).
322. A. L. Shuvalov, On the Theory of Wave Propagation in Anisotropic Plates. *Proceedings of the Royal Society of London. Series A: Mathematical, Physical and Engineering Sciences* **456**, 2197–2222 (2000) (cit. on p. 70).
323. V. Alshits, M. Deschamps, G. Maugin, Elastic Waves in Anisotropic Plates: Short-Wavelength Asymptotics of the Dispersion Branches  $v_n(k)$ . *Wave Motion* **37**, 273–292 (2003) (cit. on p. 70).
324. S. V. Kuznetsov, Abnormal Dispersion of Flexural Lamb Waves in Functionally Graded Plates. *Zeitschrift für angewandte Mathematik und Physik* **70**, 89 (2019) (cit. on p. 71).
325. J. F. Lotspeich, Explicit General Eigenvalue Solutions for Dielectric Slab Waveguides. *Applied Optics* **14**, 327 (1975) (cit. on pp. 71, 73).
326. C.-L. Chen, *Foundations for Guided-Wave Optics* (Wiley-Interscience, Hoboken, N.J, 2007); ISBN: 978-0-471-75687-3 (cit. on pp. 72–74).
327. K. Okamoto, *Fundamentals of Optical Waveguides* (Elsevier, Amsterdam ; Boston, 2nd ed, 2006); ISBN: 978-0-12-525096-2 (cit. on pp. 72, 73).
328. H. Kogelnik, V. Ramaswamy, Scaling Rules for Thin-Film Optical Waveguides. *Applied Optics* **13**, 1857–1862 (1974) (cit. on p. 74).
329. J. M. Zuo, J. C. H. Spence, *Advanced Transmission Electron Microscopy: Imaging and Diffraction in Nanoscience* (Springer-Verlag, New York, 2017); ISBN: 978-1-4939-6605-9 (cit. on pp. 78, 79, 82, 84, 88, 89, 92–94, 98–100, 102, 133, 135, 139, 148, 150, 166).
330. J. M. Zuo, J. C. H. Spence, *Electron Microdiffraction* (Springer Science & Business Media, 2013); ISBN: 978-1-4899-2353-0 (cit. on pp. 80, 133).

331. W. J. Vine, R. Vincent, P. Spellward, J. W. Steeds, Observation of Phase Contrast in Convergent-Beam Electron Diffraction Patterns. *Ultramicroscopy* **41**, 423–428 (1992) (cit. on p. 80).
332. K. Tsuda, M. Tanaka, Interferometry by Coherent Convergent-Beam Electron Diffraction. *Journal of Electron Microscopy* **45**, 59–63 (1996) (cit. on p. 80).
333. K. Ishida, Inelastic Scattering of Fast Electrons by Crystals. II. The Excess and Defect Kikuchi Bands. *Journal of the Physical Society of Japan* **30**, 1439–1448 (1971) (cit. on p. 81).
334. B. A. Lippmann, J. Schwinger, Variational Principles for Scattering Processes. I. *Physical Review* **79**, 469–480 (1950) (cit. on p. 82).
335. A. Ichimiya, P. I. Cohen, *Reflection High-Energy Electron Diffraction* (Cambridge University Press, Cambridge, 2004); ISBN: 978-0-521-45373-8 (cit. on p. 82).
336. N. F. Mott, N. H. D. Bohr, The Scattering of Fast Electrons by Atomic Nuclei. *Proceedings of the Royal Society of London. Series A, Containing Papers of a Mathematical and Physical Character* **124**, 425–442 (1929) (cit. on p. 83).
337. H. Bethe, Zur Theorie Des Durchgangs Schneller Korpuskularstrahlen Durch Materie. *Annalen der Physik* **397**, 325–400 (1930) (cit. on p. 83).
338. H. Bethe, Bremsformel für Elektronen relativistischer Geschwindigkeit. *Zeitschrift für Physik* **76**, 293–299 (1932) (cit. on p. 83).
339. J. G. Horstmann, “Ultrafast Probing and Coherent Vibrational Control of a Surface Structural Phase Transition,” PhD thesis, Georg-August-Universität Göttingen, 2021 (cit. on p. 83).
340. P. A. Doyle, P. S. Turner, Relativistic HartreeFock X-ray and Electron Scattering Factors. *Acta Crystallographica Section A* **24**, 390–397 (1968) (cit. on p. 83).
341. L.-M. Peng, G. Ren, S. L. Dudarev, M. J. Whelan, Robust Parameterization of Elastic and Absorptive Electron Atomic Scattering Factors. *Acta Crystallographica Section A: Foundations of Crystallography* **52**, 257–276 (1996) (cit. on pp. 84, 94, 99).

- 
342. A. J. C. Wilson, V. Geist, International Tables for Crystallography. Volume C: Mathematical, Physical and Chemical Tables. Kluwer Academic Publishers, Dordrecht/Boston/London 1992 (Published for the International Union of Crystallography), 883 Seiten, ISBN 0-792-3-16-38X. *Crystal Research and Technology* **28**, 110–110 (1993) (cit. on p. 84).
343. B. Fultz, J. M. Howe, *Transmission Electron Microscopy and Diffractometry of Materials* (Springer, Berlin New York, 3rd ed, 2008); ISBN: 978-3-540-73886-2 (cit. on pp. 84–86, 89, 93, 96).
344. N. W. Ashcroft, N. D. Mermin, *Festkörperphysik* (Oldenbourg, München, 2013); ISBN: 978-3-486-85476-3 (cit. on pp. 84, 85, 99).
345. J. M. Cowley, *Diffraction Physics* (North Holland, Amsterdam; New York, 3rd edition, 1995); ISBN: 978-0-444-82218-5 (cit. on pp. 85, 86, 89, 92, 133, 147).
346. M. A. Van Hove, W. H. Weinberg, C.-M. Chan, *Low-Energy Electron Diffraction: Experiment, Theory and Surface Structure Determination*, ed. by G. Ertl, R. Gomer (Springer Berlin Heidelberg, Berlin, Heidelberg, 1986); ISBN: 978-3-642-82723-5 (cit. on p. 89).
347. F. Houdellier, C. Roucau, L. Clément, J. L. Rouvière, M. J. Casanove, Quantitative Analysis of HOLZ Line Splitting in CBED Patterns of Epitaxially Strained Layers. *Ultramicroscopy* **106**, 951–959 (2006) (cit. on p. 89).
348. F. Houdellier, “Contribution Au Développement Du CBED et de l’holographie HREM Pour l’analyse Des Déformations de Couches Épitaxiées,” Thèse de Doctorat, Toulouse, INSA, 2006 (cit. on p. 89).
349. R. Henderson, The Potential and Limitations of Neutrons, Electrons and X-rays for Atomic Resolution Microscopy of Unstained Biological Molecules. *Quarterly Reviews of Biophysics* **28**, 171–193 (1995) (cit. on p. 89).
350. H. Bethe, Theorie Der Beugung von Elektronen an Kristallen. *Annalen der Physik* **392**, 55–129 (1928) (cit. on pp. 89, 91).
351. F. Bloch, Über die Quantenmechanik der Elektronen in Kristallgittern. *Zeitschrift für Physik* **52**, 555–600 (1929) (cit. on p. 89).
352. H. Alexander, *Physikalische Grundlagen der Elektronenmikroskopie* (Teubner, Stuttgart, 1997); ISBN: 978-3-519-03221-2 (cit. on pp. 90, 93, 94).

353. A. J. F. Metherell, R. M. Fisher, Consequences of Bloch's Theorem on the Dynamical Theory of Electron Diffraction Contrast. *physica status solidi (b)* **32**, 551–562 (1969) (cit. on p. 91).
354. C. J. Humphreys, The Scattering of Fast Electrons by Crystals. *Reports on Progress in Physics* **42**, 1825–1887 (1979) (cit. on pp. 91, 92).
355. E. J. Kirkland, *Advanced Computing in Electron Microscopy*. (Springer, 2014); ISBN: 978-1-4899-9509-4 (cit. on p. 92).
356. I. González Vallejo, G. Gallé, B. Arnaud, S. A. Scott, M. G. Lagally, D. Boschetto, P.-E. Coulon, G. Rizza, F. Houdellier, D. Le Bolloc'h, J. Faure, Observation of Large Multiple Scattering Effects in Ultrafast Electron Diffraction on Monocrystalline Silicon. *Physical Review B* **97**, 054302 (2018) (cit. on pp. 94, 109).
357. G. Thomas, E. Levine, Increase in Extinction Distance with Temperature in Silicon. *physica status solidi (b)* **11**, 81–90 (1965) (cit. on p. 94).
358. M. S. Tame, K. R. McEnery, . K. Özdemir, J. Lee, S. A. Maier, M. S. Kim, Quantum Plasmonics. *Nature Physics* **9**, 329–340 (2013) (cit. on p. 95).
359. S. Gambino, M. Mazzeo, A. Genco, O. Di Stefano, S. Savasta, S. Patanè, D. Ballarini, F. Mangione, G. Lerario, D. Sanvitto, G. Gigli, Exploring LightMatter Interaction Phenomena under Ultrastrong Coupling Regime. *ACS Photonics* **1**, 1042–1048 (2014) (cit. on p. 95).
360. P. Vasa, C. Lienau, Strong LightMatter Interaction in Quantum Emitter/Metal Hybrid Nanostructures. *ACS Photonics* **5**, 2–23 (2018) (cit. on p. 95).
361. Z. Liang, L. Qing, Z. Li, X. T. Nguyen, T. Xu, A. De Sio, H. Zhang, C. Lienau, W. Wang, Plasmon-Plasmon Interactions Supported by a One-Dimensional Plasmonic Crystal: Rabi Phase and Generalized Rabi Frequency. *Physical Review B* **102**, 035422 (2020) (cit. on p. 95).
362. W. Kossel, G. Möllenstedt, Elektroneninterferenzen Im Konvergenten Bündel. *Annalen der Physik* **428**, 113–140 (1939) (cit. on p. 96).
363. I. Ackermann, Beobachtungen an dynamischen Interferenzerscheinungen im konvergenten Elektronenbündel I. *Annalen der Physik* **437**, 19–40 (1948) (cit. on p. 96).

- 
364. D. Delille, R. Pantel, E. Van Cappellen, Crystal Thickness and Extinction Distance Determination Using Energy Filtered CBED Pattern Intensity Measurement and Dynamical Diffraction Theory Fitting. *Ultramicroscopy* **87**, 5–18 (2001) (cit. on p. 96).
365. D. van Dyck, The Importance of Backscattering in High-Energy Electron Diffraction Calculations. *physica status solidi (b)* **77**, 301–308 (1976) (cit. on p. 97).
366. A. Howie, M. J. Whelan, N. F. Mott, Diffraction Contrast of Electron Microscope Images of Crystal Lattice Defects - II. The Development of a Dynamical Theory. *Proceedings of the Royal Society of London. Series A. Mathematical and Physical Sciences* **263**, 217–237 (1961) (cit. on p. 97).
367. P. Debye, Interferenz von Röntgenstrahlen Und Wärmebewegung. *Annalen der Physik* **348**, 49–92 (1913) (cit. on p. 98).
368. I. Waller, Zur Frage Der Einwirkung Der Wärmebewegung Auf Die Interferenz von Röntgenstrahlen. *Zeitschrift für Physik* **17**, 398–408 (1923) (cit. on p. 98).
369. J. Laval, Crystallography. On the Diffusion of X Rays by a Crystal. *C R Hebd Seances Acad Sci* **207**, 169–170 (1938) (cit. on p. 98).
370. J. Laval, Diffusing X-Rays with Crystals Outside the Bearing of Selective Reflection. *C R Hebd Seances Acad Sci* **208**, 1512–1514 (1939) (cit. on p. 98).
371. R. F. Loane, P. Xu, J. Silcox, Thermal Vibrations in Convergent-Beam Electron Diffraction. *Acta Crystallographica Section A: Foundations of Crystallography* **47**, 267–278 (1991) (cit. on p. 98).
372. B. E. Warren, *X-Ray Diffraction* (Dover Publications Inc., New York, New ed Edition, 1990); ISBN: 978-0-486-66317-3 (cit. on pp. 98, 100, 101).
373. J. M. Ziman, *Principles of the Theory of Solids* (Cambridge University Press, 1979); ISBN: 978-1-139-64280-4 (cit. on pp. 99, 100).
374. B. W. Batterman, D. R. Chipman, Vibrational Amplitudes in Germanium and Silicon. *Physical Review* **127**, 690–693 (1962) (cit. on p. 100).
375. R. Chen, P. Trucano, Comparisons of Atomic Thermal Motions for Graphite at 300 K Based on X-ray, Neutron, and Phonon-Spectrum Data. *Acta Crystallographica Section A: Crystal Physics, Diffraction, Theoretical and General Crystallography* **34**, 979–982 (1978) (cit. on p. 100).

376. R. Xu, T. C. Chiang, Determination of Phonon Dispersion Relations by X-ray Thermal Diffuse Scattering. *Zeitschrift für Kristallographie - Crystalline Materials* **220**, 1009–1016 (2005) (cit. on p. 101).
377. M. Trigo, J. Chen, V. H. Vishwanath, Y. M. Sheu, T. Graber, R. Henning, D. A. Reis, Imaging Nonequilibrium Atomic Vibrations with X-Ray Diffuse Scattering. *Physical Review B* **82**, 235205 (2010) (cit. on p. 101).
378. T. Chase, M. Trigo, A. H. Reid, R. Li, T. Vecchione, X. Shen, S. Weathersby, R. Coffee, N. Hartmann, D. A. Reis, X. J. Wang, H. A. Dürr, Ultrafast Electron Diffraction from Non-Equilibrium Phonons in Femtosecond Laser Heated Au Films. *Applied Physics Letters* **108**, 041909 (2016) (cit. on p. 101).
379. M. J. Stern, L. P. René de Cotret, M. R. Otto, R. P. Chatelain, J.-P. Boisvert, M. Sutton, B. J. Siwick, Mapping Momentum-Dependent Electron-Phonon Coupling and Nonequilibrium Phonon Dynamics with Ultrafast Electron Diffuse Scattering. *Physical Review B* **97**, 165416 (2018) (cit. on p. 101).
380. P. Maldonado, T. Chase, A. H. Reid, X. Shen, R. K. Li, K. Carva, T. Payer, M. Horn von Hoegen, K. Sokolowski-Tinten, X. J. Wang, P. M. Oppeneer, H. A. Dürr, Tracking the Ultrafast Nonequilibrium Energy Flow between Electronic and Lattice Degrees of Freedom in Crystalline Nickel. *Physical Review B* **101**, 100302 (2020) (cit. on p. 101).
381. M. S. Grinolds, V. A. Lobastov, J. Weissenrieder, A. H. Zewail, Four-Dimensional Ultrafast Electron Microscopy of Phase Transitions. *Proceedings of the National Academy of Sciences* **103**, 18427–18431 (2006) (cit. on pp. 101, 103).
382. R. M. van der Veen, O.-H. Kwon, A. Tissot, A. Hauser, A. H. Zewail, Single-Nanoparticle Phase Transitions Visualized by Four-Dimensional Electron Microscopy. *Nature Chemistry* **5**, 395–402 (2013) (cit. on pp. 101, 103, 132).
383. Y. Zhang, D. J. Flannigan, Observation of Anisotropic Strain-Wave Dynamics and Few-Layer Dephasing in MoS<sub>2</sub> with Ultrafast Electron Microscopy. *Nano Letters* **19**, 8216–8224 (2019) (cit. on pp. 101, 102, 108).
384. A. Nakamura, T. Shimojima, K. Ishizaka, Visualizing Optically-Induced Strains by Five-Dimensional Ultrafast Electron Microscopy. *Faraday Discussions* (2022); doi:10.1039/d2fd00062h (cit. on pp. 101, 128, 129).

- 
385. D. J. Flannigan, P. C. Samartzis, A. Yurtsever, A. H. Zewail, Nanomechanical Motions of Cantilevers: Direct Imaging in Real Space and Time with 4D Electron Microscopy. *Nano Letters* **9**, 875–881 (2009) (cit. on p. 101).
386. A. J. McKenna, J. K. Eliason, D. J. Flannigan, Spatiotemporal Evolution of Coherent Elastic Strain Waves in a Single MoS<sub>2</sub> Flake. *Nano Letters* **17**, 3952–3958 (2017); doi:10.1021/acs.nanolett.7b01565 (cit. on pp. 102, 108, 132).
387. D. R. Cremons, D. A. Plemmons, D. J. Flannigan, Defect-Mediated Phonon Dynamics in TaS<sub>2</sub> and WSe<sub>2</sub>. *Structural Dynamics* **4**, 044019 (2017) (cit. on p. 102).
388. S. A. Reisbick, Y. Zhang, D. J. Flannigan, Influence of Discrete Defects on Observed Acoustic Phonon Dynamics in Layered Materials Probed with Ultrafast Electron Microscopy. *The Journal of Physical Chemistry A* **124**, 1877–1884 (2020) (cit. on p. 102).
389. D. R. Cremons, D. X. Du, D. J. Flannigan, Picosecond Phase-Velocity Dispersion of Hypersonic Phonons Imaged with Ultrafast Electron Microscopy. *Physical Review Materials* **1**, 073801 (2017) (cit. on pp. 102, 132).
390. Y.-J. Kim, Y. Lee, K. Kim, O.-H. Kwon, Light-Induced Anisotropic Morphological Dynamics of Black Phosphorus Membranes Visualized by Dark-Field Ultrafast Electron Microscopy. *ACS Nano* **14**, 11383–11393 (2020) (cit. on pp. 102, 132).
391. C. Laulhé, T. Huber, G. Lantz, A. Ferrer, S. O. Mariager, S. Grübel, J. Rittmann, J. A. Johnson, V. Esposito, A. Lübecke, L. Huber, M. Kubli, M. Savoini, V. L. R. Jacques, L. Cario, B. Corraze, E. Janod, G. Ingold, P. Beaud, S. L. Johnson, S. Ravy, Ultrafast Formation of a Charge Density Wave State in 1T-TaS<sub>2</sub>: Observation at Nanometer Scales Using Time-Resolved X-Ray Diffraction. *Physical Review Letters* **118**, 247401 (2017) (cit. on pp. 104, 132).
392. P. Ruello, V. E. Gusev, Physical Mechanisms of Coherent Acoustic Phonons Generation by Ultrafast Laser Action. *Ultrasonics* **56**, 21–35 (2015) (cit. on pp. 105, 110).
393. A. M. Lindenberg, I. Kang, S. L. Johnson, T. Missalla, P. A. Heimann, Z. Chang, J. Larsson, P. H. Bucksbaum, H. C. Kapteyn, H. A. Padmore, R. W. Lee, J. S. Wark, R. W. Falcone, Time-Resolved X-Ray Diffraction from Coherent Phonons during a Laser-Induced Phase Transition. *Physical Review Letters* **84**, 111–114 (2000) (cit. on pp. 105, 127).

394. T. Saito, O. Matsuda, O. B. Wright, Picosecond Acoustic Phonon Pulse Generation in Nickel and Chromium. *Physical Review B* **67**, 205421 (2003) (cit. on p. 105).
395. S. Nie, X. Wang, H. Park, R. Clinite, J. Cao, Measurement of the Electronic Grüneisen Constant Using Femtosecond Electron Diffraction. *Physical Review Letters* **96**, 025901 (2006) (cit. on pp. 105, 109).
396. W. Liang, G. M. Vanacore, A. H. Zewail, Observing (Non)Linear Lattice Dynamics in Graphite by Ultrafast Kikuchi Diffraction. *Proceedings of the National Academy of Sciences* **111**, 5491–5496 (2014) (cit. on pp. 105, 109).
397. C. A. Polanco, C. B. Saltonstall, P. M. Norris, P. E. Hopkins, A. W. Ghosh, Impedance Matching of Atomic Thermal Interfaces Using Primitive Block Decomposition. *Nanoscale and Microscale Thermophysical Engineering* **17**, 263–279 (2013) (cit. on p. 108).
398. M. Jansen, N. Yazdani, V. Wood, Phonon-Engineered Solids Constructed from Nanocrystals. *APL Materials* **7**, 081124 (2019) (cit. on p. 108).
399. D. H. Hurley, R. Lewis, O. B. Wright, O. Matsuda, Coherent Control of Gigahertz Surface Acoustic and Bulk Phonons Using Ultrafast Optical Pulses. *Applied Physics Letters* **93**, 113101 (2008) (cit. on p. 108).
400. M. E. Siemens, Q. Li, M. M. Murnane, H. C. Kapteyn, R. Yang, E. H. Anderson, K. A. Nelson, High-Frequency Surface Acoustic Wave Propagation in Nanostructures Characterized by Coherent Extreme Ultraviolet Beams. *Applied Physics Letters* **94**, 093103 (2009) (cit. on p. 108).
401. C. S. Kim, J. H. Kim, H. Jeong, Y. D. Jho, H. K. Kwon, H. S. Lee, J. S. Park, K. Song, S. H. Kim, Y. J. Kim, D. Lee, K. J. Yee, Control of Coherent Acoustic Phonon Generation with External Bias in InGaN/GaN Multiple Quantum Wells. *Applied Physics Letters* **100**, 101105 (2012) (cit. on pp. 108, 110).
402. M. Woerner, C. v. Korff Schmising, M. Bargheer, N. Zhavoronkov, I. Vrejoiu, D. Hesse, M. Alexe, T. Elsaesser, Ultrafast Structural Dynamics of Perovskite Superlattices. *Applied Physics A* **96**, 83 (2009) (cit. on p. 108).
403. N. Rothenbach, M. E. Gruner, K. Ollefs, C. Schmitz-Antoniak, S. Salamon, P. Zhou, R. Li, M. Mo, S. Park, X. Shen, S. Weathersby, J. Yang, X. J. Wang, R. Pentcheva, H. Wende, U. Bovensiepen, K. Sokolowski-Tinten, A. Eschenlohr, Microscopic

- Nonequilibrium Energy Transfer Dynamics in a Photoexcited Metal/Insulator Heterostructure. *Physical Review B* **100**, 174301 (2019) (cit. on p. 108).
404. A. Fiorino, D. Thompson, L. Zhu, R. Mittapally, S.-A. Biehs, O. Bezencenet, N. El-Bondry, S. Bansropun, P. Ben-Abdallah, E. Meyhofer, P. Reddy, A Thermal Diode Based on Nanoscale Thermal Radiation. *ACS nano* **12**, 5774–5779 (2018) (cit. on p. 108).
405. S.-A. Biehs, R. Messina, P. S. Venkataram, A. W. Rodriguez, J. C. Cuevas, P. Ben-Abdallah, Near-Field Radiative Heat Transfer in Many-Body Systems. *Reviews of Modern Physics* **93**, 025009 (2021) (cit. on p. 108).
406. B. Bonello, C. Charles, F. Ganot, Lamb Waves in Plates Covered by a Two-Dimensional Phononic Film. *Applied Physics Letters* **90**, 021909 (2007) (cit. on p. 108).
407. N. Chigarev, V. Tournat, V. Gusev, All-Optical Monitoring of Acoustic Waves Guided by Confined Micro-Fluidic Layers. *Applied Physics Letters* **100**, 144102 (2012) (cit. on p. 108).
408. L. Brillouin, Diffusion de la lumière et des rayons X par un corps transparent homogène - Influence de l'agitation thermique. *Annales de Physique* **9**, 88–122 (1922) (cit. on p. 108).
409. E. Pontecorvo, M. Ortolani, D. Polli, M. Ferretti, G. Ruocco, G. Cerullo, T. Scopigno, Visualizing Coherent Phonon Propagation in the 100 GHz Range: A Broadband Picosecond Acoustics Approach. *Applied Physics Letters* **98**, 011901 (2011) (cit. on p. 108).
410. A. De Sio, F. Troiani, M. Maiuri, J. Réhault, E. Sommer, J. Lim, S. F. Huelga, M. B. Plenio, C. A. Rozzi, G. Cerullo, E. Molinari, C. Lienau, Tracking the Coherent Generation of Polaron Pairs in Conjugated Polymers. *Nature Communications* **7**, 13742 (2016) (cit. on p. 108).
411. B. Huber, S. Pres, E. Wittmann, L. Dietrich, J. Lüttig, D. Fersch, E. Krauss, D. Friedrich, J. Kern, V. Lisinetskii, M. Hensen, B. Hecht, R. Bratschitsch, E. Riedle, T. Brixner, Space- and Time-Resolved UV-to-NIR Surface Spectroscopy and 2D Nanoscopy at 1 MHz Repetition Rate. *Review of Scientific Instruments* **90**, 113103 (2019) (cit. on p. 108).

412. V. R. Morrison, R. P. Chatelain, K. L. Tiwari, A. Hendaoui, A. Bruhács, M. Chaker, B. J. Siwick, A Photoinduced Metal-like Phase of Monoclinic VO<sub>2</sub> Revealed by Ultrafast Electron Diffraction. *Science* **346**, 445–448 (2014) (cit. on pp. 108, 132).
413. J. Li, W.-G. Yin, L. Wu, P. Zhu, T. Konstantinova, J. Tao, J. Yang, S.-W. Cheong, F. Carbone, J. A. Misewich, J. P. Hill, X. Wang, R. J. Cava, Y. Zhu, Dichotomy in Ultrafast Atomic Dynamics as Direct Evidence of Polaron Formation in Manganites. *npj Quantum Materials* **1**, 16026 (2016) (cit. on p. 108).
414. W. Lu, M. Nicoul, U. Shymanovich, F. Brinks, M. Afshari, A. Tarasevitch, D. von der Linde, K. Sokolowski-Tinten, Acoustic Response of a Laser-Excited Polycrystalline Au-film Studied by Ultrafast DebyeScherrer Diffraction at a Table-Top Short-Pulse x-Ray Source. *AIP Advances* **10**, 035015 (2020) (cit. on pp. 108, 109).
415. N. Del Fatti, C. Voisin, D. Christofilos, F. Vallée, C. Flytzanis, Acoustic Vibration of Metal Films and Nanoparticles. *The Journal of Physical Chemistry A* **104**, 4321–4326 (2000) (cit. on p. 108).
416. J. Hohlfeld, S. S. Wellershoff, J. Güdde, U. Conrad, V. Jähnke, E. Matthias, Electron and Lattice Dynamics Following Optical Excitation of Metals. *Chemical Physics* **251**, 237–258 (2000) (cit. on pp. 108, 110, 155).
417. P. Babilotte, P. Ruello, D. Mounier, T. Pezeril, G. Vaudel, M. Edely, J.-M. Breteau, V. Gusev, K. Blary, Femtosecond Laser Generation and Detection of High-Frequency Acoustic Phonons in GaAs Semiconductors. *Physical Review B* **81**, 245207 (2010) (cit. on pp. 108, 110).
418. D. Schick, M. Herzog, H. Wen, P. Chen, C. Adamo, P. Gaal, D. G. Schlom, P. G. Evans, Y. Li, M. Bargheer, Localized Excited Charge Carriers Generate Ultrafast Inhomogeneous Strain in the Multiferroic BiFeO<sub>3</sub>. *Physical Review Letters* **112**, 097602 (2014) (cit. on p. 108).
419. I.-C. Tung, A. Krishnamoorthy, S. Sadasivam, H. Zhou, Q. Zhang, K. L. Seyler, G. Clark, E. M. Mannebach, C. Nyby, F. Ernst, D. Zhu, J. M. Glownia, M. E. Kozina, S. Song, S. Nelson, H. Kumazoe, F. Shimojo, R. K. Kalia, P. Vashishta, P. Darancet, T. F. Heinz, A. Nakano, X. Xu, A. M. Lindenberg, H. Wen, Anisotropic Structural Dynamics of Monolayer Crystals Revealed by Femtosecond Surface X-ray Scattering. *Nature Photonics* **13**, 425–430 (2019) (cit. on p. 108).

- 
420. K. Sokolowski-Tinten, R. K. Li, A. H. Reid, S. P. Weathersby, F. Quirin, T. Chase, R. Coffee, J. Corbett, A. Fry, N. Hartmann, C. Hast, R. Hettel, M. H. von Hoegen, D. Janoschka, J. R. Lewandowski, M. Ligges, F. M. zu Heringdorf, X. Shen, T. Vecchione, C. Witt, J. Wu, H. A. Dürr, X. J. Wang, Thickness-Dependent ElectronLattice Equilibration in Laser-Excited Thin Bismuth Films. *New Journal of Physics* **17**, 113047 (2015) (cit. on p. 108).
421. C. M. Chow, H. Yu, A. M. Jones, J. Yan, D. G. Mandrus, T. Taniguchi, K. Watanabe, W. Yao, X. Xu, Unusual ExcitonPhonon Interactions at van Der Waals Engineered Interfaces. *Nano Letters* **17**, 1194–1199 (2017) (cit. on p. 108).
422. C. Jin, J. Kim, J. Suh, Z. Shi, B. Chen, X. Fan, M. Kam, K. Watanabe, T. Taniguchi, S. Tongay, A. Zettl, J. Wu, F. Wang, Interlayer ElectronPhonon Coupling in WSe<sub>2</sub>/hBN Heterostructures. *Nature Physics* **13**, 127–131 (2017) (cit. on p. 108).
423. H. S. Park, J. S. Baskin, B. Barwick, O.-H. Kwon, A. H. Zewail, 4D Ultrafast Electron Microscopy: Imaging of Atomic Motions, Acoustic Resonances, and Moiré Fringe Dynamics. *Ultramicroscopy* **110**, 7–19 (2009) (cit. on p. 109).
424. A. P. Caffrey, P. E. Hopkins, J. M. Klopf, P. M. Norris, Thin Film Non-Noble Transition Metal Thermophysical Properties. *Microscale Thermophysical Engineering* **9**, 365–377 (2005) (cit. on pp. 110, 155).
425. Z. Lin, L. V. Zhigilei, V. Celli, Electron-Phonon Coupling and Electron Heat Capacity of Metals under Conditions of Strong Electron-Phonon Nonequilibrium. *Physical Review B* **77** (2008) (cit. on p. 110).
426. M. Lejman, V. Shalagatskyi, O. Kovalenko, T. Pezeril, V. V. Temnov, P. Ruello, Ultrafast Optical Detection of Coherent Acoustic Phonons Emission Driven by Superdiffusive Hot Electrons. *JOSA B* **31**, 282–290 (2014) (cit. on p. 110).
427. K.-H. Lin, C.-T. Yu, Y.-C. Wen, C.-K. Sun, Generation of Picosecond Acoustic Pulses Using a P-n Junction with Piezoelectric Effects. *Applied Physics Letters* **86**, 093110 (2005) (cit. on p. 110).
428. V. Gusev, P. Picart, D. Mounier, J. -. Breteau, On the Possibility of Ultrashort Shear Acoustic Pulse Excitation Due to the Laser-Induced Electrostrictive Effect. *Optics Communications* **204**, 229–236 (2002) (cit. on p. 110).

429. J. R. Rumble, D. R. Lide, T. J. Bruno, *CRC Handbook of Chemistry and Physics: A Ready-Reference Book of Chemical and Physical Data. 99th Edition.* ISBN: 978-1-138-56163-2 (cit. on pp. 110, 118, 123, 147, 151).
430. M. A. Hopcroft, W. D. Nix, T. W. Kenny, What Is the Young's Modulus of Silicon? *Journal of Microelectromechanical Systems* **19**, 229–238 (2010) (cit. on pp. 118, 151).
431. A. D. Raki, A. B. Djurii, J. M. Elazar, M. L. Majewski, Optical Properties of Metallic Films for Vertical-Cavity Optoelectronic Devices. *Applied Optics* **37**, 5271 (1998) (cit. on p. 118).
432. S. M. Rytov, Acoustical Properties of a Thinly Laminated Medium. (1956) (cit. on p. 119).
433. J. E. Mark, Ed., *Physical Properties of Polymers Handbook* (Springer, New York, 2nd ed, 2006); ISBN: 978-0-387-31235-4 (cit. on p. 123).
434. A. Yurtsever, S. Schaefer, A. H. Zewail, Ultrafast Kikuchi Diffraction: Nanoscale StressStrain Dynamics of Wave-Guiding Structures. *Nano Letters* **12**, 3772–3777 (2012) (cit. on p. 127).
435. S.-i. Shirota, R. Krishnan, Y. Tanaka, N. Nishiguchi, Rectifying Acoustic Waves. *Japanese Journal of Applied Physics* **46**, L1025 (2007) (cit. on p. 128).
436. S. Danworaphong, T. A. Kelf, O. Matsuda, M. Tomoda, Y. Tanaka, N. Nishiguchi, O. B. Wright, Y. Nishijima, K. Ueno, S. Juodkazis, H. Misawa, Real-Time Imaging of Acoustic Rectification. *Applied Physics Letters* **99**, 201910 (2011) (cit. on p. 128).
437. A. de la Torre, D. M. Kennes, M. Claassen, S. Gerber, J. W. McIver, M. A. Sentef, Colloquium: Nonthermal Pathways to Ultrafast Control in Quantum Materials. *Reviews of Modern Physics* **93**, 041002 (2021) (cit. on p. 132).
438. A. S. Disa, T. F. Nova, A. Cavalleri, Engineering Crystal Structures with Light. *Nature Physics* **17**, 1087–1092 (2021) (cit. on p. 132).
439. H. J. Zeiger, J. Vidal, T. K. Cheng, E. P. Ippen, G. Dresselhaus, M. S. Dresselhaus, Theory for Displacive Excitation of Coherent Phonons. *Physical Review B* **45**, 768–778 (1992) (cit. on p. 132).

- 
440. T. Rohwer, S. Hellmann, M. Wiesenmayer, C. Sohrt, A. Stange, B. Slomski, A. Carr, Y. Liu, L. M. Avila, M. Kalläne, S. Mathias, L. Kipp, K. Rossnagel, M. Bauer, Collapse of Long-Range Charge Order Tracked by Time-Resolved Photoemission at High Momenta. *Nature* **471**, 490–493 (2011) (cit. on p. 132).
441. S. Wall, D. Wegkamp, L. Foglia, K. Appavoo, J. Nag, R. Haglund, J. Stähler, M. Wolf, Ultrafast Changes in Lattice Symmetry Probed by Coherent Phonons. *Nature Communications* **3**, 721 (2012) (cit. on p. 132).
442. X. Fu, F. Barantani, S. Gargiulo, I. Madan, G. Berruto, T. LaGrange, L. Jin, J. Wu, G. M. Vanacore, F. Carbone, Y. Zhu, Nanoscale-Femtosecond Dielectric Response of Mott Insulators Captured by Two-Color near-Field Ultrafast Electron Microscopy. *Nature Communications* **11**, 5770 (2020) (cit. on p. 132).
443. S. Ji, O. Grånäs, K. Rossnagel, J. Weissenrieder, Transient Three-Dimensional Structural Dynamics in 1T-TaSe<sub>2</sub>. *Physical Review B* **101**, 094303 (2020) (cit. on p. 132).
444. M. Mitrano, A. Cantaluppi, D. Nicoletti, S. Kaiser, A. Perucchi, S. Lupi, P. Di Pietro, D. Pontiroli, M. Riccò, S. R. Clark, D. Jaksch, A. Cavalleri, Possible Light-Induced Superconductivity in K<sub>3</sub>C<sub>60</sub>. *Nature* **530**, 461–464 (2016) (cit. on p. 132).
445. T. Konstantinova, J. D. Rameau, A. H. Reid, O. Abdurazakov, L. Wu, R. Li, X. Shen, G. Gu, Y. Huang, L. Rettig, I. Avigo, M. Ligges, J. K. Freericks, A. F. Kemper, H. A. Dürr, U. Bovensiepen, P. D. Johnson, X. Wang, Y. Zhu, Nonequilibrium Electron and Lattice Dynamics of Strongly Correlated Bi<sub>2</sub>Sr<sub>2</sub>CaCu<sub>2</sub>O<sub>8+δ</sub> Single Crystals. *Science Advances* **4**, eaap7427 (2018) (cit. on p. 132).
446. D. Afanasiev, J. R. Hortensius, B. A. Ivanov, A. Sasani, E. Bousquet, Y. M. Blanter, R. V. Mikhaylovskiy, A. V. Kimel, A. D. Caviglia, Ultrafast Control of Magnetic Interactions via Light-Driven Phonons. *Nature Materials* **20**, 607–611 (2021) (cit. on p. 132).
447. A. Singer, J. G. Ramirez, I. Valmianski, D. Cela, N. Hua, R. Kukreja, J. Wingert, O. Kovalchuk, J. M. Glowia, M. Sikorski, M. Chollet, M. Holt, I. K. Schuller, O. G. Shpyrko, Nonequilibrium Phase Precursors during a Photoexcited Insulator-to-Metal Transition in V<sub>2</sub>O<sub>3</sub>. *Physical Review Letters* **120**, 207601 (2018) (cit. on pp. 132, 169).

448. C. Mariette, M. Lorenc, H. Cailleau, E. Collet, L. Guérin, A. Volte, E. Trzop, R. Bertoni, X. Dong, B. Lépine, O. Hernandez, E. Janod, L. Cario, V. Ta Phuoc, S. Ohkoshi, H. Tokoro, L. Patthey, A. Babic, I. Usov, D. Ozerov, L. Sala, S. Ebner, P. Böhler, A. Keller, A. Oggenfuss, T. Zmofing, S. Redford, S. Vetter, R. Follath, P. Juranic, A. Schreiber, P. Beaud, V. Esposito, Y. Deng, G. Ingold, M. Chergui, G. F. Mancini, R. Mankowsky, C. Svetina, S. Zerdane, A. Mozzanica, A. Bosak, M. Wulff, M. Levantino, H. Lemke, M. Cammarata, Strain Wave Pathway to Semiconductor-to-Metal Transition Revealed by Time-Resolved X-ray Powder Diffraction. *Nature Communications* **12**, 1239 (2021) (cit. on pp. 132, 169).
449. J. N. Clark, L. Beitra, G. Xiong, A. Higginbotham, D. M. Fritz, H. T. Lemke, D. Zhu, M. Chollet, G. J. Williams, M. Messerschmidt, B. Abbey, R. J. Harder, A. M. Korsunsky, J. S. Wark, I. K. Robinson, Ultrafast Three-Dimensional Imaging of Lattice Dynamics in Individual Gold Nanocrystals. *Science* **341**, 56–59 (2013) (cit. on pp. 132, 139, 150).
450. Y. Zhu, Z. Cai, P. Chen, Q. Zhang, M. J. Highland, I. W. Jung, D. A. Walko, E. M. Dufresne, J. Jeong, M. G. Samant, S. S. P. Parkin, J. W. Freeland, P. G. Evans, H. Wen, Mesoscopic Structural Phase Progression in Photo-Excited VO<sub>2</sub> Revealed by Time-Resolved x-Ray Diffraction Microscopy. *Scientific Reports* **6**, 21999 (2016) (cit. on p. 132).
451. P. Zalden, F. Quirin, M. Schumacher, J. Siegel, S. Wei, A. Koc, M. Nicoul, M. Trigo, P. Andreasson, H. Enquist, M. J. Shu, T. Pardini, M. Chollet, D. Zhu, H. Lemke, I. Ronneberger, J. Larsson, A. M. Lindenberg, H. E. Fischer, S. Hau-Riege, D. A. Reis, R. Mazzarello, M. Wuttig, K. Sokolowski-Tinten, Femtosecond X-Ray Diffraction Reveals a Liquid-Liquid Phase Transition in Phase-Change Materials. *Science* **364**, 1062–1067 (2019) (cit. on p. 132).
452. F. Büttner, B. Pfau, M. Böttcher, M. Schneider, G. Mercurio, C. M. Günther, P. Hessian, C. Klose, A. Wittmann, K. Gerlinger, L.-M. Kern, C. Strüber, C. von Korff Schmising, J. Fuchs, D. Engel, A. Churikova, S. Huang, D. Suzuki, I. Lemesh, M. Huang, L. Caretta, D. Weder, J. H. Gaida, M. Möller, T. R. Harvey, S. Zayko, K. Bagschik, R. Carley, L. Mercadier, J. Schlappa, A. Yaroslavtsev, L. Le Guyarder, N. Gerasimova, A. Scherz, C. Deiter, R. Gort, D. Hickin, J. Zhu, M. Turcato, D. Lomidze, F. Erdinger, A. Castoldi, S. Maffessanti, M. Porro, A. Samartsev, J. Sinova, C. Ropers, J. H. Mentink, B. Dupé, G. S. D. Beach, S. Eisebitt, Observation

- 
- of Fluctuation-Mediated Picosecond Nucleation of a Topological Phase. *Nature Materials* **20**, 30–37 (2021) (cit. on p. 132).
453. S. K. Cushing, M. Zürich, P. M. Kraus, L. M. Carneiro, A. Lee, H.-T. Chang, C. J. Kaplan, S. R. Leone, Hot Phonon and Carrier Relaxation in Si(100) Determined by Transient Extreme Ultraviolet Spectroscopy. *Structural Dynamics* **5**, 054302 (2018) (cit. on p. 132).
454. Y. Zhang, D. J. Flannigan, Imaging Nanometer Phonon Softening at Crystal Surface Steps with 4D Ultrafast Electron Microscopy. *Nano Letters* **21**, 7332–7338 (2021) (cit. on p. 132).
455. B. Graczykowski, M. Sledzinska, F. Alzina, J. Gomis-Bresco, J. S. Reparaz, M. R. Wagner, C. M. Sotomayor Torres, Phonon Dispersion in Hypersonic Two-Dimensional Phononic Crystal Membranes. *Physical Review B* **91**, 075414 (2015) (cit. on p. 141).
456. A. Morawiec, Formal Conditions for Unambiguous Residual Strain Determination by CBED. *Philosophical Magazine* **85**, 1611–1623 (2005) (cit. on p. 150).
457. COMSOL: Multiphysics Software for Optimizing Designs, <https://www.comsol.com/> (cit. on p. 150).
458. A. F. Bower, *Applied Mechanics of Solids* (Taylor & Francis Inc, Boca Raton, First, 2009); ISBN: 978-1-4398-0247-2 (cit. on p. 151).
459. W. S. M. Werner, K. Glantschnig, C. Ambrosch-Draxl, Optical Constants and Inelastic Electron-Scattering Data for 17 Elemental Metals. *Journal of Physical and Chemical Reference Data* **38**, 1013–1092 (2009) (cit. on p. 151).
460. G. Hamaoui, N. Horny, Z. Hua, T. Zhu, J.-F. Robillard, A. Fleming, H. Ban, M. Chirtoc, Electronic Contribution in Heat Transfer at Metal-Semiconductor and Metal Silicide-Semiconductor Interfaces. *Scientific Reports* **8**, 11352 (2018) (cit. on p. 151).
461. Y. Li, R. B. Thompson, Influence of Anisotropy on the Dispersion Characteristics of Guided Ultrasonic Plate Modes. *The Journal of the Acoustical Society of America* **87**, 1911–1931 (1990) (cit. on p. 153).
462. I. A. Viktorov, *Rayleigh and Lamb Waves: Physical Theory and Applications* (Springer US, 1967); ISBN: 978-1-4899-5683-5 (cit. on p. 154).

463. D. Zahn, H. Seiler, Y. W. Windsor, R. Ernstorfer, Ultrafast Lattice Dynamics and ElectronPhonon Coupling in Platinum Extracted with a Global Fitting Approach for Time-Resolved Polycrystalline Diffraction Data. *Structural Dynamics* **8**, 064301 (2021) (cit. on p. 155).
464. P. Hommelhoff, Y. Sortais, A. Aghajani-Talesh, M. A. Kasevich, Field Emission Tip as a Nanometer Source of Free Electron Femtosecond Pulses. *Physical Review Letters* **96**, 077401 (2006) (cit. on pp. 161, 162).
465. M. Schenk, M. Krüger, P. Hommelhoff, Strong-Field Above-Threshold Photoemission from Sharp Metal Tips. *Physical Review Letters* **105**, 257601 (2010) (cit. on pp. 161, 162).
466. S. Meier, P. Hommelhoff, Coulomb Interactions and the Spatial Coherence of Femtosecond Nanometric Electron Pulses. (2021) (cit. on p. 162).
467. B. Cho, T. Ichimura, R. Shimizu, C. Oshima, Quantitative Evaluation of Spatial Coherence of the Electron Beam from Low Temperature Field Emitters. *Physical Review Letters* **92**, 246103 (2004) (cit. on p. 162).
468. E. Fill, L. Veisz, A. Apolonski, F. Krausz, Sub-Fs Electron Pulses for Ultrafast Electron Diffraction. *New Journal of Physics* **8**, 272–272 (2006) (cit. on p. 163).
469. A. Gliserin, A. Apolonski, F. Krausz, P. Baum, Compression of Single-Electron Pulses with a Microwave Cavity. *New Journal of Physics* **14**, 073055 (2012) (cit. on p. 163).
470. A. Gliserin, M. Walbran, F. Krausz, P. Baum, Sub-Phonon-Period Compression of Electron Pulses for Atomic Diffraction. *Nature Communications* **6**, 8723 (2015) (cit. on p. 163).
471. M. Gao, H. Jean-Ruel, R. R. Cooney, J. Stampe, M. de Jong, M. Harb, G. Sciaini, G. Moriena, R. J. D. Miller, Full Characterization of RF Compressed Femtosecond Electron Pulses Using Ponderomotive Scattering. *Optics Express* **20**, 12048–12058 (2012) (cit. on p. 163).
472. A. Gliserin, M. Walbran, P. Baum, Passive Optical Enhancement of Laser-Microwave Synchronization. *Applied Physics Letters* **103**, 031113 (2013) (cit. on p. 163).

- 
473. F. B. Kiewiet, A. H. Kemper, O. J. Luiten, G. J. H. Brussaard, M. J. van der Wiel, Femtosecond Synchronization of a 3GHz RF Oscillator to a Mode-Locked Ti:Sapphire Laser. *Nuclear Instruments and Methods in Physics Research Section A: Accelerators, Spectrometers, Detectors and Associated Equipment* **484**, 619–624 (2002) (cit. on p. 163).
474. M. R. Otto, L. P. René de Cotret, M. J. Stern, B. J. Siwick, Solving the Jitter Problem in Microwave Compressed Ultrafast Electron Diffraction Instruments: Robust Sub-50 Fs Cavity-Laser Phase Stabilization. *Structural Dynamics* **4**, 051101 (2017) (cit. on p. 163).
475. D. Ehberger, C. Kealhofer, P. Baum, Electron Energy Analysis by Phase-Space Shaping with THz Field Cycles. *Structural Dynamics* **5**, 044303 (2018) (cit. on p. 163).
476. M. Born, E. Wolf, *Principles of Optics: Electromagnetic Theory of Propagation, Interference and Diffraction of Light* (Cambridge University Press, Cambridge ; New York, 7th expanded ed, 1999); ISBN: 978-0-521-64222-4 (cit. on p. 164).
477. R. Erni, *Aberration-Corrected Imaging in Transmission Electron Microscopy: An Introduction* (Imperial College Press, London, 2nd edition, 2015); ISBN: 978-1-78326-528-2 (cit. on pp. 164, 165).
478. O. Scherzer, Über einige Fehler von Elektronenlinsen. *Zeitschrift für Physik* **101**, 593–603 (1936) (cit. on p. 164).
479. H. Rose, Abbildungseigenschaften Sphärisch Korrigierter Elektronenoptischer Achromate. *Optik* **33**, 1–24 (1971) (cit. on p. 165).
480. A. V. Crewe, A System for the Correction of Axial Aperture Aberrations in Electron Lenses. *Optik* **60** (1982) (cit. on p. 165).
481. O. L. Krivanek, N. Dellby, A. R. Lupini, Towards Sub-Å Electron Beams. *Ultramicroscopy* **78**, 1–11 (1999) (cit. on p. 165).
482. M. Haider, H. Müller, S. Uhlemann, J. Zach, U. Loebau, R. Hoeschen, Prerequisites for a Cc/Cs-corrected Ultrahigh-Resolution TEM. *Ultramicroscopy* **108**, 167–178 (2008) (cit. on p. 165).
483. O. Scherzer, Sphärische Und Chromatische Korrektur von Elektronen-Linsen. *Optik* **2**, 114–132 (1947) (cit. on p. 165).

484. V. Beck, A Hexapole Spherical Aberration Corrector. *Optik* **52**, 241–255 (1979) (cit. on p. 165).
485. H. Rose, Outline of a Spherically Corrected Semi-Aplanatic Medium-Voltage TEM. *Optik* **85**, 19–24 (1990) (cit. on p. 165).
486. M. Haider, H. Rose, S. Uhlemann, E. Schwan, B. Kabius, K. Urban, A Spherical-Aberration-Corrected 200 kV Transmission Electron Microscope. *Ultramicroscopy* **75**, 53–60 (1998) (cit. on p. 165).
487. H. Sawada, T. Tomita, M. Naruse, T. Honda, P. Hambridge, P. Hartel, M. Haider, C. Hetherington, R. Doole, A. Kirkland, J. Hutchison, J. Titchmarsh, D. Cockayne, Experimental Evaluation of a Spherical Aberration-Corrected TEM and STEM. *Journal of Electron Microscopy* **54**, 119–121 (2005) (cit. on p. 165).
488. H. Müller, S. Uhlemann, P. Hartel, M. Haider, Advancing the Hexapole  $C_s$ -Corrector for the Scanning Transmission Electron Microscope. *Microscopy and Microanalysis* **12**, 442–455 (2006) (cit. on p. 165).
489. R. Erni, M. D. Rossell, C. Kisielowski, U. Dahmen, Atomic-Resolution Imaging with a Sub-50-pm Electron Probe. *Physical Review Letters* **102**, 096101 (2009) (cit. on p. 165).
490. R. Sagawa, A. Yasuhara, H. Hashiguchi, T. Naganuma, S. Tanba, T. Ishikawa, T. Riedel, P. Hartel, M. Linck, S. Uhlemann, H. Müller, H. Sawada, Exploiting the Full Potential of the Advanced Two-Hexapole Corrector for STEM Exemplified at 60kV. *Ultramicroscopy* **233**, 113440 (2022) (cit. on p. 165).
491. P. Hartel, V. Gerheim, M. Linck, H. Müller, S. Uhlemann, Z. Zach, M. Haider, On the Residual Six-Fold Astigmatism in DCOR/ASCOR. *Ultramicroscopy* **206**, 112821 (2019) (cit. on p. 165).
492. J. Wen, J. Mabon, C. Lei, S. Burdin, E. Sammann, I. Petrov, A. B. Shah, V. Chobpattana, J. Zhang, K. Ran, J.-M. Zuo, S. Mishina, T. Aoki, The Formation and Utility of Sub-Angstrom to Nanometer-Sized Electron Probes in the Aberration-Corrected Transmission Electron Microscope at the University of Illinois. *Microscopy and Microanalysis* **16**, 183–193 (2010) (cit. on p. 165).
493. D. Geiger, H. Lichte, M. Linck, M. Lehmann, Electron Holography with a  $C_s$ -Corrected Transmission Electron Microscope. *Microscopy and Microanalysis* **14**, 68–81 (2008) (cit. on p. 165).

- 
494. R. F. Egerton, K. Wong, Some Practical Consequences of the Lorentzian Angular Distribution of Inelastic Scattering. *Ultramicroscopy* **59**, 169–180 (1995) (cit. on p. 167).
495. J.-W. Henke, A. S. Raja, A. Feist, G. Huang, G. Arend, Y. Yang, F. J. Kappert, R. N. Wang, M. Möller, J. Pan, J. Liu, O. Kfir, C. Ropers, T. J. Kippenberg, Integrated Photonics Enables Continuous-Beam Electron Phase Modulation. *Nature* **600**, 653–658 (2021) (cit. on p. 167).
496. M. Tanaka, M. Terauchi, K. Tsuda, K. Saitoh, *Convergent-Beam Electron Diffraction* (JEOL Ltd, Tokyo, 2002) (cit. on p. 167).
497. C. Schaal, A. Mal, Lamb Wave Propagation in a Plate with Step Discontinuities. *Wave Motion* **66**, 177–189 (2016) (cit. on p. 168).
498. F. Legrand, B. Gérardin, J. Laurent, C. Prada, A. Aubry, Negative Refraction of Lamb Modes: A Theoretical Study. *Physical Review B* **98**, 214114 (2018) (cit. on p. 168).
499. F. D. Philippe, T. W. Murray, C. Prada, Focusing on Plates: Controlling Guided Waves Using Negative Refraction. *Scientific Reports* **5**, 11112 (2015) (cit. on p. 168).
500. M. Germano, A. Alippi, A. Bettucci, G. Mancuso, Anomalous and Negative Reflection of Lamb Waves in Mode Conversion. *Physical Review B* **85**, 012102 (2012) (cit. on p. 168).
501. I. A. Veres, C. Grünsteidl, D. M. Stobbe, T. W. Murray, Broad-Angle Negative Reflection and Focusing of Elastic Waves from a Plate Edge. *Physical Review B* **93**, 174304 (2016) (cit. on p. 168).
502. C. Prada, D. Clorennec, D. Royer, Local Vibration of an Elastic Plate and Zero-Group Velocity Lamb Modes. *The Journal of the Acoustical Society of America* **124**, 203–212 (2008) (cit. on p. 168).
503. A. L. Shuvalov, O. Poncelet, On the Backward Lamb Waves near Thickness Resonances in Anisotropic Plates. *International Journal of Solids and Structures* **45**, 3430–3448 (2008) (cit. on p. 168).
504. J. B. Pendry, D. R. Smith, Reversing Light With Negative Refraction. *Physics Today* **57**, 37–43 (2004) (cit. on p. 168).

505. V. G. Veselago, E. E. Narimanov, The Left Hand of Brightness: Past, Present and Future of Negative Index Materials. *Nature Materials* **5**, 759–762 (2006) (cit. on p. 168).
506. D. M. Stobbe, T. W. Murray, Conical Dispersion of Lamb Waves in Elastic Plates. *Physical Review B* **96**, 144101 (2017) (cit. on p. 168).
507. A. Castellanos-Gomez, M. Buscema, R. Molenaar, V. Singh, L. Janssen, H. S. J. van der Zant, G. A. Steele, Deterministic Transfer of Two-Dimensional Materials by All-Dry Viscoelastic Stamping. *2D Materials* **1**, 011002 (2014) (cit. on p. 169).
508. M. ikins, M. Lee, F. Alijani, M. R. van Blankenstein, D. Davidovikj, H. S. J. van der Zant, P. G. Steeneken, Highly Anisotropic Mechanical and Optical Properties of 2D Layered As<sub>2</sub>S<sub>3</sub> Membranes. *ACS Nano* **13**, 10845–10851 (2019) (cit. on p. 169).
509. M. C. Lemme, S. Wagner, K. Lee, X. Fan, G. J. Verbiest, S. Wittmann, S. Lukas, R. J. Dolleman, F. Niklaus, H. S. J. van der Zant, G. S. Duesberg, P. G. Steeneken, Nanoelectromechanical Sensors Based on Suspended 2D Materials. *Research* **2020** (2020) (cit. on p. 169).
510. C. Lee, X. Wei, J. W. Kysar, J. Hone, Measurement of the Elastic Properties and Intrinsic Strength of Monolayer Graphene. *Science* **321**, 385–388 (2008) (cit. on p. 169).
511. D. Akinwande, C. Brennan, J. Bunch, P. Egberts, J. Felts, H. Gao, R. Huang, J.-S. Kim, T. Li, Y. Li, K. Liechti, N. Lu, H. Park, E. Reed, P. Wang, B. Yakobson, T. Zhang, Y.-W. Zhang, Y. Zhou, Y. Zhu, A Review on Mechanics and Mechanical Properties of 2D Materials - Graphene and Beyond. *Extreme Mechanics Letters* **13** (2016) (cit. on p. 169).
512. C. Androulidakis, K. Zhang, M. Robertson, S. Tawfick, Tailoring the Mechanical Properties of 2D Materials and Heterostructures. *2D Materials* **5**, 032005 (2018) (cit. on p. 169).
513. A. Eichler, J. Moser, J. Chaste, M. Zdrojek, I. Wilson-Rae, A. Bachtold, Nonlinear Damping in Mechanical Resonators Made from Carbon Nanotubes and Graphene. *Nature Nanotechnology* **6**, 339–342 (2011) (cit. on p. 169).

- 
514. A. Kekekler, O. Shoshani, M. Lee, H. S. J. van der Zant, P. G. Steeneken, F. Alijani, Tuning Nonlinear Damping in Graphene Nanoresonators by Parametric Direct Internal Resonance. *Nature Communications* **12**, 1099 (2021); doi:10.1038/s41467-021-21334-w (cit. on pp. 169, 170).
515. D. Davidovikj, F. Alijani, S. J. Cartamil-Bueno, H. S. J. van der Zant, M. Amabili, P. G. Steeneken, Nonlinear Dynamic Characterization of Two-Dimensional Materials. *Nature Communications* **8**, 1253 (2017) (cit. on p. 169).
516. J. S. Huber, G. Rastelli, M. J. Seitner, J. Kölbl, W. Belzig, M. I. Dykman, E. M. Weig, Spectral Evidence of Squeezing of a Weakly Damped Driven Nanomechanical Mode. *Physical Review X* **10**, 021066 (2020) (cit. on p. 169).
517. P. Prasad, N. Arora, A. K. Naik, Parametric Amplification in MoS<sub>2</sub> Drum Resonator. *Nanoscale* **9**, 18299–18304 (2017) (cit. on p. 169).
518. R. J. Dolleman, S. Hourii, A. Chandrashekar, F. Alijani, H. S. J. van der Zant, P. G. Steeneken, Opto-Thermally Excited Multimode Parametric Resonance in Graphene Membranes. *Scientific Reports* **8**, 9366 (2018) (cit. on p. 169).
519. J. Güttinger, A. Noury, P. Weber, A. M. Eriksson, C. Lagoin, J. Moser, C. Eichler, A. Wallraff, A. Isacsson, A. Bachtold, Energy-Dependent Path of Dissipation in Nanomechanical Resonators. *Nature Nanotechnology* **12**, 631–636 (2017) (cit. on p. 169).
520. A. Kavokin, Ed., *Microcavities* (Oxford University Press, Oxford ; New York, NY, Second Edition, 2017); ISBN: 978-0-19-878299-5 (cit. on p. 171).
521. N. Müller, V. Hock, H. Koch, N. Bach, C. Rathje, S. Schäfer, Broadband Coupling of Fast Electrons to High-Q Whispering-Gallery Mode Resonators. *ACS Photonics* **8**, 1569–1575 (2021) (cit. on p. 228).



---

## Publications, conferences and awards

---

### Publications

The present cumulative thesis comprises the following articles, reprinted in Chapters 3, 6 and 7, that fulfill the requirements for a cumulative thesis according to the doctoral degree regulations at the Carl-von-Ossietzky University:

- N. Bach, T. Domröse, A. Feist, Th. Rittmann, S. Strauch, C. Ropers, S. Schäfer, Coulomb interactions in high-coherence femtosecond electron pulses from tip emitters. *Structural Dynamics* **6**, 04301 (2019); doi: 10.1063/1.5066093 (see Ref. [173]).
- N. Bach, S. Schäfer, Ultrafast Strain Propagation and Acoustic Resonances in Nanoscale Bilayer Systems. *Structural Dynamics* **8**, 035101 (2021); doi:10.1063/4.0000079 (see Ref. [277]).
- N. Bach, A. Feist, M. Möller, C. Ropers, S. Schäfer, Tailored Nanophononic Wavefield in a Patterned Bilayer System Probed by Ultrafast Convergent Beam Electron Diffraction. *Structural Dynamics* **9**, 034301 (2022); doi:10.1063/4.0000144 (see Ref. [116]).

The experimental work described in the first and third publication was conducted during the first phase (December 2016 – August 2018) of the PhD in the group *Nano-Optics and Ultrafast Dynamics* of Professor C. Ropers at the University of Göttingen.

The following articles originated over the course of this work and are not a direct part of the cumulative thesis:

- A. Ungeheuer, N. Bach, A. Hassanien, M. Mir, L. Nöding, S. Schäfer, T. Baumert, A. Senftleben, Coherent acoustic phonons in a hBN-graphite heterostructure observed by ultrafast electron diffraction. (in preparation)
- N. Müller, V. Hock, H. Koch, N. Bach, C. Rathje, S. Schäfer, Broadband Coupling of Fast Electrons to High-Q Whispering-Gallery Mode Resonators. *ACS Photonics* **8**, 1569–1575 (2021); doi.org/10.1021/acsp Photonics.1c00456 (see Ref. [521]).

## **Conference talks**

- *Highly coherent femtosecond electron pulses for ultrafast transmission electron microscopy*, IVNC, Regensburg (2017).
- *Ultrashort electron pulses in the space charge regime*, Workshop Winterschool, Delmenhorst (2017).
- *Highly coherent femtosecond electron pulses for ultrafast transmission electron microscopy*, Ultrafast Phenomena (UP), Hamburg, Germany (2018).
- *Structural Dynamics in Nanostructured Systems Probed by Ultrafast Convergent Beam Electron Diffraction*, Virtual Early Career European Microscopy Congress (EMC), virtual conference (2020).

## **Conference posters**

- *Source Development for Ultrafast Transmission Electron Microscopy*, DPG Spring Meeting (SKM), Dresden, Germany (2017).
- *Highly coherent femtosecond electron pulses for ultrafast transmission electron microscopy*, Electron Microscopy at High Temporal Resolution (EMHTR), Strasbourg, France (2017).
- *Ultrafast transmission electron microscopy of structural dynamics in nanostructured systems*, Gordon Research Conference and Seminar (GRC/GRS): Ultrafast Phenomena in Cooperative Systems, Galveston, TX, USA (2018).

- *Ultrashort electron pulses in the space charge regime*, DPG Spring Meeting (SKM), Berlin, Germany (2018).
- *Highly coherent femtosecond electron pulses for ultrafast transmission electron microscopy*, Ultrafast Phenomena (UP), Hamburg, Germany (2018).
- *Ultrafast transmission electron microscopy of structural dynamics in nanostructured systems*, Son et Lumière 2019 – Wave interactions at the nanoscale, Les Houches, France (2019).
- *Structural dynamics in nanostructured systems probed by ultrafast transmission electron microscopy*, Gordon Research Conference and Seminar (GRC/GRS): Ultrafast Phenomena in Cooperative Systems, Barga, Italy (2020).
- *Coulomb Interactions in High-Coherence Femtosecond Electron Pulses from Tip Emitters*, Virtual Early Career European Microscopy Congress (EMC), virtual conference (2020).

## **Awards and scholarships**

- Doctoral scholarship by the *German Academic Scholarship Foundation* (2018–2019).
- Participant at the 70th Lindau Nobel Laureate Meeting (2021)
- “Best Poster Award” award at the *UP 2018* hosted by the European Physical Society (EPS) (2018).



---

## Danksagung

---

An dieser Stelle möchte ich mich bei all denjenigen bedanken, die mich während meiner Promotion unterstützt und zum Entstehen dieser Dissertation beigetragen haben.

Insbesondere gilt mein Dank *Prof. Dr. Sascha Schäfer*, der mir die Möglichkeit der Promotion eröffnet hat und durch seine Betreuung maßgeblich zum Erfolg der Arbeit beigetragen hat. Vielen Dank für die Geduld und die Unermüdlichkeit, immer wieder neu über anschauliche Erklärungen nachzudenken und damit die Grundlage für wertvolle Gespräche zu legen. Zugleich schätze ich mich glücklich über einige Besuche nationaler und internationaler Konferenzen.

Weiterhin danke ich *Prof. Dr. Christoph Lienau* für die interessierten Gespräche zu meinem Projekt, für Ratschläge, Vorschläge und Hilfe, wann immer ich darum gebeten habe, und nicht zuletzt für die Übernahme des Korreferats.

Mein ausdrücklicher Dank geht an *Prof. Dr. Claus Ropers*, der mir speziell zu Beginn meiner Promotion seine Labore mit vollem Vertrauen zur Verfügung gestellt hat und ich so wesentliche experimentelle Daten für meine Dissertation aufnehmen konnte. Trotz der anschließenden Distanz und der Herausforderungen in der aktuellen Zeit bestand ein fortlaufender wissenschaftlicher und persönlicher Kontakt, für den ich sehr dankbar bin.

*Ela Chojnowski* danke ich für die schnelle, unkomplizierte Bearbeitung aller administrativer Angelegenheiten und den persönlichen Kontakt, der weit über diese Aufgaben hinaus ging.

Dank *Thomas Danz* konnte ich ein perfektes L<sup>A</sup>T<sub>E</sub>X-Template direkt mit Inhalt füllen. *Thomas Rittmann*, *Hugo Lourenço* und *Till Domröse* haben meine Dissertation mit großem Engagement und einer motivierenden Mischung aus Liebe zum Detail und dem Blick auf das große Ganze Korrektur gelesen. Vielen Dank, dass ich mich immer auf euch verlassen konnte! Zu einem guten wissenschaftlichen Text gehören auch überzeugende Abbildungen. Danke an *Gerrit Horstmann*, der diese Kunst meisterhaft beherrscht und mich immer wieder inspiriert hat.

Meine Promotionszeit war auf zwei Arbeitsgruppen in Göttingen und Oldenburg aufgeteilt. Mein besonderer Dank gilt zum einen dem Oldenburger UTEM-Team mit

*Alexander Schröder, Christopher Rathje, Niklas Müller, Lina Hansen, Rieke von Seggern und Jonathan Weber.* Vielen Dank für die gemeinsame Zeit im Büro, das Tüfteln rund um die UTEM gun mit technischer Hilfe von *Matthias Macke* und *Holger Koch* und all die Gespräche völlig unabhängig von der Physik. Zum anderen möchte ich dem gesamten UTEM-Team in Göttingen danken, das über die Jahre seit meiner Masterarbeit auf sehr viele Arten und Weisen zum Gelingen meines Projekts beigetragen hat. Sowohl die tolle, kompetente und engagierte Zusammenarbeit bis zu meinem Wechsel nach Oldenburg, als auch der danach weiterhin bestehende Kontakt sind nicht selbstverständlich. Dies gilt insbesondere für *Karin Ahlborn, Till Domröse, Thomas Danz, Thomas Rittmann, Armin Feist, Marcel Möller, Nara Rubiano da Silva* und *John Gaida*.

Ich möchte mich auch bei meiner Familie, meiner Patentante und meinem Patenonkel und engen Freundinnen und Freunden bedanken. Ihr habt mich mit Rat und Tat beständig unterstützt, mit mir spannende und fröhliche Momente in und außerhalb der Uni erlebt, mit mir Musik gemacht oder Theater gespielt, ihr seid mit mir an die geliebte Nordsee gefahren, und habt mir dadurch insgesamt eine sehr schöne Zeit in Göttingen, Oldenburg und Umgebung beschert.

In Bezug auf meine Leidenschaft für Musik und Theater danke ich allen aus meinem Freundeskreis, meinen Oboenlehrern und dem physikalischen Umfeld für die gemeinsamen Erlebnisse in Proben und auf der Bühne, sowie für das Mitfiebern in Auswahlverfahren und im Publikum. Dadurch sind die Auftritte für mich unvergesslich geworden und mein Traum, Physik und Kunst zu kombinieren, hat sich auf wunderbare Weise erfüllt. Mein ausdrücklicher Dank geht an dieser Stelle an *Britta Vinçon*. Ich freue mich sehr über die Entwicklung unserer Freundschaft seit Beginn meines Bachelorstudiums.

In Oldenburg hat mir *Ghassem Rasuli* viele schöne Ecken gezeigt, meine Freude über künstlerische und wissenschaftliche Seifenblasen-Spielereien geteilt und mich mit viel Empathie durch Höhen und Tiefen meiner Promotionszeit begleitet. Vielen Dank dafür!

Ein ganz herzlicher Dank gilt *Jusara Moser*, die mir seit dem Ende der Schulzeit nicht nur eine enge Freundin geworden ist, mit der ich viele Opern- und Konzertabende auf der Bühne und im Publikum geteilt habe, sondern die mich auch auf meinem wissenschaftlichen Weg immer bestärkt hat. Vielen Dank für dein offenes Ohr, Aufmunterungen, wenn es nicht so lief wie gewünscht, und all die schönen Momente bei gegenseitigen Besuchen.

---

## Erklärung

---

Hiermit versichere ich, dass ich die vorliegende Arbeit unter Berücksichtigung der Leitlinien guter wissenschaftlicher Praxis an der Carl-von-Ossietzky Universität Oldenburg selbstständig angefertigt und keine anderen als die angegebenen Quellen und Hilfsmittel verwendet habe. Zusätzlich erkläre ich, dass diese Dissertation weder in ihrer Gesamtheit noch in Teilen einer anderen wissenschaftlichen Hochschule zur Begutachtung in einem Promotionsvorhaben vorliegt oder vorgelegen hat und dass im Zusammenhang mit dem Promotionsvorhaben keine kommerziellen Vermittlungs- und Beratungsdienste in Anspruch genommen worden sind.